universität wien

DISSERTATION

Titel der Dissertation

„Non-centrosymmetric superconducting compounds“

Verfasserin

Mag. Isolde Zeiringer

angestrebter akademischer Grad

Doktorin der Naturwissenschaften (Dr. rer. nat.)

Wien, 2015

Studienkennzahl lt. Studienblatt:	A 791 419
Dissertationsgebiet lt. Studienblatt:	Chemie
Betreuerin / Betreuer:	Univ.-Prof. i.R. Dr. Peter Franz Rogl

Table of Content

Acknowledgement

First and foremost I want to express my deepest gratitude to my supervisor Prof. Peter Franz Rogl for getting the opportunity to work in his group and for all his strong support. I also gratefully acknowledge Dr. Andriy Grytsiv, Dr. Gerda Rogl, Dr. Matthias Falmbigl and all my present and former colleagues from the department of Physical Chemistry for their help and scientific discussions. Furthermore, I want to thank Dr. Stephan Puchegger from the Faculty Center for Nanostructure Research for his support with the SEM measurements. I would like to express my sincere acknowledgements to Prof. Ernst Bauer, Dr. Friedrich Kneidinger and all the other members of his group from the Technical University of Vienna and also Prof. Raimund Podloucky and his group for their collaboration. I am thankful to Prof. Julian Sereni (Div. Bajas Temperaturas, CAB-CNEA, Bariloche, Argentina) for all the measurements, discussions and for his efforts to make my stay in Barilloche very pleasant. I also want to thank Dr. Pavel Brož, Dr. J. Sopousek, Dr. J. Buršík, Prof. J. Vrestal and Mgr. O. Zobac (Faculty of Science, Department of Chemistry, Masaryk University, Brno, Czech Republic) for their DSC/DTA measurements as well as their collaboration.

I gratefully acknowledge the financially support by the Austrian Science Fund FWF under Grant P22295 and by the OEAD.

Finally I want to thank my husband, my parents and my whole family, as without their support this work would not have been possible.

Abstract

Superconductivity in compounds without inversion symmetry in the crystal structure induced intensive research interest during the last decades as many superconducting properties and parameters do not comply with the standard BCS theory. The present work primary focuses on the preparation and characterization of non-centrosymmetric intermetallic compounds and the corresponding ternary systems and comprises of three main parts.

The first one deals with the reinvestigations of the superconducting equiatomic silicides or germanides LaPtSi, LaIrSi and HfRhGe with ordered non-centrosymmetric crystal structures, deriving from the binary compounds α-$ThSi_2$, $SrSi_2$ or AlB_2. Additionally, the compound CeIrSi has been studied.

The second part concentrates on crystal structures and/or phase diagram investigations of binary, ternary and quaternary borides. The binary Ir-B system has been reinvestigated between 10 and 70 at. % boron by means of differential scanning calorimetry, electron probe micro analysis, X-ray powder diffraction, X-ray single crystal diffraction and electron probe micro analysis. Four binary phases have been found, namely Ir_4B_{5+x}, Ir_5B_{4+x} and the high and low temperature modification of Ir_4B_{3-x}. X-ray single crystal diffraction studies have been performed on Ir_4B_{5+x} (Ir_4B_5 type), Ir_5B_{4+x} (Ir_5B_4 type) and on the non-centrosymmetric low temperature modification of Ir_4B_{3-x} ($IrB_{0.9}$ type). The high temperature modification of Ir_4B_{3-x} (WC type; also non-centrosymmetric) has been confirmed by X-ray powder diffraction.

The crystal structure of $W_{1-x}B_3$ has been reinvestigated by X-ray single crystal diffraction and revealed isotypism with the $Mo_{1-x}B_3$ structure type. The solubility of Rh, Ir, Ni, Pd and Pt in $W_{1-x}B_3$ as well as of Rh in $Mo_{1-x}B_3$ has been investigated in as cast state and after annealing. Furthermore, phase equilibria in the boron rich part of the corresponding isothermal sections W-TM-B (TM = Rh, Ir at 1100°C, TM = Ni, Pd at 900°C and TM = Pt at 800°C) and Mo-Rh-B (at 1100°C) have been established. A ternary compound $W_{1-x}Ir_xB_2$ (ReB_2 type) only forms in the system W-Ir-B. The type of formation and crystal structure of diborides $W_{1-x}TM_xB_2$ (TM = Ru, Os, Ir) isotypic with ReB_2 were studied by X-ray powder diffraction and electron probe microanalysis in as cast state and after annealing at 1500°C.

The solid solution $CeRh_{3-x}Pd_xB_{0.5}$ (x=0, 0.5, 1.2, 1.5, 1.7, 2.5, 3) has been studied in as cast state with respect to the crystal structure (superstructure formation) and valence change of cerium.

The third part summarizes the results from the investigations of a large number of ternary compounds EpT_2X_2 or $EpTX_3$ (*Ep* = Sr, Ba; *T* = Ni, Pd, Pt, Cu, Ag, Au; *X* = Si, Ge, Sn) crystallizing with the non-centrosymmetric $BaNiSn_3$ structure type or another $BaAl_4$ derivative structure type. Superconductivity (< 3 K) has been found for 7 compounds adopting the $BaNiSn_3$ structure type. Group – subgroup relations with the aristotype $BaAl_4$ were constructed focussing on the non-centrosymmetric structure types. In order to elucidate formation, structure and properties of clathrate structures and other ternary compounds, the silicon or germanium rich part of the ternary systems Sr-{Cu,Ag,Au}-{Si,Ge} and Ba-{Ag,Au}-{Si,Ge} were investigated at 700 or 800 °C, depending on the system. Beside the partial isothermal sections at 600 and 800°C, also the liquidus and solidus projections have been constructed for the ternary system Ba-Ag-Ge. The ternary invariant reactions are shown in form of a Schulz-Scheil diagram. The crystal structures and homogeneity ranges of more than 20 new or already reported compounds have been explored by electron probe microanalysis, X-ray powder diffraction and X-ray single crystal diffraction in several cases:

$Sr_8Cu_xGe_{46-x}$ (clathrate type-I); $SrCu_{2-x}Ge_{2+x}$ ($ThCr_2Si_2$ type); $Ba_{8-y}Sr_yCu_xGe_{46-x}$ (clathrate type-I); $Sr_2Ag_{1+x}Si_{3-x-y}\square_y$ (Sr_2LiSi_3 type); $SrAg_{2-x}Si_{2+x}$ ($ThCr_2Si_2$ type); $Sr(Ag_xGe_{1-x})_2$ (AlB_2 type); $SrAg_{2-x}Ge_{2+x}$ ($ThCr_2Si_2$ type); $Sr(Au_{1-y}\square_y)(Si_{1-x}Au_x)_3$ ($BaNiSn_3$ type); $SrAu_{5-x}\square_xSi_2$ ($BaAu_5Si_2$-type); $Sr(Au_xSi_{1-x})_2$ (x=0.25: Ca_2AgSi_3 type; x=0.375: AlB_2 type); $Sr(Au_xGe_{1-x})_2$ (AlB_2 structure type); $SrAu_{2-x}Ge_{2+x}$ (x=0: $ThCr_2Si_2$ type; x=0.5: $CaBe_2Ge_2$ type and x=0.45: $BaCu_2Sb_2$ type); $Ba_8Ag_xSi_{46-x}$ (clathrate type-I); Ba_2AgSi_3 ($Ba_4Li_2Si_6$ type); $Ba_8Ag_xGe_{46-x-y}\square_y$ (clathrate type-I); $BaAg_{2-x}Ge_{2+x}$ ($ThCr_2Si_2$ type); $BaAg_xGe_{2-x}$ (AlB_2-type); $Ba_8Au_xSi_{46-x}$ (clathrate type-I); $Ba(Au_{1-x}Si_x)_2$ (AlB_2-type); $BaAu_{3+x}Si_{1-x}$ ($BaAu_3Ge$-type); $BaAu_{5+x}Si_{2-x}$ ($BaAu_5Si_2$-type); $Ba_8Au_xGe_{46-x-y}\square_y$ (clathrate type-I); $Ba(Au_{1-x}Ge_x)_2$ (AlB_2-type); $BaAu_{1+x}Ge_{3-x}$ (x=0.1: $BaNiSn_3$ type; x=1.7: $Ce(Ni,Sb)_4$-type); $BaAu_3Ge$ ($BaAu_3Ge$-type); $BaAu_{5+x}Ge_{2-x}$ (x=0: $BaAu_5Si_2$-type; x=0.3: $BaAu_{5.3}Ge_{1.7}$ type).

As an additional contributions, the transport properties of various clathrates type-I are presented and the resistivity and heat capacity measurements of $Sr_8Cu_{5.3}Si_{40.7}$. Resistivity measurements of the new ternary compounds $BaAu_3Ge$ and $BaAu_3Si$ show metallic behaviour with a superconducting transition at T_c=2.4 and 1.6 K, respectively.

Kurzfassung

Supraleitung in Verbindungen ohne Inversionszentrum in der Kristallstruktur erlangte in den letzten Jahrzenten reges Forschungsinteresse, da viele Eigenschaften nicht mit der Standard BCS Theorie übereinstimmen. Die vorliegende Arbeit konzentriert sich hauptsächlich auf die Darstellung und Charakterisierung einfacher nicht-zentrosymmetrischer intermetallischer Verbindungen und die dazugehörigen ternären Systeme und besteht im Wesentlichen aus drei großen Kapiteln.

Das erste Kapitel besteht aus Ergebnissen der Untersuchungen an den supraleitenden ternären äquiatomaren Siliziden und Germaniden LaIrSi, LaPtSi und HfRhGe mit geordneten nicht-zentrosymmetrischen Kristallstrukturen, die sich von den binären Aristotypen α-$ThSi_2$, $SrSi_2$ oder AlB_2 ableiten. Des Weiteren wurde die Verbindung CeIrSi untersucht.

Der zweite Teil der Arbeit konzentriert sich auf die Untersuchungen von Kristallstrukturen und/oder Phasendiagrammen von binären, ternären und quaternären Boriden. Das binäre Phasendiagramm Ir-B wurde im Konzentrationsbereich 10 bis 70 at. % Bor mittels dynamischer Differenzkalorimetrie, Elektronenstrahlmikroanalyse, Röntgenpulverdiffraktometrie und Röntgeneinkristalldiffraktometrie untersucht und erstellt. Das System wird durch vier binäre Phasen Ir_4B_{5+x}, Ir_5B_{4+x} sowie die hoch- und tief Temperatur Modifikation von Ir_4B_{3-x} bestimmt. Röntgenstrukturuntersuchungen wurden für Einkristalle von Ir_4B_{5+x} (Ir_4B_5 type), Ir_5B_{4+x} (Ir_5B_4 type) und für die nicht-zentrosymmetrische tief Temperatur Modifikation of Ir_4B_{3-x} (x=0: $IrB_{0.9}$ type) durchgeführt wohingegen die hoch Temperatur Modifikation von Ir_4B_{3-x} (WC type; auch nicht-zentrosymmetrisch) mittels Röntgenpulverdiffraktometrie bestätigt wurde.

Außerdem wurde die Kristallstruktur von $W_{1-x}B_3$ mittels Röntgeneinkristalldiffraktometrie untersucht und ergab Isotypie mit dem $Mo_{1-x}B_3$ Strukturtyp. Die Löslichkeit von Rh, Ir, Ni, Pd und Pt in $W_{1-x}B_3$ als auch von Rh in $Mo_{1-x}B_3$ wurde direkt nach dem Schmelzen im Lichtbogen als auch nach dem Glühen untersucht. Die Phasengleichgewichte wurden für den borreichen Teil der zugehörigen isothermen Schnitte W-TM-B (TM = Rh, Ir bei 1100°C, TM = Ni, Pd bei 900°C und TM = Pt bei 800°C) und Mo-Rh-B (bei 1100°C) erstellt. Nur im System W-Ir-B bildet sich eine ternäre Phase $W_{1-x}Ir_xB_2$ (ReB_2 type). Außerdem wurde die Bildung und Kristallstruktur der isotypen Diboride $W_{1-x}TM_xB_2$ (TM = Ru, Os, Ir) im

ungeglühten Zustand als auch nach dem Sintern bei 1500°C mittels Röntgenpulverdiffraktometrie und Elektronenstrahlmikroanalyse untersucht.

Die feste Lösung $CeRh_{3-x}Pd_xB_{0.5}$ (x=0, 0.5, 1.2, 1.5, 1.7, 2.5, 3) wurde im ungeglühten Zustand sowohl bezüglich der Bildung einer Überstruktur als auch der Änderung der Cer Valenz untersucht.

Im dritten Teil der Arbeit sind die Ergebnisse der Untersuchungen zahlreicher ternärer Verbindungen EpT_2X_2 oder $EpTX_3$ (*Ep* = Sr, Ba; *T* = Ni, Pd, Pt, Cu, Ag, Au; *X* = Si, Ge, Sn) zusammengefasst, die mit dem nicht-zentrosymmetrischen $BaNiSn_3$ Strukturtyp oder mit einem anderen $BaAl_4$ Abkömmling kristallisieren. Supraleitung (< 3 K) wurde für 7 Verbindungen mit $BaNiSn_3$ Strukturtyp gefunden. Gruppe-Untergruppe Beziehungen mit dem Aristotyp $BaAl_4$ wurden mit dem Fokus auf die nicht-zentrosymmterischen Strukturtypen erstellt. Darüber hinaus wurden der Silizium beziehungsweise Germanium reiche Teil der ternären Systeme Sr-{Cu,Ag,Au}-{Si,Ge} und Ba-{Ag,Au}-{Si,Ge} bei 700 oder 800°C, entsprechend dem jeweiligen System, untersucht. Neben den teilweisen isothermen Schnitten bei 800 und 600°C wurden für das Ba-Ag-Ge System auch die Liquidus- und Solidus Projektionen erstellt, die ternären invarianten Reaktionen bestimmt und diese in Form eines Schultz-Scheil Diagramms dargestellt. Die Kristallstrukturen und Homogenitätsbereiche von mehr als 20 neuen oder bereits beschriebenen Phasen wurden mittels Elektronenstrahlmikroanalyse, Röntgenpulverdiffraktometrie und in einigen Fällen mittels Röntgeneinkristalldiffraktometrie untersucht.

$Sr_8Cu_xGe_{46-x}$ (Klathrate Typ-I); $SrCu_{2-x}Ge_{2+x}$ ($ThCr_2Si_2$ Typ); $Ba_{8-y}Sr_yCu_xGe_{46-x}$ (Klathrate Typ-I); $Sr_2Ag_{1+x}Si_{3-x-y}\square_y$ (Sr_2LiSi_3 Typ); $SrAg_{2-x}Si_{2+x}$ ($ThCr_2Si_2$ Typ); $Sr(Ag_xGe_{1-x})_2$ (AlB_2-Typ); $SrAg_{2-x}Ge_{2+x}$ ($ThCr_2Si_2$ Typ); $Sr(Au_{1-y}\square_y)(Si_{1-x}Au_x)_3$ ($BaNiSn_3$ Typ); $SrAu_{5-x}\square_xSi_2$ ($BaAu_5Si_2$ Typ); $Sr(Au_xSi_{1-x})_2$ (x=0.25: Ca_2AgSi_3 Typ; x=0.375: AlB_2 Typ); $Sr(Au_xGe_{1-x})_2$ (AlB_2 Typ); $SrAu_{2-x}Ge_{2+x}$ (x=0: $ThCr_2Si_2$ Typ; x=0.5: $CaBe_2Ge_2$ Typ and x=0.45: $BaCu_2Sb_2$ Typ); $Ba_8Ag_xSi_{46-x}$ (Klathrate Typ-I); Ba_2AgSi_3 (Sr_2LiSi_3 Typ); $Ba_8Ag_xGe_{46-x-y}\square_y$ (Klathrate Typ-I); $BaAg_{2-x}Ge_{2+x}$ ($ThCr_2Si_2$ Typ); $BaAg_xGe_{2-x}$ (AlB_2 Typ); $Ba_8Au_xSi_{46-x}$ (Klathrate Typ-I); $Ba(Au_{1-x}Si_x)_2$ (AlB_2 Typ); $BaAu_{3+x}Si_{1-x}$ ($BaAu_3Ge$ Typ); $BaAu_{5+x}Si_{2-x}$ ($BaAu_5Si_2$ Typ); $Ba_8Au_xGe_{46-x-y}\square_y$ (Klathrate Typ-I); $Ba(Au_{1-x}Ge_x)_2$ (AlB_2 Typ); $BaAu_{1+x}Ge_{3-x}$ (x=0.1: $BaNiSn_3$ Typ; x=1.7: $Ce(Ni,Sb)_4$ Typ); $BaAu_3Ge$ ($BaAu_3Ge$ Typ); $BaAu_{5+x}Ge_{2-x}$ (x=0: $BaAu_5Si_2$ Typ; x=0.3: $BaAu_{5.3}Ge_{1.7}$ Typ).

Als zusätzliche Beiträge sind die Transporteigenschaften von zahlreichen Klathraten Typ-I zusammengefasst als auch die Ergebnisse der Widerstand- und Spezifischen Wärme Messungen von $Sr_8Cu_{5.3}Si_{40.7}$. Widerstandsmessungen der neuen Verbindungen $BaAu_3Ge$ und $BaAu_3Si$ zeigen metallisches Verhalten mit einem supraleitendem Übergang bei T_c=2.4 sowie 1.6 K.

1 Introduction

After the first liquefaction of Helium by Kamerlingh-Onnes in 1908, he investigated the electrical resistivity of very pure metals and found for mercury a precipitously drop below a measureable value at ~ 4.2 K. Kamerlingh-Onnes called this phenomena superconductivity and the transition temperature from the normal to the superconducting state the critical temperature (T_c). Beside the temperature, the superconducting state is also limited by the current density (j_c) and the external applied magnetic fields (H_c). Superconductors also expel magnetic fields, which is called the ``Meißner-Ochsenfeld Effect´´ (Meissner W. 1933). Superconductivity is related to the formation of Cooper pairs [BCS theory (Bardeen J. 1957); bound state of two electrons of opposite momentum and spin close to the Fermi energy, forming a coherent condensate], mediated by electron-phonon interaction, for most of the known superconducting (SC) materials. This pair formation is rather short ranged, so that only pairing states are favourable, having the highest possible symmetry. In case of full rotational symmetry, this refers to a relative angular momentum (l = 0) and a spin-singlet confirmation (S = 0). This "s-wave" pairing state is representing the "conventional*"* superconducting phase (Sigrist M. 2005).

When the magnetic intermetallic compound $CeCu_2Si_2$ was found to undergo a transition into a superconducting ground state around 0.7 K (Steglich F. 1979), many of the superconducting properties and parameters did not coincide with the standard BCS theory. $CeCu_2Si_2$ and the large family of high T_c superconductors [f.e. layered perovskite copper oxides (Bednorz J.G. 1986)] caused intense research activities on a growing group of superconducting materials, known as "unconventional superconductors". In these materials, time reversal and/or crystal symmetry can be violated spontaneously in addition to the gauge symmetry (Sigrist M. 2005). Strong deviations from usual Cooper pairing are expected, if time reversal and inversion symmetry are missing in the normal state (Sigrist M. 2005). The absence of inversion symmetry together with parity violating antisymmetric spin-orbit coupling (ASOC) allows an admixture of spin singlet and spin triplet components and the structure of the quasiparticle gap function may include point or line nodes [(A. D. Sigrist M. 2007), (Frigeri P.A. 2004)]. Therefore, a power law thermal dependence of the thermodynamic properties (f.e. specific heat: $C_S \propto T^2$) is expected for such a superconductor (U. K. Sigrist M. 1991).

There are still only a few further Ce-based heavy fermion superconductors known in literature. Pressure induces SC in the compounds such as $CeCu_2Ge_2$ [P=101 kbar: T_c=0.64 K (Jaccard D. 1992)], $CePd_2Si_2$ [P ~ 28 kbar: T_c ~ 430 mK (Grosche F.M. 1996)], $CeRh_2Si_2$ [P ~ 9 kbar: T_c ~ 350 mK (Movshovich R. 1996)], $CePtSi_2$ [P ~ 1.7 GPa: T_c ~ 140 mK (Nakano T. 2009)] and $CeRhIn_5$ [T_c^{max} = 2.1 K, (Hegger H. 2000)]. Superconductivity at ambient pressure has been found in $CeMIn_5$ [M = Co: T_c = 2.3 K (P. P. Petrovic C. 2001); M = Ir: T_c = 0.4 K (Petrovic C. 2001)]. All these compounds crystallize with a centrosymmetric structure type. $CePt_3Si$ [T_c = 0.75 K (Bauer E. 2004)] was the first examples of a heavy fermion SC without inversion symmetry. Other members of this class of materials are f.e. UIr [P ~ 2.6-2.7 GPa: T_c < 140 mK (Akazawa T. 2004)], $CeRhSi_3$ [P ~ 20 kbar: T_c ~ 1 K (Kimura N. 2005)] and $CeIrSi_3$ [P ~ 2.5 GPa: T_c ~ 1.6 K (Sugitani I. 2006)] but only $CePt_3Si$ shows SC already at ambient pressure.

Superconductivity at ambient pressure also appears in the non-magnetic homologues $LaPt_3Si$ [T_c ~ 0.6 K (Shiotsuki M. 2011)], $LaRhSi_3$ and $LaIrSi_3$ [T_c=1.9-2.7 K (Lejay P. 1984)]. Further examples of already studied non-centrosymmetric superconductors are $Y_2C_{3\pm x}$ [T_c = 6-18 K, depending on x (Krupka M.C. 1969), (Amano G. 2004)], $Li_2(Pd_{1-x}Pt_x)_3B$ [T_c = 2.8-8 K, depending on x (Badica P. 2005), (Togano K. 2004)] and Mo_3Al_2C [T_c = 9 K (R. G. Bauer E. 2010)].

The present work has been carried out as one part of the research project "Non-centrosymmetric Superconductors" with the aim to discover, prepare and characterize non-centrosymmetric compounds. For this work, the knowledge about phase formation, crystal structures and also about the phase equilibria is mandatory. Therefore, microstructures of the as cast (after arc melting) and annealed alloys have been analysed using scanning electron microscopy and the chemical composition has been determined with electron probe microanalysis. The melting temperatures (behaviors) of compounds, phase transitions and/or invariant reactions have been studied by differential scanning calorimetry. The crystal structures have been investigated by X-ray powder diffraction and X-ray single crystal diffraction.

The tasks of this work more detailed are:

i) The preparation and characterization of already known intermetallic non-centrosymmetric superconducting materials without strong correlations among *f*-

electrons, which have not been investigated with respect to the lack of symmetry (equiatomic silicides or germanides LaPtSi, LaIrSi and HfRhGe).

ii) The crystal structures and/or phase diagram investigations of binary (Ir-B system), ternary [W-TM-B (TM = Rh, Ir at 1100°C, TM = Ni, Pd at 900°C and TM = Pt at 800°C) and Mo-Rh-B (at 1100°C)] and quaternary borides [solid solution $CeRh_{3-x}Pd_xB_{0.5}$ (x=0, 0.5, 1.2, 1.5, 1.7, 2.5, 3].

iii) The systematic search for novel ordered non-centrosymmetric and possible superconducting compounds in the ternary systems *Ep-T-X* (*Ep* = Sr, Ba; *T* = Ni, Pd, Pt, Cu, Ag, Au; *X* = Si, Ge, Sn) inclusively phase formation, crystal structures and phase equilibria.

iv) The investigations of novel even centrosymmetric ternary compounds and thermoelectric materials like clathrates, which are present in the *Ep-T-X* systems and which might exhibit interestingly physical properties.

The corresponding physical properties of the non-centrosymmetric compounds have been studied in the group of Prof. Ernst Bauer at the Technical University of Vienna and are therefore only briefly summarized and all calculations have been performed in the group of Prof. Raimund Podloucky from the University of Vienna as concluding part of this project.

2 Experimental techniques

2.1 SAMPLE PREPARATION

Samples of about 0.5-1.5g were prepared by arc melting under an argon atmosphere. An extra amount of the most volatile element has been added in advanced to compensate the weight loss during arc melting. Weight losses were therefore much smaller 1 mass.%. Either stoichiometric quantities of the pure metal ingots (Sr 99.9, Ba 99.9, La 99.9, Ce 99.9, Eu 99.9, Yb, 99.9, Ni 99.99, Pd 99.99, Pt, 99.9, Cu 99.9, Ag 99.9, Au 99.9, Si 99.999, Ge 99.999 and Sn 99.99 mass.%, all from Alfa Aesar) or of metal powders (V 99.99, Hf 99.9, Mo 99.9, W 99.99, Ru 99.99, Os 99.99, Ir 99.99, Rh 99.99, Ni and crystalline B 98-99% mass.%, all from Alfa Aesar) have been used. The moisture/oxygen sensitive alkaline and rare earth elements were mechanically surface cleaned and handled and weight under cyclohexane. Metal powders were carefully mixed and cold compacted before arc melting. The arc melted buttons were cut and appropriate pieces, vacuum-sealed in quartz tubes (wrapped in Ta or Mo foil, depending on the system) and annealed at temperatures between 600 and 1100 °C. The accurate annealing conditions are given separately in each chapter. Above 1100 °C, the samples were annealed on a BN-substrate in a high vacuum furnace of 3×10^{-4} Pa with a W-sheet metal heater.

To achieve large (~ 1 cm^3) dense clathrate samples (from the ternary systems Ba-{Ag,Au}-{Si,Ge}) for physical properties measurements, appropriate amounts of the annealed arc-melted buttons (800°C for 1 week) were crashed inside the glove box and hand milled to gain first powders (grain size < 100 µm). Afterwards, these powders were ball milled via high energy ball milling under argon and then compacted in a hot press. In a final step, the alloys were annealed again for 5 days at 800°C. To determine the relative density (ρ_r in %), we used Archimedes` principle for the density ρ, which we measured on the cylindrical sample in distilled water. In comparison with the calculated X-ray density ($\rho_x = \frac{M_r \cdot Z}{V_u \cdot N_A}$; M_r…molar mass; Z… number of formula units/unit cell; V_u… volume of the unit cell and N_A…Avogadro constant) a relative density (ρ/ρ_x) was achieved higher than 96%.

2.1.1 Arc furnace

A standard arc melting furnace consists of a copper hearth, tungsten electrode and water cooling system and reaches temperatures up to 3500°C. The furnace chamber is evacuated with a vacuum pump and backfilled with argon. This procedure is repeated between 3 and 5 times. Before melting, the chamber is filled with argon up to a pressure of 0.7-0.8 bar. Titanium is always molten as a getter first and afterwards the sample. The arc melted buttons were reversed and remelted at least 3 times to ensure homogenisation in the alloy.

2.1.2 Ball mill

Pregrinded powders of the alloys were filled inside the ball milling containers in a glove box. The ball milling was performed in a Vario-Planetary Mill Pulverisette 4 (see Figure 1(a)) using containers and balls of steel. The grinding containers can be fixed on a rotating support disc (see Figure 1(b)) and the rotation speed of the disc and the grinding bowls (can be set independently) is connected via the planetary ratio $= \frac{Speed\ of\ container}{Speed\ of\ the\ disc}$.

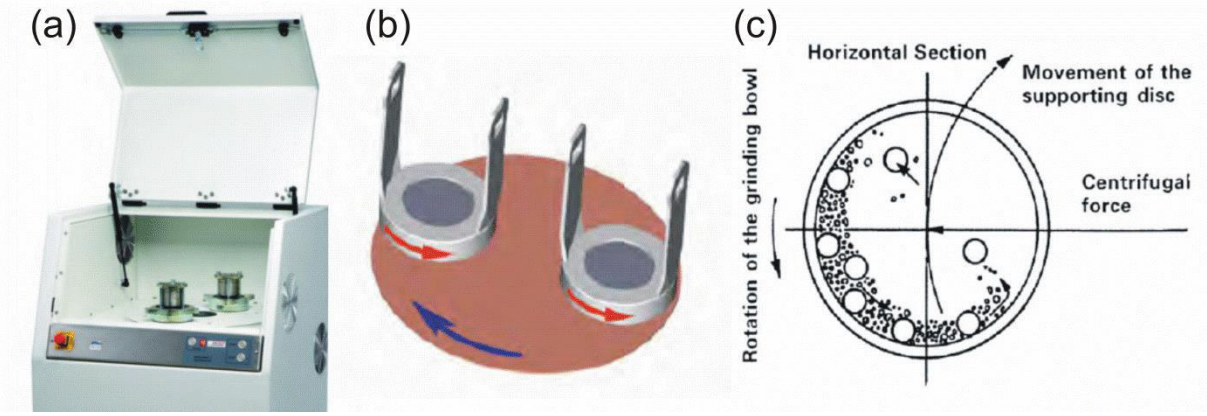

Figure 1:(a) Picture of the Vario-Planetary Mil Pulverisette 4; (b) schematic representation of the rotating support disc with the container holders and (c) possible movement/trajectories of the balls inside the bowl (Fritsch GmbH).

As the support disc and the vials are rotating in opposite directions (see Figure 1(b)), the centrifugal forces alternately act in forward and opposite direction. The movement or trajectories of the balls inside the containers can be determined by changing PR. The balls can impact the walls (see Figure 1(c)) vertically (high impact energy), tangentially (high friction) or roll along the walls of the container (centrifugal milling) (Fritsch GmbH). Various parameters like size and material of the balls and container (Cr-Ni steel, WC, chrome steel,

corundum, zirconia), the ball to powder ratio, the size of the balls, the temperature, the milling time, the milling atmosphere (vacuum, inert gas, air) and/or a process control agent (stearic acids, ethanol, hexane…) influence the result and therefore should be optimized. The applied ball milling parameters are in this case are: rotation speed of the disc = 175 rpm, *PR* = -2.5, size of the balls = 10 mm, milling atmosphere: Argon.

2.1.3 Hot Press

A hot press (HP W 200/250-2200-200-Ks, FCT System GmbH; see Figure 2) has finally been used to compact the fine powders after ball milling into a bulk sample. The powders are transferred inside the glove box to a graphite die with a diameter of 10 mm. The furnace is also build-up of high density graphite. Working temperatures and forces can achieve 2200°C and 140 kN. The sintering process can be operated under vacuum, nitrogen or argon. Ge-based alloys were hot pressed at 700°C (56 MPa) and Si-based at 800°C (56 MPa).

Figure 2: Hot Press HP W 200/250-2200-200-Ks, FCT System GmbH (FCT System GmbH 2006).

2.2 SAMPLE CHARACTERIZATION

All alloys have been characterized in as cast state (after arc melting) and/or after annealing by X-ray powder diffraction (XPD) and electron probe micro analysis (EPMA). X-ray single crystal diffraction (XSCD) studies have been done in various cases in order to investigate the

crystal structure of new compounds or to verify already reported structure types from literature. Differential scanning calorimetry (DSC or differential thermal analysis (DTA)) experiments have been carried out to study the melting temperature (behavior) of compounds, phase transitions and invariant reactions.

2.2.1 X-ray diffraction

Only short wavelength X-rays, which are in the range of a few Ångströms to 0.1 Ångström (1 keV - 120 keV), can be used for diffraction experiments. As the wavelengths of X-rays are comparable to the spacing of lattice planes, they are ideally suited for probing the structural arrangement of atoms in a wide range of materials. The 3-dimensional periodic lattice works as diffraction grating for X-rays as discovered by Max and Laue. The energetic X-rays can penetrate deep into the investigated material and provide information about the bulk structure.

The X-rays are generated in an X-ray tube, when a focused electron beam is accelerated across a high voltage field (30-60 kV) and strikes a stationary or rotating solid target. Through the deceleration of the electrons in the electric fields of the metal ions, the kinetic energy is partially transferred into radiation. This continuous spectrum of X-rays (Bremsstrahlung) is always emitted (Massa W. 2011). The high energy electrons also eject inner shell electrons from the atoms. When an electron from a higher orbital fills this level, an X-ray photon is emitted with a characteristic energy for the transition. Therefore, each metal has its characteristic X-ray emission spectrum. Common targets used in X-ray tubes are Fe, Cu or Mo, which emit X-rays with corresponding wavelengths of $K_{\alpha1}$(Fe)=1.93604 Å ($K_{\alpha2}$=1.93997 Å), $K_{\alpha1}$(Cu)=1.54059 Å ($K_{\alpha2}$=1.54443 Å) and $K_{\alpha1}$(Mo)=0.70932 Å ($K_{\alpha2}$=0.71361 Å), respectively (Int. Tabl. of Crystallogr. C 2004). The energy (E) of an X-ray photon and its wavelength (λ) is related by the equation $E = hc/\lambda$, where h is Planck's constant and c the speed of light.

When X-ray photons collide with electrons, some photons from the incident beam will be scattered without changing the wavelength (coherent or elastic scattering) at various angle θ, depending on the d spacing between the lattice planes. Constructive interference occurs according to Bragg if: $2d \sin\theta = n\lambda$. In this equation, λ is the wavelength of the X-ray, θ is the scattering angle and n is an integer representing the order of the diffraction peak. The present background in all diffraction experiments mainly results from fluorescence X-

rays and inelastic scattering (incoherent scattering) of X-rays (Materials Research Laboratory, 2014). The intensity of the diffracted X-rays is equal (proportional) to the square of the structure factor. The structure factor for any plane *hkl* with N atoms in the unit cell and the n^{th} atom located at ($x_n y_n z_n$) is given as:

$$F = \sum_{n=1}^{N} f_n^{'} e^{i\phi_n} = \sum_{n=1}^{N} f_n^{'} (cos\,\phi_n + i\,sin\,\phi_n) \quad (1)$$

with the total phase difference $\phi_n = 2\pi(hx_n + ky_n + lz_n)$ (2)

The atomic scattering factor of the n^{th} atom (f_n) is dependent from the number of electrons and therefor from the atomic number (Z). It is given as (Swaminathan P. 2013):

$$f = \frac{amplitude\ of\ wave\ scattered\ by\ atom}{amplitude\ of\ wave\ scattered\ by\ electron} \leq Z \quad (3)$$

At 2θ=0 it correspond to the atomic number and decreases with increasing θ values. The polynomials with 9 parameter and values of *f* are given for almost all atoms and ions in the International Tables of Crystallography C (Int. Tabl. of Crystallogr. C 2004). The oscillation of an atom around the ideal position leads to a further weakening of *f* with increasing θ and can be expressed as:

$$f^{'} = f \cdot e^{-8\pi^2 U(sin^2\,\theta/\lambda^2)} \quad (4)$$

where U is the isotropic displacement factor (formerly called temperature factor), which is the squared mean oscillation amplitude u^2 (Massa W. 2011).

2.2.1.1 X-ray Powder Diffraction (XPD)

XPD is currently the most established X-ray diffraction technique for characterizing materials in laboratories. The sample is usually in a powdery form, consisting of very fine grains of a crystalline material and the crystalline domains should be randomly oriented. XPD data are most frequently collected using reflection (Bragg-Brentano geometry) or transmission (Guinier geometry) geometry, as shown in Figure 3. In the Bragg-Brentano geometry, either the X-ray tube is fixed (θ:2θ instrument) and the sample rotates at θ °/min and the detector at 2θ °/min (2θ-diffraction angle) or the sample is fixed (θ:θ instrument) and the X-ray tube rotates with a rate of -θ °/min and the detector with a rate of θ °/min. The diffraction vector v_d is always normal to the sample (see Figure 3(a)).

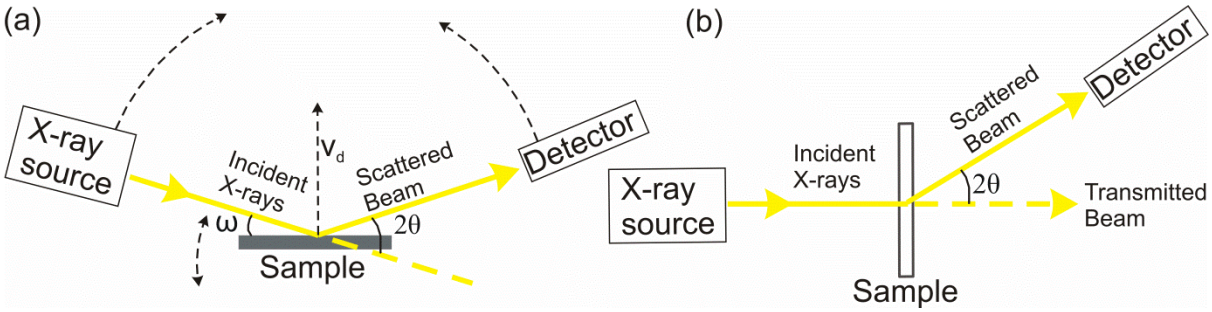

Figure 3: Schematic drawing of the (a) reflection and (b) transmission geometry (ω-incident angle; 2θ-reflection angle; v_d-diffraction vector).

The transmission geometry is realised in the Huber Guinier camera G670 (see Figure 4; Cu-$K_{\alpha 1}$ or Fe-$K_{\alpha 1}$ radiation) applying an image plate (IP) to allow the entire diffraction pattern to be collected in a single exposure ($8° \leq 2\theta \leq 100°$). The used incident beam monochromator (oriented Si or Ge single crystal) eliminates the bothersome $K_{\alpha 2}$ radiation. The Camera consists of an image storage foil positioned inside the camera housing with the sensitive site facing inward on the focal circle with radius 90 mm (Huber). This foil consists of polyester and is coated with a homogeneous powder of photo-stimulatable phosphor consisting of bariumflourobromide with traces of Europium (2+) which acts as a luminescence centre ($BaFBr:Eu^{2+}$). After the exposure, the image plate is scanned by a vertical linear red diode laser beam (~5 seconds). The thus resulting blue photo-stimulated luminescence (PSL) eradiating from the areas subject to X-ray exposure is amplified during the scanning process by a photomultiplier and then registered. This initially analogue signal is then converted into digital number counts by a 16-bit A/D converter. A white halogen lamp is deleting the registered image structure and the system is ready for the next exposure (Huber). The received data can be stored in different formats for visualization programs or for performing a Rietveld refinement.

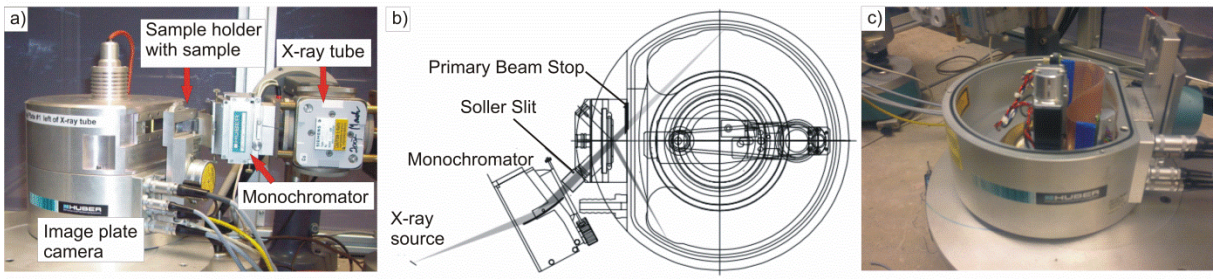

Figure 4: (a) Picture of the Huber Guinier Camera G670 with X-ray tube (Cu-radiation) and monochromator (b) schematic drawing (Huber) and (c) picture from the inner part of the camera (laser recording unit with photomultiplier and preamplifier.

2.2.1.1.1 Determination of the Lattice parameter

The X-ray powder diffraction patterns were measured also with small amounts of Si or Ge as standard for precise lattice parameter determination. External or internal standards are used to eliminate the total error caused by a lot of different influences like sample displacement or misalignment of the diffractometer parts. High symmetric substances with already very precisely measured lattice parameters are suitable as standards. Only those sample reflections in between the first and the last reflection of the standard substance should be taken, as extrapolation can cause severe errors. Furthermore, the peaks of the standard and the sample should not overlap and the strongest reflection of the sample and the standard should have about the same intensity. The difference of $2\theta_{obs}$ and $2\theta_{calc}$ ($\Delta 2\theta$) is plotted versus $2\theta_{obs}$ to define a proper correction function. Usually a polynomial function of 0^{th} to 4^{th} order is calculated as an approach function. The procedure has been carried out with the programs STRUKTURE (Wacha W. 1989), X15, LAZY PULVERIX and GITTER. The last two are integrated in the program MENUE.

2.2.1.1.2 The Rietveld refinement

H.M. Rietveld developed in the 1970´s ((H.M. Rietveld 1967), (H.M. Rietveld 1969)) a method for the mathematical description of powder patterns (first it was developed for neutron diffraction data only) applying structure related, profile related and instrument related parameters, which are refined in least square processes. Mandatory for the implementation of a Rietveld refinement is a proper structure model (space group, lattice parameter, atomic positions) for all phases. The profile can be modeled with the following expression:

$$y_{ci} = \sum_{\phi} S_{\phi} \sum_{h} I_{\phi,h} \Omega\left(T_i - T_{\phi,h}\right) + b_i \qquad (5)$$

where y_{ci} are the calculated counts at step i, the vector h labels the Bragg reflection and the subscript ϕ labels the phase and ranges from 1 to the number of phases existing in the model (Rodriguez-Carvajal J. 2006). The integrated intensity $I_{\phi,h}$ can be written as:

$$I_{\phi,h} = \{LACPMF^2\}_{\phi,h} \qquad (6)$$

The meanings of the various terms in the previous equations are:

S_{ϕ} – Scale factor of the phase ϕ

Ω – Reflection profile function that models sample and instrumental effects

T – Scattering variable (here: scattering angel θ or 2θ)

b_i – Background intensity

L_h – Lorentz polarization

M_h – multiplicity factor

A_h – Absorption correction

C_h – Special corrections (non linearity, efficiencies, special absorption corrections, extinction)

P_h – Preferred orientation function

F_h – Structure factor

The Rietveld method can be expressed basically as the minimization of the weighted squared differences between the observed $\{y_i\}_{i=1,..,n}$ and calculated pattern $\{y_{ci}(\alpha)\}_{i=1,..,n}$ against a parameter vector $\alpha=(\alpha_1 \ldots \alpha_p)$ (Rodriguez-Carvajal J. 2006). The function is written as:

$$\chi^2 = \sum_{i=1}^{n} w_i \{y_i - y_{ci}(\alpha)\}^2 \quad (7)$$

with $w_i = 1/\sigma_i^2$ (σ_i^2- variance of y_i) (Rodriguez-Carvajal J. 2006).

The generally given agreement factors from the Rietveld refinement are:

Weighted Profile factor: $R_{WP} = 100 \left[\frac{\sum_{i=1,n} w_i |y_i - y_{ci}|^2}{\sum_{i=1,n} w_i y_i^2}\right]^{1/2}$ (8)

Bragg factor: $R_B = 100 \frac{\sum_h |I_{obs,h} - I_{calc,h}|}{\sum_h |I_{obs,h}|}$ (9)

and the crystallographic RF factor: $R_F = 100 \frac{\sum_h |F_{obs,k} - F_{calc,h}|}{\sum_h |F_{obs,k}|}$ (10)

All Rietveld refinements have been carried out within the program FULLPROF (Rodriguez-Carajalv J. 1993).

2.2.1.2 X-ray single crystal diffraction

Small pieces of suitable samples (details about sample composition and preparation conditions are given in each chapter) were mechanically crushed in a mortar and single crystals with a size of 20-50 µm were presorted under a light microscope. Proper crystals were glued on top of a glass capillary, which is fixed with wax in a small brass tube. An AXS-GADDS (General Area Detector Diffraction system using a HI-STAR Area Detector System) texture goniometer has been used for checking the crystal quality, unit cell dimensions and Laue symmetry. X-ray single crystal diffraction (XSCD) data were collected at room temperature on a Bruker APEXII

diffractometer and at low temperatures (200 and 100 K) on a four-circle Nonius Kappa diffractometer. The crystal structures were solved applying direct methods (SHELXS-97, (Sheldrick 1990)) and refined against F^2 (SHELXL-97-2, (Sheldrick G. M. 1997)) within the programs WINGX (Farrugia L. J. 1999) or OSCAIL (McArdle P. 2004). All crystal structures were standardized with the program Structure Tidy (Gelato L.M. 1987). For the graphical representation of the Difference Fourier Synthesis the program GFourier has been used, which is integrated in the program FULLPROF (Rodriguez-Carajalv J. 1993). Pictures of the unit cells and coordination polyhedra have been created with the program 'Diamond'.

2.2.1.2.1 Bruker Kappa APEXII and Nonius Kappa diffractometer

Single crystal diffraction experiments have been carried out either on a Bruker Kappa APEXII diffractometer or on a Nonius Kappa diffractometer when measurements at different temperatures were required. Both diffractometer (see Figure 5(a) and (b)) basically consists of the X-ray source, X-ray optics, a Microscope or video camera (Bruker APEXII), the 4 axis goniometer (Kappa, omega, phi) for orienting the crystal and 2-Teta for the detector. Additional, the distance D_x from the crystal to the detector (charge coupled device (CCD)) can be changed. A phosphor converts X-rays to light in this 2-dimensional detector, a fibre optic taper reduces the image and cooled CCD measures the light signal. The APEXII detector is a 4k by 4k solid state CCD full frame sensor. The X-rays are generated in the Nonius kappa diffractometer through an X-ray tube with rotating anode (Mo K_α radiation; C-monochromated) and in the Bruker APEXII diffractometer by an Incoatec Microfocus Source IμS (30 W, multilayer mirror, Mo-K_α). The descriptions of the instruments are mainly based on the user manuals of the 2 diffractometers. Several sets of phi- and omega-scans with 2.0° scan width were measured at a crystal-detector distance of 3 cm (full sphere; 2° <2θ< 70°).

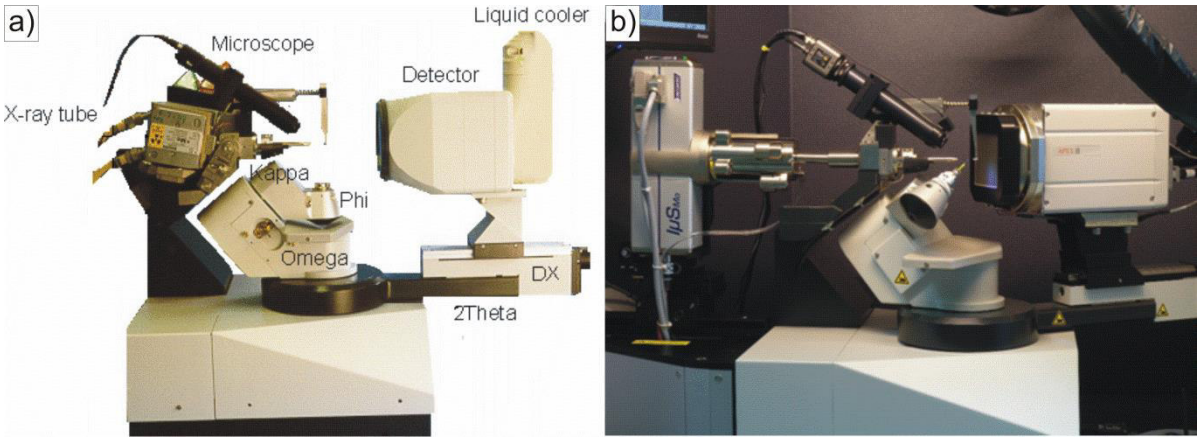

Figure 5: Kappa 4 axis goniometer components (a) Nonius kappa diffractometer (http://www.nonius.nl/KappaCCD/manuals/technical/userman.html) and (b) Bruker Kappa APEXII (http://www.univie.ac.at/Mineralogie/ccd.htm).

2.2.1.2.2 Crystal structure solution

After the XSCD, the collected diffraction data consist of a list of miller indices and corresponding intensities. The electron density map within the unit cell in the crystal is reconstructed by a Fourier transformation of the integrated intensities of the diffraction peaks. A high degree of completeness as well as redundancy in diffraction data is necessary to achieve a high accuracy, which means that all possible reflections are measured multiple times to reduce systematic and statistical errors (Materials Research Laboratory, 2014).

The main difficulty in X-ray crystal structure determination is known as the "phase problem":

$$\phi = arctan\left(\frac{\sum_n f_n \sin\phi_n}{\sum_n f_n \cos\phi_n}\right) \quad (11)$$

ϕ cannot be determined experimentally, as only the absolute value of the amplitudes can be calculated through the conversion of the measured intensities (Massa W. 2011). Several methods have been developed for crystal structure solutions, like direct methods or Patterson method.

2.2.2 Scanning Electron Microscopy (SEM, Electron Probe Microanalysis (EPMA))

For SEM and EPMA, sample pieces were embedded in a conductive resin by a SIMPLIMET 3 hot mounting press (Buehler, Lake Bluff, Illinois USA, operation parameters: 2.9×10^7Pa; 150°C; duration 1.5 min). The embedded samples were grinded using sand papers of different SiC grit size and polished afterwards on fine polishing towels with Al_2O_3 powders (grain size 0.3, 0.1 and 0.05 micron) under water or glycerine (moisture or oxidation sensitive materials). Finally, they were cleaned with acetone.

In a Scanning electron microscope (SEM, Zeiss Supra 55 VP; operated at 20 kV and 60 µA), an electron beam generated by an electron source (field emission cathode) is focused through an electromagnetic lens system to a point and scans in a raster pattern over the surface of the sample. The high energetic electrons can be elastic (backscattered electrons (BSE)) or inelastic scattered (secondary electrons (SE)) in the surface layers of the sample ((SEM)

2014). These two types of electrons are used for making an image of the sample. As SE´s have low energy, only electrons very close to the surface can escape and they have to be attracted towards the SE detector using a positive bias on the front of the detector. The signal strength and brightness of a SE image is depending on the angle between sample and detector and the image is therefore highly topographical ((SEM) 2014). BSE images display an atomic number contrast, as the probability for the generation of BSE is larger in areas with higher average atomic number. Higher energetic BSE are more likely scattered at higher angles and therefore, the detector is placed directly above the sample ((SEM) 2014). Characteristic X-rays (and Bremsstrahlung) are also emitted through the interaction of the primary electrons (PE) with the sample, which can be used for a quantitative analysis (EPMA). These X-rays can be detected either sensitive to variations in energy (energy dispersive X-ray analysis (EDX)) or wavelength (wavelength dispersive X-ray analysis (WDX)). The main advantage of the EDX detection is the rapid data collection, since X-rays from all detectable elements are collected parallel. Also impurities and contaminating elements can be detected. An example of an EDX spectrum measured on a phase containing Ba, Ag and Ge with an acceleration voltage of 20 kV is shown Figure 6. The sampling volume of X-rays is between 1 and 2 μm^3 and is therefore much larger than the incident beam (Moore J.C. 2003). EDX detectors have usually a resolution of 100-150 eV, so overlapping peaks are quite often a problem.

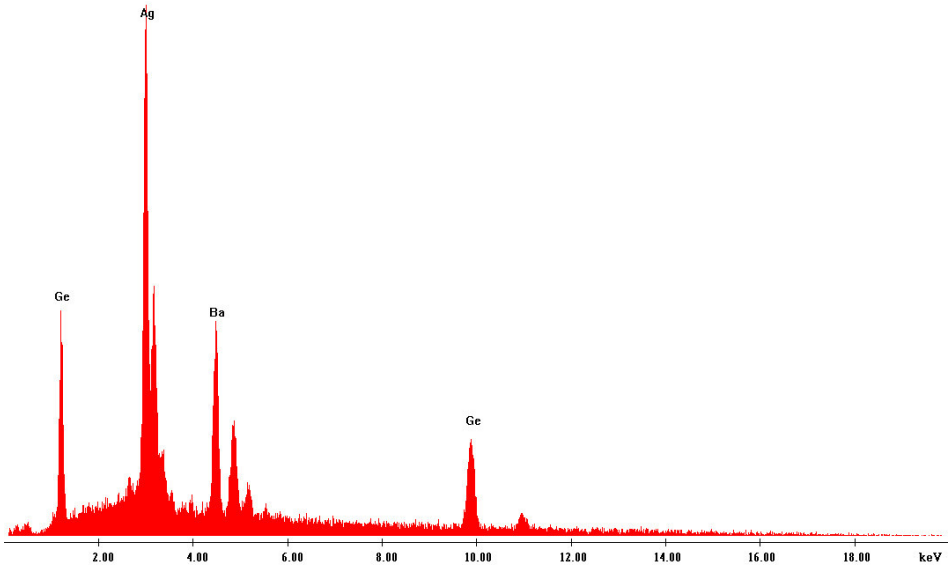

Figure 6: EDX spectrum of a phase containing 20.4 at.% Ba, 35 at.% Ag and 44.6 at.% Ge.

With a WDX detector, the emitted X-rays from the sample are analysed by their characteristic wavelength. The wavelength is measured using Bragg-diffraction by a spectrometer crystal, with a mechanical system changing the angle between sample, crystal and X-ray detector (Moore J.C. 2003). Therefore, a large number of different crystals are required, so that many different wavelengths can be accessed. This procedure is much slower compared with EDX detection and can only be used for a number of preselected elements. The biggest advantage is the energy resolution of 5-10 eV (Moore J.C. 2003). This removes most of the problems with overlapping peaks using EDX detection. Also the detection limit can be improved and with the appropriate standards, the compositional accuracy can be at least 1 at.% (Moore J.C. 2003). The weight fraction of the element in the sample is not directly related to the measured intensities of the X-rays and so a number of corrections have to be applied in both cases to gain a quantitative compositional analysis (Moore J.C. 2003).

2.2.3 Differential scanning calorimetry (DSC) and Differential Thermoanalysis (DTA)

In both techniques, a sample and an inert reference material are heated up applying a strict linear temperature program. In the DTA method, the temperature difference between sample and reference is recorded versus temperature or measurement time (Höhne G.W.H. 2003). In the DSC setup, the sample and the reference are kept at the same temperature. A thermal effect (exothermic or endothermic) is compensated through an increased heating of the colder site. The DSC measures the change of the difference in the heat flow rate to the sample and to a reference material (Höhne G.W.H. 2003).

The DSC is a widely used technique to gain information on:

- Melting -, re-crystallization -, polymorphous transition -, reaction -, or glass transition temperatures
- Melting -, crystallization -, transformation -, or reaction heats (enthalpies)
- Decomposition, thermal stability
- Oxidative stability
- Specific heat etc.

DSC/DTA measurements have been carried out on the annealed samples in either a Netzsch 404 Pegasus DSC in our laboratory or in a 409 STA CD /3/403/5/G equipment in the faculty of Science at the Masaryk university under a stream of 6N argon and heating rates of 5 or 10

K/min. The samples were measured in standard Al_2O_3 crucibles coated with Y_2O_3 or BN (Borides). Alloys containing moisture sensitive $BaGe_2$, were measured in sealed quartz ampoules using the DTA setup. Both equipments were calibrated in the temperature range from 300 to 1400°C against pure standard metals supplied by Netzsch to be within ±1°C (in case of the DTA setup within ±3 °C).

2.3 PHYSICAL PROPERTIES

Physical properties were measured in collaboration with the group of Prof. E. Bauer at the TU Vienna. For the electrical resistivity, thermopower (Seebeck coefficient), Hall effect and low temperature thermal conductivity measurements, the samples were cut into thin bars and for high temperature thermal conductivity measurements a thin carbon coated disk has been used. The electrical resistivity has been measured either in a conventional ^{4}He cryostat using a dc four point technique in the low temperature range between 4.2 and 300 K or by an ac resistance bridge (Lakeshore 370). Resistivity measurements from 350 mK to room temperature at magnetic fields up to 12 Tesla were performed in a cryogenic ^{3}He setup. At high temperatures (>300 K), electrical resistivity and thermopower have been measured simultaneously on an ULVAC ZEM-3 equipment. Thermopower measurements at low temperatures have been performed employing a differential method. The absolute thermopower $S_x(T)$ can be calculated with the equation: $S_x(T) = S_{Pb}(T) - V_{Pb}/x/\Delta T$. S_{Pb} is the absolute thermopower of lead, V_{Pb}/x is the thermally induced voltage across the sample and ΔT the temperature difference. Hall effect and specific heat measurements have been carried out in a conventional Quantum Design Physical Property Measurement System (PPMS). Specific heat measurements were carried out down to 400 mK with a ^{3}He inset. Thermal conductivity data were obtained below room temperature by a steady state heat flow method and above room temperature from a Anter Flashline FL3000 unit.

3 The Non-Centrosymmetric Equiatomic Compounds HfRhGe, LaPtSi, LaIrSi and CeIrSi

The first experimental chapter focuses on formation and crystal structures of the non-centrosymmetric compounds HfRhGe, LaPtSi, LaIrSi and CeIrSi and briefly summarizes the results from physical properties measurements. Results are partially published in the paper ``Synthesis, characterization, electronic structure, and phonon properties of the noncentrosymmetric superconductor LaPtSi´´ (Kneidinger F. 2013) and in the PhD thesis on ``Non-centrosymmetric superconductivity of intermetallic compounds in absence of strong correlations among electrons´´ (Kneidinger F. 2014).

3.1 THE NON-CENTROSYMMETRIC SUPERCONDUCTING COMPOUND HfRhGe

A wide variety of intermetallic crystal structures without an inversion center can be found in the AlB_2 family (see (Hoffmann R. D. 2001), (Zumdick M. F. 1999)). One of them is the ZrNiAl structure type ((Krypyakevich P.I. 1967); space group $P\bar{6}2m$; a=0.6917(4) and c=0.3472(2) nm), which is considered as an ordered variant of the non-centrosymmetric Fe_2P structure type and therefore a ternary derivative structure type of AlB_2 (see (Kußmann D. 1998)). Superconductivity for the isotypic compound HfRhGe (a=0.6595 and c=0.3883 nm, from X-ray powder diffraction) at T_c=1.7 K has been reported from resistivity measurements by Zhong et al. (Zhong W.X. 1987). According to these authors HfRhGe exhibits an allotropic transition from a non-centrosymmetric high temperature modification (ZrNiAl type) to a low temperature centrosymmetric form (TiNiSi type; space group *Pnma*; a=0.6511, b=0.3936 and c=0.7547 nm; T_c=2.46 K).
The results from the reinvestigation of the crystal structure of HfRhGe by X-ray single crystal diffraction particularly in respect to a possible homogeneity range are summarized in this part.

3.1.1 Results and Discussion

3.1.1.1 Formation and Crystal structure of HfRhGe

As the high temperature non-centrosymmetric modification (ZrNiAl type) has been reported for quickly quenched stoichiometric HfRhGe alloys (Zhong W.X. 1987), the compound has been studied in as cast state by EPMA, XPD and XSCD. Annealing even at rather high

temperatures (1100°C and quenching in cold water) leads to the formation of the centrosymmetric HfRhGe modification (TiNiSi type) and results in a mixture of both structure types in the sample. EPMA measurements on alloys with slight off-stoichiometric compositions showed a very small phase width for $Hf_{1+x}Rh_{1-x}Ge$ with $-0.5 \leq x \leq 0.5$ in as cast state. One single crystal has been selected from a mechanically fragmented alloy with nominal composition HfRhGe right after arc melting. The single crystal diffraction data confirmed the hexagonal primitive unit cell (a=0.65919(3) and c=0.38838(2) nm) without further systematic extinctions. Single crystal solution and refinement in space group $P\bar{6}2m$ rapidly converged to a rather low R_F=0.029 value revealing a fully ordered arrangement of Hf atoms in the crystallographic site 3f (0.57641(6),0,0), Rh in 3g (0.2479(1),0,1/2) and Ge atoms in the crystallographic sites 1a (0,0,0) and 2d (1/3,2/3,1/2). After isotropic refinement of the displacement parameters, the difference Fouriere map showed electron density peaks approximately 0.02 nm outside the mirror plane for the Rh atoms in 3g. These residual electron densities could be covered by the anisotropic refinement of the displacement parameters but results in more than 2 times larger U_{33} (0.0102 $10^{-2}nm^2$) compared with U_{11} (0.0033(2) $10^{-2}nm^2$) or U_{22} (0.0046(3) $10^{-2}nm^2$). Therefore, the rhodium atoms have been placed on the half-filled general position 6i (0.2479,0,0.4799). Refinement in this case yielded spherical ADPs in all sites, R_F=0.018 and residual electron densities less than ± 1.75 e/Å^3. Details of the crystal structure refinement are given in Table I.

Table I: X-Ray single crystal data for HfRhGe at RT (ZrNiAl-type; Anisotropic displacement parameters U_{ij} in [$10^{-2}nm^2$]

Parameter/ Compound	**HfRhGe**
Space Group	$P\bar{6}2m$
Formula from EPMA	HfRhGe
Formula from refinement	HfRhGe
a, c [nm]	0.65912(2), 0.38821(1)
a, c (Ge) [nm]	0.65919(3), 0.38838(2)
μ_{abs} [mm^{-1}]	50.9
V (nm^3)	0.14607
ρ_x (gcm^{-3})	12.1
Reflections in refinement	367≥4σ(F_o) of 369
Number of variables	17
$R_F = \Sigma\|F_0-F_c\|/\Sigma F_0$	0.018
R_{Int}	0.063

wR2			0.038		
GOF			1.102		
Extinction (Zachariasen)			0.00023(4)		
Residual density $e^-/Å^3$; max; min			1.70; -1.75		
Atom parameters					
Hf in 3f (x,0,0); occ.			1.02(2)		
x,			0.57641(6)		
U_{11}, $U_{22}=U_{33}$			0.0064(2), 0.0045(1)		
Rh in 6i (x,0,z); occ.			0.504(2)		
x, z			0.2479*, 0.4799(1)		
U_{11}, U_{22}, U_{33}			0.0037(2), 0.0049(3), 0.0040(3)		
Ge1 in 1a (0,0,0); occ.			0.99(1)		
$U_{11}=U_{22}$, U_{33}			0.0093(4), 0.0052(5)		
Ge2 in 2d (1/3,2/3,1/2); occ.			1.01(1)		
$U_{11}=U_{22}$, U_{33}			0.0042(2), 0.0021(3)		
Interatomic distances [nm]; Standard deviation < 0.0001					
Hf –	4Ge2	0.2764		–2Rh	0.2830
	–1Ge1	0.2792		–2Rh	0.2834
	–2Rh	0.2856		–1Hf	0.2857
	–2Rh	0.2961		–1Hf	0.2960
	–4Rh	0.3062		–2Hf	0.3062
	–4Rh	0.3159		–2Hf	0.3159
	–4Hf	0.3409	Ge1 –	6Rh	0.2478
Rh –	1Rh	0.0156		–6Rh	0.2597
	–1Ge1	0.2478		–3Hf	0.2792
	–2Ge2	0.2527	Ge2 –	6Rh	0.2527
	–1Ge1	0.2597		–6Hf	0.2764

*fixed during refineme

The unit cell of HfRhGe including the coordination polyhedra is shown in Figure 1(a).

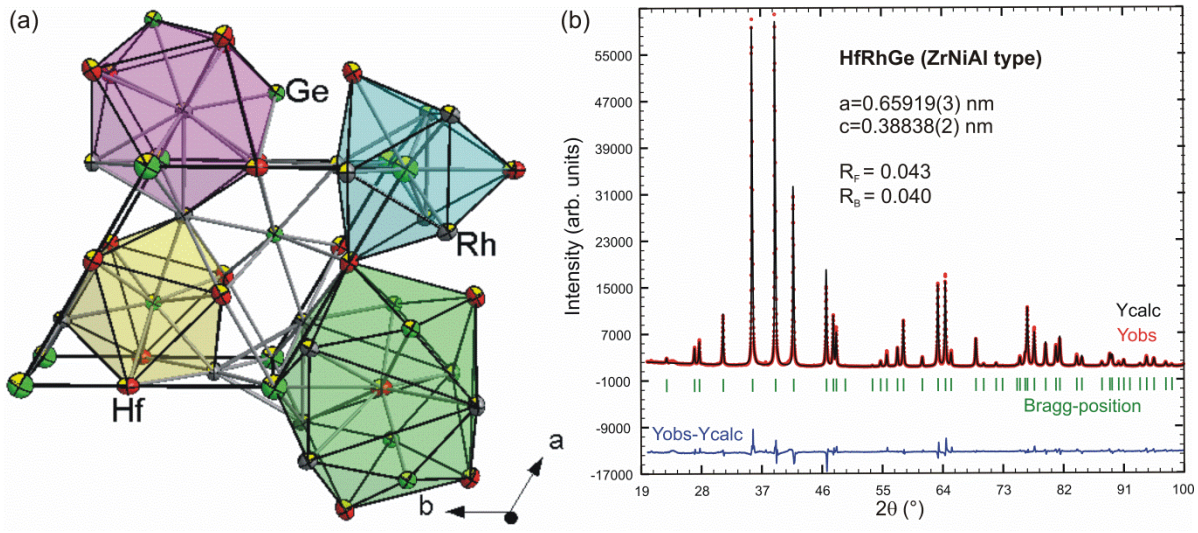

Figure 1: (a) Unit cell of HfRhGe including the coordination polyhedra for hafnium (green: $Hf[Hf_4Rh_6Ge1_1Ge2_4]$), rhodium (violet: $Rh[Hf_6Rh_2Ge1_2Ge2_2]$) and germanium atoms (blue: $Ge1[Hf_3Rh_6]$ and yellow: $Ge2[Hf_6Rh_3]$); rhodium atoms at the half-filled split position are only counted as one atom; (b) Rietveld refinement of HfRhGe.

Tricapped trigonal prisms (tetrakaidecadra) can be found around the germanium atoms (Ge1[Hf3Rh6] and Ge2[Hf6Rh3]) and larger coordination polyhedra with 12 vertices for rhodium (Rh[Hf6Rh2Ge12Ge22]) and 15 vertices for hafnium (Hf[Hf4Rh6Ge11Ge24]). No superstructure reflections have been observed either from XSCD or XPD (see Figure 1(b)) which would lead to the formation of a larger unit cell as has been reported for the compounds ZrIrSn, HfCoSn and HfRhSn (space group $P\bar{6}2c$; $a=a_{ZrNiAl}$ and $c=2c_{ZrNiAl}$) by Zumdick and Pöttgen (Zumdick M. F. 1999). Detailed discussions on the ZrNiAl structure type also in terms of group-subgroup relations with the aristoptype AlB_2 can be found f.e. in the papers of Hoffmann et al. (Hoffmann R. D. 2001), Zumdick and Pöttgen (Zumdick M. F. 1999) and Kußmann et al. (Kußmann D. 1998).

3.1.1.2 *Physical properties*

Results from electrical resistivity and heat capacity measurements show a superconducting transition at 1.69 and 1.66 K, which is in good agreement with the reported transition at 1.7 K (Zhong W.X. 1987). Further details concerning the physical properties of HfRhGe can be found in (Kneidinger F. 2014).

3.2 THE NON-CENTROSYMMETRIC COMPOUNDS LaPtSi, LaIrSi and CeIrSi

The crystal structures of the non-centrosymmetric compounds LaPtSi and LaIrSi have already been defined by Klepp and Parthe in 1982 ((Klepp K. 1982), (Parthe E. 1982)) from single crystal investigations. Simultaneously, Chevalier and coworker (Chevalier B. 1982) solved the crystal structure of LaIrSi from X-ray powder diffraction and found isotypism with the cubic ZrOS structure type. A superconductive transition at 2.3 K has been determined by resistivity measurements and an a.c. induction method (Chevalier B. 1982) in annealed samples (800°C). Evers et al. (Evers J. 1984) reinvestigated the superconducting transition of LaIrSi samples in as cast and annealed state by a.c. susceptibility measurements. As the critical temperature differs in as cast (T_c=1.5 K) and annealed (T_c=2.3 K) state, they suggested that superconductivity in LaIrSi is not a bulk property. In the same work (Evers J. 1984), superconductivity has been reported for LaPtSi with a transition temperature of 3.3 K. Ramakrishnan and coworker (Ramakrishnan S. 1995) studied in detail the superconducting properties (T_c=3.3 K from resistivity, specific heat, susceptibility) of LaPtSi and the influence of substitution with Ce and Nd on the transition temperature but no investigations have been made concerning the non-centrosymmetry. The isotypic compound CePtSi has been defined as a heavy fermion and coherent dense Kondo lattice compound without a magnetic or superconducting transition down to 70 mK by Lee and Shelton (Lee W.H. 1987).

Synthesis, structure and magnetic properties (measured between 2 and 300 K) of CeIrSi have been reported by Heying et al. (Heying B. 2004) together with other rare earth silicides *RE*IrSi (*RE* = Pr, Er, Tm, Lu) and $SmIr_{\sim 0.3}Si_{\sim 1.7}$. Magnetic susceptibility measurements on CeIrSi showed Curie-Weiss paramagnetism above 100 K. Deviations below 50 K from Curie-Weiss law have been interpreted as crystal field splitting of the ground state of Ce^{3+}-ions and the beginning of short range magnetic fluctuations as well (Heying B. 2004).

This chapter covers formation and crystal structures of LaIrSi, CeIrSi and LaPtSi. The results from physical properties measurements are briefly summarized for LaIrSi and LaPtSi.

3.2.1 Results and Discussion

3.2.1.1 Formation and crystal structure of LaIrSi, CeIrSi and LaPtSi

The compounds LaIrSi and CeIrSi form incongruently from the melt. In both cases, the 1:2:2 compound $LaIr_{2.1}Si_{1.9}$ or $CeIr_2Si_2$ (Compositions from EPMA) is the primary crystallizing phase. Therefore, both compounds have been annealed at 800 °C for 2 weeks. The LaIrSi

sample contained small amounts (< 1%) of $LaIr_2Si_2$ as an impurity phase and the CeIrSi contained also about 2% of $CeIr_2Si_2$ and $CeSi_{1.7}$ as impurities after annealing. Results from XPD and EPMA for the annealed alloys LaIrSi and CeIrSi are summarized in Table II.

Table II: Crystallographic data from XPD and results from EPMA measurements.

	LaIrSi	**CeIrSi**
Space group	$P2_13$	$P2_13$
a (nm)	0.63766(3)	0.62951(1)
RE 4a (x,x,x) x =	0.36714(6)	0.3683(2)
Ir 4a (x,x,x) x =	0.07740(5)	0.0830(2)
Si 4a (x,x,x) x =	0.6635(2)	0.6693(6)
R_F	0.028	0.062
EPMA (at.%) *RE*; Ir; Si	33.4; 34.7; 31.9	34.3; 32.7; 33.0

The compounds LaIrSi and CeIrSi crystallize in the primitive cubic ZrOS structure type (space group $P2_13$; a = 0.5881(2) nm (McCullough J.D. 1948)), an ordered ternary derivative of the also non-centrosymmetric $SrSi_2$-type (space group $P4_132$; a = 0.6515 nm (Pringle G.E. 1972)) ((Parthe E. 1982), (Chevalier B. 1982)). The unit cells of both compounds and the group-subgroup relations in form of a Bärnighausen tree ((Bärnighausen H. 1980), (M. U. Bärnighausen H. 1996)) are shown in Figure 2 together with the Rietveld refinement for LaIrSi.

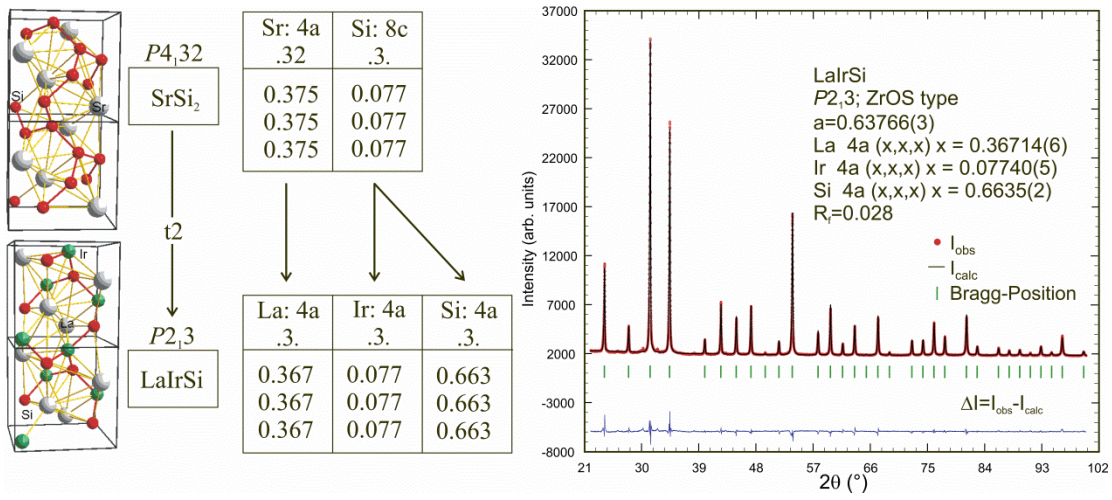

Figure 2: Group-subgroup relations for $SrSi_2$-LaIrSi (for a better representation, two unit cells are shown in b-direction for both compounds) and Rietveld refinement for LaIrSi.

In spite of LaPtSi forms congruently from the melt, the sample has been annealed for 1 week at 800°C.

LaPtSi (space group $I4_1md$; a = 0.42490(3), c = 1.4539(2) nm (Klepp K. 1982)) is and ordered ternary derivative structure type of α-$ThSi_2$ (space group $I4_1/amd$; a = 0.4126, c = 1.4346 nm (Brauer G. 1942). The corresponding group-subgroup relations are shown in Figure 3.

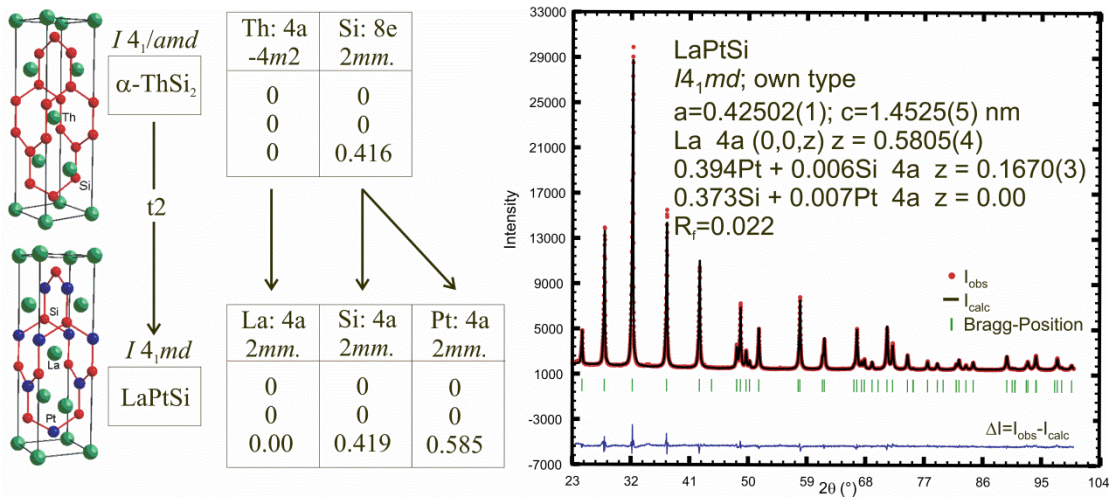

Figure 3: Group-subgroup relations in form of a Bärnighausen tree for α-$ThSi_2$ - LaPtSi (non-standardized setting) and the Rietveld refinement for LaPtSi (standardized setting).

Note that in this case, this is not the standardized setting of this crystal structure. The three-dimensional Si-Pt framework formed by two sets of perpendicular Si-Pt zig-zag chains can be seen in Figure 3. Intrachain and interchain distances are rather homogeneous. Also, the Pt-Si-Pt bond angles are almost identical, with only a slight deviation from 120°. This reflects the fact that LaPtSi is an ordered representative of the α–$ThSi_2$-type structure, which in turn is a shift variant of the hexagonal AlB_2 type.

The Rietveld refinement for this compound including crystallographic data is also shown on the right side in Figure 3. Refinement of the occupations in the crystallographic sites 4a (0,0,0.1670(3)) and 4a (0,0,0.00) revealed a slight mixture of Si and Pt in both sites.

3.2.1.2 Physical Properties

As the superconducting transition in LaIrSi varies with the preparation conditions (1.5 K as cast (Evers J. 1984), 2.3 K after annealing at 950 °C ((Evers J. 1984), (Chevalier B. 1982)), Evers (Evers J. 1984) concluded, that is probably not a bulk property. Specific heat

measurements for LaIrSi showed an almost perfect metallic behavior without any hint for a phase transition.

The reported values for the superconducting transition of LaPtSi vary from 3.18 to 3.8 K ((Evers J. 1984), (Klepp K. 1982), (Lee W.H. 1987)). Bulk superconductivity below 3.35 K for LaPtSi has been proven by electrical resistivity-, heat capacity- and magnetic susceptibility measurements. As an example of these measurements, the temperature dependent electrical resistivity of LaPtSi is shown in Figure 4.

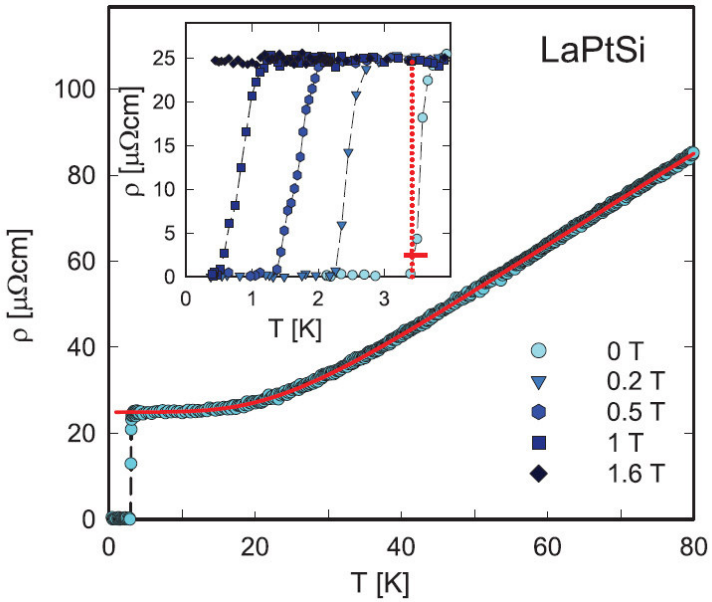

Figure 4: Temperature-dependent electrical resistivity ρ of LaPtSi. The red solid line is a least-squares fit. The inset shows the magnetic field dependence of the resistive superconducting transition. The dotted line indicates the phase transition temperature at $\mu_0 H$ = 0 T.

The superconducting transition is obvious from the drop of the electrical resistivity from about 25 μΩ to zero at 3.4 K. Above the superconducting transition, the resistivity curve follows a metallic behavior. A least squares fit (Wilson model (Wilson A. H. 1938)) to the experimental data is shown in Figure 4. The suppression of superconductivity through external applied magnetic fields can be seen from the inset in Figure 4. Further details concerning physical properties and performed DFT calculations can be found in (M. H.-S. Kneidinger F. 2013).

In conclusion, CeIrSi has not been found superconducting and bulk superconductivity has been excluded for LaIrSi. Analysis of all experimental results for LaPtSi revealed a fully gapped s-wave superconducting state.

4 Crystal Structures and Phase Diagram Investigations of Various Transition Metal Borides

The second part concentrates on crystal structure and/or phase diagram investigations of binary, ternary and quaternary borides. The results shown in this chapter are partially reported in the publications ``Crystal Structure of $W_{1-x}B_3$ and Phase Equilibria in the Boron-rich Part of the Systems Mo-Rh-B and W-{Ru,Os,Rh,Ir,Ni,Pd,Pt}-B´´ (Zeiringer I. 2014) and ``Crystal structure and Ce valence variation in the solid solution $CeRh_{3-x}Pd_xB_{0.5}$´´ (S. J. Zeiringer I. 2014).

4.1 CRYSTAL STRUCTURES AND CONSTITUTION OF THE BINARY SYSTEM IRIDIUM - BORON

The search for superhard and/or incompressible materials has led to a renewed research interest in binary transition metal borides especially on those with the highest boron contents (see (Ivanovskii A.L. 2011)). For example, $W_{1-x}B_3$ possesses a load independent Vickers hardness of 31.8 GPa (but 46.2 GPa at 0.5 N, (Gu Q. 2008)) and polycrystalline ReB_2 exceeds an average load independent Vickers hardness of about 30 GPa (48 GPa (0.5 N), (Chung H.Y. 2007)) or 26.6 GPa (39.3 GPa (0.5 N), (Gu Q. 2008)) with rather different hardness values due to the anisotropic crystal structure (details on the crystal structure of $W_{1-x}B_3$ can be found in the next chapter). Vicker's hardness measurements on the boron richest iridium boride $IrB_{1.35}$ revealed a load independent value of 18.2 GPa (at 9.81 N) and 49.8 GPa at 0.49 N (Rau J.V. 2009) and at such low loads is therefore comparable with bulk samples of ReB_2. Quite high hardness values were also recorded for $IrB_{1.1}$ thin films (on SiO_2 substrate) revealing an intrinsic film hardness of 43(±5) GPa (Latini A. 2010).

First investigations on the constitution of the binary system Ir-B revealed the existence of three compounds Ir_3B_2, IrB and IrB_2 ((Buddery J.H. 1951), (Samsonov G.V. 1972), (Haschke H. 1966), (Brukl C.E. 1967)). Some of the early reports were mainly concerned with the metal-rich eutectic (1046°C at 21.4 at.% B, (Reinacher G. 1965)), with the

optimization of synthesis techniques (Samsonov G.V. 1972) and with the stability of $IrB_{1.1}$ against various acids and bases (Kosenko und Zhidkova 1974). Melting point (T_m=1190±20°C), microhardness 1652±80 kgf/mm^2, Seebeck coefficient (20-800°C, $S_{V,min}$ = -9 μV/K at 350°C) and electrical resistance (20-800°C) for $IrB_{1.1}$ were reported by Samsonov et al. (Samsonov G.V. 1972). X-ray powder and single crystal (Weissenberg) photographs served to evaluate the crystal structure of $IrB_{1.1}$, which was reported to be isotypic with the α-$ThSi_2$ structure type (space group $I4_1/amd$; a = 0.2810, c =1.0263 nm) exhibiting a severe defect at the boron sites (8e sites randomly occupied by ~50 % of B atoms) (Aronsson B. 1960). For the compound richest in boron, "IrB_2", monoclinic symmetry (space group $C2/m$) was established from X-ray single crystal multi-film Weissenberg photographs yielding a crystal structure described as a stacking of puckered boron layers (A) and puckered double layers of metal atoms (B) in the simple sequence ABAB in c-direction (Aronsson B. 1963). Due to boron defects in two of the four B-sites a formula of $IrB_{1.35}$ was derived. A reinvestigation of the structure employing X-ray single crystal data from an automatic diffractometer by Lundström et al. (Lundström T. 1973) confirmed the monoclinic symmetry (space group $C2/m$; a ~ 1.053, b ~ 0.290, c ~ 0.610 nm and β = 91.1°) but suggested Ir-atoms off the mirror plane in the general position 8j (x,y,z) with an occupation of ½. Difference Fourier maps furthermore gave hints for only 3 boron positions instead of 4 with one of them only half occupied. The corresponding composition was thus close to Ir_5B_4.

For the third iridium–boride, "Ir_3B_2", richest in Ir, it is interesting to note that the X-ray powder photograph obtained by Haschke at 1200°C (labelled as "$Ir_{\sim 1.2}B$", (Haschke H. 1966) showed remarkable differences to that one, for which Brukl et al. (Brukl C.E. 1967) reported $\sin^2\theta$ values. Obviously a low- and high-temperature modification exist, the crystal structures of which were determined by Rogl et al. (Rogl P. 1971). The high temperature modification (labelled "$IrB_{0.9}$", WC type; space group $P\bar{6}m2$; a = 0.2815, c = 0.2823 nm) was observed above 1200°C, whereas the low temperature modification crystallizes with a unique structure type (space group $Cmc2_1$; a = 0.2771, b = 0.7578, c = 0.7134 nm; from X-ray single crystal multi-film Weissenberg photographs, R_F=0.07). Vandenberg et al. (Vandenberg J. H. 1975) searched for superconductivity in the high temperature modification, but the alloy remained normal down to 1.28 K.

Theoretical studies of IrB and IrB_2 using first principle calculations (Zhao W.J. 2009) revealed a hexagonal structure (space group $P6_3/mmm$; a ~ 0.35, c ~ 0.39 nm) to be

elastically stable for IrB and a stable orthorhombic structure for IrB_2 (space group *Pmmn*; a ~ 0.31; b ~ 0.45, c ~ 0.40 nm). In a later work, Wang et al. (Wang D.Y. 2012) predicted also an orthorhombic structure for IrB (space group *Pnma*; a ~ 0.443, b ~ 0.287 and c ~ 0.702 nm) while IrB_2 was said to be isotypic with OsB_2 (space group *Pmmn*; a ~ 0.315, b ~ 0.445 and c ~ 0.404 nm) ((Wang D.Y. 2012), (Hao X. 2007)). The calculations considered a series of alternative structure types: CsCl, FeB, WC, anti-NiAs, as well as AlB_2, ReB_2, WB_2. Among all these structures orthorhombic IrB (space group *Pnma*; a ~ 0.443, b ~ 0.287 and c ~ 0.702 nm) and IrB_2 with the OsB_2-type were found to be dynamically and mechanically stable. At a pressure of about 5 GPa orthorhombic IrB was said to undergo a phase transition to the anti-NiAs phase. In another theoretical study (Wang Y. 2012) on the 4d and 5d transition metal monoborides, IrB with WC crystal structure has been found to be thermodynamically stable at zero pressure. From the calculation, stoichiometric IrB is mechanically unstable, indicating together with the difference in experimental and calculated lattice parameters, the presence of boron vacancies in the crystal structure.

First experimental studies concerning the binary Ir-B phase diagram have been carried out by Reinacher on a hot stage microscope under argon (Reinacher G. 1965). He reports a very low melting eutectic at 1046°C on the iridium rich side (~21 at.% B). Brukl and Rudy (Brukl C.E. 1967) established the first binary phase diagram on the basis of metallography, XPD and pyrometric melting point data employing the Pirani method. Later, Spear (Spear K.E. 1977) predicted a phase diagram on the basis of some intermediate phases, but it is not in good agreement with crystallographic findings. Isothermal reactions, reported in the literature, are summarized in Table I.

Table I: Isothermal reactions in the binary Ir-B system reported in literature.

Reaction Type: Temperature (°C)	**Reaction**	**B content (at.%)**	**Ref.**
Eutectic: 1259 ± 4	$L \leftrightarrow (Ir)+IrB_{0.7}$	37.5	(Ipser H. 1981)
	$L \leftrightarrow (Ir)+IrB_{1-x}$		(Rogl P. 1988)
Eutectic: ~1040	$L \leftrightarrow (Ir)+IrB_{1-x}$	21	(Reinacher G. 1965)
Eutectic: 1250 ± 6	$L \leftrightarrow (Ir)+Ir_3B_2$	36±1	(Brukl C.E. 1967)
Eutectic: ~1045	$L \leftrightarrow (Ir)+IrB_{1-x}$	~35	(Spear K.E. 1977)
Congruent Melting: 1287 ± 5	$L \leftrightarrow IrB_{0.7}$	38.5	(Ipser H. 1981)
	$L \leftrightarrow IrB_{1-x}$		(Rogl P. 1988)
Congruent Melting: 1270 ± 20	$L \leftrightarrow Ir_3B_2$	~40	(Brukl C.E. 1967)
Congruent Melting: ~1057	$L \leftrightarrow IrB_{1-x}$	~38.5	(Brukl C.E. 1967)
Eutectic: 1258 ± 5	$L \leftrightarrow IrB_{0.7}+IrB_{0.9}$	~40	(Ipser H. 1981)

	$L \leftrightarrow IrB_{1-x}+IrB_{2-x}$		(Rogl P. 1988)
Eutectic: 1238 ± 8	$L \leftrightarrow Ir_3B_2+IrB_{0.89}$	~43	(Brukl C.E. 1967)
Eutectic: ~917	$L \leftrightarrow IrB_{1-x}+IrB_{2-x}$	~44	(Spear K.E. 1977)
Congruent Melting: 1333 ± 5	$L \leftrightarrow IrB_{0.9}$	46.5	(Ipser H. 1981)
	$L \leftrightarrow IrB_{2-x}$		(Rogl P. 1988)
Congruent Melting: 1328 ± 10	$L \leftrightarrow IrB_{0.89}$	~47	(Brukl C.E. 1967)
Congruent Melting: ~1093	$L \leftrightarrow IrB_{2-x}$	~49	(Spear K.E. 1977)
Peritectic: 1274 ± 5	$L+IrB_{0.9} \leftrightarrow IrB$	50	(Ipser H. 1981)
	$L+IrB_{2-x} \leftrightarrow IrB$		(Rogl P. 1988)
Eutectoid: 1209 ± 3	$IrB \leftrightarrow IrB_{0.9}+ IrB_{1.35}$	50	(Ipser H. 1981)
	$IrB \leftrightarrow IrB_{2-x}+Ir_4B_5$		(Rogl P. 1988)
Eutectic: 1248 ± 3	$L \leftrightarrow IrB+IrB_{1.35}$	54	(Ipser H. 1981)
	$L \leftrightarrow IrB+Ir_4B_5$		(Rogl P. 1988)
Eutectic: 1250 ± 10	$L \leftrightarrow IrB_{0.89}+IrB_{1.5}$	51	(Brukl C.E. 1967)
Metastable Eutectic: 1235	$L \leftrightarrow IrB_{0.9}+IrB_{1.35}$	53	(Ipser H. 1981)
	$L \leftrightarrow IrB_{2-x}+Ir_4B_5$		(Rogl P. 1988)
Congruent Melting: 1287 ± 5	$L \leftrightarrow IrB_{1.35}$	57.5	(Ipser H. 1981)
	$L \leftrightarrow Ir_4B_5$		(Rogl P. 1988)
Congruent Melting: 1315 ± 15	$L \leftrightarrow IrB_{1.5}$	~60	(Brukl C.E. 1967)
Eutectic: 1255 ± 4	$L \leftrightarrow IrB_{1.35}+(B)$	60	(Ipser H. 1981)
	$L \leftrightarrow Ir_4B_5+(B)$		(Rogl P. 1988)
Eutectic: 1240 ± 8	$L \leftrightarrow IrB_{1.5}+(B)$	~66	(Brukl C.E. 1967)
Eutectic: ~1000	$L \leftrightarrow IrB_{2-x}+(B)$	~52	(Spear K.E. 1977)

Ipser and Rogl (Ipser H. 1981) published invariant reaction temperatures and liquidus temperatures for the binary system and the complete phase diagram in the range from 20 to 70 at.% boron has been reported by Rogl (Rogl P. 1988). Based on this phase diagram evaluation, Zikovic et al. (Zivkovic D. 2005) estimated the thermodynamic activities in the liquid state at 2800 K, 2900 K and 3000 K for $0<x_{Ir}<0.35$ and $0.6<x_{Ir}<1.0$ (regular solution approach). For $IrB_{1.35}$ the standard enthalpy of formation ($\Delta H_f^0 = -49.1 \pm 2.4$ kJ/mol) has been derived by Meschel and Kleppa (Meschel S.V. 1991) from direct synthesis calorimetry at 1200°C. A high temperature mass spectrometric study reported a stable gaseous monoboride IrB and prompted the dissociation energy (D_o^0=508.5±17 kJ/mol IrB(g)) as well as the heat of formation ΔH_o^0(3rd law) = 43.6 kJ/mol for "IrB" (structure not specified) (Van der Auwera-Mahieu A. 1970).

As there still remained open questions concerning crystal structures and especially the

composition of the reported phases, this part focuses on crystal structures and compositions of the Ir-B phases and the re-evaluation of the constitution of the binary phase diagram on the basis of differential scanning calorimetry, X-ray powder diffraction as well as by electron probe microanalysis.

4.1.1 Results and Discussion

4.1.1.1 Binary phases in the Ir-B system

In the binary Ir-B system, four intermediate phases have been reported so far in literature, namely Ir_4B_5 (earlier labelled as $IrB_{1.35}$), $IrB_{1.1}$, h-$IrB_{0.9}$ (high temperature modification) and ℓ-$IrB_{0.9}$ (low temperature modification). Crystallographic data for all phases are summarized in Table II.

Table II: Crystallographic data on the binary Ir-B phases.

Phase	Space group	Structure type	Lattice parameter [nm]			Method	Ref.
			a	b	c		
(βB) 1800°, 24 h	$R\bar{3}m$	βB	1.09276(5)	-	2.38141(15)	XPD	(Crespo A.J. 1981)
(βB) 0.02 at% Ir #	$R\bar{3}m$	βB	1.09287(5)	-	2.38274(24)	XPD	(Crespo A.J. 1981)
$Ir_4B_{5.4}$	*C*2/*m*	Ir_4B_5	1.0525	0.2910 β= 91.07 °	0.6099	XSCD	(Aronsson B. 1963)
	*C*2/*m*	Ir_4B_5	1.052(1)	0.2889(1) β= 91.09(4) °	0.6094(7)	XPD	&
Ir_4B_5	*C*2/*m*	Ir_4B_5	1.05300(9)	0.29038(3) β=91.119(9)°	0.61013(5)	XSCD	(Lundström T. 1973) boron rich
Ir_4B_5	*C*2/*m*	Ir_4B_5	1.05421(10)	0.28905(3) β=91.143(6)°	0.61003(4)	XPD	(Lundström T. 1973) boron poor
Ir_4B_5	*C*2/*m*	Ir_4B_5	1.05200(2)	0.289564(6) β=91.156(2)°	0.60958(1)	XSCD	*
$IrB_{1.1}$	$I4_1/amd$	$ThSi_2$	0.2810	-	1.0263	XPD	(S. E. Aronsson B.

							1960)
$IrB_{1.1}$	$I4_1/amd$	$ThSi_2$	0.2808 0.2811	-	1.0259 1.0248	XPD XPD	$Ir_{55}B_{45}$ $Ir_{50}B_{50}$ (Brukl C.E. 1967)
$IrB_{1.1}$	$I4_1/amd$	$ThSi_2$	0.281	-	1.026	XPD	(Samsonov G.V. 1972)
Ir_5B_4	$I4_1/a$	Ir_5B_4	0.62777(1)	-	1.02599(2)	XSCD	*
$IrB_{0.9}$	$P\bar{6}m2$	WC	0.2815	-	0.2823	XPD	(N. H. Rogl P. 1971)
(hT)	$P\bar{6}m2$	WC	0.2813(1)	-	0.2826(2)	XPD	&
$IrB_{0.9}$ (lT)	$Cmc2_1$	$IrB_{0.9}$	0.2771	0.7578	0.7314	XSCD	(N. H. Rogl P. 1971)
Ir_4B_3 (lT)	$Cmc2_1$	$IrB_{0.9}$	0.27728(1)	0.75742(2)	0.73152 (2)	XSCD	*
(Ir)	$Fm\bar{3}m$	Cu	0.38392	-	-		(Villars P. 2013/14)

*This work; # calculated from the original data (0.31 mass% Ir in (βB)) as published by Crespo et al. (Crespo A.J. 1981); & evaluated from XPD un-indexed sin²θ values published by Brukl and Rudy (Brukl C.E. 1967)

A solubility of about 2 at.% iridium in beta-boron (space group $R\bar{3}m$; a = 1.09287(5) and c = 2.38274(24) nm) has been reported by Crespo et al. (Crespo A.J. 1981). However, a recalculation of the mass.% Ir in ßB, as published by Crespo et al., revealed a much smaller solubility of only 0.02 at.% Ir consistent with the small volume expansion observed (Crespo A.J. 1981). The crystal structures of the binary phases are discussed in detail in the next chapters.

4.1.1.2 The crystal structure of Ir_4B_{5+x} (formerly $IrB_{1.35}$)

A single crystal suitable for X-ray structure analysis was selected from an arc melted sample with nominal composition $Ir_{46}B_{54}$ (in at.%) which was crushed in a WC-mortar. Careful inspection of the extinction conditions confirmed the monoclinic symmetry and structure solution by direct methods was successful in space group *C*2/*m*. A first refinement shows consistency with iridium atoms in two 4i (x,0,z) sites (both on a mirror plane), however, with rather strong anisotropic atom displacement parameters (ADPs). This structure model (see model 1 in Table III) is essentially consistent with the one earlier described by Aronson et al. (Aronsson B. 1963).

Table III: Comparison of different structural models for Ir_4B_5 (earlier "$IrB_{1.35}$"). The non-standardized setting is kept for an easier comparison with the literature data. Anisotropic displacement parameters (U_{ij}) and isotropic temperature factors U_{iso} and B_{iso} (= $8\pi^2U_{iso}$) are given in $10^{-2}nm^2$.

Compound	**$IrB_{1.35}$ (model 1)** Aronsson et al. 1963	**Ir_4B_5 (model 2)** Lundström et al. 1973	**Ir_4B_5 (model 1)** This work	**Ir_4B_5 (model 2)** This work
Space group	*C*2/*m*	*C*2/*m*	*C*2/*m*	*C*2/*m*
Lattice parameter [nm]	a=1.0525, b=0.2910, c=0.6099	a=1.05300(9), b=0.29038(3), c=0.61013(5)	a=1.05200(2), b=0.289564(6), c=0.60958(1)	a=1.05200(2), b=0.289564(6), c=0.60958(1)
β (°)	91.07	91.119(9)	91.156(2)	91.156(2)
R	0.095 (h0ℓ), (h1ℓ)	0.082 (632 refls)	0.033	0.030
Atomic parameter				
Ir1/Wycoff Pos.;	4i (0.0994(1),0, 0.1387(2))	8j (0.09933(9),0.0310(5), 0.1386(1))	4i (0.09936(4),0, 0.13840(7))	8j (0.09936(3),0.0188*, 0.13838(4))
Occ.; U_{11}=U_{33}, U_{22}; B_{iso}	1 - 0.2	0.5 - 0.56(2)	1.001(3) 0.0014(2), 0.0043(4)	0.47(5) 0.0011(1), 0.0012(2)
Ir2/Wycoff Pos.;	4i (0.3575(1),0, 0.2885(2))	8j (0.35745(9),0.0292(5), 0.2886(1))	4i (0.35747(4),0, 0.28853(7))	8j (0.35746(3),0.0165*, 0.2883(5))
Occ. U_{11}=U_{33}, U_{22}; B_{iso}	1 - 0.2	0.5 - 0.59(2)	0.988(4) 0.0016(2), 0.0038(2)	0.48(4) 0.0011(1), 0.0010(2)
B1/Wycoff Pos.;	4i (0.555(4),0,0.388(6))	4i (0.554(4),0,0.381(5))	4i (0.558(1),0,0.385(1))	4i (0.558(1),0,0.384(1))
Occ. U_{iso}	1 B_{iso}=0.4	1 B_{iso}=1.3(3)	0.99(1) 0.004(1)	1.0 0.005(2)
B2/Wycoff Pos.;	4i (0.183(4),0,0.468(6))	4i (0.180(2),0,0.469(3))	4i (0.178(2),0,0.462(2))	4i (0.180(1),0,0.462(1))
Occ. U_{iso}	1 B_{iso}=0.5	1 B_{iso}=0.6(2)	0.98(7) 0.003(1)	0.93(5) 0.004(2)
B3/Wycoff Pos.;	4i (0.74(2),0,0.06(2))	4i (0.75(1),0,0.06(1))	4i (0.739(2),0,0.053(4))	4i (0.738(2),0,0.053(3))
Occ. U_{iso}	0.37 B_{iso}=2.9	0.5(1) B_{iso}=1.9(9)	0.47(4) 0.003	0.44(3) 0.003
B4/Wycoff Pos.;	4i (0.73(2),0,0.32(3))	-	-	-
Occ. U_{iso}	0.37 B_{iso}=2.4	-	-	-

*fixed before anisotropic refinement of the displacement parameter

However, the boron atoms located from our difference Fourier map unambiguously revealed only 3 boron positions (B1, B2, B3) instead of the 4 sites reported by Aronson et al. (Aronsson B. 1963) of which one (B3) was only half occupied. A difference Fourier map after isotropic refinement of the iridium atoms and subtracting the contribution of the boron atoms, revealed electron density peaks at ~0.1 Å off the mirror plane (see Figure 1) as has been previously described by Lundström et al. (Lundström T. 1973).

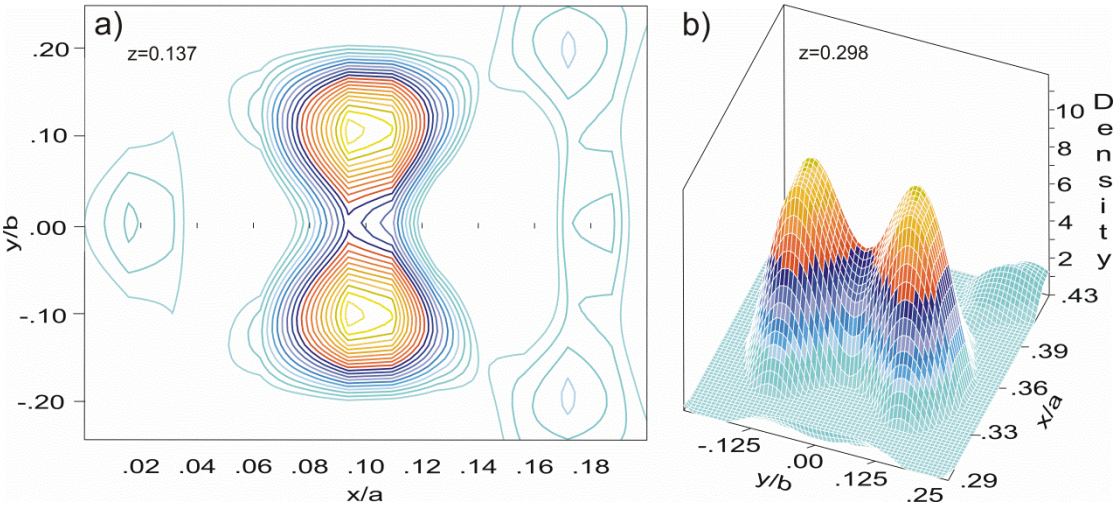

Figure 1: Difference Fourier maps for a) Ir1 and b) Ir2 after subtracting the contribution of the iridium atoms in the crystallographic sites 4a (x,0,z).

Following the arguments by Lundström et al. (Lundström T. 1973), Ir-atoms were placed in a half filled general position 8j (x,y,z) to satisfy the electron density peaks observed in the difference Fourier map. Refinement in this case (see model 2 in Table III) yields rather spherical ADPs for both Ir-atoms and low residual electron densities < 4.88 e/Å^3 at R_F=0.033. Needless to say that model 2 in all features confirms the crystal structure reported by Lundström (Lundström T. 1973). Figure 2 shows the unit cell of Ir_4B_5 and the corresponding coordination polyhedra for all atoms.

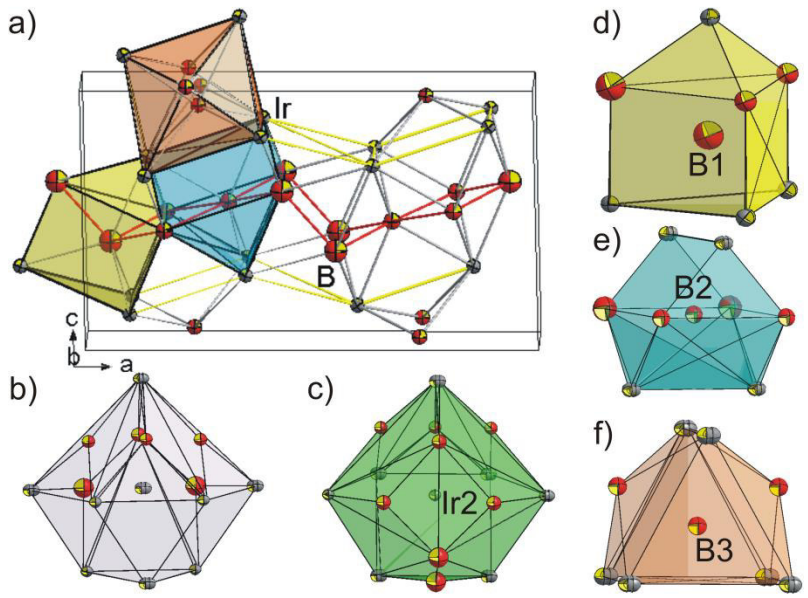

Figure 2: (a) Unit cell of Ir_4B_5 (model 2) and corresponding coordination polyhedra (b) $Ir1[B1_2B2_1B3_3Ir1_6Ir2_6]$, (c) $Ir2[B1_2B2_3B3_3Ir1_{10}Ir2_4]$, (d) $B1[B1_1B2_2Ir1_4Ir2_4]$, (e) $B2[B1_2B2_2Ir1_2Ir2_6]$ and (f) $B3[B3_2Ir1_6Ir2_6]$). Ir atoms are presented with anisotropic displacement parameters, whereas B-atoms are presented with isotropic ADP's from single crystal refinement.

The shortest interatomic bonding distances between the iridium atoms, the iridium and boron atoms and the boron atoms are: $d_{Ir\text{-}Ir}$=0.2660 nm, $d_{Ir\text{-}B}$=0.2089 nm, $d_{B1\text{-}B1}$=0.1877 nm, $d_{B1\text{-}B2}$=0.1990 nm, $d_{B2\text{-}B2}$=0.2106 nm and $d_{B3\text{-}B3}$=0.1610 nm. These values are in good agreement with those reported earlier (Lundström T. 1973). Further details of the crystal structure refinement including interatomic distances for the standardized setting of the structure are summarized in Table IV.

Table IV: X-Ray single crystal data for Ir_4B_5 at RT (Anisotropic displacement parameters U_{ij} in $[10^{-2}nm^2]$).

Parameter/Compound	**Ir_4B_5**
Space Group	*C* 2/*m*
Formula from EPMA	Ir_4B_5
Formula from refinement	Ir_4B_5
a, b [nm]	1.05200(2), 0.289564(6)
c [nm]	0.60958(1)
β (°)	91.156(2)
μ_{abs} [mm^{-1}]	71.3
V (nm^3)	0.1856
ρ_x (gcm^{-3})	14.68
Reflections in refinement	469≥4σ(F_o) of 512
Number of variables	33

$R_I = \Sigma\|F_0-F_c\|/\Sigma F_0$			0.033	
R_{Int}			0.052	
wR2			0.059	
GOF			1.136	
Extinction (Zachariasen)			0.0052(4)	
Residual density $e^-/Å^3$; max; min			4.88; -3.94	
Atom parameters				
Ir1 in 8j (x,y,z); occ.			0.47(5)	
x, *y*, *z*			0.09936(4), 0.48120 0.13840(7)	
$U_{11}= U_{33}$, U_{22}			0.0011(2), 0.0012(2)	
Ir2 in 8j (x,y,z); occ.			0.47(4)	
x, *y*, *z*			0.35747(4), 0.48347 0.28853(7)	
$U_{11}= U_{33}$, U_{22}			0.0011(1), 0.0010(1)	
B1 in 4i (x,0,z); occ.			1.0	
x, *z*			0.058(1), 0.385(1)	
U_{iso}			0.005(2)	
B2 in 4i (x,0,z); occ.			0.93(5)	
x, *z*			0.320(2), 0.538(4)	
U_{iso}			0.004(2)	
B3 in 4i (x,0,z); occ.			0.44(3)	
x, *z*			0.239(2), 0.054(4)	
U_{iso}			0.003*	
Interatomic distances in nm; Standard deviation < 0.0001				
Ir1 –	1Ir1	0.0109#	–1Ir2	0.2800
	–1B3	0.2089	–1Ir1	0.2848
	–1B3	0.2093	–1Ir1	0.2850
	–1B1	0.2100	–2Ir2	0.2896
	–1B2	0.2140	–1Ir1	0.2973
	–1B3	0.2167	–1Ir2	0.2991
	–1B1	0.2174	–1Ir1	0.3017
	–1Ir1	0.2660	–1Ir1	0.3023
	–1Ir1	0.2662	–1Ir1	0.3036
	–1Ir1	0.2787	–1Ir1	0.3071
	–1Ir2	0.2848	–1Ir1	0.3086
	–1Ir2	0.2850	–1Ir1	0.3132

	–2Ir1	0.2896	B1 –	1B1	0.1877
	–1Ir2	0.2973		–2B2	0.1990
	–1Ir1	0.3004		–2Ir1	0.2100
	–1Ir2	0.3017		–2Ir2	0.2167
	–1Ir2	0.3023		–2Ir1	0.2174
	–1Ir2	0.3036		–2Ir2	0.2175
	–1Ir2	0.3071	B2 –	2B1	0.1989
	–1Ir2	0.3080		–2B2	0.2106
	–1Ir2	0.3086		–2Ir2	0.2109
	–1Ir2	0.3132		–2Ir1	0.2135
Ir2 –	1Ir2	0.0096#		–2Ir2	0.2164
	–1B2	0.2109		–2Ir2	0.2174
	–1B2	0.2164	B3 –	2B3	0.1610
	–1B1	0.2168		–2Ir1	0.2089
	–1B2	0.2174		–2Ir1	0.2093
	–1B1	0.2175		–2Ir1	0.2167
	–1B3	0.2301		–2Ir2	0.2301
	–1B3	0.2344		–2Ir2	0.2344
	–1B3	0.2403		–2Ir2	0.2403

*fixed before refining the occupancy; # across mirror plane

B1 and B2 atoms form a puckered $^{2}_{\infty}$ layer and Ir_4B_5 is thus classified as a net-boride structure (Rogl P. 1991). With only a 50% occupation of the B3 site, B3 atoms are considered to be isolated in the structure. However, in case of a full occupation of the B3 site, infinite B-B chains would exist at a rather short distance ($d_{B3\text{-}B3}$=0.1610 nm) and further assuming a random (disordered) B3 occupation, only chain fragments may exist.

4.1.1.3 The crystal structure of Ir_5B_{4+x} (formerly $IrB_{1.1}$)

Although our X-ray powder pattern of a single-phase alloy (nominal composition $Ir_{52}B_{48}$ in at.%) annealed at 900 °C could be indexed on the basis of the α-$ThSi_2$ structure type (see Figure 3) as published for the compound labelled in the literature as "$IrB_{1.1}$" (space group $I4_1/amd$; a = 0.281 and c = 1.026 nm; (S. E. Aronsson B. 1960)), the calculated intensities from Rietveld refinement did not fit well to the experimental observation.

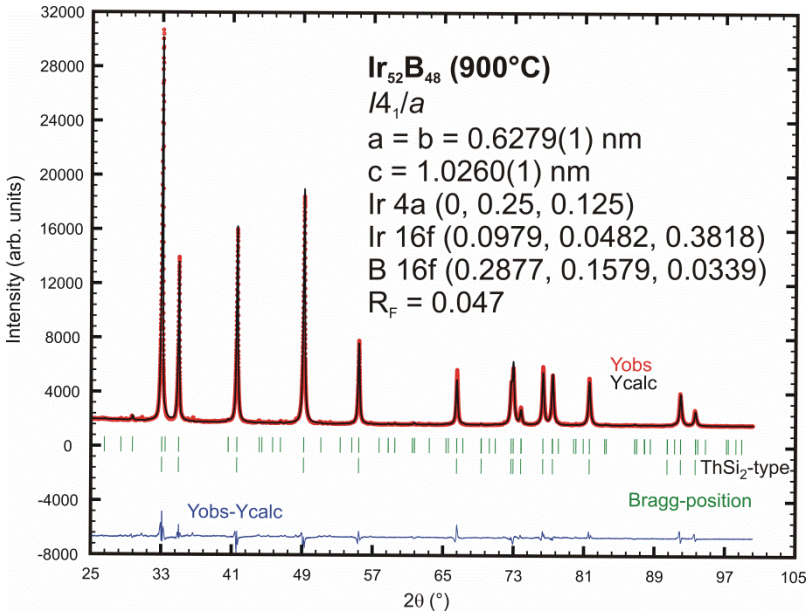

Figure 3: Rietveld refinement for an alloy with nominal composition $Ir_{52}B_{48}$ annealed at 900°C applying the Ir_5B_4 structure type and Bragg positions for the $ThSi_2$ structure type.

Therefore, a structure analyses has been attempted on a single crystal specimen mechanically isolated from the sample with nominal composition $Ir_{53}B_{47}$ (in at.%) obtained after the DSC measurement. Diffraction data for this crystal confirmed the tetragonal symmetry but revealed a 5 times larger unit cell ($a = \sqrt{5}a_{ThSi2} = 0.62777(1)$ and $c = c_{ThSi2} = 1.02599(2)$ nm) compared with the α-$ThSi_2$ type. The analysis of the systematic extinctions arrived at the space group $I4_1/a$ as the one with the highest symmetry. The corresponding refinement prompted iridium atoms in the crystallographic site 4a (0,¼,⅛) and in the general position 16f (0.10581(4), 0.04891(3), 0.37895(3)). After subtracting the contribution of the iridium atoms, the difference Fourier map contained only one set of electron density peaks, which could correspond to boron atoms (16f (0.2876(8), 0.1578(8), 0.0339(6)). A final refinement with anisotropic atom displacement parameters (ADPs) for the iridium atoms but isotropic temperature factors for the boron atoms revealed rather spherical shapes for both Ir-atoms and converged to a low R-value of $R_F = 0.031$ and residual electron densities smaller than ±4.5 $Å^3$. Occupancies were refined for all atoms, but within 3σ indicated no deviation from a full occupation. Results of the refinement are summarized in Table V and describe a completely ordered atom arrangement with the structure formula Ir_5B_4.

Table V: X-Ray single crystal data for Ir_5B_4 at RT (Anisotropic displacement parameters U_{ij} in $[10^{-2}nm^2]$).

Parameter/Compound	**Ir_5B_4**
Space Group	$I4_1/a$
Formula from EPMA	$Ir_5B_{4.2}$
Formula from refinement	Ir_5B_4
a, c [nm]	0.62777(1), 1.02599(2)
μ_{abs} [mm^{-1}]	32.8
V (nm^3)	0.40434
ρ_x (gcm^{-3})	16.5
Reflections in refinement	$426 \geq 4\sigma(F_o)$ of 495
Number of variables	19
$R_I = \Sigma\|F_0-F_c\|/\Sigma F_0$	0.031
R_{Int}	0.067
wR2	0.10
GOF	1.090
Extinction (Zachariasen)	0.0038(4)
Residual density $e^-/Å^3$; max; min	3.03; -4.49
Atom parameters	
Ir1 in 16f (x,y,z); occ.	0.99(2)
x, *y*, *z*	0.10581(4), 0.04891(3), 0.37895(3)
$U_{11}= U_{22}, U_{33}$	0.0031(2), 0.0028(3)
Ir2 in 4a (0,¼,⅛); occ.	0.99(3)
$U_{11}= U_{33}, U_{22}$	0.0027(2), 0.0029(2)
B1 in 16f (x,y,z); occ.	0.99(3)
x, *y*, *z*	0.2876(8), 0.1578(8), 0.0339(6)
U_{iso}	0.0061(7)

Interatomic distances [nm]; Standard deviation < 0.0001					
Ir1 –	1B1	0.2152	Ir2 –	4B1	0.2114
	–1B1	0.2153		–4Ir1	0.2778
	–1B1	0.2160		–4Ir1	0.2970
	–1B1	0.2201	B1 –	1Ir2	0.2114
	–1B1	0.2292		–1Ir1	0.2152
	–1Ir2	0.2778		–1Ir1	0.2153
	–2Ir1	0.2816		–1Ir1	0.2160

–1Ir1	0.2853	–1Ir1	0.2201
–1Ir1	0.2883	–1Ir1	0.2906
–2Ir1	0.2899	–1B1	(0.2906)
–1Ir2	0.2970		

A 3-dimensional view of the unit cell is presented in Figure 4a.

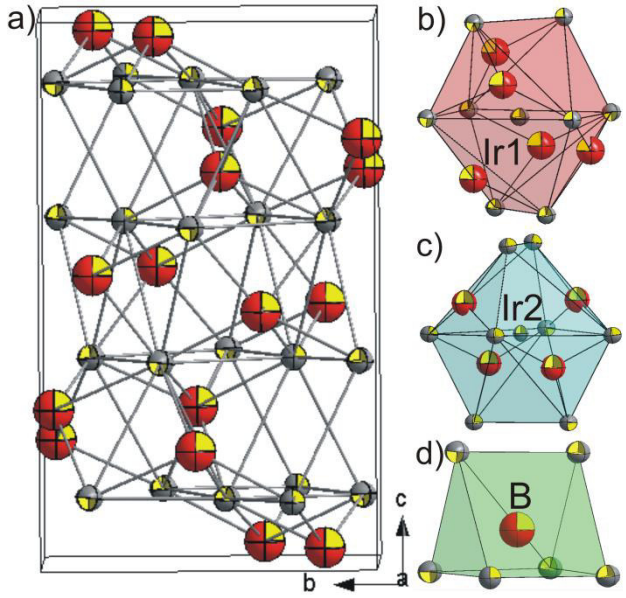

Figure 4: Crystal structure of Ir_5B_4 (a) 3-dim view of the unit cell, coordination figures (b) $Ir1[B_5Ir1_6Ir2_2]$, (c) $Ir2[B_4Ir1_8]$, (d) $B[Ir1_5Ir2_1]$. Ir atoms are presented with anisotropic displacement parameters, whereas B-atoms are presented with isotropic DP's from single crystal refinement.

Figure 4b-d show the corresponding coordination polyhedra for all atoms. The shortest interatomic bonding distances, $d_{Ir\text{-}Ir}$=0.2778 nm and $d_{Ir\text{-}B}$=0.2114 nm, are consistent with the sum of atom radii and a strong Ir-B bond (for atom radii see (Taetum E. 1972)). Although the parent $ThSi_2$-type exhibits a 3-dimensionally linked Si-framework, no direct boron-boron bonds are present in Ir_5B_4 ($d_{B\text{-}B}$=0.2906 nm).

Following the structural-chemical classification of borides as a function of B-B aggregation (Rogl P. 1991), the structure of Ir_5B_4 classifies as a new structure with isolated boron atoms in trigonal prismatic metal environment (Figure 4d). The crystal structure can be conceived as a new and ordered derivative of the α-$ThSi_2$ type. The corresponding crystallographic group-subgroup scheme in form of a Bärnighausen tree (Bärnighausen H. 1980) is shown in Figure 5 and compares the unit cells of the α-$ThSi_2$ type (Figure 5a) and Ir_5B_4 (Figure 5b).

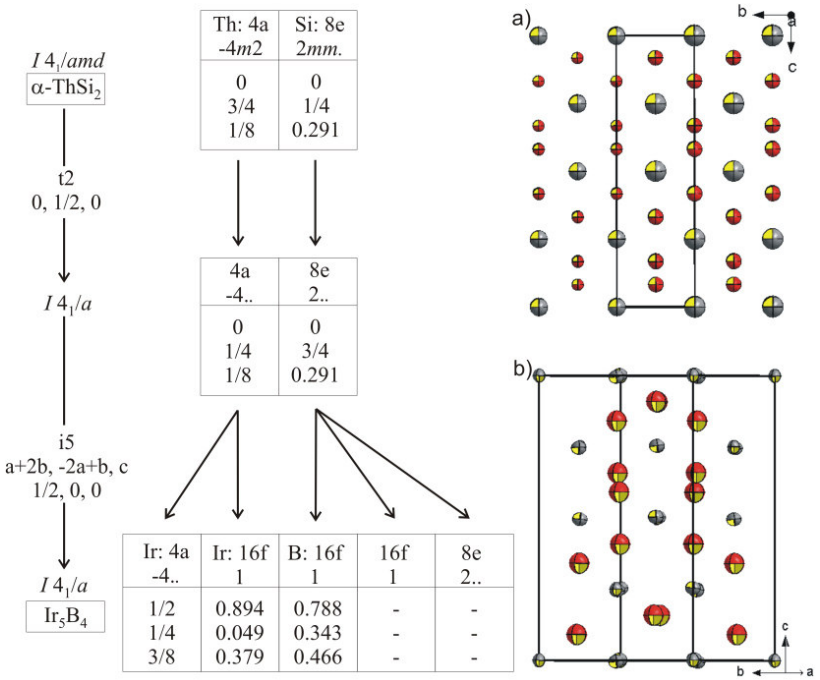

Figure 5: Group-Subgroup relations in form of a Bärnighausen tree for the pair of structures: α-$ThSi_2$-Ir_5B_4; the unit cells of (a) α-$ThSi_2$ and (b) Ir_5B_4 (origin has been shifted for both compounds) are shown for comparison.

As can be seen at the bottom of the scheme, the Wyckoff positions 16f and 8e (parent B-sites) are not occupied in the Ir_5B_4 structure type. Therefore, one can assume that boron-vacancy ordering leads to the formation of this new structure type. A Rietveld refinement of the X-ray powder pattern with the new structure type is shown in Figure 3. It should be noted here that the intensities of the superstructure reflections are rather small and almost indistinguishable from the background.

4.1.1.4 High and low temperature modification of Ir_4B_{3-x} (formerly $IrB_{0.9}$)

Rogl et al. (N. H. Rogl P. 1971) reported for $IrB_{0.9}$ a high temperature (hT) modification with WC- type (space group $P\bar{6}m2$; a = 0.2815 and c = 0.2823 nm) and a low temperature (ℓT) modification (own type; space group $Cmc2_1$; a = 0.2771, b = 0.7578 and c = 0.7134 nm). A reversible transformation from single phase low temperature material (alloy $Ir_{55}B_{45}$ (in at.% B) obtained at 1100°C) into a practically single phase high temperature modification was observed, when heated to ~1200°C: high and low temperature phases were simultaneously present at temperatures of 1100 to 1200°C, but transformed to a single low temperature phase after annealing for 12 h at 800°C (N. H. Rogl P. 1971). The ℓT modification has been assigned from single crystal X-ray Weissenberg multiple film data whereas the hT modification from XPD. In the WC

structure type, the Ir atoms occupy the crystallographic site 1a (0,0,0) and the boron atoms the site 1d (⅓,⅔,½), which is only partially filled. Reinvestigations of this phase by XPD and EPMA confirm the small hexagonal unit cell but with a slightly lower boron content (EPMA; $IrB_{0.7\text{-}0.75} \equiv IrB_{1-x}$; a = 0.28132(2) and c = 0.28298(2) nm). Although the precise boron site occupancy has not been determined yet, the formula suggests a defect WC-type. In the AlB_2 structure type, rather short B-B distances ($d_{B\text{-}B}$=0.1624 nm) would arise from a statistic distribution over the 2 fold site (Ir in 1a (0,0,0) and B in 2d (⅓,⅔,½)), which is more unlikely (see also (N. H. Rogl P. 1971)). For a new evaluation of the crystal structure of the low temperature phase, a single crystal specimen was mechanically isolated from the sample with nominal composition $Ir_{60}B_{40}$, which was slowly cooled in a DSC experiment. Analysis of the X-ray diffraction spots confirmed the previously reported orthorhombic C-centered unit cell (a=0.27728(1), b=0.75742(2) and c=0.73152(2) nm) and the observed extinctions lead to the possible space groups *Cmcm*, *C*2*cm* (standardized setting *Ama*2) and *Cmc*2_1. Placing the iridium atoms in the crystallographic sites 4a (0,0,0) and 4c (0,y,¼) in the highest symmetric centrosymmetric space group *Cmcm* results immediately in an R_F value lower than 4 %. A difference Fourier analysis showed two possible crystallographic sites for the boron atoms (B1 in 4c and B2 in 8f (0,y,z)), however, with only partial filling in both sites (occ.(B1)=0.80(6) and occ.(B2) = 0.32(7)). The highest residual electron density (8.9 e/Å^3) is too close to Ir1 (0.139 nm) for another boron atom. The shortest interatomic distances are: $d_{Ir\text{-}Ir}$=0.2771, $d_{Ir\text{-}B}$=0.2057 and $d_{B2\text{-}B2}$=0.1751 nm. The Ir-B distances are slightly smaller than the sum of the atomic radii as an indication of strong bonding. Smaller values are not exceptional for platinum metal borides, especially as both boron sites are only partially filled. The boron-boron aggregation in this space group reveals isolated atoms B1 ($d_{B1\text{-}B2}$=0.2254 nm) but atoms B2 form boron zig-zag chains along the *a* axis at an unlikely low occupancy of the B2-site (occ.(B2) = 0.32(7)). Therefore in search for B-sites of lower multiplicity alternative refinements were performed in the lower symmetry non-centrosymmetric space groups *C*2*cm* and *Cmc*2_1. Through the standardization process from the non-standard setting *C*2*cm* to the standard setting *Ama*2, the axis have been changed to *c, -b, a* and also the atomic coordinates (see Table VI), however, symmetry did not allow boron ordering i.e. a separation of the 8-fold B2-site into two 4-fold sites.

Table VI: Comparison of the crystal structure refinements for Ir_4B_{3-x} in the 3 possible space groups *Cmcm* (the non-standard setting is used for an easier comparison), *C*2*cm* (standardized setting *Ama*2) and *Cmc*2_1.

Composition from Refinement	**$Ir_4B_{2.9}$**	**Ir_4B_3**	**Ir_4B_3**
Space group	*Cmcm* (63)	*Ama*2 (40)	*Cmc*2_1 (36)
Lattice parameter (nm)	a=0.27728(1)	a=0.73152(2)	a=0.27728(1)
	b=0.75742(2)	b=0.75742(2)	b=0.75742(2)
	c=0.73152(2)	c=0.27728(1)	c=0.73152(2)
$R_F = \Sigma\|F_0-F_C\|/\Sigma F_0$	0.038	0.032	0.034
Number of variables	8	20	16
Residual density $e^-/Å^3$; max, min	8.93, -7.9	8.88, -7.67	8.27, -6.25
Reflections in refinement	$217 \geq 4\sigma(F_o)$ of 231	$342 \geq 4\sigma(F_o)$ of 361	$371 \geq 4\sigma(F_o)$ of 394
Atomic parameter			
Ir1/Wycoff Pos.;	4a (0,0,0);	4a (0,0,0*);	4a (0,0.0015(2),0.051(1));
Occ.; U_{11}, U_{22},	1; 0.0004(3), 0.0001(4),	1; 0.0012(4), 0.0001(3),	1; 0.0001(3), 0.0001(3),
U_{33}	0.0013(4)	0.0009(4)	0.0010(3)
Ir2/Wycoff Pos.;	4c (0,0.27591(7),1/4);	4b(1/4,0.27602(7),0.003(1));	4a (0,0.27600(9),0.302(1));
Occ.; U_{11}, U_{22},	1; 0.0007(4), 0.0010(4),	1; 0.0009(4); 0.0009(4),	1; 0.0003(2), 0.0006(3),
U_{33}	0.0009(4)	0.0003(4)	0.0009(3)
B1/Wycoff Pos.;	4c (1/2,0.064(2),1/4);	4b (1/4,0.065(2),0.475(1));	4a (0,0.289(1),0.0004(3));
Occ.; U_{11}, U_{22}, U_{33}	0.80(6); 0.003(3)	0.82(4); 0.004(1)	0.71(8); 0.002(7)
B2/Wycoff Pos.;	8f (1/2,0.204(5),0.055(4));	8c (0.051(4),0.205(4),	4a (0,0.559(1),0.306(1))
Occ.; U_{11}, U_{22}, U_{33}	0.32(7); 0.004(6)	0.513(6)); 0.35(4); 0.004(2)	0.79(9); 0.005(3)
Shortest distances (nm)			
d_{Ir-Ir}; d_{Ir-B}; d_{B-B}	0.2771; 0.2057; 0.1751	0.2772; 0.2080; 0.1689	0.2761; 0.2119; 0.1988
Unit Cell (yellow: Ir-Ir bonds; red: B-B bonds and grey: Ir-B bond)	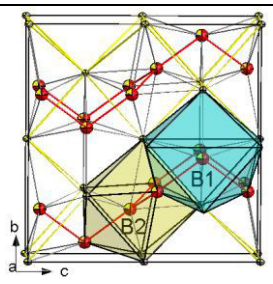	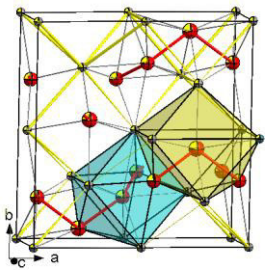	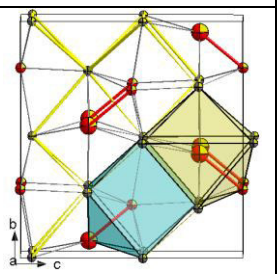

*fixed during refinement

Therefore the refinement leads to a similar atom arrangement with practically identical R values, occupancies and interatomic distances. Refinement in the non-centrosymmetric space group *Cmc*2_1 finally offers a reduction of the multiplicity of the B2-site (4a) yielding also full occupancy for the metal atom sites in 4a (0,y,z), but also about 75 to 80% for both boron atoms in sites 4a (occ.(B1)=0.71(8) and occ.(B2)=0.79(9)). Interatomic distances (d_{Ir-B}=0.2119 and d_{B1-B2}=0.1988 nm) are within the sum of the atomic radii. Final refinement with ADPs for iridium but isotropic thermal parameters for the light boron atoms in all 3 cases converged to R-

values between 0.032 and 0.038 ($R_{F(Cmcm)}$ = 0.038, $R_{F(Ama2)}$ = 0.032, $R_{F(Cmc21)}$ = 0.035). The atom site distributions in the unit cells of Ir_4B_3, as refined in the different space groups, are shown at the bottom of Table VI. A comparison of the crystal structure data of Ir_4B_3 for all the three space group types is given in Table VI. Considering fully occupied boron sites, boron chains are present in the first two, whereas only boron pairs (d_{B1-B2}=0.1988 nm) are present after refinement in $Cmc2_1$. The complete results of the crystal structure refinement in this space group can be found in Table VII.

Table VII: X-Ray single crystal data for Ir_4B_{3-x} at RT (Anisotropic displacement parameters U_{ij} in [$10^{-2}nm^2$]).

Parameter/Compound	**Ir_4B_3**
Space Group	$Cmc2_1$
Formula from EPMA	$Ir_4B_{2.8}$
Formula from refinement	Ir_4B_3
a, b [nm]	0.27728(1), 0.75742(2)
c [nm]	0.73152 (2)
μ_{abs} [mm^{-1}]	107.8
V (nm^3)	0.15349
ρ_x (gcm^{-3})	17.3
Reflections in refinement	371≥4σ(F_o) of 394
Number of variables	16
$R_I = \Sigma\|F_0-F_c\|/\Sigma F_0$	0.034
R_{Int}	0.029
wR2	0.078
GOF	1.665
Extinction (Zachariasen)	0.0008(8)
Residual density $e^-/Å^3$; max; min	8.27; -6.51
Atom parameters	
Ir1 in 4a (0,y,z); occ.	0.999(3)
y, z	0.0015(2), 0.051(1)
U_{iso}	0.0003(2)
Ir2 in 4a (0,y,z); occ.	1.000(3)
y, z	0.27600(9), 0.302(1)
U_{iso}	0.0006(2)
B1 in 4a (0,y,z); occ.	0.71(8)
y, z	0.289(1), 0.0000*

U_{iso}			0.002(7)		
B2 in 4a (0,y,z); occ.			0.79(9)		
y, *z*			0.559(1), 0.306(1)		
U_{iso}			0.007(3)		
Interatomic distances [nm]; Standard deviation < 0.0001					
Ir1 –	2B2	0.2119		–2Ir2	0.2772
	–2B1	0.2219		–1Ir1	0.2793
	–2B2	0.2239		–2Ir1	0.2853
	–2B1	0.2469		–2Ir1	0.2854
	–1Ir2	0.2761	B1 –	1B2	0.1988
	–2Ir1	0.2772		–2Ir2	0.2137
	–1Ir2	0.2793		–1Ir2	0.2171
	–2Ir2	0.2853		–2Ir1	0.2219
	–2Ir2	0.2854		–2Ir1	0.2469
Ir2 –	2B2	0.2123	B2 –	1B1	0.1988
	–2B1	0.2137		–2Ir1	0.2119
	–1B2	0.2143		–2Ir2	0.2123
	–1B1	0.2171		–1Ir2	0.2143
	–1Ir1	0.2761		–1Ir1	0.2239

*fixed during refinement

The unit cell with the corresponding coordination polyhedra is shown in Figure 6.

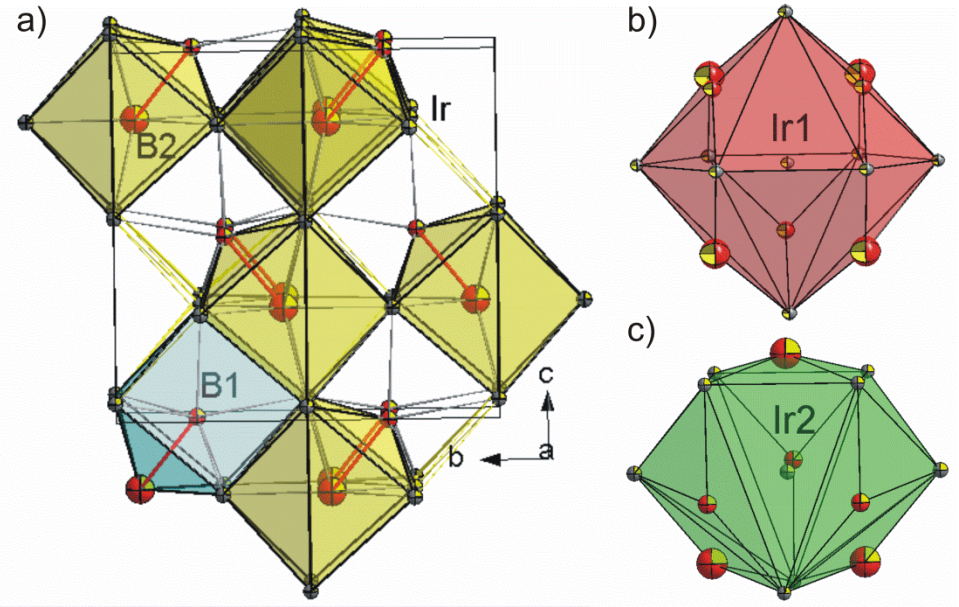

Figure 6: Crystal structure of Ir_4B_3 (a) unit cell including coordination polyhedra around the boron atoms (B1[$B2_1Ir1_3Ir2_3$], B2[$B1_1Ir1_4Ir2_3$]) and coordination polyhedra for the iridium atoms (b) Ir1[$B1_3B2_4Ir1_2Ir2_6$] and (c) Ir2[$B1_3B2_3Ir1_6Ir2_2$]. Ir atoms are presented with

anisotropic displacement parameters, whereas B-atoms are presented with isotropic DP's from single crystal refinement.

The finally refined composition of this crystal is Ir_4B_3, which is in rather good agreement with the result from EPMA measurement ($Ir_4B_{2.8}$). As has been mentioned also previously (N. H. Rogl P. 1971), neutron diffraction studies would be helpful for a final decision about the exact atom distribution in the boron sublattices.

4.1.1.5 The binary Ir-B system

Phase formation/decomposition and isothermal reactions in the binary system Ir-B have been studied on a series of samples in the composition range between 20 and 90 at.% boron by XPD, EPMA and DSC. The microstructures of several alloys in as cast state are shown in Figure 7 and the corresponding results from EPMA and XPD are summarized in Table VIII.

Table VIII: Results from EPMA measurements and X-ray phase analysis for Ir-B alloys in as cast state and/or after annealing; (a)-(f) correspond to the SEM pictures shown in Figure 7.

Sample	Phases	Structure Type	Composition EPMA (at.%)		Lattice Parameter (nm)		
			Ir	B	a	b	c
$Ir_{42}B_{58}$	(B)	B	0.2	99.8	-	-	-
as cast	Ir_4B_{5+x}	Ir_4B_5	44.9	55.1	1.0533(7)	0.29018(1)	0.6100(1)
(a)						β=91.15(1)	
$Ir_{47}B_{53}$	Ir_4B_{5+x}	Ir_4B_5	46.0	54.0	1.0525(2)	0.28982(8)	0.61008(9)
as cast						β=91.15(7)	
(b)	Ir_5B_{4+x}	Ir_5B_4	53.2	46.8	0.62741(9)	-	1.0262(2)
$Ir_{52}B_{48}$	Ir_4B_{5+x}	Ir_4B_5	45.8	54.2	1.0530(1)	0.2894(1)	0.6088(3)
as cast						β=91.14(1)	
(c)	Ir_5B_{4+x}	Ir_5B_4	52.7	47.3	0.6279(3)	-	1.0263(3)
$Ir_{58}B_{42}$	Ir_5B_{4+x}	Ir_5B_4	53.3	46.7	0.6282(2)	-	1.0267(3)
as cast	Ir_4B_{3-x}	WC	56.8	43.2	-	-	-
(d)	Ir_4B_{3-x}	Ir_4B_3	56.8	43.2	0.27719(2)	0.7580(2)	0.73144(9)
	(Ir)	Cu	100*	0	-	-	-
$Ir_{62}B_{38}$	Ir_4B_{3-x}	WC	58.3	41.7	0.28115(2)	-	0.28315(8)
as cast	Ir_4B_{3-x}	Ir_4B_3	58.3	41.7	0.27717(2)	0.7580(3)	0.7315(3)
(e)	(Ir)	Cu	100*	0	0.3837(3)	-	-
$Ir_{90}B_{10}$	Ir_4B_{3-x}	WC	58.7	41.3	0.28137(5)	-	0.2828(1)
as cast	Ir_4B_{3-x}	Ir_4B_3			traces	-	-

(f)	(Ir)	Cu	100*	0	0.38345(1)	-	-

*fixed values

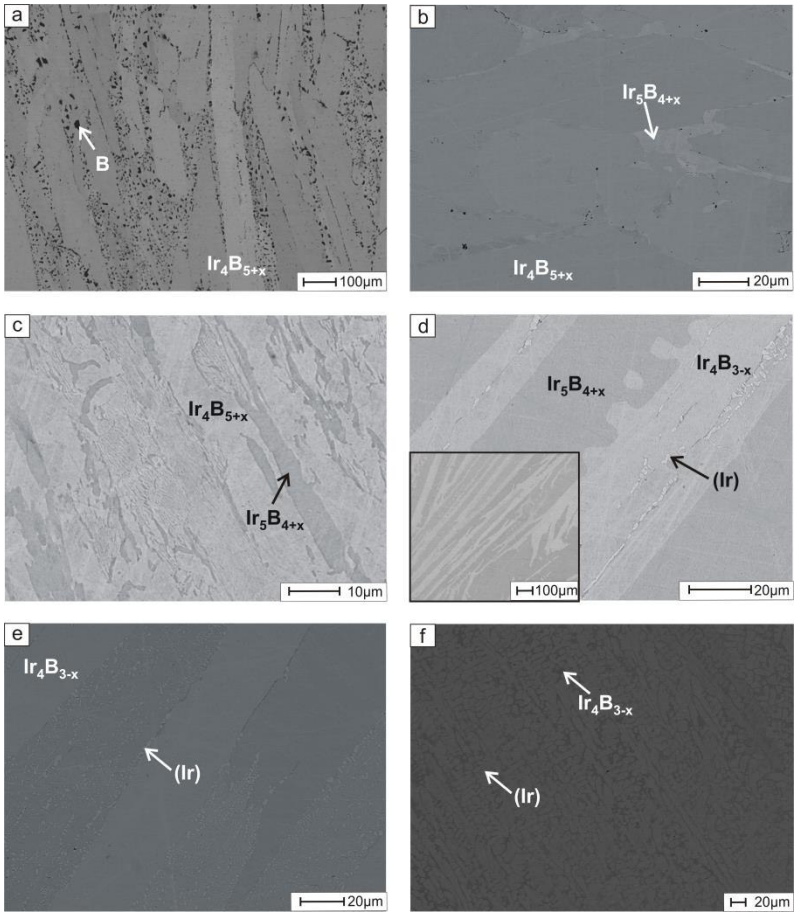

Figure 7: Microstructures of several alloys in as cast state with nominal composition (in at.%) (a) $Ir_{42}B_{58}$, (b) $Ir_{47}B_{53}$, (c) $Ir_{52}B_{48}$, (d) $Ir_{58}B_{42}$, (e) $Ir_{62}B_{38}$ and (f) $Ir_{90}B_{10}$; results from EPMA and XPD for these alloys are summarized in Table VIII.

The microstructure of an alloy with nominal composition $Ir_{42}B_{58}$ (Figure 7a) shows primary crystallization of Ir_4B_{5+x} followed by the crystallization of a boron rich eutectic e_1: L↔βB+Ir_4B_{5+x} at 1256±6 °C. The invariant reaction temperature correspond well with those reported earlier (1255 ±4°C at 60 at.% B (Ipser H. 1981), 1240 ±8 °C at ~66 at.% B (Brukl C.E. 1967) and also the location of the eutectic at ~ 60 at.% B. The Ir_4B_{5+x} phase melts congruently at 1288±4 °C (1287±5 °C (Ipser H. 1981), 1313±15 °C (Brukl C.E. 1967), see also Table I). As has been also previously reported (Aronsson B. 1963), this compound is not stable at lower temperatures (T ≤ 1100°C) and decomposes at 1083±10 °C into Ir_5B_{4+x} and boron. Lattice parameter determined in as cast state decrease slightly with decreasing boron content (see Table VIII) but are generally 0.01Å smaller than those reported by Lundström (Lundström T. 1973). Figure 7b (alloy with nominal composition

$Ir_{47}B_{53}$) shows primary grains of Ir_4B_{5+x} and the crystallization of the last liquid in form of Ir_5B_{4+x}. A rather fine eutectic like microstructure consisting of Ir_4B_{5+x} and Ir_5B_{4+x} is visible from the alloy $Ir_{52}B_{48}$ in Figure 7c. Brukl and Rudy (Brukl C.E. 1967) determined 1250±5 °C as the isothermal reaction temperature for the eutectic e_2: $L \leftrightarrow Ir_4B_{5+x}+Ir_5B_{4+x}$ (at ~51 at.% B), whereas Ipser and Rogl (Ipser H. 1981) assigned this temperature to another invariant reaction namely e_3: $L \leftrightarrow Ir_4B_{5+x}+IrB$ (at 54 at.% B). In that work, the peritectic formation of the IrB phase is reported at 1274±4 °C (p_1: $L+Ir_5B_{4+x} \leftrightarrow IrB$ at 50 at.% B) and a metastable eutectic e_2: $L \leftrightarrow Ir_4B_{5+x}+Ir_5B_{4+x}$ at ~1235°C has been found instead with the approximate composition $Ir_{47}B_{53}$. The WC structure type has been assigned for IrB and the phase decomposes eutectoidally at 1209±3 °C into Ir_5B_{4+x} and Ir_5B_{4+x}. In this work, all alloys in the composition range between $Ir_{53}B_{47}$ – $Ir_{47}B_{53}$ (in at.%) exhibit an invariant effect at 1210±3 °C followed by several effects close to the afore mentioned temperatures. As the alloys were only investigated in as cast state, after DSC and after annealing at lower temperatures (<1000°C), no other phase has been detected with approximately 50 at.% boron by XPD or EPMA. The next boron rich phase Ir_5B_{4+x} is congruently forming and melts at 1339±5 °C (1333±5 °C (Ipser H. 1981), 1328±10 °C (Brukl C.E. 1967)). The microstructure of an alloy with nominal composition $Ir_{58}B_{42}$ is shown in Figure 7d. Large grains of Ir_5B_{4+x} are present (see inset Figure 7d) together with the hT and lT form of Ir_4B_{3-x} (assigned from XPD) and small amounts of (Ir). Ir_4B_{3-x} has been reported to melt congruently at 1287±5 °C by Ipser and Rogl and at 1270±20 °C by Brukl and Rudy. Although the microstructure of the shown as cast alloy gives hints to a peritectic formation of this phase, the results from the DSC measurements confirm the congruent melting at around 1289±5 °C. Both groups of authors also agree on an eutectic e_4: $L \leftrightarrow Ir_5B_{4+x}+Ir_4B_{3-x}$ at 1258±5 °C (~40 at.% B, (Ipser H. 1981) or at 1238±8 °C (~43 at.% B, (Brukl C.E. 1967)). Nevertheless, in none of the alloys investigated in this work or in the work of Brukl and Rudy this eutectic has been observed. As argued also previously, the eutectic is placed there because of the 2 neighboring congruent melting compounds (Brukl C.E. 1967). The microstructure of an alloy with nominal composition $Ir_{62}B_{38}$ (Figure 7e) shows primary grains of Ir_4B_{3-x} and an eutectic with (Ir). The invariant reaction temperature for this eutectic e_5: $L \leftrightarrow (Ir)+Ir_4B_{3-x}$ is 1259±4 °C (1259±4 °C at 37.5 at.% B (Ipser H. 1981), 1250±6 °C at ~36 at.% B (Brukl C.E. 1967)). Rogl et al. (N. H. Rogl P. 1971) investigated the hT and lT modification and found above 1200°C only the hT form, in the temperature range

1100-1200 °C both modifications and below 1100°C only the lT form and therefore suggested a two phase transition. Figure 7f shows primary grains of (Ir) followed by the crystallization of the same eutectic but almost only the hT modification of Ir_4B_{3-x} (and traces of the lT form) is present on the XPD pattern of this alloy in as cast state. From the combination of literature data with new ones, the binary Ir-B phase diagram shown in Figure 8 has been constructed.

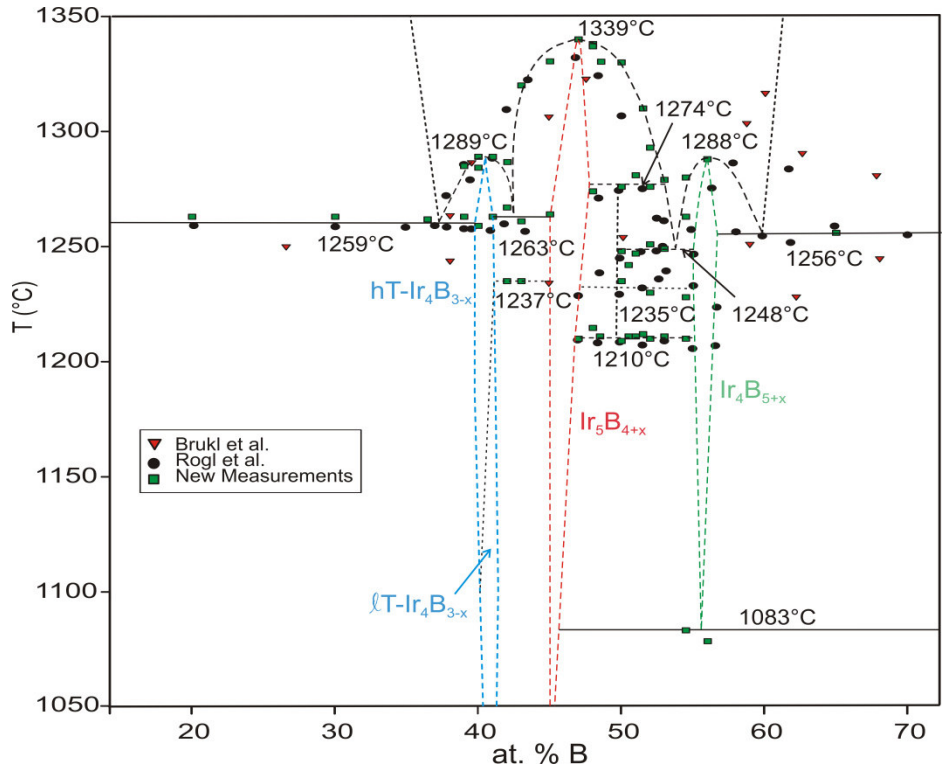

Figure 8: Proposed binary phase diagram Ir-B including literature data from Rogl et al. (Rogl P. 1988) and Brukl et al. (Brukl C.E. 1967) above 1050°C.

Further investigations at temperatures above 1200°C in the composition range around 50 at.% B and between 1250 and 1100 °C < 60 at.% B would be necessary to complete this diagram.

4.1.1.6 Summary

The binary system Ir-B has been investigated in the composition range between 10 and 70 at.% boron. Four binary phases have been found namely Ir_4B_{5+x}, Ir_5B_{4+x} and the high and low temperature modification of Ir_4B_{3-x}. X-ray single crystal diffraction studies have been performed on Ir_4B_{5+x} (x=0, Ir_4B_5 structure type; Space group *C*2/*m*; a = 1.05200(2), b = 0.289564(6) and c = 0.60958(1) nm, β = 91.156(2)°), Ir_5B_{4+x} (x=0, Ir_5B_4 structure type; Space group $I4_1/a$; a = 0.62777(1) and b = 1.02599(2) nm) and on the low temperature modification of Ir_4B_{3-x} (x=0, $IrB_{0.9}$ structure type; Space group $Cmc2_1$; a =

0.27728(1), b = 0.75742(2) and c = 0.73152(2) nm). Ir_5B_{4+x} (x=0) crystallizes with a new ordered α-$ThSi_2$ derivative structure type. The high temperature modification of Ir_4B_{3-x} (WC structure type; Space group $P\bar{6}m2$; a = 0.28137(5) and c = 0.2828(1) nm) has been confirmed by X-ray powder diffraction. A proposition for the binary Ir-B phase diagram has been constructed from combination of the results from XPD, EPMA and DSC with literature data.

4.2 CRYSTAL STRUCTURE OF $W_{1-x}B_3$ AND PHASE EQUILIBRIA IN THE BORON-RICH PART OF THE SYSTAMS Mo-Rh-B AND W-{Ru,Os,Rh,Ir,Ni,Pd,Pt}-B

Superhard materials (i.e. a material with a hardness surmounting 40 GPa ((Riedel R. 1994), (Veprek S. 1999), (Haines J. 2001), (Ivanovskii A.L. 2011)) are generally found in three different categories: I) crystalline and disordered carbon modifications, II) compounds formed by the light elements B, C, N, O, Si and III) compounds of transition metals (TMs) with light elements B, C, N or O ((V.V. Brazhkin 2002), (Gu Q. 2008)). The main important parameters guiding high hardness have been identified as (i) the presence of directional covalent bonding and (ii) a high electron concentration (electrons per atomic volume) of the transition metal (TM) ((Gu Q. 2008), (Gilman J.J. 2006)). Among borides particularly those richest in boron in the systems with W ("WB_4" at about 80 at.% B) and Re ("ReB_2" at about 66.7 at.% B) have triggered intensive research interest as potential superhard compounds. Although in many cases indentation hardness values beyond 40 GPa have been measured at miniaturized loads, load independent hardness, which essentially characterizes the true hardness of a material, never surpassed the superhardness criterion of 40 GPa. In the following we list a few of these examples referring to transition metal borides. "WB_4" was reported to possess a load independent Vickers hardness of 31.8 GPa (but 46.2 GPa at 0.5 N (Gu Q. 2008)). Load dependent hardness measurements and Re substitution studies by Mohammadi et al. (Mohammadi R. 2011) yield a load independent hardness of 28.1 GPa (but 43.3 GPa at 0.5 N) for WB_4 and an increase to 32.5 GPa (49.8 GPa (0.5 N)) with an addition of about 1 mole% Re. Polycrystalline ReB_2 exceeds an average load independent Vickers hardness of about 30 GPa (48 GPa

(0.5 N) (Chung H.Y. 2007)) or 26.6 GPa (39.3 GPa (0.5 N) (Gu Q. 2008)) with rather different hardness values obtained due to the anisotropic crystal structure. From Vickers hardness measurements on various crystallographic planes of a single crystal, Levine et al. determined the crystallographic (002) plane to be the hardest of ReB_2 (Levine J.B. 2008). The isotypic substitution of Re by W/Os, W/Ir and W/Ru has been studied first by Rogl and coworkers (N. H. Rogl P., Ternary Complex Borides in the Systems: {Mo, W}-{Ru, Os}-B and W-Ir-B 1970), (B. F. Rogl P. 1970) Vickers hardness measurements on $W_{0.5}Os_{0.5}B_2$ revealed a load independent hardness of 26.6 GPa (40.4 GPa (0.5 N)) (Gu Q. 2008) and single crystal studies confirmed the ReB_2 structure type with a random occupancy of the TM site (Gu Q. 2008). As the hardness of a material above the asymptotic leveling is not meaningful ((Brazhkin V. 2004), (Dubrovinskaia N. 2007)), all the aforementioned compounds cannot be considered as superhard materials but nevertheless are among the hardest metal borides.

Despite several structure models have been proposed in the past for the boron richest W-boride ((Chretien A. 1961), (Rudy E. 1963), (Romans P. A. 1966), (Nowotny H. 1967), (Lundström T. 1973)), $W_{1-x}B_3$ ("WB_4"), the structure type of isotypic $Mo_{1-x}B_3$ (Lundström T. 1973) has been widely accepted. However, more recent theoretical calculations of band structure and physical properties (density functional theory calculations DFT) of this compound have inferred some confusion on the true crystal structure of "WB_4" ((Liang Y. 2001), (Gou H. 2012), (F. Z. Liang Y. 2012), (Zhang R.F. 2012), (Zang C. 2012), (Li Q. 2013), (Y. X. Liang Y. 2012)). Whereas the first studies by A. Chretien and J. Helgorsky (Chretien A. 1961) reported a tetragonal unit cell for "WB_4" (a=0.634 nm, c=0.450 nm), Rudy et al. (Rudy E. 1963) claimed a hexagonal cell (a=0.3004 nm, c=0.3174 nm) but proposed "WB_{12}" as a more appropriate composition. A first structure model was derived by Romans and Krug (Romans P. A. 1966) from X-ray powder data backed by single crystal Laue and precession photographs indexed on a hexagonal lattice (a=0.5200 nm, c=0.6340nm). The proposed structure of stoichiometric WB_4 was derived from the AlB_2 structure, by replacing one third of the metal atoms by pairs of boron atoms (dumbbells) linking the two-dimensional planar boron layers into a three-dimensional covalently bonded boron framework (Romans P. A. 1966). The boron dumbbells are located just in the voids (two per unit cell) created by the metal atom missing in the planar hexagonal closed packed metal atom layers at z=¼, ¾. Independently Nowotny et al. (Nowotny

H. 1967) proposed a similar structure on the basis of X-ray powder and rotating crystal data (a=0.5206 nm, c= 0.6335 nm), where [B_6]-octahedra replace one third of the metal atoms in the hexagonal metal layer creating a three-dimensional boron-skeleton at a composition of $W_{2-x}B_9$ ($x \approx 1/6 \equiv W_{17}B_{83}$ in at.%). Nowotny et al. (Nowotny H. 1967) also evaluated the relation among the different sets of unit cell dimensions (see Figure 9).

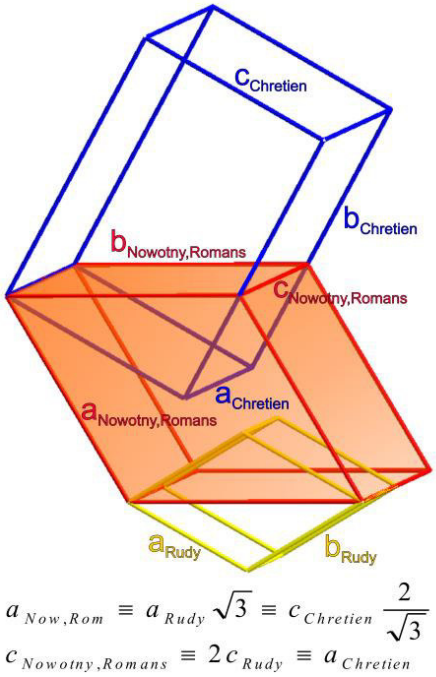

Figure 9: Relation of the different unit cell propositions for "WB_4" from Nowotny et al. (Nowotny H. 1967), Romans and Krug (Romans P. A. 1966), Rudy et al. (Rudy E. 1963) and Chretien et al. (Chretien A. 1961).

From the X-ray powder spectra reported there is no doubt that the phases "WB_4" and "$W_{2-x}B_9$" of the various aforementioned research groups ((Chretien A. 1961), (Rudy E. 1963), (Romans P. A. 1966), (Nowotny H. 1967), (Lundström T. 1973)) are all identical and secondly are isotypic with the homologous phases observed in the Mo-B system: "MoB_4" and "$Mo_{2-x}B_9$" (Lundström T. 1973). Nowotny et al. (Nowotny H. 1967) furthermore reported on a considerable solubility of Rh, Ni, Pd and Pt in $W_{2-x}B_9$ and particularly the PhD work of Haschke (Haschke H. 1966) indicated the existence of ternary compounds $(Mo,Rh)_{2-x}B_9$ and $(W,M)_{2-x}B_9$ (M=Rh, Ni, Pd, Pt) at 900°C.

Lundström and Rosenberg (Lundström T. 1973) analyzed in detail the X-ray powder pattern of the crystal structure of $Mo_{1-x}B_3$ (x~0.2; $P6_3/mmc$, a=0.52026 nm, c=6.3489 nm, B-rich) from which they derived defect close-packed metal layers sandwiched by

planar boron honeycomb layers stacked along the c-direction (Lundström T. 1973). There are no direct B-B contacts between B-layers. The boron honeycomb layers in z=0 are planar ((Romans P. A. 1966), (Lundström T. 1973)) or slightly puckered (Nowotny H. 1967); a planar boron honeycomb layer also exists in the structures at z=0.5 ((Romans P. A. 1966), (Lundström T. 1973)). Lundström and Rosenberg (Lundström T. 1973) confirmed isotypism with the homologous $W_{1-x}B_3$.

The theoretical DFT studies on the structural assignment and stability of WB_4 or MoB_4 (WB_3 or MoB_3) ((Liang Y. 2001), (Gou H. 2012), (F. Z. Liang Y. 2012), (Zhang R.F. 2012), (Zang C. 2012), (Li Q. 2013), (Y. X. Liang Y. 2012)) claimed that WB_3 (MoB_3) with a two-dimensional boron net is thermodynamically more stable than WB_4 (MoB_4) with a three-dimensional boron skeleton ((Liang Y. 2001), (Gou H. 2012), (F. Z. Liang Y. 2012), (Zhang R.F. 2012), (Zang C. 2012), (Li Q. 2013), (Y. X. Liang Y. 2012)). Zhang et al. (Zang C. 2012) reopened the question on the correct crystal structure of WB_4 or WB_3, as the calculated indentation hardness of WB_4 is lower than that of ReB_2 in contrast to the experimental result and the calculated normalized c/a ratio of WB_3 exhibits a negative pressure dependence, inconsistent with the observed trend. Li et al. (Li Q. 2013) in their latest study presented new thermodynamically stable structures for WB_3 ($R\bar{3}m$-"6u") and WB_4 ($P6_3/mmc$-"2u"). However, the DFT stability calculations so far never considered nonstoichiometric $W_{1-x}B_3$ with defects in metal atom sites.

As most transition metal diborides exhibit superconductivity, Simonson et al. (Simonson J.W. 2010) tested various transition metal-doped alloys $Mo_{1-x}M_xB_4$ (M = Ti, Zr, Hf, V, Nb, Ta, Re) and the corresponding $W_{1-x}M_xB_4$ alloys. Indeed Ti and Nb doped $Mo_{1-x}M_xB_4$ alloys were claimed to reveal superconductivity below critical temperatures around 6.5 K (Ti) and 7.5 K (Nb), whereas no superconductivity has been detected in all the tungsten-based alloys.

In view of all these inconsistencies among experimental and DFT structural information, the present chapter comprises crystal structure investigations of $W_{1-x}B_3$, solubility studies of Rh, Ir, Ni, Pd and Pt in $W_{1-x}B_3$ as well as of Rh in $Mo_{1-x}B_3$, phase equilibria in the boron rich part of the isothermal sections W-TM-B at 1100°C (TM = Rh, Ir), at 900°C (TM = Ni, Pd) and at 800°C for TM=Pt and of Mo-Rh-B at 1100°C and the formation and crystal structure of ReB_2 isotypic compounds in the ternary systems W-TM-B (TM=Ru, Os, Ir) and V-Ir-B in as cast state and at 1500°C.

4.2.1 Results and Discussion

4.2.1.1 The crystal structure of $W_{1-x}B_3$

As described in the introduction the compound $W_{1-x}B_3$ (or WB_4) is already known since the early 1960's, its correct crystal structure, however, seems to be still under debate, because the established isotypism of $W_{1-x}B_3$ ((Chretien A. 1961), (Romans P. A. 1966), (Nowotny H. 1967), (Rudy E. 1963)) with the structure type of $Mo_{1-x}B_3$ (Lundström T. 1973) has been ignored in more recent studies ((Liang Y. 2001), (Gou H. 2012), (F. Z. Liang Y. 2012), (Zhang R.F. 2012), (Zang C. 2012), (Li Q. 2013), (Y. X. Liang Y. 2012)). As boron is difficult to detect by X-rays beside such a heavy metal element, several propositions have been made concerning the arrangement of the boron atoms in the crystal structure. Table IX presents a listing of the crystallographic parameters for the three different structural models reported in the literature, which have been established for WB_4 (Romans P. A. 1966), $W_{2-x}B_9$ (Nowotny H. 1967) and for $Mo_{1-x}B_3$ (Lundström T. 1973). At the bottom of Table IX one can compare these structure models in three-dimensional view. All structure models agree on planar hexagonal metal layers from which 1/3 of the atoms is removed. However, a (additional) significant metal atom defect in the crystallographic site (0,0,0.25) was only described for $W_{2-x}B_9$ (≡ $W_{1.83}B_9$) (Nowotny H. 1967) and for $Mo_{1-x}B_3$ (≡ $Mo_{0.80}B_3$) (Lundström T. 1973).

Table IX: Comparison of different structural models in standardized settings for WB_4 or $W_{2-x}B_9$ and the isotypic compound $Mo_{1-x}B_3$; only the B-B and metal-metal bonds are drawn in the unit cells.

	Romans & Krug; stoichiometric WB_4	**Nowotny et al.; $W_{2-x}B_9$ (x~1/6 ≡ $W_{0.61}B_3$)**	**Lundström & Rosenberg; $Mo_{1-x}B_3$ (x~0.2 ≡ $Mo_{0.80}B_3$)**
Space group Lattice parameter [nm]	$P6_3/mmc$ a = 0.5200 c = 0.6340	$P\bar{3}$ a = 0.5207 c = 0.6303	$P6_3/mmc$ a = 0.52026(2) c = 0.63489(3) B-rich
$R_I = \Sigma\|I_0-I_c\|/\Sigma I_0$	-	-	0.088
Atomic parameter			

M1/Wycoff Pos.;	W1 in 2c (1/3,2/3,1/4);	W1 in 2d (1/3,2/3,0.250);	Mo1 in 2c (1/3,2/3,1/4);
Occ.	1	1	1
M2/Wycoff Pos.;	W2 in 2b (0,0,1/4);	W2 in 2c (0,0,0.250);	Mo2 in 2b (0,0,1/4);
Occ.	1	~0.83	0.60(4)
B1/Wycoff Pos.;	12i (0.333,0,0);	6g (0.0,0.333,0.023);	12i (0.333,0,0);
Occ.	1	1	1
B2/Wycoff Pos.;	4f (1/3,2/3,0.615);	6g (0.472, 0.331, 0.202);	-
Occ.	1 (form a dumbell)	1	
B3/Wycoff Pos.;	-	6g (0.475, 0.141, 0.427);	-
Occ.		1	
Unit Cell	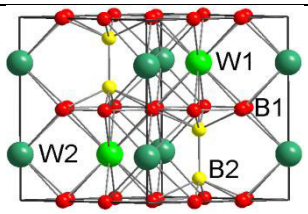	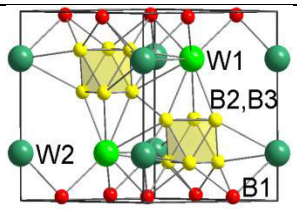	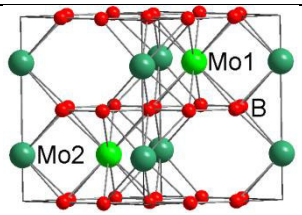

To reinvestigate the crystal structure, a single crystal has been selected from the crushed arc-melted sample with nominal composition WB_9. The observed extinctions are consistent with the space groups $P6_3mc$, $P\bar{6}2c$ or $P6_3/mmc$. The crystal structure has been solved employing direct methods in the hexagonal space group with highest symmetry $P6_3/mmc$ (Nr.194; a = 0.52012(1), c = 0.63315(3) nm). Although direct methods prompt the crystallographic sites 2c (⅓,⅔,¼) and 2b (0,0,¼) for the heavy scatterers i.e. the W atoms, the Fourier series undoubtedly reveals a reduced occupancy for the latter site (2b) of only about 72% (see Table X).

Table X: X-Ray single crystal data for $W_{1-x}B_3$ at RT (Anisotropic displacement parameters in [10^{-2}nm^2]).

Parameter/compound	
Space Group	$P6_3/mmc$
Formula from refinement	$W_{0.86}B_3$ (≡ $W_{22.3}B_{77.8}$ at. %)
a, c [nm]	0.52012(1), 0.63315(3)
μ_{abs} [mm^{-1}]	38.6
V (nm^3)	0.1483
ρ_x (gcm^{-3})	5.08
Reflections in refinement	152≥4σ(F_o) of 159
Number of variables	7
$R_F = \Sigma\|F_0-F_c\|/\Sigma F_0$	0.040
R_{Int}	0.040
wR2	0.119

GOF		1.207
Extinction (Zachariasen)		0.019(5)
Residual density $e^-/Å^3$; max; min		6.17; -6.28
Atom parameters		
W1 in 2c (⅓, ⅔, ¼); occ.		1
$U_{11}=U_{22}=U_{33}$		0.0018(6)
W2 in 2b (0,0,¼); occ.		0.725(7)
$U_{11}=U_{22}=U_{33}$		0.0019(5)
B1 in 12i (x, 0, 0); occ.		1
x		0.3341(8)
U_{iso}		0.0026(3)
Interatomic distances [nm]; Standard deviation < 0.0001		
W1 –	12B2	0.2346
W2 –	12B2	0.2351
B1 –	1B1	0.1725
	– 2B1	0.1738
	– 2W1	0.2346
	– 2B2	0.2346
	– 2W2	0.2350

The metal defects in 2b appear randomly as there is no indication for a long-range metal/vacancy order. Boron atoms are located from the difference Fourier and occupy only the Wyckoff site 12i (x,0,0) leading to the final composition $W_{0.86}B_3$ (≡ $W_{22}B_{78}$ in at.%). Table X comprises the results of the single crystal refinement, which converged to a final R-factor R_F = 0.040 employing anisotropic atom displacement parameters for the W-sites but isotropic temperature factors for the boron atom. The largest residual electron density and the deepest hole (6.62; -6.23 e/Å³) are close (~0.4 Å) to the tungsten atom in the 2c site and merely reflect the Fourier ripples to the large W-peak. It should be emphasized that the residual electron density reveals neither hints for B-B dumbbells nor for B_6 octahedra as proposed earlier. Wyckoff sequence and atom positions in $W_{0.86}B_3$ confirm isotypism with the structure model presented by Lundström and Rosenberg for $Mo_{1-x}B_3$. A three-dimensional view on the crystal structure of $W_{1-x}B_3$ is shown in Figure 10, which also presents the coordination polyhedra for all atom sites.

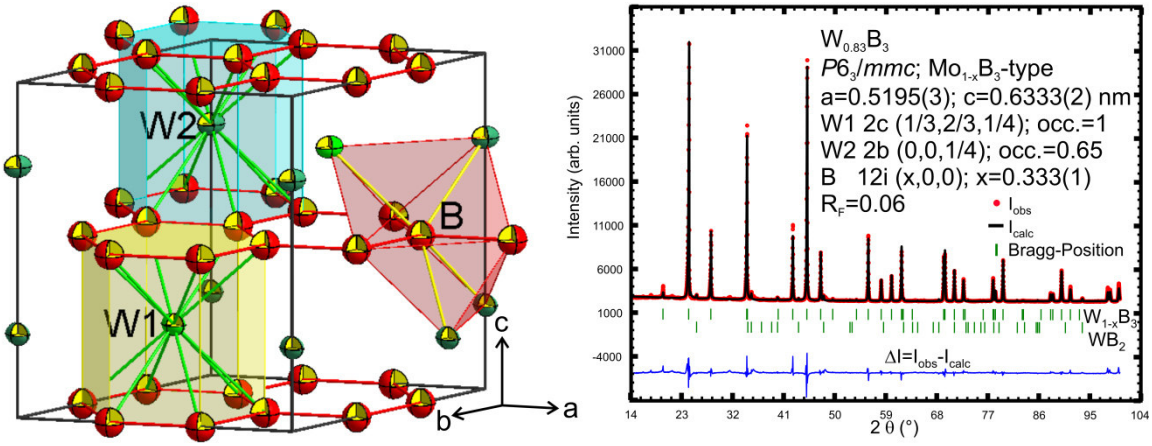

Figure 10: Unit cell of $W_{1-x}B_3$ including coordination polyhedra for all atoms and Rietveld refinement of the X-ray powder pattern for $W_{0.83}B_3$.

The structure solution obtained from the single crystal data fits well with the X-ray powder diffraction data as can be seen from the Rietveld refinement in the right part of Figure 10. The interatomic bonding distances in Table X merely reflect strong metal–boron bonding in the coordination figures as $d_{W\text{-}B}$ = 0.235 nm is always smaller than the sum of the W-metal (R_W = 0.139 nm) and covalent B-radius (R_B = 0.088 nm) (Pearson W.B. 1972). The in-plane boron boron contacts $d_{B\text{-}B}$ = 0.173 nm are fully consistent with the covalent radius sum, but W-W contacts $d_{W\text{-}W}$ = 0.300 nm are slightly larger than the sum of their metal atom radii. As seen from Figure 10, the metal coordination around the B-atom is a truncated triangular tungsten prism of which only 4 next nearest neighbours remain in form of a rather distorted tetrahedron. The strong metal-boron and boron-boron bonds in the structure are responsible for the high mechanical stability i.e. the high hardness and the ultra-incompressibility discussed in the literature ((Liang Y. 2001), (Gou H. 2012), (F. Z. Liang Y. 2012), (Zhang R.F. 2012), (Zang C. 2012), (Li Q. 2013), (Y. X. Liang Y. 2012)) similar to the transition metal diborides (Chen X.-Q. 2008). It should be mentioned that the two identical next nearest neighbour coordination figures around the two W-sites do not contain any hint for the defect in the W2 site – this may be explained in future DFT calculations.

4.2.1.2 Isothermal sections of the boron rich part of the ternary systems W-TM-B (TM = Rh, Ir, Ni, Pd, Pt) and Mo-Rh-B

The isothermal sections {Mo,W}-Rh-B at 1100°C, {Mo,W}-Ni-B at 900°C, {Mo,W}-

Pd-B at 950°C, and Mo-Pt-B at 900°C and 800°C have been investigated by Haschke ((Nowotny H. 1967), (Haschke H. 1966)), whilst phase relations in the ternary system W-Ir-B at 1200°C were published by Rogl et al. (N. H. Rogl P. 1972). Haschke (Haschke H. 1966) reported in all the aforementioned tungsten-based ternary systems and in the Mo-Rh-B system at the respective temperatures a ternary phase labeled as $\{W(Mo)_{1-x}TM_x\}_2B_9$ (x~0.33 to 0.5) with the structure type of "$W_{2-x}B_9$" (≡ $Mo_{1-x}B_3$–type; Figure 11).

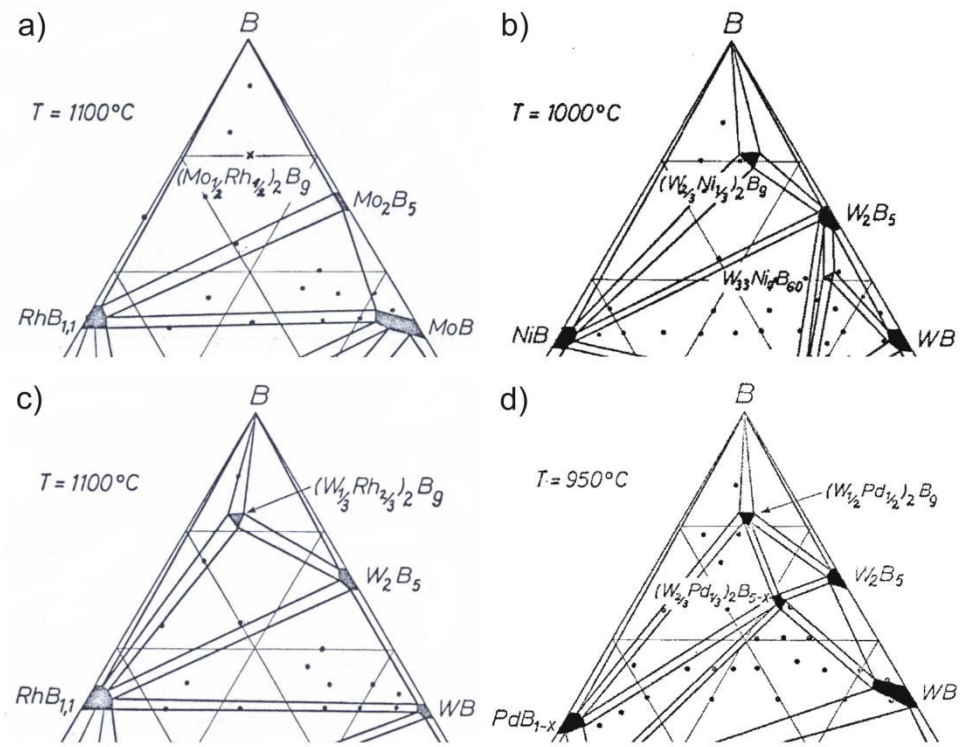

Figure 11: Boron rich part of the isothermal sections of the ternary systems a) Mo-Rh-B and b) W-Ni-B at 1000°C, c) W-Rh-B at 1100°C and d) W-Pd-B at 950°C; all as published by Haschke (Haschke H. 1966).

Interestingly, the isothermal sections at these low temperatures neither contained the binary phase "$W_{2-x}B_9$" nor isotypic "$Mo_{2-x}B_9$", thus reporting the compounds $\{W(Mo)_{1-x}TM_x\}_2B_9$ as truly ternary phases. As thermal instability at lower temperatures was never reported for the binary borides richest in W or Mo (both at about 80 at.% B; for details see also refs. ((Duschanek H. 1995), (W. W. Rudy E. 1965)), we decided to reinvestigate the boron rich part of these isotherms. Additionally, we studied the B-rich isothermal sections W-Ir-B and W-Pt-B at 1100 and 800°C, respectively. We also investigated the possible solid solutions starting from binary $(W,Mo)_{1-x}B_3$ in as cast state and after annealing at 1100, 900 or 800°C by

XPD using Ge as a standard for the lattice parameter determination and EPMA. Crystallographic details of all appearing phases in the investigated regions are presented in Table XI.

Table XI: Crystallographic data on the solid phases of the boron rich part of the ternary systems W-TM-B (TM= Rh, Ir, Ni, Pd, Pt) and Mo-Rh-B.

Phase	Space group	Structure type	Lattice parameter [nm]			Ref.
			a	b	c	
(B)	$R\bar{3}m$	βB	1.09382(5)	-	2.38356(18)	(Massalski T.B. 1990)
WB_2	*P6₃/mmc*	WB_2	0.29831(1)	-	1.38790(3)	(Lundström T. 1969)
RT-MoB_2	$R\bar{3}m$	MoB_2	0.30116(2)	-	2.0937(2)	(Klesnar H.P. 1996)
HT-MoB_2	*P6/mmm*	AlB_2	0.30049(3)	-	0.31726(4)	(Klesnar H.P. 1996)
$W_{1-x}B_3$	*P6₃/mmc*	$Mo_{1-x}B_3$	0.5207	-	0.6303	(Nowotny H. 1967)
$Mo_{1-x}B_3$	*P6₃/mmc*	$Mo_{1-x}B_3$	0.52026(2)	-	0.63489(3)	(Hassler E. 1979)
RhB	*P6₃/mmc*	NiAs	0.3309	-	0.4224	(S. E. Aronsson B. 1960)
Ir_4B_5	*C2/m*	Ir_4B_5	1.05300(9)	0.29038(3) β=91.119(9)°	0.61013(5)	(Aronsson B. 1963)
NiB	*Cmcm*	TlI	0.2929	0.7392	0.2961	(Lugscheider E. 1974)
Pd_2B	*Pnnm*	$CaCl_2$	0.46918(4)	0.51271(4)	0.31096(3)	(Hassler E. 1979)
$PtB_{0.67}$	*Cmcm*	$PtB_{0.67}$	0.3371(1)	0.5817(2)	0.4045(1)	(Ellner M. 1993)
$W_{0.52}Ir_{0.38}B_2$	*P6₃/mmc*	ReB_2	0.2926	-	0.7559	(B. F. Rogl P. 1970)
$W_{0.3}Ru_{0.7}B_2$	*P6₃/mmc*	ReB_2	0.2906	-	0.7452	(B. F. Rogl P. 1970)
$W_{0.3}Os_{0.7}B_2$	*P6₃/mmc*	ReB_2	0.2911	-	0.7497	(N. H. Rogl P. 1970)
$W_{0.5}Os_{0.5}B_2$	*P6₃/mmc*	ReB_2	0.29120(2)	-	0.75681(7)	(K. G. Gu Q. 2008)
RuB_2	*Pmmn*	RuB_2	0.46443(3)	0.28668(8)	0.40449(4)	(Roof R.B. Jr. 1962)
OsB_2	*Pmmn*	RuB_2	0.4684	0.2872	0.4076	(Aronsson B. 1963)

VB_2	*P6/mmm*	AlB_2	0.2998(2)	-	0.3057(2)	(Norton J.T. 1949)

Results are summarized in Table XII together with the lattice parameters reported in the literature.

Table XII: Results from EPMA and XPD including literature data for $W_{1-x}B_3$, $W_{1-x}TM_xB_3$ and $Mo_{1-x}B_3$.

Nominal Composition	EPMA [at.%]			Accepted Composition[a]	Lattice parameter [nm]		Heat treatment	Ref.
	W	TM	B		a	c		
WB_9	17.2	-	82.8	$W_{0.81}B_3$ $W_{0.86}B_3$	0.51953(3) 0.52012(1)	0.6333(2) $0.63315(3)^{SC}$	as cast	*
WB_4	-	-	-	$W_{0.75}B_3$	0.5200	0.6340	as cast	(Romans P. A. 1966)
$W_{1.83}B_9$	-	-	-	$W_{0.61}B_3$	0.5207	0.6303	1400°C	(Nowotny H. 1967)
WB_4	-	-	-	$W_{0.75}B_3$	0.5195(2)	0.6332(1)	1300°C	(K. G. Gu Q. 2008)
$W_{0.5}Rh_2B_{7.5}$	16.4 17.3	- 0.8	83.6 81.9	$W_{0.8}B_3$ $W_{0.82}B_3$	0.51981(5) 0.52006(8)	0.6331(1) 0.6342(2)	as cast 1100°C	*
$(W_{1/3}Rh_{2/3})_2B_9$	-	-	-	$W_{0.22}Rh_{0.44}B_3$	0.520	0.627	1100°C	(Nowotny H. 1967)
$W_{0.8}Ir_2B_{7.2}$	26.4	-	73.6	$W_{0.8}B_3$	0.52001(3)	0.63249(7)	as cast	*
$W_1Ni_{0.5}B_{8.5}$	23.0 25.1	0.8 0.3	76.2 74.6	$W_{0.8}B_3$ $W_{0.83}B_3$	0.51990(5) 0.51979(5)	0.6334(2) 0.63366(7)	as cast 900°C	*
$(W_{2/3}Ni_{1/3})_2B_9$	-	-	-	$W_{0.44}Ni_{0.22}B_3$	0.520	0.630	1000°C	(Nowotny H. 1967)
$W_{0.6}Pd_{1.4}B_8$	19.2 21.8	- 0.1	80.8 78.1	$W_{0.83}B_3$ $W_{0.85}B_3$	0.51977(5) 0.51962(6)	0.6334(1) 0.6331(1)	as cast 900°C	*
$(W_{1/2}Pd_{1/2})_2B_9$	-	-	-	$W_{0.33}Ni_{0.33}B_3$	0.520	0.631	950°C	(Nowotny H. 1967)
$W_{0.6}Pt_{1.4}B_8$	76.2 75.4	- -	23.8 24.6	$W_{0.83}B_3$ $W_{0.83}B_3$	0.51980(3) 0.52006(2)	0.63302(7) 0.6333(2)	as cast 900°C	*
$(W_{2/3}Pt_{1/3})_2B_9$	-	-	-	$W_{0.44}Pt_{0.22}B_3$	0.520	0.631	1050°C	(Nowotny H. 1967)
$Mo_{1-x}B_3$	-	-	-	$Mo_{0.8}B_3$	0.52026(2)	0.63489(3)	1800°C	(R. I. Lundström T. 1973)
$Mo_{1-x}B_3$	-	-	-	$Mo_{0.91}B_3$	0.52646(6)	0.6121(1)	1400°C	(Klesnar H.P. 1996)
$Mo_{0.8}Rh_2B_{7.2}$	18.0	0.1	81.9	$Mo_{0.82}B_3$	0.5209(2)	0.6348(3)	as cast	*

	19.6	0.6	79.8	$Mo_{0.8}B_3$	0.51902(5)	0.6334(3)	1100°C	

[sc]…from single crystal, *This work, [a]from Rietveld refinement

As various formulae have been reported in the literature, we refer to the formula $W_{1-x}B_3$ or $W_{1-x}TM_xB_3$ for an easier comparison in the column 'accepted composition' in Table XII. The 'accepted composition' for our alloys results from Rietveld refinement. We also investigated the solubility of Rh in $Mo_{1-x}B_3$ in as cast state and after annealing at 1100°C. As a very accurate quantitative boron measurement is not possible by EPMA using EDX detection (see Table XII), we mainly focused in the samples with transition metals, on measuring the metal ratios. Information on the binary phase diagrams and phases for Mo-B, Rh-B, Ni-B and Pd-B is taken from Massalski (Massalski T.B. 1990), for W-B from Duschanek and Rogl (Duschanek H. 1995) and for Ir-B and Pd-B from Rogl (P. Rogl 1988). Particularly the binary solid solubilities of the various transition metals in ß-rhombohedral boron in the temperature region from 900 to 1500°C were taken from Crespo et al. (Crespo A.J. 1981) as less than 0.25 at.% for Mo and W (see also Rudy et al. (W. W. Rudy E. 1965)), and less than 0.1 at.% for Ru, Os, Rh, Ir. For vanadium (~1.5 at.% V at 1500°C) and nickel (~2 at.% Ni at 900°C) we follow the investigations of Garbouskas et al. (Gabouskas M.F. 1986) and Smid et al. (Smid I. 1986), respectively. For all systems investigated, except for the W-Ir-B system, a three-phase equilibrium exists between ßB, $W_{1-x}B_3$ or $Mo_{1-x}B_3$ and the transition metal boride richest in boron (RhB, NiB, Pd_2B, $PtB_{0,67}$, see Figure 12).

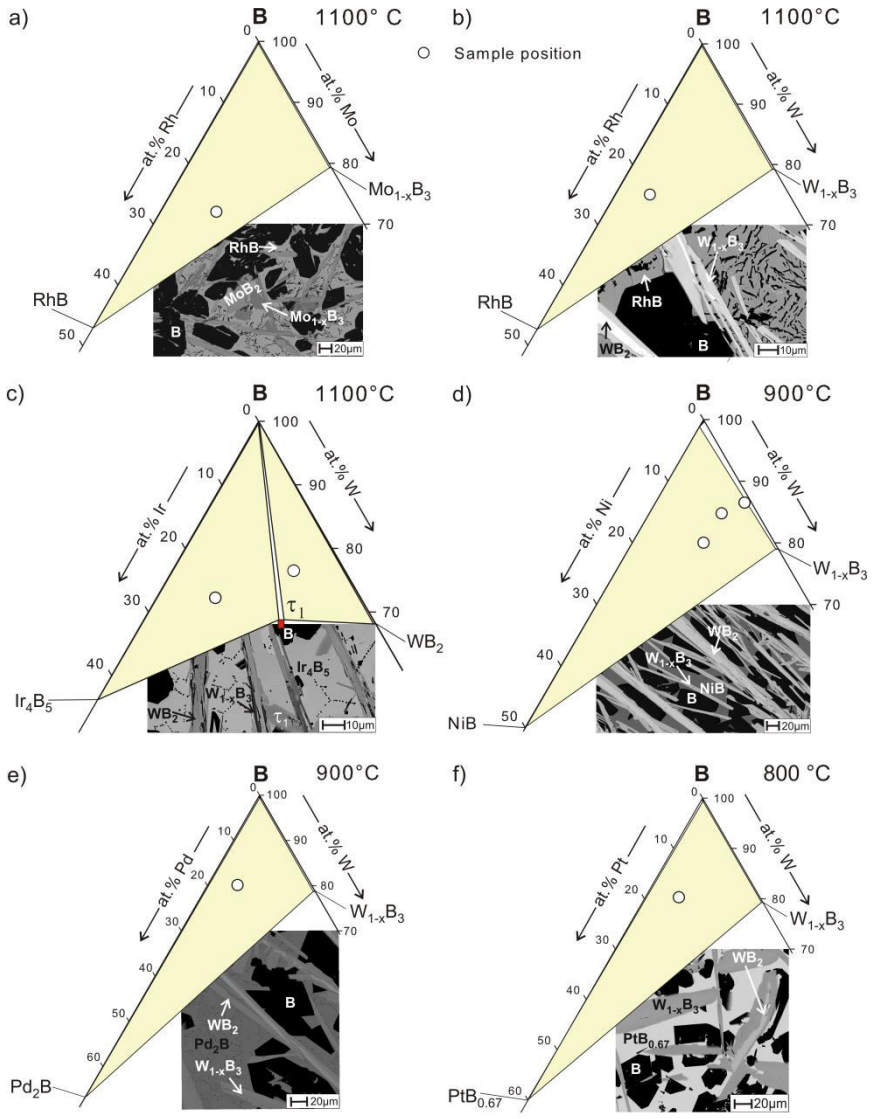

Figure 12: Partial isothermal sections of the ternary systems (a) Mo-Rh-B and (b) W-Rh-B and (c) W-Ir-B at 1100°C and of the ternary systems (d) W-Ni-B, (e) W-Pd-B at 900°C and of (f) W-Pt-B at 800°C. The shown microstructures are from the alloys in as cast state.

The peritectic formation of $W_{1-x}B_3$ around grains of WB_2 (labeled earlier as W_2B_{5-x}-type) is documented in all tungsten-based alloys (see microstructures in Figure 12). The last liquid crystallizes in form of a transition metal rich boride or eutectic. The same can be derived from the microstructure of the Mo-Rh-B alloy. In the boron rich part of the isothermal section of the W-Ir-B system, a three-phase equilibrium exists between B, WB_2 and τ_1-$W_{1-x}Ir_xB_2$ (ReB_2-type) and another between B, Ir_4B_5 and τ_1 (see Figure 12c). The invariant reaction temperatures were measured for all systems with DSC and are summarized in Table XIII together with the results from EPMA measurements and X-ray phase analysis.

Table XIII: Results from EPMA measurements and X-ray phase analysis including invariant reaction temperatures from DTA measurements.

Sample	Phases	Structure Type	Composition EPMA [at.%]			DTA [°C]	Lattice Parameter [nm]		
			Mo, W	TM	B		a	b	c
$Mo_{0.8}Rh_2B_{7.2}$ 1100	B $Mo_{1-x}B_3$ RhB	B $Mo_{1-x}B_3$ NiAs	0.2 19.6 0.0	0.4 0.6 43.9	99.4 79.8 56.1	1115	- 0.51902(5) 0.3313(2)	- - -	- 0.6334(3) 0.4218(2)
$W_{0.5}Rh_2B_{7.5}$ 1100	B $W_{1-x}B_3$ RhB	B $Mo_{1-x}B_3$ NiAs	0.2 17.3 0.0	0.1 0.8 43.2	99.7 81.9 56.8	1115	- 0.52006(8) 0.33233(1)	- - -	- 0.6342(2) 0.42010(4)
$W_{0.8}Ir_2B_{7.2}$ 1100	B Ir_4B_5 τ_1	B Ir_4B_5 ReB_2	0.5 0.0 16.1	0.2 43.3 11.1	99.3 56.7 72.8	1264	- 1.0535(4) 0.29266(2)	- 0.2904(1) β=91.15(3) -	- 0.6103(1) 0.7538(1)
$W_{1.6}Ir_{0.8}B_{7.6}$ 1100	B τ_1 WB_2	B ReB_2 WB_2	0.5 16.4 32.8	0.0 10.1 0.0	99.5 73.5 67.2	-	- 0.29272(2) 0.29855(2)	- - -	- 0.7535(1) 1.3887(4)
$WNi_{0.5}B_{8.5}$ 900	B $W_{1-x}B_3$ NiB	B $Mo_{1-x}B_3$ TlI	0.3 25.1 0.1	1.4 0.3 50.6	98.3 74.6 49.3	1041	- 0.51979(5) -	- - -	- 0.63366(7) -
$W_{0.6}Pd_{1.4}B_8$ 900	B $W_{1-x}B_3$ Pd_2B	B $Mo_{1-x}B_3$ $CaCl_2$	0.4 21.8 0.0	0.1 0.1 65.9	99.5 78.1 33.9	963	- 0.51962(6) 0.4691(1)	- - 0.5135(2)	- 0.6331(1) 0.3136(2)
$W_{0.6}Pt_{1.4}B_8$ 800	B $W_{1-x}B_3$ $PtB_{0.67}$	B $Mo_{1-x}B_3$ $PtB_{0.67}$	0.4 24.8 0.3	0.0 0.0 79.1	99.6 75.2 30.6	777	- 0.52006(2) 0.3372(1)	- - 0.5820(1)	- 0.6333(2) 0.4031(1)

τ_1-$W_{1-x}Ir_xB_2$

The DSC data on ternary reaction isotherms in Table XIII demonstrate that on heating liquification temperatures in the ternary systems investigated are all close to or slightly below the binary boron-rich TM-B eutectic temperatures. Above these temperatures "burning" of alloys may appear even close to the high melting Mo-B and W-B binaries.

As a result of our investigations, the phase equilibria in the boron-rich parts of the systems {Mo,W}-Rh-B, {Mo,W}-{Ni,Pd,Pt}-B and W-Ir-B, all reveal the existence of binary borides with the $Mo_{1-x}B_3$-type (at about 80 at.% B) without any extension (solid solubilities) into the corresponding ternaries. Accordingly there is practically no difference between the lattice parameters (within the error bars) of the binary Mo_{1-}

$_xB_3$-type phases and those measured from ternary alloys (compare data in tables III and IV). This argument also holds for a comparison of lattice parameters of the phases "$\{W(Mo)_{1-x}TM_x\}_2B_9$" reported by Haschke ((Haschke H. 1966), (Nowotny H. 1967)) with the binary $Mo_{1-x}B_3$-type borides. Ternary compounds neither appeared in as cast condition nor in annealed alloys. The reason for the severe discrepancy between (i) the existence of ternary compounds $\{W(Mo)_{1-x}TM_x\}_2B_9$ (x~0.33 to 0.5) as reported by Haschke (Haschke H. 1966) and (ii) the absence of ternary compounds but observation of isotypic phases in the binary with the structure type of "W_2B_9" (≡ $Mo_{1-x}B_3$–type), may be found (a) in the slow reaction kinetics of the binary peritectically formed borides $\{Mo,W\}_{1-x}B_3$ as well as (b) in the significantly enhanced reaction kinetics concomitant with the severely lowered melting and liquidus temperatures (see DSC data in Table XIII) in the ternary systems investigated.

4.2.1.3 The Tungsten-Based Ternary Transition Metal Diborides $W_{1-x}TM_xB_2$ (TM=Ru, Os, Ir)

Isotypic diborides with the structure type of ReB_2 (space group $P6_3/mmc$; a=0.2900, c=0.7475nm (Aronsson B. 1960)) can be achieved by combination of metal elements from the 6th (Mo, W) and 8th (Ru, Os) group of the periodic table as they form a pseudo element from the 7th group. The electronegativity is approximately the same as for rhenium, if the metal ratio 6th/8th is ~1/2 ((N. H. Rogl P. 1970), (B. F. Rogl P. 1970)). More general, all isotypic compounds keep an electron/atom ratio between 4.3-4.4 (T. S. Levine J.B. 2009) f. e. $V_{0.4}Os_{0.6}B_2$ (R. E. Rogl P. 1978), $W_{0.5}Ir_{0.4}B_2$ ((N. H. Rogl P. 1972), (N. H. Rogl P. 1970) and $Mo_xIr_{1-x}B_2$ (x=0.3, 0.6; (B. F. Rogl P. 1970), (Crespo A.J. 1981)). In this work, we investigated the type of formation and crystal structure of compounds with nominal composition $W_{13}Ru_{18}B_{69}$, $W_{15}Os_{16}B_{69}$, $W_{18}Ir_{13}B_{69}$ and $V_{17}Ir_{16}B_{67}$ in as cast state and after annealing at 1500°C for 3 days. The compounds $W_{0.4}Ru_{0.6}B_2$ and $W_{0.6}Ir_{0.4}B_2$ (composition determined with EPMA, see Table XIV) form incongruently (see Figure 13a and c) whereas $W_{0.5}Os_{0.5}B_2$ forms directly from the melt (Figure 13b).

Table XIV: Results from EPMA measurements and X-ray phase analysis for the alloys $W_{18}Ru_{13}B_{69}$, $W_{15}Os_{16}B_{69}$, $W_{18}Ir_{13}B_{69}$ and $V_{17}Ir_{16}B_{67}$ in as cast state and/or after annealing at 1500°C.

Sample	Phases	Structure Type	Composition EPMA [at.%]			Lattice Parameter [nm]		
			W,V	TM	B	a	b	c
	B	B	-	0.4	99.6	-	-	-
$W_{13}Ru_{18}B_{69}$	WB_2	WB_2	30.6	1.7	67.7	0.29850(1)	-	1.3866(5)
as cast	RuB_2	RuB_2	1.1	35.9	63.0	0.28715(3)	0.4641(1)	0.40494(5)
	$W_{1-x}Ru_xB_2$	ReB_2	10.1	17.3	72.6	0.29027(1)	-	0.74673(2)
$W_{15}Os_{16}B_{69}$	B	B	0.1	0.9	99.0	-	-	-
1500	OsB_2	RuB_2	0.7	36.6	62.7	-	-	-
	$W_{1-x}Os_xB_2$	ReB_2	19.7	20.6	59.7	0.29127(1)	-	0.7562(1)
	B	B	0.4	-	99.6	-	-	-
	WB_2	WB_2	42.3	0.1	57.6	0.29864(1)	-	1.3880(5)
$W_{18}Ir_{13}B_{69}$	$W_{1-x}B_3$	$Mo_{1-x}B_3$	26.4	-	73.6	-	-	-
as cast	Ir_4B_5	Ir_4B_5	14.9	-	85.1	-	-	-
	$W_{1-x}Ir_xB_2$	ReB_2	25.9	22.7	51.4	0.29298(2)	-	0.7539(1)
$W_{18}Ir_{13}B_{69}$	B	B	0.1	0.1	99.8	-	-	-
1500	Ir_4B_5	Ir_4B_5	-	42.6	57.4	-	-	-
	$W_{1-x}Ir_xB_2$	ReB_2	25.8	19.1	55.1	0.29263(1)	-	0.75404(8)
$V_{17}Ir_{16}B_{67}$	B	B	1.6	-	98.4	-	-	-
1500	VB_2	AlB_2	26.7	-	73.3	0.2999(1)	-	0.3056(1)
	Ir_4B_5	Ir_4B_5	-	44.2	55.8	1.0524(5)	0.29042(2)	0.6102(1)
							β=91.12(4)	

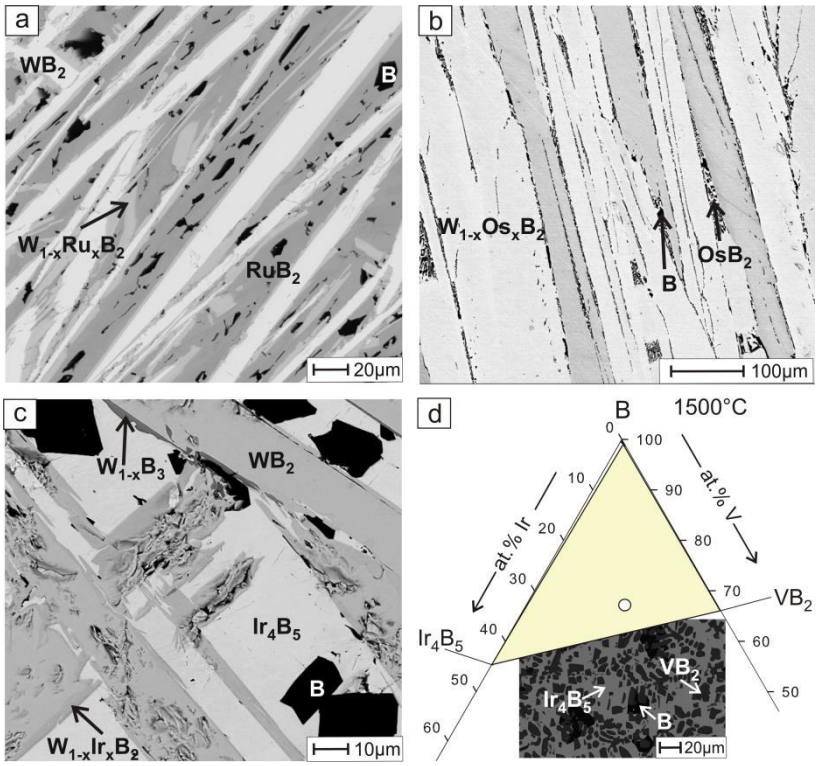

Figure 13: SEM images of the alloys (a) $W_{13}Ru_{18}B_{69}$, (b) $W_{15}Os_{16}B_{69}$, (c) $W_{18}Ir_{13}B_{69}$ in as cast state and (d) partial isothermal section of the V-Ir-B phase diagram at 1500°C.

$W_{0.4}Ru_{0.6}B_2$ forms in a peritectic reaction around large primary grains of WB_2 (W_2B_{5-x}-type; Figure 13a). However, annealing at 1500°C does not change much the microstructure or composition of the appearing phases in the W-Ru-B system and therefore these results are not included in Figure 13 and Table XIV. On the other hand, annealing of the carefully mixed and cold pressed powders (W, Ru and B) at 900 to 1200°C for 50 hours in an argon atmosphere leads to homogeneous products (B. F. Rogl P. 1970). Therefore we suggest that probably the diffusion at 1500°C is to slow due to a rather high liquidus temperature. In case of the $W_{18}Ir_{13}B_{69}$ sample, annealing at 1500°C leads to an almost single-phase sample $W_{0.6}Ir_{0.4}B_2$ with only about 2% impurity phases (Ir_4B_5 and B,Table XIV) but here even lower annealing temperatures (≥ 1100°C) are sufficient. $W_{0.5}Os_{0.5}B_2$ forms congruently and the SEM image in Figure 13b shows large grains and a three-phase eutectic at the grain boundaries consisting of $W_{0.5}Os_{0.5}B_2$, OsB_2 and B (Table XIV, results for the annealed alloy). The X-ray powder patterns of the $W_{15}Os_{16}B_{69}$ in as cast state and after annealing contain sharp (h00, hk0) and rather diffuse and broad reflexions (00l, h0l). This has been observed already previously in some X-ray powder diffractograms of W-Ru-B (B. F. Rogl P. 1970) and Mo-Os-B (N. H. Rogl P. 1970) alloys and has been explained by irregular stacking faults in the crystal structure in the c-direction (B. F. Rogl P. 1970). The possible formation of a ReB_2 isotypic compound has also been tested for V-Ir-B but neither in as cast state or after annealing at 1500°C any ternary compound appeared. At 1500°C, a three-phase equilibrium exists: B +VB_2 + Ir_4B_5 (see Figure 13d and Table XIV).

4.2.1.4 Summary

The reinvestigation of the crystal structure of $W_{1-x}B_3$ (≡$WB_{\sim 4}$) by X-ray single crystal diffraction revealed isotypism with the $Mo_{1-x}B_3$ structure type (space group $P6_3/mmc$; a=0.52012(1), c=0.63315(3) nm; R_F=0.040). Boron occupies only the crystallographic site 12i (x,0,0) and tungsten the sites 2c (1/3,2/3,1/4) and 2b (0,0,1/4), the latter being filled to only about 72%. It should be emphasized that although $W_{1-x}B_3$ at about 80 at. % B is the metal boride richest in boron, it shows no directly linked three-dimensional boron framework. No solubility of Rh, Ir, Ni, Pd and Pt in $W_{1-x}B_3$ as well as of Rh in $Mo_{1-x}B_3$ has been found in as cast state and after annealing by EPMA measurements

and by comparing the lattice parameter with those of the binary alloys. Furthermore, the boron rich parts of the corresponding isothermal sections W-TM-B (TM = Rh, Ir at 1100°C, TM = Ni, Pd at 900°C and TM = Pt at 800°C) and Mo-Rh-B (at 1100°C) have been established. Except for the W-Ir-B system, a three-phase equilibrium exists between β–boron, $W_{1-x}B_3$ or $Mo_{1-x}B_3$ and the transition metal boride richest in boron (RhB, NiB, Pd_2B, $PtB_{0,67}$). In the W-Ir-B system, two three-phase equilibria exist in the investigated part. βB is in equilibrium with Ir_4B_5 and τ_1-$W_{1-x}Ir_xB_2$ (ReB_2 type) and with WB_2 and τ_1. Formation and crystal structure of diborides $W_{1-x}TM_xB_2$ (TM = Ru, Os, Ir) with ReB_2 structure type (space group $P6_3/mmc$; a=0.2900, c=0.7475nm) were studied by X-ray powder diffraction and electron probe microanalysis in as cast state and after annealing at 1500°C. $W_{0.5}Os_{0.5}B_2$ (a=0.29127(1), c=0.7562(1) nm) forms directly from the melt, whereas $W_{0.4}Ru_{0.6}B_2$ (a=0.29027(1), c=0.74673(2) nm) and $W_{0.6}Ir_{0.4}B_2$ (a=0.29263(1), c=0.75404(8) nm) are incongruently melting. Annealing at 1500°C leads in case of the iridium compound to an almost single-phase product but the same procedure does not increase the amount of the ruthenium diboride.

4.3 CRYSTAL STRUCTURE AND Ce VALENCE VARIATION IN THE SOLID SOLUTION $CeRh_{3-x}Pd_xB_{0.5}$

A significant effort was done during the last decades studying the rich variety of physical properties of the $CeTM_3$ family of compounds (where TM = Rh and Pd) and related systems like $CeRh_{3-x}Pd_x$ ((Harris I. R. 1972), (Mihalisin P. 1981)). Its simple cubic primitive $AuCu_3$ structure (defect perovskite) provides the possibility to incorporate light interstitial elements like B (in $CePd_3B_y$ ((Perez I. 1987), (Sereni J. 1986), (Sereni J. G. 2013), (Dhar S. K. 1981), (Malik S. K. 1984)), $CeRh_3B_y$ ((Perez I. 1987), (Malik S. K. 1984), (Yubuta K. 2006)), C (in $CeRh_3C_{1-y}$ ((Holeck H. 1972), (Joshi D. A. 2009)), small amounts of Be (in $CePd_3Be_y$ ((Sereni J. G. 2013), (Nieva G.L. 1988)) and Si (in $CePd_3Si_y$ ((Sereni J. G. 2013), (Malik S. K. 1984)).

One of the most interesting properties of these alloys is the possibility to study, within a continuous alloy series, the electronic transition of Ce from its Ce^{4+} configuration to the Ce^{3+} one.

It is well known that crystal and electronic structures are intimately related, and the study of one of them has to be complemented by the knowledge of the other.

Magnetic properties were preferably used to identify the electronic characteristics of materials, particularly for systems containing rare earth elements, able to adapt their electronic configuration to the volume (V_{av}) available within the crystal structure and consequently their valence (Z). Among such elements, cerium is known to adjust the occupation of its $4f^1$ orbital to the surrounding chemical potential (μ) through its local Z/V_{av} ratio modification. Concomitantly, the electronic configuration of Ce varies between a magnetic state (at $4f^1$ full occupation) and a non-magnetic state (for a $4f^{1-n}$ partial occupation). Consequently, these Ce-based compounds provide the unique possibility to tune the Z/V_{av} ratio by changing μ or, inversely, to trace the variation of μ by measuring V_{av}. Indeed for the alloy series $CeRh_{3-x}Pd_x$ and $CeAg_{3-z}Pd_z$ (Mihalisin P. 1981) a transition from the Ce^{4+} regime (Rh-rich) to the Ce^{3+} regime (Pd-rich) has already been monitored (Gambke T. 1981).

In order to better understand the aim of this work, a brief overview on the properties of the family of $CeTM_3B_y$ compounds related to this work is given in the following.

$CePd_3B_y$: The valence of Ce in $CePd_3B_y$ was found to increase in the concentration range y<0.4 as the lattice volume increases with rising B content ((Perez I. 1987), (Sereni J. 1986), (Dhar S. K. 1981), (Malik S. K. 1984)); it saturates at y~0.4 once the Ce trivalent state is reached. Coincidentally, the lattice parameter also stops growing (see Figure 14).

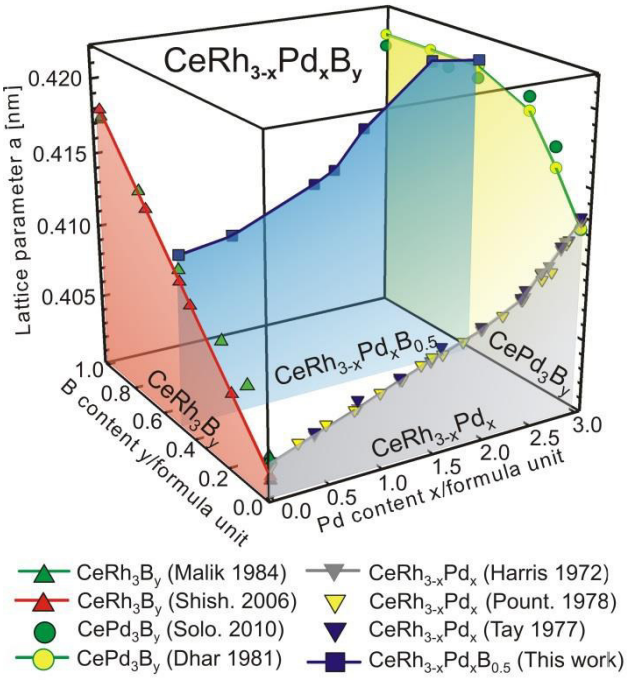

Figure 14: Lattice parameter vs. Pd content x and B content y for $CeRh_{3-x}Pd_xB_y$.

Accordingly, low temperature properties show that magnetic interactions develop some short range order that increases in intensity up to y=0.35 (Sereni J. 1986). Unexpectedly, for y>0.4 the specific heat anomaly related to those short range correlations smears out and transforms into a continuous increase of C_m /T as temperature decreases (Sereni J. G. 2013). The strengthening of magnetism observed for $CePd_3B_y$ at y~0.25 was backed by specific heat measurements ((Sereni J. 1986), (G. K. Dhar S. K. 1989), (Kuentzler R. 1984)). X-ray photoemission, Bremsstrahlungs-Isochromat and electron energy loss spectroscopy (Wuilloudt E. 1984) revealed a $4f^n$ occupation varying from n_f ~ 0.9 in $CePd_3$ to n_f ~ 1 in $CePd_3B$ at 90 K and an almost constant hybridization of *f*-electrons with conduction electrons (Δ=150±20 meV).

Phase equilibria studies in the system Ce-Pd-B at 850°C (Sologub O. 2010) defined the extension of the homogeneity range of $CePd_3B_y$ for $0 \leq y \leq 0.65$ at 850°C limiting the boron incorporation to 13 at.% B (Sologub O. 2010). Alloys with $y \leq 0.15$ behave as a Kondo lattice, whereas the behavior for y>0.2 becomes completely different, tracking the valence change of Ce. Concerning transport properties, $CePd_3$ ranks among the materials with the highest Seebeck coefficients (110-120 µV/K around 150 K) amid correlated thermoelectric systems ((Lackner R. 2006), (Jones C. D. W. 1999)). Boron incorporation leads to a strong decrease of the Seebeck coefficient (~40 µV/K around 150 K for $CePd_3B_{0.1}$) ((Lackner R. 2006), (Jones C. D. W. 1999)) but also to a large drop of the phonon thermal conductivity, attributed to the rattling modes of the loosely bonded B atoms (Lackner R. 2006).

The observed disappearance of magnetic correlations for y>0.4 is an open question, tentatively attributed to atomic disorder produced by the random distribution of interstitial B atoms.

$CeRh_3B_y$: Lattice parameters as a function of the incorporation of boron in $CeRh_3$ were found to increase almost linearly with increasing boron content ((Malik S. K. 1984), (Shishido T. 2006)), whereas the magnetic susceptibility of $CeRh_3$ is almost temperature independent down to 50 K [(Harris I. R. 1972), (Malik S. K. 1984)), consistent with Pauli-paramagnetic behavior and suggesting a tetravalent state of Ce (Malik S. K. 1984). Correspondingly the valence of cerium changes from Ce^{4+} in $CeRh_3$ [(Harris I. R. 1972), (Malik S. K. 1984)) to a mixed valency in $CeRh_3B$ ((Malik S. K. 1984), (Joshi D. A. 2009)). The lattice parameters of $CeRh_3B$ determined

by Takei et al. (Takei H. 1984) in as cast state and after annealing at 1400°C, exhibit a difference probably due to slightly different atomic arrangement. Shishido et al. (Shishido T. 2006) observed an anomalous drop of the Vickers hardness around y=0.444. An electron diffraction (ED) and high resolution electron microscopy (HRTEM) study of the crystal structure of $CeRh_3B_{0.5}$ by Yubuta et al. (Yubuta K. 2006) revealed ½½½-type superlattice reflections and fine satellite reflections around all reflections. The new superstructure is formed by an ordered arrangement of B atoms and is modulated by the appearance of fine domains with an average size of ~ 3 nm (Yubuta K. 2006). The authors suggested that weakness of chemical bonding strength in the boundaries between the fine domains causes the anomalous decrease of hardness in the region of the new structure (N. A. Yubuta K. 2008). Ab initio calculations of the atomic and electronic structure and elastic properties of $CeRh_3B_y$ revealed (i) a strong covalent bonding between boron 2p and Rh 4d electrons, (ii) the Fermi level in a pseudogap and (iii) a significant *f-d* hybridization (Hidenobu K. 2007).

$CeRh_{3-x}Pd_xB_y$: Measurements of magnetic susceptibility and lattice parameters for the $CeRh_{3-x}Pd_x$ alloy ((Harris I. R. 1972), (Tay C. Y. 1977)) indicated Ce to be in the tetravalent state for the composition range $0 \le x \le 2.4$, whereas with increasing x the effective valency decreases to intermediate valence values at $CePd_3$ (Harris I. R. 1972). Consistently, L_{III} X-ray absorption edge measurements revealed an increase of the valence of Ce between $CePd_3$ and $CeRh_{1.2}Pd_{1.8}$, but a constant value for higher Rh contents (Beaurepaire E. 1984). From temperature dependent resistivity and Ce-L_{III}-valence state measurements Perez and coworkers (Perez I. 1987) concluded that the solid solution $CeRh_{3-x}Pd_xB$ passes continuously from a Kondo local-moment regime ($0 \le x \le 0.6$) to a mixed valent regime ($0.6 < x \le 2.1$) and further to a saturated valence regime ($2.1 < x \le 3$).

The purpose of this work is an attempt to expand the $AuCu_3$ lattice of $CeRh_{3-x}Pd_x$ alloys by Boron addition in order to tune the electronic configuration from $4f^0$ towards $4f^1$. Such a transformation cannot be completed by a simple Rh/Pd substitution because $CePd_3$ is in an intermediate valence state. By adding more conduction electrons to the band (e.g., by a Pd/Ag substitution), the Ce valence variation can be driven up to the Ce^{3+} configuration. Boron incorporation, however, promotes a shift of the Rh/Pd electronic substitution effect to lower Rh content because of the B-driven

lattice expansion. Once tuned at the proper B concentration, this shift should allow covering the full Ce^{4+} to Ce^{3+} transformation into the unique Rh to Pd range, avoiding the extension into the Pd by Ag substitution.

With respect to the incipient short range magnetic order observed in $CePd_3B_y$ up to y=0.35 - which vanishes for y>0.4 - it is necessary to elucidate whether or not short range order is an atomic disorder effect or has an intrinsic origin. To that respect one can mention that the heavy fermion behavior of $CePd_3B_{0.6}$ was improved after annealing ((Sereni J. 1986), (Nieva G.L. 1988)). For such a purpose a detailed structure investigation concerning boron/vacancy ordering was carried out in this work, to better control the degree of disorder introduced by doping. Taking profit of previous investigations on $CeRh_3B_{0.5}$ (N. A. Yubuta K. 2006), which evidenced a ½½½–type superstructure, the alloy system with the $CeRh_{3-x}Pd_xB_{0.5}$ was chosen for this investigation.

The chapter provides details on the crystal structures and valence instability region of Ce within the solid solution $CeRh_{3-x}Pd_xB_{0.5}$.

4.3.1 Results and discussion

4.3.1.1 Homogeneity range of the solid solution $CeRh_{3-x}Pd_xB_y$

Samples of the solid solution $CeRh_{3-x}Pd_xB_{0.5}$ (x=0, 0.5, 1.2, 1.5, 1.7, 2.5, 3) have been studied by XPD and EPMA in the as cast state. X-ray powder patterns of the alloys were indexed on the basis of a cubic primitive $AuCu_3$ lattice (space group $Pm\bar{3}m$; a_0~0.4 nm). The dependency of the lattice parameters, *a*, of the solid solution $CeRh_{3-x}Pd_xB_y$ ($AuCu_3$ type) with increasing Pd content, *x,* and increasing B content *y* is given in Figure 14, in comparison with data available from the literature. On the pure Rh side of the figure, a linear increase of the lattice parameter with increasing B content has been reported by Shishido and coworkers (Shishido T. 2006) for $CeRh_3B_y$. This parameter ranges from a=0.4015(1) nm (y=0) to a=0.4180(1) nm (y=1) for alloys annealed at 1300°C, whereas the lattice parameters determined by Malik et al. (Malik S. K. 1984) for alloys in as cast state show deviations from linearity at low boron contents. In this area (y=0.12 and 0.25) the authors. (Malik S. K. 1984) observed a splitting of the peaks in the X-ray powder pattern whereby one set of lines

could be fitted with the lattice parameter of $CeRh_3$ and the other with an expanded lattice (see Figure 14).

The rather large difference of the lattice parameters in as cast state (a=0.4147 nm) and after annealing at 1400°C (a=0.4213 nm) reported by Takei et al. (Takei H. 1984) for $CeRh_3B$, might be due to different compositions. For comparison, on the axis without B content, i.e. $CeRh_{3-x}Pd_x$, the lattice parameters increase linearly between x=0 and x=2.4 and between x=2.4 and x=3 ((Harris I. R. 1972), (Tay C. Y. 1977), (Pountney J. M. 1978)) as previously reported. Even $Ce_{1-u}Pd_{3+u}$ has a small homogeneity range (Massalski T.B. 1990) extending from stoichiometric $CePd_3$ (a=0.4129(2) nm) to $Ce_{0.92}Pd_{3.08}$ (a=0.4112(2) nm) at 800°C (Massalski T.B. 1990). The lattice parameters of the solid solution $CePd_3B_y$ increase with increasing boron content up to y=0.4 (a=0.4203 nm) in as cast alloys (M. S. Dhar S. K. 1981) and up to y=0.25 (a=0.41954(5) nm) (Sologub O. 2010) for samples annealed at 850°C, but saturate for higher boron contents. The maximum solubility of boron in this solid solution was found to be about 13 at.% B (y=0.65) (Sologub O. 2010). For the solid solution $CeRh_{3-x}Pd_xB_{0.5}$ (x=0, 0.5, 1.2, 1.5, 1.7, 2.5, 3), investigated in this work, lattice parameters increase slightly with increasing Pd content from a=0.41147(5) nm (x=0) to a=0.41501(5) nm (x=1.5), followed by a strong increase up to a=0.42104(6) nm (x=2.5) and a slight decrease afterwards to a=0.42073 nm (x=3) (see Figure 14). Our lattice parameters of $CeRh_3B_{0.5}$ and $CePd_3B_{0.5}$ are slightly larger but still in good agreement with literature data. The results of XPD and EPMA are summarized in Table XV. Only the metal ratios were measured over several areas, as it is not possible to precisely and reliably determine the small boron content by EPMA. The lattice parameters are given for the cubic $AuCu_3$ parent type from which any possible superstructures can be derived.

Table XV: Results of XPD, EPMA and ED measurements.

Nominal composition	Composition from EPMA	a_{AuCu3} [nm]	½½½ Superstructure reflections	Satellite reflections
$CeRh_3B_{0.5}$	$CeRh_3$	0.41147(5)	yes	yes
$CeRh_{2.5}Pd_{0.5}B_{0.5}$	$CeRh_{2.5}Pd_{0.5}$	0.41249(5)	yes	yes
$CeRh_{1.7}Pd_{0.3}B_{0.5}$	$CeRh_{1.7}Pd_{0.3}$	0.41433(2)	no	yes
$CeRh_{1.5}Pd_{1.5}B_{0.5}$	$CeRh_{1.5}Pd_{1.5}$	0.41501(5)	no	yes
$CeRh_{1.2}Pd_{1.8}B_{0.5}$	$CeRh_{1.2}Pd_{1.8}$	0.41741(3)	no	yes
$CeRh_{0.5}Pd_{2.5}B_{0.5}$	$CeRh_{0.5}Pd_{2.5}$	0.42104(6)	no	yes

$CePd_3B_{0.5}$	$CePd_3$	0.42073(2)	no	Yes

4.3.1.2 Electron diffraction studies on the solid solution $CeRh_{3-x}Pd_xB_{0.5}$

Selected area electron diffraction (SAED) patterns with the incident beams along the directions [001], [011] and [111] were obtained using a 200 kV electron microscope (JEOL JEM-2000EXII). High-resolution electron microscopy (HREM) images were taken with a 200 kV electron microscope (TOPCON EM-002B). Precession electron diffraction (PED) patterns were obtained by using a Spinning Star (NanoMEGAS) device with a precession angle of 3.0°. All these measurements have been carried out by Prof. Kunio Yubuta at the Institute for Materials Research, Tohoku University in Japan.

SAED patterns of the $CeRh_{3-x}Pd_xB_{0.5}$ compounds, taken with incident beam along the directions [001] (left), [011] (centre) and [111] (right) are shown in Figure 15.

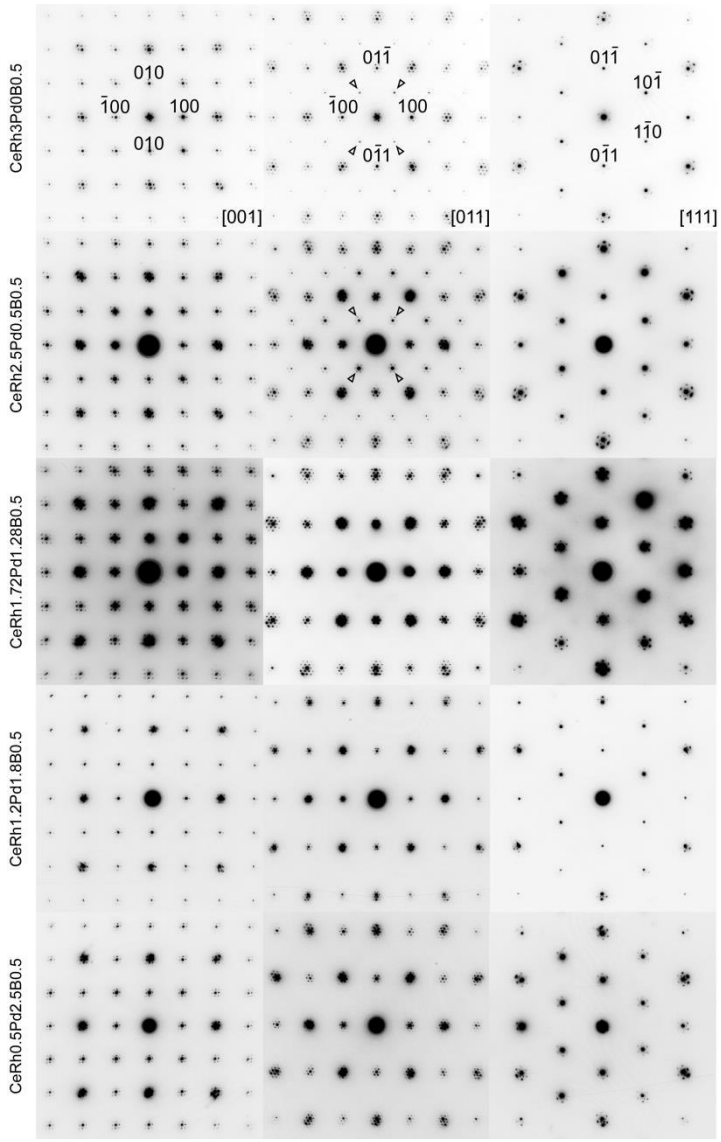

Figure 15: SAED patterns of the $CeRh_{3-x}Pd_xB_{0.5}$ compounds, taken with incident beam parallel to the directions [001] (left), [011] (center) and [111] (right). Reflections are indexed on the basis of the $AuCu_3$-type structure.

Reflections are indexed with respect to the $AuCu_3$-type structure. The presence of ½½½–type superstructure and satellite reflections is summarized in Table XV.

4.3.1.3 ½½½ –type superstructure reflections

As indicated by arrowheads in Figure 15, ½½½–type superstructure reflections are observed only in $CeRh_3B_{0.5}$ and $CeRh_{2.5}Pd_{0.5}B_{0.5}$. Therefore, the ½½½–type superstructure, which has been discussed in detail for $CeRh_3B_{0.5}$ (N. A. Yubuta K. 2006), might be dominant only in the Ce-Rh-B system.

4.3.1.4 Satellite reflections

For all compounds investigated, many fine satellite reflections appear around the Bragg reflections. The characteristic features of the satellite spots are significant and similar to those of the $CeRh_3B_{0.5}$ compound (N. A. Yubuta K. 2006). It is reasonable to consider that the fine satellite reflections indicate the existence of a domain structure enclosed by anti-phase boundaries. The appearance of only satellite reflections without superstructure reflections has not been observed in the ternary solid solution $CeRh_3B_x$. Figure 16 shows HREM images of (a) $CeRh_{2.5}Pd_{0.5}B_{0.5}$ with the ½½½–type superstructure reflections and (b) $CeRh_{1.7}Pd_{1.3}B_{0.5}$ without the ½½½–type superstructure reflections, taken with the incident beam parallel to the [011] direction, and PED patterns in insets.

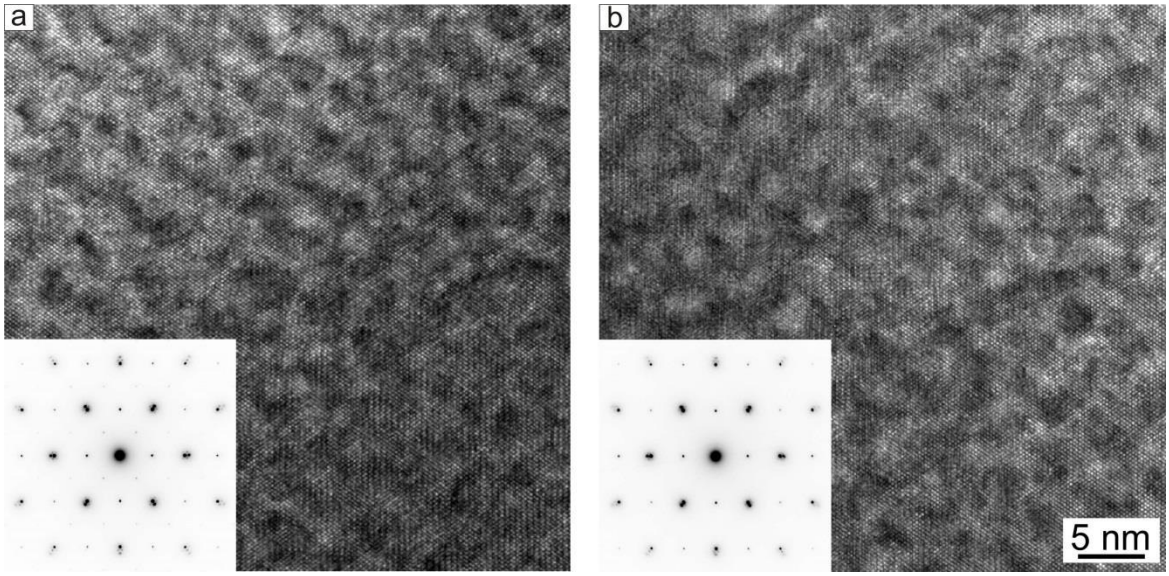

Figure 16: HREM images and corresponding PED pattern taken with the incident beam parallel to the [011] direction (inset) of (a) $CeRh_{2.5}Pd_{0.5}B_{0.5}$ and (b) $CeRh_{1.7}Pd_{1.3}B_{0.5}$.

In the images, one can see a modulation with a domain structure, which is similar to that of $CeRh_3B_{0.5}$. At the boundaries between the domains, one can see anti-phase displacements of lattice fringes and dislocation-like defects.

4.3.1.5 Crystal Chemistry

The group-subgroup relations for perovskite ($CaTiO_3$) and its large number of derivative structure types have been shown by Bock and Müller (Bock O. 2002) in form of several Bärnighausen trees, classified after coordination octahedra, Jahn Teller distortion, substitution variants or distortion variants. One small part of the

Bärnighausen tree is shown in Figure 17, relevant to the defect ordered structure types among borides.

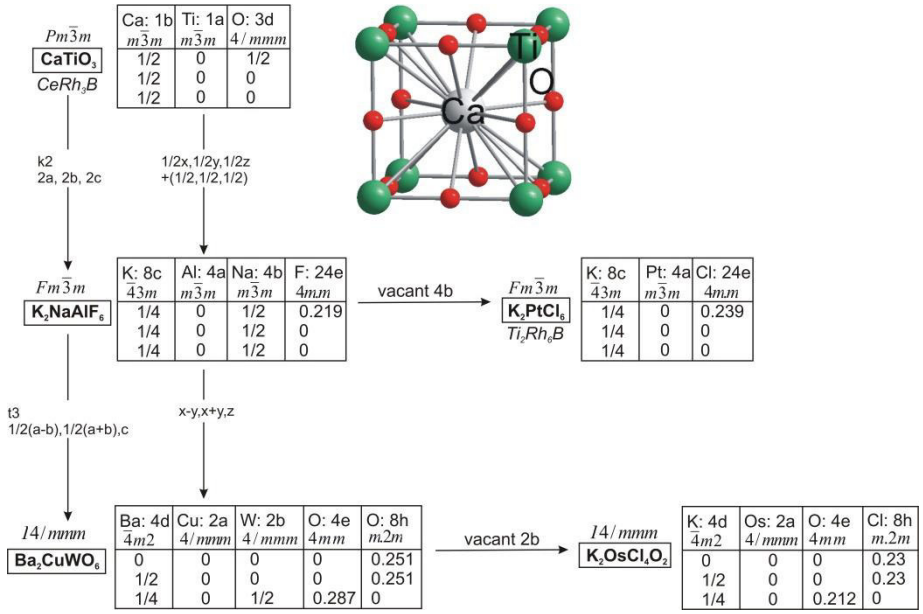

Figure 17: Branch of the Bärnighausen tree of the perovskite family including ordered defect structures.

Ordering of B-atoms and vacancies in Zr_2Ir_6B (Hermus M. 2010) and Ti_2Rh_6B (Fokwa B.P.T. 2006) leads to an 8 times larger unit cell ($a=b=c=2a_0$; space group $Fm\bar{3}m$, K_2PtCl_6 type, see Figure 17), which has been defined for these compounds by X-ray single crystal studies.

As the ½½½ superstructure reflections in the SAED pattern of $CeRh_3B_{0.5}$ are relatively strong, Yubuta et al. independently suggested that in this structure besides the boron ordering, also displacements of the Rh atoms around the B atoms appear (N. A. Yubuta K. 2006). Another possibility for B/vacancy ordering would exist in the $K_2OsCl_4O_2$ structure type with lower tetragonal symmetry ($a=b=\sqrt{a_0}$, $c=2a_0$, space group *I*4/*mmm,* see Figure 17).

In the system under study, the ½½½ superlattice reflections, leading to an enlargement of the unit cell, are clearly visible for $CeRh_3B_{0.5}$ and $CeRh_{2.5}Pd_{0.5}B_{0.5}$ on the SAED pattern. This is in contrast to Zr_2Ir_6B for which the reflections caused by the ordering are also visible on the X-Ray powder spectrum (Hermus M. 2010). Figure 18 shows the Rietveld refinement of the X-ray powder pattern for $CeRh_{2.5}Pd_{0.5}B_{0.5}$ including Miller indexes (bars) for the simple $CaTiO_3$ type and the K_2PtCl_6 type.

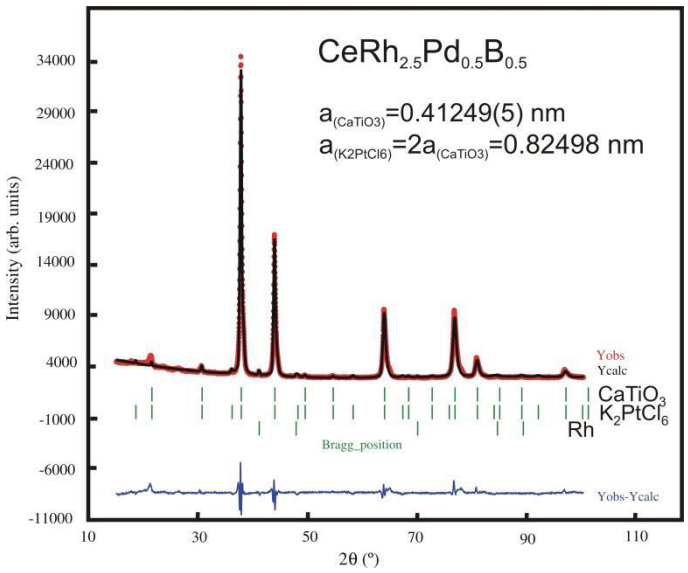

Figure 18: Rietveld refinement for $CeRh_{2.5}Pd_{0.5}B_{0.5}$ including the simple $CaTiO_3$ type and the K_2PtCl_6 type.

In case of $CeRh_3B_{0.5}$ or $CeRh_{2.5}Pd_{0.5}B_{0.5}$ the small reflections found on the powder patterns in addition to those of the parent $AuCu_3$-type cannot unambiguously be attributed to the superstructure but in addition with the results of the electron diffraction the K_2PtCl_6 structure type can be considered.

4.3.1.6 Electron density and volume effects

As mentioned before, atomic valence and volume are intimately related parameters through the Coulomb potential acting on the valence electrons of the atoms. Stable valent elements participate in compound formation when their Wigner-Seitz cell border is compatible with those of the neighboring ligand atoms within an appropriate crystalline structure. Although the equilibrium values for these parameters have some range of flexibility, they are more restricted in ionic and covalent compounds than in intermetallics. That flexibility allows to form large families of compounds, with the same composition and structure, within an ample range of volume variation as typically observed in trivalent rare earth (RE^{+3}) compounds.

Certain elements, known to exhibit valence instabilities, are capable to access different electronic configurations compatible with different states of valence. Those elements, in general, form a large number of compounds, because they can adapt their valence/volume ratio (Z_{eff}/V_{av}) to those of the neighboring ligand atoms. Since ligand electrons are those from the valence band, in the case of Ce^{3+} only the [$6s^2 5d^1$] electrons participate in bonding; the $4f^1$ orbital is excluded due to its strong localized

character. On the contrary, in the case of Ce^{4+}, with the $4f^0$ electronic configuration, also a fourth delocalized electron may form the conduction band. Since the Ce^{3+} band, with the electronic structure [$6s^2 5d^1$] is the same than La^{3+}, the existence of isotypic La compounds indicate that the electronic band of Ce atoms is compatible with a Ce^{3+} state. On the other hand, if isotypic Zr^{4+} compounds form with a [$6s^2 5d^2$] band, like e. g. $ZrFe_2$, $ZrCo_2$ Laves phases or $ZrRh_3$ (for the present case), it indicates that in the isotypic compounds the Ce electronic configuration is compatible with a Ce^{4+} state. The possibility to have intermediate valence states allows Ce atoms to adjust their Z_{eff}/V_{av} ratio as it occurs in the $CeRh_{3-x}Pd_x$ alloy above x = 2.4, whereas the stable valent Zr cannot do it like in $ZrRh_{3-x}Pd_x$ where a change of structure (i.e. V_{av}) occurs (Pountney J. M. 1978).

A further characteristic of the elements with valence instabilities is to adapt their Z_{eff}/V_{av} ratio to chemical potential modifications, allowing the stability of a crystalline structure in an extended range of concentrations like in $CeRh_{3-x}Pd_x$. This possibility contrasts with $ZrRh_{3-x}Pd_x$, included in Figure 19, because the stable valence of Zr^{4+} constrains the system to modify the crystal structure from $AuCu_3$ to $TiNi_3$, once the available atomic volume V_{av} of Zr becomes mismatched with the neighboring electronic conditions.

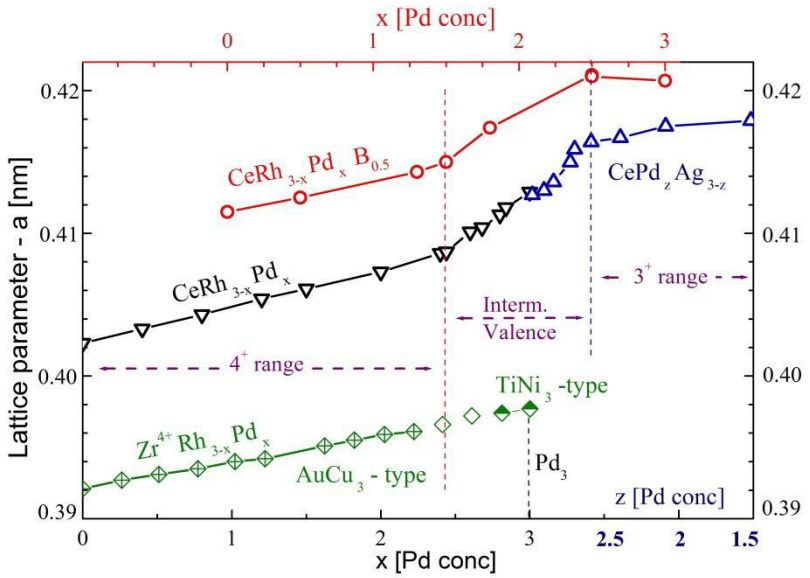

Figure 19: Variation of lattice parameters ($AuCu_3$-unit cell) for the alloy series $ZrRh_{3-x}Pd_x$, $CeRh_{3-x}Pd_x$, $CeRh_{3-x}Pd_xB_{0.5}$ and $CeAg_{3-z}Pd_z$ as a function of the Pd-content. The individual lattice parameter curves are shifted with respect to each other to comply with the region of Ce-intermediate valence and transition from the Ce^{4+} to the Ce^{3+} regime.

There is a useful heuristic constant provided by the product: $Z_{eff} \times V_{av}$ (i.e. the effective valence Z_{eff} times the available volume) for this analysis because for metallic Ce, $Z_{eff} \times V_{av} \approx 80$ A^3 (Sereni J. G. 1982). Similar values can be obtained for other instable valence elements like 5f-Pu, for example. The present study of $CeRh_{3-x}Pd_xB_{0.5}$ allows to check these features directly because the Ce-V_{av} increases with Pd concentration whereas Z_{eff} deceases from 4+ to 3+ as indicated in Figure 19. The figure summarizes the lattice parameters of the $AuCu_3$-unit cell as a function of the Pd-content for the alloys $ZrRh_{3-x}Pd_x$ (Pountney J. M. 1978), $CeRh_{3-x}Pd_x$ (Mihalisin P. 1981) and $CeAg_{3-z}Pd_z$ (Mihalisin P. 1981). Notice that $CeRh_{3-x}Pd_xB_{0.5}$ refers to the upper x-axis, which is shifted by the equivalent of one Pd atom because, according to $Z_{eff} \times V_{av}$ = constant, the expansion produced by 0.5 B atoms is equivalent to such a variation in the electronic configuration of the conduction band. Three different regions are identified in the figure according to the Ce valence configurations: i) a Ce^{4+} region on the left side, ii) the Ce intermediate valence range around the middle of the phase diagram, and iii) a Ce^{3+} one on the right side. The detailed analysis of each region is the following: i) a linear increase of the unit cell dimensions throughout $ZrRh_{3-x}Pd_x$ essentially reflects the substitution of the smaller Rh atoms (metal radius R_{Rh}=0.1345 nm (Taetum E. 1972)) by slightly larger Pd atoms (R_{Pd}=0.1376 nm (Taetum E. 1972)) at a stable Zr^{4+} valency. Consistently, a similar slope (Δ'a' parameter/ΔPd-content) encountered on the Rh-rich side of $CeRh_{3-x}Pd_x$ up to x_{Pd}<2.4 confirms a stable valency of the Ce^{4+} electronic configuration. The same applies to $CeRh_{3-x}Pd_xB_{0.5}$ after shifting the x_{Pd} concentration value to 1.5. ii) With higher Rh/Pd-substitution the intermediate valence region for Ce commences as documented by a series of physical properties. Interestingly, the isotypic Zr compound undergoes the mentioned structural modification at that Pd concentration. In the case of $CeRh_{3-x}Pd_x$, the Ce intermediate valence regime was explored beyond the $CePd_3$ limit ((Mihalisin P. 1981), (Gambke T. 1981)), revealing a further expansion of the unit cell when substituting Pd by Ag (R_{Ag}=0.1445 nm (Taetum E. 1972)). This provides a further increase of carriers in the electronic band. Backed by measurements of specific heat, magnetic susceptibility and electrical resistivity (Mihalisin P. 1981), this further increase refers to the fact that in $CePd_3$ the Ce atom is still within its intermediate valence regime. For $CeRh_{3-x}Pd_xB_{0.5}$, the addition of band electrons allocated by Ag atoms is not required because of the 0.5 Boron content; the full range of Ce valence

instability is developed within the Rh/Pd substitution range. iii) A plateau-like behavior is reached in $CeAg_{3-z}Pd_z$, indicating that at $z_{Pd}>2.4$ Ce atoms have reached their Ce^{3+} regime. The same limit is reached for $CeRh_{3-x}Pd_xB_{0.5}$, but in this case at $x_{Pd} \approx 2.5$. Notably, no magnetic order is observed in this limit. For comparison, one can mention that $CePd_{2.58}Ag_{0.42}$ (Mihalisin P. 1981) also shows a divergent $C_m(T\rightarrow 0)/T$ dependence like the present Pd-rich samples, but do not reach such a high value.

4.3.1.7 Conclusions

Crystal structure and physical properties studied for the solid solution $CeRh_{3-x}Pd_xB_{0.5}$ have shown that the lattice expansion produced by B interstitial atoms increases the Ce valence in an extent that is nearly equivalent to the value obtained by increasing the concentration of one Pd atom in $Ce(Rh_{1-x}Pd_x)_3$. This indicates that both mechanisms generate a similar variation of the chemical potential of the system. Thus, the concentration dependence of Pd scales with the previously observed one for $Ce\{Rh,Pd,Ag\}_3$. As a consequence of the shift of the Pd content, produced by doping with 0.5 B atoms, the complete variation of the valence between Ce^{4+} and Ce^{3+} can be obtained solely by the Rh/Pd substitution, i.e., without any further increase of the number of electrons in the band, as created by a Pd/Ag substitution.

The evolution from the Ce^{4+} to the Ce^{3+} configuration can be traced directly by the lattice parameter throughout three different regimes. For $0\leq x\leq 1.5$ the volume increase corresponds merely to the substitution of Rh by Pd atoms, which sizes are rather close. In this regime the tetravalent character of cerium is unaffected. This simple fact proves that each electronic configuration can be stable enough, requiring a significant modification of the electronic/volume environment in order to drive it into an intermediate valence regime.

For $x>1.5$ the lattice expansion is much steeper and is thus attributed to a gradual valence change of the cerium atoms, finally approaching a predominant trivalent state for $x>2.4$. SAED patterns of the $CeRh_{3-x}Pd_xB_{0.5}$ compounds revealed the appearance of ½½½ type superstructures and satellite reflections with respect to the parent $AuCu_3$ structure. The former is confined to the Rh-rich part of the solid solution, whereas the satellite reflections are observed throughout the solid solution and hint towards the existence of a domain structure enclosed by anti-phase boundaries.

5 Non-centrosymmetric $EpTX_3$ compounds and related ternary systems

The last chapter deals with $BaAl_4$ derivative structure types, especially with the investigations on the non-centrosymmetric $EpTX_3$ compounds ($BaNiSn_3$ structure type; *Ep* = Sr, Ba; *T* = Ni, Pd, Pt, Cu, Ag, Au; *X* = Si, Ge, Sn) and studies concerning the related ternary systems Sr-{Cu,Ag,Au}-{Si,Ge} and Ba-{Ag,Au}-{Si,Ge}. Physical properties are presented for several clathrates type-I and for the new superconductors $BaAu_3Si$ and $BaAu_3Ge$. As the Ba-Ag-Ge system has been studied most detailed, the results are presented first followed by the other ternary systems with barium and strontium. The results presented in this chapter are partially published in the papers ``Superconductivity in non-centrosymmtric $BaAl_4$ derived structures´´ (F. Kneidinger 2014), ``Phase equilibria, crystal chemistry, electronic structure and physical properties of Ag–Ba–Ge clathrates (C. M. Zeiringer I. 2011), `` Liquidus projection of the Ag–Ba–Ge system and melting points of clathrate type-I compounds´´ (G. A. Zeiringer I. 2012), ``Phase Equilibria, Crystal Chemistry, and Physical Properties of Ag-Ba-Si Clathrates´´ (B. E. Zeiringer I. 2011), ``The ternary system Au–Ba–Si: Clathrate solution, electronic structure, physical properties, phase equilibria and crystal structures´´ (C. M. Zeiringer I. 2012), ``Phase Equilibria, Crystal Chemistry and Physical Properties of Au-Ba-Ge Clathrates´´ (M.-K. N. Zeiringer I. 2011), ``Clathrate formation in the systems Sr–Cu–Ge and {Ba,Sr}–Cu–Ge´´ (G. A. Zeiringer I. 2014) and in the PhD Thesis ``Non-centrosymmetric superconductivity of intermetallic compounds in absence of strong correlations among electrons´´ (Kneidinger F. 2014).

5.1 SUPERCONDUCTIVITY IN NON-CENTROSYMMETRIC $BaAl_4$ DERIVED STRUCTURES

The $EpTX_3$ compounds (*Ep* = Sr, Ba; *T* = Ni, Pd, Pt, Cu, Ag, Au; *X* = Si, Ge, Sn) investigated in this work are isotypic to the non-centrosymmetric $BaNiSn_3$ structure type, which belongs to the $BaAl_4$ family. The structural relation of $BaNiSn_3$ and many other derivative structure types to $BaAl_4$ have been shown by Kußmann et al. in form of a Bärnighausen tree (Kußmann D. 1999). The $BaNiSn_3$ structure type has been reported

first by Dörrscheidt and Schäfer (S. H. Dörrscheidt W. 1978) together with the isotypic compounds $SrNiSn_3$ and $BaPtSn_3$. Since that time a large number of $EpTX_3$ compounds have been found, where Ep is an alkaline earth or rear earth element, T is a transition element and X is an element from the 3rd or 4th main group of the periodic table.

Fujii et al. (Fujii H. 2010) reported the absence of superconductivity above 1.8 K (DC magnetization measurements) for $SrMGe_3$ (M = Rh, Ir, Ni, Pd, Pt). However, superconductivity has been found in $SrPdGe_3$ and $SrPtGe_3$ by Miliyanchuk et al. (Miliyanchuk K. 2011) at ambient pressure at 1.49 and 1.0 K, respectively. $BaPtSi_3$ ((G. A. Koblyuk-M. N. 2008), (Bauer E. 2009)) also exhibits superconductivity at 2.25 K and the experimental results of these compounds are accompanied by density functional theory (DFT) calculations ((Miliyanchuk K. 2011), (Bauer E. 2009)). The unambiguous conclusion drawn from these studies was the presence of conventional s-wave BCS-type superconductivity. The compounds $SrNiSi_3$ (Nasir N. 2010), $BaPdGe_3$ (G. A. Koblyuk-M. N. 2007), $BaPdSi_3$ (G. A. Koblyuk-M. N. 2008), $BaPtGe_3$ (Demchyna R. 2006), $BaAuGe_3$ (this work), $SrPdSn_3$ and $BaPdSn_3$ (Tkachuk A.V. 2007) have already been reported in literature but without any information on physical properties.

This work is to provides complete information on the existence of $EpTX_3$ and EpT_xX_{4-x} compounds with Ep = Sr, Ba; T = Ni, Pd, Pt, Cu, Ag, Au and X = Si, Ge, Sn including structural details and physical properties of the superconducting compounds.

5.1.1 Results and Discussion

5.1.1.1 The $BaAl_4$ family

The group-subgroup relations in form of a Bärnighausen tree (Bärnighausen H. 1980) have been shown for $BaAl_4$ and its binary and ternary derivative structure types by Kußmann et al. (Kußmann D. 1999). Several new structure types, which have been reported in literature since that time, are added in red color to the original tree (black) in Figure 1.

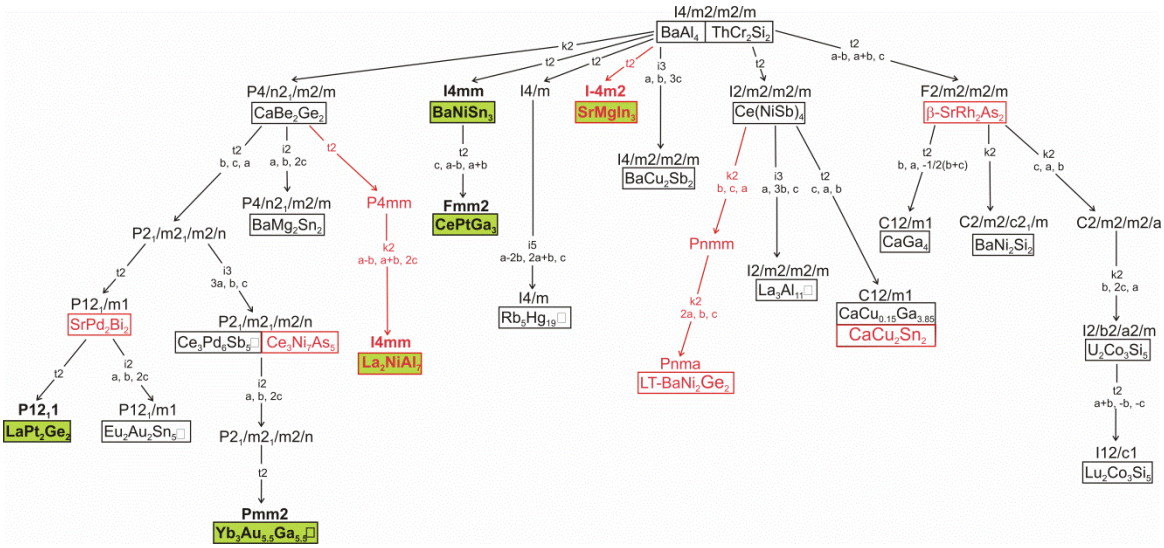

Figure 1: Group-subgroup relations for $BaAl_4$ and several binary and ternary derivative structure types in form of a Bärnighausen tree. The original tree from Kußmann et al. (Kußmann D. 1999) is shown in black, new branches or structure types are shown in red and non-centrosymmetric structure types are shown bold and in a green box.

The crystal structure of $Ce_3Ni_7As_5$ has been reported by Babizheztskyy et al. (Babizheztskyy V. 2003), those of La_2NiAl_7 by Gout et al. (Gout D. 2005), of $SrMgIn_3$ by Bin and Corbett (Bin L. 2007) and of $SrPd_2Bi_2$ by Frik et al (Frik L. 2006). Details concerning group-subgroup relations and on other derivative structure types can be found in Ref. ((Kußmann D. 1999), (Bärnighausen H. 1980), (M. U. Bärnighausen H. 1996)). Six of the 21 shown derivative structure types of $BaAl_4$ are non-centrosymmetric and are marked with green color in Figure 1.

In the next two sections the $BaNiSn_3$ structure type and other tetragonal or orthorhombic $BaAl_4$ derivative structure types, which appear in the investigated ternary systems Ep-T-X (Ep = Sr, Ba; T = Ni, Pd, Pt, Cu, Ag, Au; X = Si, Ge, Sn) will be discussed in more details. Figure 2 shows a graphical summary of all the formed phases with any $BaAl_4$ derivative structure type appearing in these ternary systems.

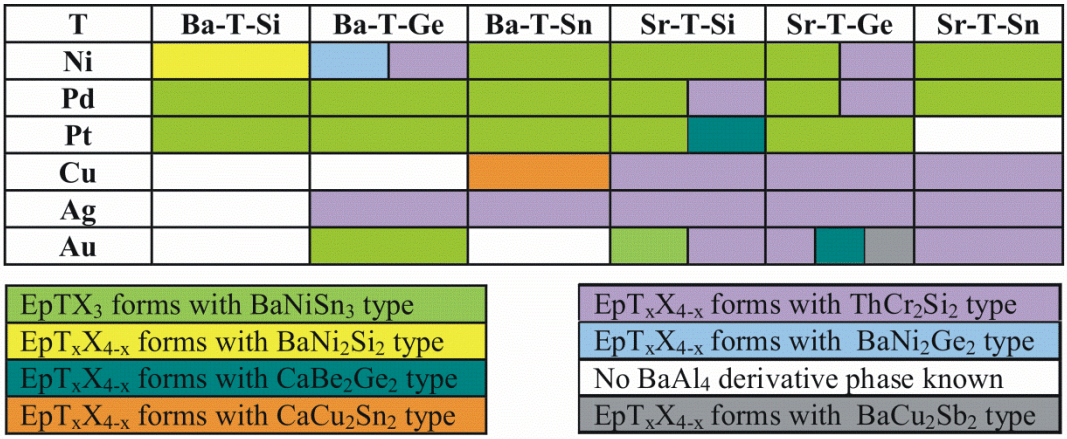

Figure 2: Graphical summary of all formed phases with any $BaAl_4$ derivative structure type in the ternary systems Ep-T-X (Ep = Sr, Ba; T = Ni, Pd, Pt, Cu, Ag, Au; X = Si, Ge, Sn).

5.1.1.2 Tetragonal $BaAl_4$ derivative structure types

5.1.1.2.1 $EpTX_3$ compounds with $BaNiSn_3$ structure type

The ternary systems Ep-T-X (Ep = Sr, Ba; T = Ni, Pd, Pt, Cu, Ag, Au; X = Si, Ge, Sn) have been investigated systematically concerning the appearance of $EpTX_3$ compounds with $BaNiSn_3$ structure type in as cast state (after arc melting) and after annealing at 800 or 900°C. Table I gives a summary of these investigations and literature data.

Table I: Crystallographic data of all $EpTX_3$ compounds (Lattice parameter a and c; Ep = Sr, Ba; T = Ni, Pd, Pt, Cu, Ag, Au; X = Si, Ge, Sn; $BaNiSn_3$ type; Space group *I4mm;* Ep in 2a (0,0,z), T in 2a (0,0,z), X in 2a (0,0,z), X in 4b (0, 0.5, z).

Compound	a (nm) c (nm)	Ep in 2a; z	T in 2a; z	X in 2a; z	X in 4b; z	Method	Ref.
$BaNiSi_3$	-					XPD	*
$BaNiGe_3$	-					XPD	*
$BaNiSn_3$	0.482(1) 1.093(2)	0.5759	0.2313	0.000	0.3253	XSCD	(S.H. Dörrscheidt W. 1978)
$SrNiSi_3$	0.41958(3) 0.97915(7) 0.4193(1) 0.9791(3)	0.5984 0.596	0.2413 0.242	0.000 0.000	0.3530 0.352	XPD XPD	(Nasir N. 2010) *
$SrNiGe_3$	0.44677(4) 1.0286(1)	0.590	0.241	0.000	0.340	XPD	*
$SrNiSn_3$	0.474(1) 1.088(2) 0.4717(3) 1.0966(2)	0.5710 0.544	0.2300 0.230	0.000 0.000	0.321 0.302	XSCD XPD	(S.H. Dörrscheidt W. 1978) *

$BaPdSi_3$	0.43963(3) 1.0186(2)	0.6156	0.2607	0.000	0.3702	XPD	(Nasir N. 2010)
$BaPdGe_3$	0.45508(2) 1.0365(1)	0.6048	0.2499	0.000	0.3568	XSCD	(Nasir N. 2010)
$BaPdSn_3$	0.487(1) 1.117(2) 0.48789(2) 1.1174(2)	0.587 0.5901	0.236 0.2391	0.000 0.000	0.337 0.3385	XSCD XPD	(S. H. Dörrscheidt W. 1980) *
$SrPdSi_3$	0.4296(3) 1.0029(3)	0.6072	0.2477	0.000	0.3667	XPD	*
$SrPdGe_3$	0.44623(2) 1.02737(7) 0.44677(4) 1.0286(1)	0.6006 0.600	0.2425 0.2419	0.000 0.000	0.3538 0.355	XSCD XPD	(Fujii H. 2010) *
$SrPdSn_3$	0.479(1) 1.123(2) 0.47928(7) 1.1252(2)	0.591 0.585	0.233 0.227	0.000 0.000	0.336 0.333	XSCD XPD	(S. H. Dörrscheidt W. 1980) *
$SrPtSi_3$	0.43132(3) 0.98893(9)	0.605	0.250	0.000	0.365	XPD	*
$SrPtGe_3$	0.4478(2) 1.01366(9) 0.44859(3) 1.01364(8)	0.5988 0.600	0.2436 0.245	0.000 0.000	0.3558 0.357	XSCD XPD	(Fujii H. 2010) *
$SrPtSn_3$	-					XPD	*
$BaPtSi_3$	0.44094(2) 1.0013(2) 0.44079(2) 1.0017(2)	0.6022 0.5991	0.2502 0.2477	0.000 0.000	0.3608 0.356	XPD XSCD	(Bauer E. 2009) (Nasir N. 2010)
$BaPtGe_3$	0.45636(2) 1.02341(6) 0.45636(2) 1.02341(6)	0.6065 0.5999	0.2475 0.2469	0.000 0.000	0.3533 0.3532	XSCD XSCD	(Demchyna R. 2006) (Nasir N. 2010)
$BaPtSn_3$	0.485(1) 1.107(2)	0.5778	0.2313	0.000	0.3253	XSCD	(S. H. Dörrscheidt W. 1978)
$BaCuSi_3$	-					XPD	(Yan X. 2010)
$BaCuGe_3$	-					XPD	(G. A. Koblyuk-M. N. 2009)
$BaCuSn_3$	-					XPD	*

$SrCuSi_3$	-					XPD	*
$SrCuGe_3$	-					XPD	*
$SrCuSn_3$	-					XPD	*
$BaAgSi_3$	-					XPD	*
$BaAgGe_3$	-					XPD	*
$BaAgSn_3$	-					XPD	*
$SrAgSi_3$	-					XPD	*
$SrAgGe_3$	-					XPD	*
$SrAgSn_3$	-					XPD	*
$BaAuSi_3$	-					XPD	*
$BaAu_{1.1}Ge_{2.9}$	0.4615(2) 1.0492(5)	0.6312	0.2512	0.000	0.387	XPD	*
$SrAuSi_3$	-					XPD	*
$SrAuGe_3$	-					XSCD	*
$SrAuSn_3$	-					XSCD	(Tkachuk A.V. 2007)

* This work; - Compound does not form

As can be seen from Figure 3, the transition $BaAl_4 \rightarrow BaNiSn_3$ is 'translationengleich' of index 2 and leads to a symmetry reduction from the centrosymmetric space group *I*4/*mmm* to the non-centrosymmetric *I*4*mm* due to the loss of the mirror plane perpendicular to the c-axis.

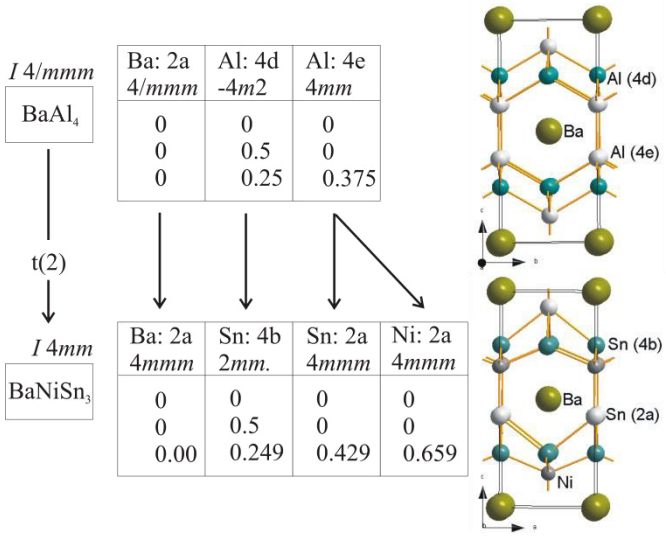

Figure 3: Group-subgroup relations for $BaAl_4$-$BaNiSn_3$ including the unit cells for both compounds.

The barium and nickel atoms occupy the crystallographic site 2a (0,0,*z*) and the tin atoms the 2a and 4b (0,½,*z*) sites.

5.1.1.2.2 EpT_xX_{4-x} compounds with $ThCr_2Si_2$ structure type

In the investigated ternary systems, a large number of phases have been reported in literature, crystallizing with the $ThCr_2Si_2$ structure type (Ban Z. 1965) (see Table II).

Table II: EpT_xX_{4-x} phases in the ternary systems Ep-T-X (Ep = Sr, Ba; T = Ni, Pd, Pt, Cu, Ag, Au; X = Si, Ge, Sn) with a $BaAl_4$ derivative structure type.

Compound	Lattice Parameter (nm)	Space group	Structure type	Method	Ref.
$BaNi_2Si_2$	a = 0.650(1) b = 0.535(1) c = 1.133(2)	*Cmcm*	$BaNi_2Si_2$	XSCD	(Doerrscheidt W. 1980)
HT-$BaNi_2Ge_2$	a = 0.42665(1) c = 1.12545(3)	*I*4/*mmm*	$ThCr_2Si_2$	XPD	(Hlukhyy V. 2007)
LT-$BaNi_2Ge_2$	a = 0.84693(4) b = 1.13503(5) c = 0.43212(2)	*Pnma*	$BaNi_2Ge_2$	XSCD	(Hlukhyy V. 2007)
$SrNi_2Ge_2$	a = 0.417(1) c = 1.025(2)	*I*4/*mmm*	$ThCr_2Si_2$	XSCD	(N. N. Dörrscheidt W. 1976)
$SrPd_2Si_2$	a = 0.4310 c = 0.9876	*I*4/*mmm*	$ThCr_2Si_2$	XPD	(Palenzona 1987)
$SrPd_2Ge_2$	a = 0.44088(2) c = 1.01270(8)	*I*4/*mmm*	$ThCr_2Si_2$	XSCD	(Fujii H. 2009)
$SrPt_2Si_2$	a = 0.427 c = 0.9895	*I*4/*mmm*	$ThCr_2Si_2$	XPD	(Mayer I. 1977)
	a = 0.42914(7) c = 0.9904(2)	*P*4/*nmm*	$CaBe_2Ge_2$	XSCD	(Fischer H. A. 2000)
$SrCu_2Si_2$	a = 0.42 c = 1.0	*I*4/*mmm*	$ThCr_2Si_2$	XSCD	(M. N. Eisenmann B. 1970)
$SrCu_{1.7}Si_{2.3}$	a = 0.41881(5) c = 1.00267(8)	*I*4/*mmm*	$ThCr_2Si_2$	XPD	(Nasir N. 2010)
$SrCu_2Ge_2$	a = 0.428(1) c = 1.031(2)	*I*4/*mmm*	$ThCr_2Si_2$	XSCD	(N. N. Dörrscheidt W. 1976)
$SrCu_2Sn_2$	a = 1.1197(4) b = 0.4322(2) c = 0.4859(1) β = 108.41(1)°	*C2/m*	$CaCu_2Sn_2$	XSCD	(F. M.–C.–S. Pani M. 2011)
$BaAg_2Ge_2$	a = 0.458	*I*4/*mmm*	$ThCr_2Si_2$	XSCD	(M. N. Eisenmann B.

	c = 1.069				1970)
$BaAg_{1.3}Ge_{2.7}$	a = 0.4652(9) c = 1.0606(2)	*I*4/*mmm*	$ThCr_2Si_2$	XPD	*
$BaAg_2Sn_2$	a = 0.481(2) c = 1.135(2)	*I*4/*mmm*	$ThCr_2Si_2$	XSCD	(May N. 1972)
$SrAg_2Si_2$	a = 0.438(2) c = 1.048(2) a = 0.43835(6) c = 1.0464(2)	*I*4/*mmm*	$ThCr_2Si_2$	XSCD XPD	(May N. 1972) *
$SrAg_2Ge_2$	a = 0.445 c = 1.085	*I*4/*mmm*	$ThCr_2Si_2$	XSCD	(M. N. Eisenmann B. 1970)
$SrAg_2Sn_2$	a = 0.467(1) c = 1.173(2)	*I*4/*mmm*	$ThCr_2Si_2$	XSCD	(N. N. Dörrscheidt W. 1976)
$BaAu_2Ge_2$	a = 0.4577(2) b = 0.5656(2) c = 1.0558(5)	*Immm*	$Ce(Ni,Sb)_4$	XSCD	*
$SrAu_2Si_2$	a = 0.437(1) c = 1.014(2)	*I*4/*mmm*	$ThCr_2Si_2$	XSCD	(N. N. Dörrscheidt W. 1976)
$SrAu_{1.6}Ge_{2.4}$	a = 0.44796(2) c = 1.06315(5)	*P*4/*nmm*	$CaBe_2Ge_2$	XSCD	*
$SrAu_{1.9}Ge_{2.1}$	a = 0.44866(2) c = 3.1808(2)	*I*4/*mmm*	$BaCu_2Sb_2$	XSCD	*
$SrAu_2Ge_2$	a = 0.451(2) c = 1.035(2)	*I*4/*mmm*	$ThCr_2Si_2$	XSCD	(May N. 1972)
$SrAu_{1.4}Sn_{2.6}$	a = 0.46447(7) c = 1.1403(2)	*I*4/*mmm*	$ThCr_2Si_2$	XSCD	(Hellmann A. 2007)

The $ThCr_2Si_2$ structure type is the ordered ternary substitution variant of $BaAl_4$, where Th occupies the 2a (0,0,0) site, Cr the 4d (0,½,¼) and Si the 4e (0,0,z) site (Figure 2). In several of these phases, a rather large homogeneity region has been reported for example $SrCu_xSi_{4-x}$ ($1.6 \leq x \leq 2$ at 800°C) (Nasir N. 2010), $BaAg_xGe_{4-x}$ ($1.3 \leq x \leq 1.8$ at 800°C) (This work) or $SrAu_xSn_{4-x}$ ($1.3 \leq x \leq 2.2$ at 700°C) (Tkachuk A.V. 2007). A mixed occupancy of Au and Sn in the sites 4d and 4e has been reported by Tkachuk and Mar (Tkachuk A.V. 2007) for $SrAu_{1.4}Sn_{1.6}$ from single crystal investigations whereas for $BaAg_xGe_{4-x}$ a mixed occupancy of Ag and Ge occurs only in 4d (This work).

5.1.1.2.3 EpT_xX_{4-x} compounds with $CaBe_2Ge_2$ structure type

A 'klassengleiche' symmetry reduction of index 2 (k2) leads from the body centered tetragonal unit cell of $BaAl_4$ to the primitive cell of $CaBe_2Ge_2$ (see Figure 1; space group *P*4/*nmm*; a = 0.402(2), c = 0.992(2) nm (M. N.-T.-T. Eisenmann B. 1972)). Calcium occupies the crystallographic site 2c (¼,¼,z), beryllium the crystallographic sites 2a (¾,¼,0) and 2c and germanium the sites 2b (¾,¼,½) and 2c.

The crystal structure of $SrAu_{1.6}Ge_{2.4}$ has been solved from X-ray single crystal investigations and has been found to be isotypic with $CaBe_2Ge_2$. The refinement showed a mixed occupancy of Au and Ge in both Ge and both Ge sites. Crystallographic details of the refinement are given in the chapter on the ternary system Sr-Au-Ge.

5.1.1.2.4 EpT_xX_{4-x} compounds with $BaCu_2Sb_2$ structure type

The crystal structure of $BaCu_2Sb_2$ (space group *I*4/*mmm*; a = 0.4655(1), c = 3.2709(6) nm (DünnerJ. 1995)) is built of blocks of $CaBe_2Ge_2$ and $ThCr_2Si_2$ at the ratio of 2:1 in c-direction (isomorphic symmetry reduction (i3); $c_{BaCu2Sb2} = 3c_{BaAl4}$). Barium occupies the crystallographic sites 2a (0,0,0) and 4e (0,0,z), Cu the 4e and 8g (0,½,z) sites and Sb the crystallographic sites 4d (0,½,¼) and 2 times site 4e.

The $BaCu_2Sb_2$ structure type has been found for $SrAu_{1.55}Ge_{2.45}$ from XSCD. The refinement of the occupancies of all Wyckoff sites showed full ordering of strontium in the sites 2a and 4e, of gold in one 4e site and of germanium in the 4d site. A mixed occupancy of Au and Ge has been found in the sites 8g and in the other two 4e sites Details of the crystal structure refinement can be found in the chapters on the ternary system Sr-Au-Ge.

5.1.1.3 Orthorhombic $BaAl_4$ derivative structure types

Different site occupations and slight distortions in the crystal lattice cause symmetry reductions and lead to many different orthorhombic or even monoclinic $BaAl_4$ derivative structure types. A 'translationengleiche' symmetry reduction of index 2 (t2) leads from the body centered tetragonal unit cell of $BaAl_4$ either to a body centered orthorhombic unit cell of $Ce(Ni,Sb)_4$ (space group *Immm*; a = 0.4312(3), b = 0.4285(3), c = 1.00205(7) nm (Percharskij V.K. 1982)) or to a face centered orthorhombic cell of β-$SrRh_2As_2$ (space

group *Fmmm*; a = 0.5760(3) , b = 0.6067(4), c = 1.1264(5) nm (Hellmann A. 2007)).

In the $Ce(Ni,Sb)_4$ structure type, cerium occupies the Wyckoff position 2a (0,0,0) and Ni and Sb the sites 4j (½,0,z) and 4i (0,0,z). $BaAu_2Ge_2$ has been found to be isotypic with $Ce(Ni,Sb)_4$ (see Table II) from X-ray single crystal investigations. Two lower symmetry structure types deriving from the $Ce(Ni,Sb)_4$ structure type (see Figure 1) have been reported in literature concerning our ternary systems, namely the low temperature $BaNi_2Ge_2$ and the $CaCu_2Sn_2$ structure type. In the low temperature modification of $BaNi_2Ge_2$ (space group *Pnma*; a = 0.83852(4), b = 1.13174(8), c = 0.42902(9) nm (Hlukhyy V. 2007)), the Ba atoms are located on the Wyckoff position 4c (x,¼,z) and the Ni and Ge atoms on the 8d (x,y,z) sites.

Pani et al. (F. M.–C.–S. Pani M. 2011) reported isotypism for $SrCu_2Sn_2$ (see Table II) with the $CaCu_2Sn_2$ structure type (space group *C*2/*m*; a = 1.0943(3), b = 0.4222(1), c = 0.4834(1) nm, β = 107.94(1)° (M. F. Pani M. 2007)), where Ca is occupying the 2a (0,0,0) site and Cu and Sn the sites 4i (x,0,z).

Concerning the second orthorhombic branch of the Bärnighausen tree in Figure 1, a 'klassengleiche' symmetry reduction of index 2 leads from a face centered orthorhombic unit cell of β-$SrRh_2As_2$ to a C-centered one of $BaNi_2Si_2$ (space group *Cmcm*; a = 0.650(1), b = 0.535(1), c = 1.133(2) nm) reported by Doerrscheidt and Schäfer (Doerrscheidt W. 1980). In this structure type, Ba is located in the crystallographic site 4c (0,y,¼), Ni in 8e (x,0,0) and Si in the 8f (0,y,z) site.

5.1.1.4 Physical Properties

5.1.1.4.1 Specific heat

As Specific heat measurements, provide a deep insight into the thermodynamic behavior of a superconductor, the results for the six superconducting $EpTX_3$ compounds are shown in Figure 4, plotted as *Cp*/*T* vs. *T*.

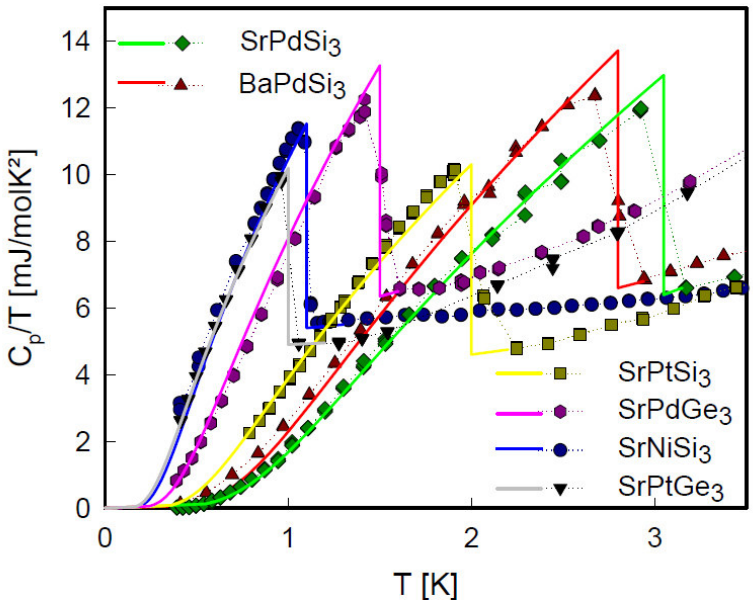

Figure 4: Temperature dependent heat capacity C_p of various superconducting $EpTX_3$ compounds. The solid lines are the numerical data of the heat capacity of an s-wave BCS superconductor as derived by Mühlschlegel (Mühlschlegel B. 1959).

Right at the superconducting transition at $T = T_c$ a pronounced anomaly in $C_p(T)$ is seen from the measurements carried out at 0 Tesla. This anomaly stems from the condensation of a fraction of the electrons into Cooper pairs, which causes the formation of an energy gap. The size of this jump for BCS superconductors in the weak coupling limit is $\Delta C_p/\gamma T = 1.43$. Consequently, a larger value of $\Delta C_p/\gamma T$ than the BCS value might refer to a stronger coupling, whereas a smaller value can show that the bulk is either not completely superconducting or gives a first hint to a non-isotropic gap-function. Numerical BCS values of the temperature dependent specific heat were first calculated by Mühlschlegel (Mühlschlegel B. 1959) in the scope of the weak coupling limit. While the model itself is normalized to T_c and the Sommerfeld value γ, it is independent of other parameters. Therefore, a comparison with the experimental specific heat data can already point out deviations from a conventional superconducting behavior. Below about 40% of T_c, this model renders the famous exponential heat capacity behavior of BCS superconductors. Taking into account the data set as compiled by Mühlschlegel (Mühlschlegel B. 1959) the temperature dependent specific heat of all six $EpTX_3$ samples displayed in Figure 4 could be well described from $T = T_c$ down to 0 K. This, in turn, indicates that the superconducting state is predominantly of an s-wave BCS-type. As a consequence, spin-singlet Cooper pairs are forming the superconducting condensate and spin-triplet pairs do not contribute in any substantial amount. Above the superconducting

transition temperature, the $EpTX_3$ compounds are simply accounted for by $C_p = \gamma T + \beta T^3$, where γ is the Sommerfeld value and β is related to the Debye-temperature of the system. The critical temperatures, Sommerfeld values and the Debye-temperatures derived from the present experimental data are listed in Table III.

Table III: Experimental critical temperatures (T_c), Sommerfeld values γ and the Debye temperatures (Θ_D) of superconducting $EpTX_3$ compounds.

Compound	T_c [K]	γ [mJ/molK^2]	Θ_D [K]
$SrNiSi_3$	1.1	5.3	458
$SrPdSi_3$	3.0	4.5	359
$BaPdSi_3$	2.8	4.9	344
$SrPdGe_3$	1.5	5.0	268
$SrPtSi_3$	2.0	3.9	343
$BaPtSi_3$	2.3	5.8	370
$SrPtGe_3$	1.0	4.0	271

Overall, rather small values are observed which, in turn, indicate rather low values of the electronic density of states (DOS) at the Fermi energy. Furthermore, since the superconducting transition- temperature is dependent on the DOS, the fairly low T_c values observed for the $EpTX_3$ series can then be understood.

5.1.1.5 Conclusions

An exploration of the ternary phase diagrams Ep-T-X (Ep = Sr, Ba; T = Ni, Pd, Pt, Cu, Ag, Au; X = Si, Ge, Sn) revealed six new non-centrosymmetric superconductors crystallizing in the tetragonal $BaNiSn_3$ structure. Superconductors from this series ($T_c \leq 3$ K) exhibit antisymmetric spin-orbit coupling (ASOC); its strength is dependent on the composition of each material and increases with the atomic number of the elements involved. This phenomenological statement is corroborated from DFT calculations, revealing, in general, an increase of the ASOC for the sequences Sr-Ba, Ni-Pd-Pt and Si-Ge. However, there is a strong variation of the ASOC within the Brillouin zone and also a dependence on the specific band. Overall, ASOC in the present compounds is rather small, specifically in the proximity of the Fermi energy, which might not favour unconventional superconductivity (see (F. Kneidinger 2014).

In view of the heat capacity data for $T < T_c$, which almost perfectly could be described in the framework of s-wave BCS superconductivity, it is rather likely that spin-singlet

pairing dominates the superconducting ground state, while spin-triplet components are negligible. Although heavy elements like Pt are involved in the present materials, unconventional superconductivity triggered by the ASOC is absent in this non-centrosymmetric family of compounds. This, most likely, allows to conclude that materials without substantial correlations among electrons will not show a significant fraction of spin-triplet paired Cooper-pairs. This would be in line with the predictions made by Takimoto and Thalmeier ((Takimoto T. 2009), (Takimoto T. 2010)) that anomalous spin-fluctuations are needed to provide a basis for superconductivity away from the simple s-wave channel.

5.2 THE TERNARY SYSTEM Ba-Ag-Ge

In various cases, the clathrate type-I solid solution offers the possibility to tune its promising thermoelectric properties from a metal towards an insulator and to obtain *n*- and *p*-type properties by varying the transition metal content in the crystal structure ((H. M. Anno H. 2005), (S. K. Anno H. 2007), (Candolfi C. 2012), (Slack G.A. 1995), (Bobev S. 2000), (Shevelkov A.V. 2011), (Toberer E.S. 2010)). In the primitive cubic clathrate type-I crystal structure, the transition metal atoms and atoms from the 3rd or 4th main group of the periodic table form a 3-dimensional network of cages (see Figure 5), which are filled by electropositive elements from the alkali, alkaline earth or rare earth groups.

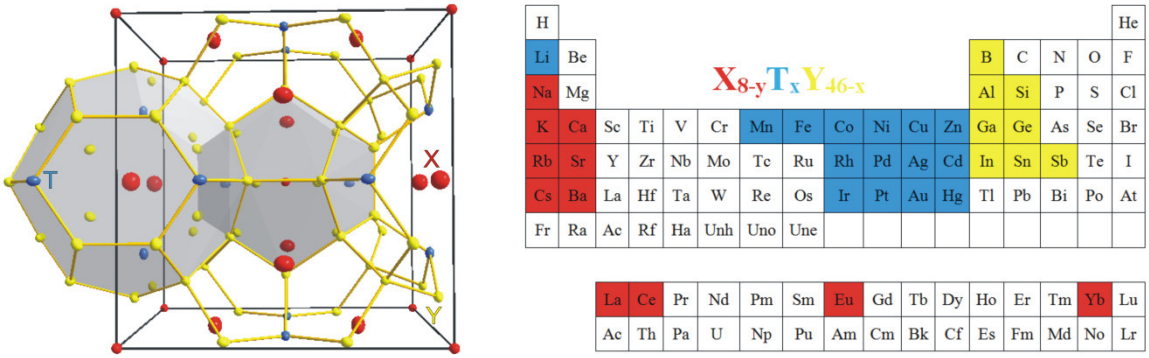

Figure 5: Unit cell of the clathrate type-I and schematic periodic table with all elements marked, which are known to form clathrates type-I.

Although several investigations dealt already with compounds of the Ba - Ag - Ge

system, there is still little known about the phase equilibria in the ternary system and about the solubility range of ternary phases at a defined temperature. Beside the type-I clathrate $Ba_8Ag_6Ge_{40}$, for which perfect atomic ordering has been elucidated from an X-ray single crystal study (Cordier G. 1991) and for which thermoelectric properties have been described (p-type material) (Johnsen S. 2007), two more ternary compounds have been evaluated in the literature, namely (a) $BaAg_{0.8}Ge_{1.2}$ with the AlB_2 structure type and a small undefined homogeneity region at 550°C (P. M. Merlo F. 1996) and (b) $BaAg_2Ge_2$ with the $ThCr_2Si_2$ structure type (M. N. Eisenmann B. 1970).

The following chapter provides consistent information on the phase relations in the isothermal sections at 800 and 600°C for the region with Ba-contents less than 33 at% and on the partial liquidus projection in order to define especially the primary crystallization field of the type-I clathrate. The reaction scheme for the appearing ternary compounds is shown in form of a Schultz-Scheil diagram. Melting points for several of the type-I clathrates $Ba_8T_xGe_{46-x-y}\square_y$, $Ba_8T_xSi_{46-x}$ (T = Al, Ga, Zn, Cd, Cu, Ag, Au, Ni, Pd, Pt) and inverse clathrates are given including all melting point data available in the literature. Finally, thermoelectric data on the clathrate type I as a function of temperature and of composition throughout the homogeneity region are given.

5.2.1 Results and Discussion

5.2.1.1 Binary phase diagrams Ag-Ge, Ba-Ge and Ba-Ag

Information on the binary phase diagram Ag-Ge was taken from Massalski (Massalski T.B. 1990), for the Ba-Ge system from Okamoto (Okamoto H. 2009), who combined the partial phase diagrams of Carrillo-Cabrera et al. (Ge-rich part) (W. Carrillo-Cabrera 2005) and Pani et al. (0-75 at.% Ge) (P. A. Pani M. 2008). Crystallographic data for solid phases in the Ag-Ba system are accepted from Bruzzone et al. (F. M. Bruzzone G. 1987). Crystallographic details on the solid phases of the binary systems are given in Table IV.

Table IV: Crystallographic data on the solid phases of the binary Ba-Ge, Ag-Ba and Ag-Ge systems and the ternary Ag-Ba-Ge system.

Phase	Space group	Struct. type	Lattice parameter [nm]			Ref.
			a	b	c	
(Ge)	$Fd\bar{3}m$	C_{diam}	0.56574	-	-	(Massalski T.B. 1990)
(Ba)	$Im\bar{3}m$	W	0.50227	-	-	(Massalski T.B. 1990)
(Ag)	$Fm\bar{3}m$	Cu	0.40857	-	-	(Massalski T.B. 1990)
Ba_8Ge_{43}	$Ia\bar{3}d$	Ba_8Ge_{43}	2.13123(5)	-	-	(B. S. Carrillo-Cabrera W. 2004)
(κ_I)	$Pm\bar{3}n$	K_4Ge_{23-x}	1.0688(2)	-	-	x=1*
			1.0843(3)	-	-	x=5.3*
$BaGe_5$	*Pmna*	$BaGe_5$	1.0727(1)	0.92844(7)	1.4794(1)	(Aydemir U. 2010)
Ba_6Ge_{25}	$P4_132$	Ba_6Ge_{25}	1.45564(2)		-	(Carrillo Cabrera W. 2000)
(κ_{IX})			1.4560(1)	-	-	x=0.5*
$BaGe_2$	*Pnma*	$BaSi_2$	0.9078(3)	0.6829(2)	1.1653(3)	(Vaughey J.T. 1997)
βBa_3Ge_4	$P4_2/nmm$	Ba_3Ge_4	0.8621(2)	-	1.2031(3)	(Zuercher F. 1998)
αBa_3Ge_4	*Cmmm*	Ba_3Ge_4	1.1799(6)	1.2210(6)	1.2097(6)	(Zuercher F. 1998)
BaGe	*Cmcm*	CrB	0.5058(5)	1.198(1)	0.4300(2)	(F. M. Merlo F. 1967)
Ba_5Ge_3	*P4/nmn*	Ba_5Si_3	0.8538(2)	-	1.6495(5)	(F. M. Bruzzone G. 1987)
Ba_2Ge	*Pnma*	Co_2Si	0.838(2)	0.548(2)	1.004(2)	(Turban K. 1973)
$BaAg_{5\pm x}$	*P6/mmm*	$CaCu_5$	0.5826(1)	-	0.4598(1)	x= -0.5
			0.5681(1)	-	0.4698(1)	x=1 (F. M. Bruzzone G. 1987)
			0.56797(3)	-	0.47021(7)	x=2.1*
$BaAg_2$	*Imma*	$CeCu_2$	0.4952(1)	0.8058(3)	0.8447(2)	(Okamoto H. 2009)
BaAg	*Pnma*	FeB	0.8657(3)	0.4982(3)	0.6651(3)	(F. M. Merlo F. 1981)
Ba_3Ag_2	$R\bar{3}$	Er_3Ni_2	1.0385(5)	-	1.9332(5)	(F. M. Bruzzone G. 1987)
τ_1	*P6/mmm*	AlB_2	0.4427(1)	-	0.4882(8)	x=0.65
			0.4485(1)	-	0.4814(3)	x=0.75*
			0.4428(1)	-	0.4881(1)	x=0.6 (P. M. Merlo F. 1996)
τ_2	*I4/mmm*	$ThCr_2Si_2$	0.4652(9)	-	1.0606(2)	x=0.7
			0.4610(7)	-	1.0697(9)	x=0.2*
			0.458	-	1.069	x=0 (M. N. Eisenmann B. 1970)

κ_{IX}-$Ba_6Ag_xGe_{25-x}$; κ_I-$Ba_8Ag_xGe_{46-x-y}\square_y$; τ_1-$Ba(Ag_{1-x}Ge_x)_2$; τ_2-$BaAg_{2-x}Ge_{2+x}$; *this work

However, the melting point of $BaAg_5$ (710°C) and the temperature of the invariant eutectic reaction (700°C) in the silver rich part (>86 at.% Ag) were found to be

inconsistent with equilibria (eutectic at 710°C) in the ternary system. In order to reinvestigate the corresponding binary eutectic reaction temperature, we prepared two binary alloys, 12.8Ba-87.2Ag and 10Ba-90Ag (at. %; one part of this sample has been measured in Al_2O_3 crucible on the Netzsch 404 Pegasus DSC equipment and the other in a sealed quartz vial with the STA 409 equipment). The measurements in both cases clearly showed an invariant reaction at 726°C and a liquidus temperature of 730°C for alloy $BaAg_{6.8}$ and 738°C for $BaAg_9$. These results are in perfect agreement with earlier findings of F. Weibke (Weibke F. 1930), who reported the existence of a eutectic in this region at 726°C. To confirm our temperature data, we re-measured the melting points of pure silver metal, which we used in our sample preparation as well as the standard silver and aluminium supplied by Netzsch. The results corresponded within ±1°C to the accepted melting points of these elements and thus confirm the higher temperature for the binary eutectic L ↔ (Ag) + $BaAg_5$ at 726°C.

5.2.1.2 The clathrate I solid solution $Ba_8Ag_xGe_{46-x-y}\square_y$

The solubility range of the ternary type-I clathrate was studied by XRPD and EPMA on a series of samples with nominal composition $Ba_8Ag_xGe_{46-x}$ ($1 \leq x \leq 8$), which were annealed at 800°C. Table V shows a comparison of the EPMA data with the results of Rietveld refinement of the X-ray intensity data.

Table V: Composition from EPMA and crystallographic data from XRPD and XSCD refinement.

Nominal composition	EPMA [at.%]			Accepted composition	Lattice parameter [nm]	Ge2 (16i) x	Ge31(24k) y, z; occ.	Ge32 (24k) y, z; occ.	Ge33 (24k) y, z; occ.
	Ba	Ag	Ge						
$Ba_8Ag_2Ge_{44}$	15.3	4.1	80.6	$Ba_8Ag_{2.1}Ge_{41.9}\square_{2.0}$ [a]	1.0743(4)	0.183(2)	0.11(4), 0.30(4); 0.40(5)	0.11(4), 0.31(4); 0.46(5)	0.13(4), 0.35(4); 0.14(4)
$Ba_8Ag_{2.5}Ge_{43.5}$	15.4	4.6	80.0	$Ba_8Ag_{2.3}Ge_{41.9}\square_{1.8}$ [b]	1.0748(4)	0.1835(1)	0.113(2), 0.297(2); 0.40(1)	0.1205(9), 0.319(1); 0.46(1)	0.133(3,) 0.348(3); 0.14(1)
$Ba_8Ag_3Ge_{43}$	15.3	6.5	78.2	$Ba_8Ag_{3.4}Ge_{41.5}\square_{1.1}$ [a]	1.0781(2)	0.182(6)	0.12(1), 0.30(7); 0.45(6)	0.11(2), 0.30(9); 0.46(6)	0.13(5), 0.35(3); 0.09(6)
$Ba_8Ag_4Ge_{42}$	14.9	7.7	77.3	$Ba_8Ag_{4.1}Ge_{41.4}\square_{0.5}$ [a]	1.0814(2)	0.182(8)	0.12(2), 0.30(5); 0.42(6)	0.11(1), 0.30(7); 0.50(6)	0.12(1), 0.35(1); 0.08(6)

$Ba_8Ag_{4.5}Ge_{41.5}$	14.7	8.2	77.1	$Ba_8Ag_{4.4}Ge_{41.3}\square_{0.3}$[b]	1.0829(7)	0.1832(1)	0.1143(9), 0.3033(5); 0.423(3)	0.1195(7), 0.3129(3); 0.569(4)	0.1333(8), 0.3482(4); 0.008(1)
$Ba_8Ag_5Ge_{41}$	14.9	8.9	76.2	$Ba_8Ag_{4.8}Ge_{41.2}$[a]	1.0842(1)	0.182(7)	-	0.116(1), 0.307(4); 1.00(2)	-
$Ba_8Ag_5Ge_{41}$	15.4	9.7	74.9	$Ba_8Ag_5Ge_{41}$[a]	1.0843(3)	0.182(7)	-	0.116(5), 0.307(7); 1.00(1)	-
$Ba_8Ag_{5.3}Ge_{40.7}$	15.2	10.2	74.6	$Ba_8Ag_{5.3}Ge_{40.7}$[a]	1.0841(5)	0.182(1)	-	0.116(2), 0.306(7); 1.00(2)[c]	-

[a] from Rietveld refinement, [b] from XSCD refinement, [c] 0.98(2)Ge + 0.02(2)Ag

In all cases the X-ray spectra ($x \leq 5.3$) were fully indexed on the basis of a cubic clathrate type I lattice with minor amounts of Ge (< 2.2%). Starting from binary $Ba_8Ge_{43}\square_3$ the maximum solubility for Ag at 800°C was found by EPMA to be 5.3 atoms per formula unit (= 9.8 at%) (Figure 6).

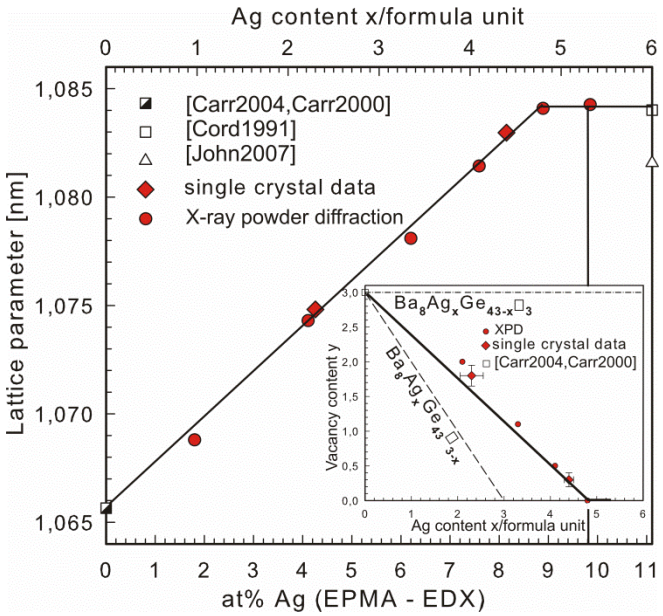

Figure 6: Lattice parameter vs. silver content x for $Ba_8Ag_xGe_{46-x-y}\square_y$ (x = 1, 2, 3, 4, 5) and literature data; the inset shows the decreasing amount of vacancies with increasing silver content received from Rietveld refinement (X-ray powder diffraction) and from single crystal refinement.

The lattice parameters show a linear increase with increasing Ag content up to 4.8 silver atoms per unit cell (a = 1.0840(9) nm). Clathrate samples with higher Ag content show only slightly different lattice parameters which are close to the reported values of Cordier and Woll for a single crystal of stoichiometric $Ba_8Ag_6Ge_{40}$ (melted at 1300°C and cooled

at 100 K/hr, a = 1.0840(1) nm (Cordier G. 1991)). The decreasing content of Ba in the EPMA data (see Table V) in combination with increasing Ag content is related to the amount of vacancies in the crystal lattice of $Ba_8Ag_xGe_{46-x-y}\square_y$. Assuming full occupancies for the Ba sites in the 2a and 6c positions of space group $Pm\bar{3}n$ (standardized setting; see also single crystal refinements in Table VI), the vacancy concentrations calculated from EPMA, correspond well to the amount of vacancies obtained from a Rietveld refinement. These findings are backed up by single crystal data from the two single crystals $Ba_8Ag_xGe_{46-x-y}\square_y$ (x = 2.3 and 4.4; see Table VI).

Table VI: X-ray single crystal data for $Ba_8Ag_xGe_{46-x-y}\square_y$ at RT (Anisotropic displacement parameters in [$10^{-2}nm^2$]).

Parameter/compound	**$Ba_8Ag_{2.5}Ge_{43.5}$[a]**	**$Ba_8Ag_{4.5}Ge_{41.5}$[a]**
Space Group	$Pm\bar{3}n$	$\boldsymbol{Pm\bar{3}n}$
Composition from EPMA	$Ba_8Ag_{2.3}Ge_{41.5}\square_{2.2}$	$Ba_8Ag_{4.4}Ge_{41.6}$
Formula from refinement	$Ba_8Ag_{2.3}Ge_{41.9}\square_{1.8}$	$Ba_8Ag_{4.4}Ge_{41.3}\square_{0..3}$
a [nm]	1.0748(4)	1.0829(7)
μ_{abs} [mm^{-1}]	33.14	32.19
V (nm^3)	1.2414	1.2699
ρ_x (gcm^{-3})	5.87	5.98
Reflections in refinement	451≥4σ(F_o) of 522	435 > 4sig(Fo) of 528
Number of variables	28	28
$R_F^2 = \Sigma\|F_0^2-F_c^2\|/\Sigma F_0^2$	0.0307	0.0316
R_{Int}	0.018	0.018
wR2	0.0423	0.0369
GOF	1.315	1.203
Extinction (Zachariasen)	0.0004(5)	0.0003(7)
Residual density $e^-/Å^3$; max; min	0.81; -0.73	0.90; -0.96
Atom parameters		
Ba1 in 2a(0, 0, 0); occ.	1.00	1.00
$U_{11}= U_{22}=U_{33}$	0.012(8)	0.012(1)
Ba2 in 6c(1/4, 0, 1/2); occ.	1.00	1.00
$U_{11}= U_{22}; U_{33}$	0.033(4); 0.041(2)	0.033(4); 0.044(5)
M in 6d(1/4, 0, 1/2); occ.	0.38Ag + 0.32(3)Ge + 0.30□	0.73Ag + 0.22(1)Ge + 0.05□
$U_{11}= U_{22}; U_{33}$	0.020(4); 0.012(7)	0.021(7); 0.014(0)
Ge2 in 16i(*x*, *x*, *x*); occ.	1.00	1.00
x	0.1834(8)	0.1832(1)
$U_{11}=U_{22}=U_{33}$	0.015(9)	0.013(7)
Ge31 in 24k(0,*y*,*z*); occ.	0.40(1)	0.422(3)

y, *z*	0.113(8), 0.297(2)	0.115(8), 0.303(4)
U_{11}; U_{22}=U_{33}	0.016(8); 0.018(7)	0.016(5); 0.022(0)
Ge32 in 24k(0,*y*,*z*); occ.	0.46(1)	0.569(4)
y, *z*	0.120(5), 0.319(6)	0.117(3), 0.311(2)
U_{11}; U_{22}=U_{33}	0.016(8); 0.018(7)	0.016(5); 0.022(0)
Ge33 in 24k(0,*y*,*z*); occ.	0.14(1)	0.009(1)
y, *z*	0.133(3), 0.348(7)	0.133(0), 0.348(1)
U_{11}; U_{22}=U_{33}	0.016(8); 0.018(7)	0.016(5); 0.022(0)
Interatomic distances [nm]	**Standard deviation ≤0.0004**	**Standard deviation ≤0.0003**
Ba1 – 8Ge2	0.3416	0.3437
–12Ge31	0.3423	0.3517
–12Ge32	0.3671	0.3602
–12Ge33	0.4013	0.4059
Ba2 – 8Ge33	0.3452	0.3508
–8Ge32	0.3557	0.3623
–8Ge31	0.3668	0.3666
– 4M	0.3799	0.3829
–8Ge2	0.3996	0.4029
–4Ge33	0.4081	0.4051
–4Ge31	0.4146	0.4197
–4Ge32	0.4182	0.4199
M – 4Ge33	0.2053	0.2037
–4Ge32	0.2386	0.2499
–4Ge31	0.2623	0.2578
–4Ba2	0.3799	0.3829
–8Ge2	0.3996	0.4028
Ge2– 3Ge31	0.2439	0.2483
–1Ge2	0.2476	0.2505
–3Ge32	0.2547	0.2524
–3Ge33	0.2718	0.2712
–1Ba1	0.3416	0.3437
Ge31– 1Ge32	0.0249	0.0086
–1Ge33	0.0590	0.0545
–1Ge31	0.2466	0.2509
–2Ge2	0.2439	0.2483
–1M	0.2623	0.2598
–1Ge33	0.2713	0.2803
–1Ba1	0.3423	0.3517

	–2Ba2	0.3668	0.3666
Ge33	1Ge32	0.0342	0.0463
	–1Ge31	0.0590	0.0545
	–1M	0.2053	0.2037
	–2Ge2	0.2708	0.2172
	–1Ge31	0.2713	0.2803
	–1Ge32	0.2746	0.2805
	–1Ge33	0.2865	0.3012
	–2Ba2	0.3452	0.3508
	1Ge31	0.0249	0.0086
Ge32–	–1Ge33	0.0342	0.0463
	–1M	0.2386	0.2499
	–2Ge2	0.2527	0.2524
	–1Ge31	0.2591	0.2527
	–1Ge32	0.2694	0.2541
	–1Ge33	0.2746	0.2805
	–2Ba2	0.3528	0.3697
	–1Ba1	0.3557	0.3622

[a]nominal composition

The amount of vacancies shows only a weakly positive deviation from linear decrease with increasing Ag content whereby all vacant sites are filled at an amount of 4.8 atoms of Ag per unit cell (inset Figure 6). In addition to the experimental data, there are two boundary models drawn in Figure 6. Model A assumes substitution of Ge by Ag at a constant level of vacancies according to the compound $Ba_8Ag_xGe_{43-x}\square_3$. The second model eliminates all the vacancies prior to substitution. Because the experimental data are in between these two models, it seems plausible that Ag atoms ($x \leq 4.8$) successively fill vacancies and simultaneously replace Ge atoms. At higher Ag content, when no more vacancies are available, only Ge atoms are substituted by Ag atoms. This behaviour is well reflected in the lattice parameters and is in line with results derived for other clathrates in the systems Ba-Pd-Ge (G. A. Koblyuk-M. N. 2007), Ba-Cd-Ge (B. S. Koblyuk-M. N. 2007), Ba-Cu-Ge (G. A. Koblyuk-M. N. 2009), Ba-Zn-Ge (G. A. Koblyuk-M. N. 2007), Ba-Pt-Ge (R. M. Koblyuk-M. N. 2007).

No extra reflections referring to a larger unit cell with a' = 2a as reported for binary $Ba_8Ge_{43}\square_3$ in refs. ((Carrillo Cabrera W. 2000), (B. S. Carrillo-Cabrera W. 2004)) were

observed in the X-ray spectra for x >1. In all cases Rietveld refinement confirmed that Ba atoms reside in 2a (0, 0, 0) and 6c (¼, 0, ½) sites, Ge atoms are located in 16i (x, x, x) and 24k (0, y, z) sites, whereas Ag, Ge atoms and vacancies are found in the 6d (¼,½,0) site. Because a refinement of occupancies for three species in one site is not reliable, the Ag content was fixed from EPMA measurements. X-ray single crystal data for $Ba_8Ag_xGe_{46-x-y}\square_y$ with x = 2.3 and 4.4 (see Table VI) confirm the overall distribution of atoms on the lattice sites as well as the existence of vacancies (y = 1.8 and 0.3 respectively) in 6d sites. This occurrence of vacancies in the 6d sites infers a disturbance in the neighboring shell of 24k sites of Ge3: the atomic displacement parameters (ADPs) are quite anisotropic and the anisotropy disappears with disappearing 6d defects. A Difference Fourier calculated for the clathrate structure without the 24k Ge atoms (Ge3-atoms, see Figure 7a) reveals clearly a triple-peak structure indicating three positions of the Ge3 atom with slightly different xyz coordinates depending on the existence of a neighbouring 6d-Ge atom, a 6d-Ag atom or a 6d-vacancy.

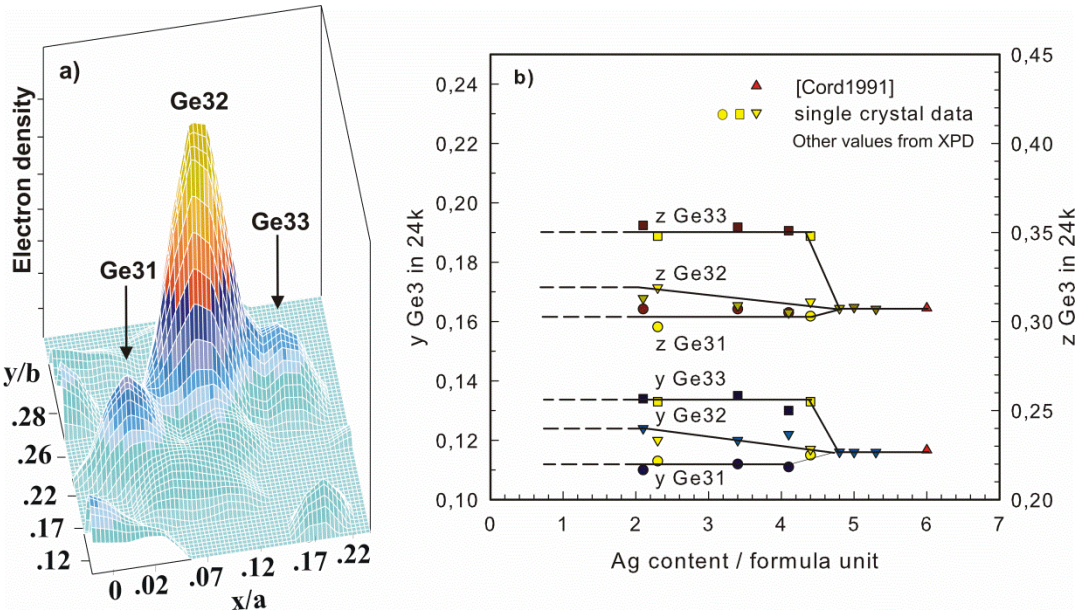

Figure 7: a) Three dimensional view of the contour plot of the electron density (Ge in 24k) from difference Fourier map for $Ba_8Ag_{2.3}Ge_{41.9}\square_{1.8}$; b) Ag content x per formula unit vs. compositional parameters y and z for the Ge3 site (0, y, z) in $Ba_8Ag_xGe_{46-x-y}\square_y$.

The variation of the free parameters y and z for the site 24k (0, y, z) for Ge31, Ge32 and Ge33 with increasing Ag content is shown in Figure 7b. Details of the structure based on x-ray single crystal and Rietveld refinements are given in Table V.

The 6d-site preference of Ag was also reported by Cordier et al. (Cordier G. 1991) as well as by Johnsen et al. (Johnsen S. 2007) for the ideal compound "$Ba_8Ag_6Ge_{40}$". The refinement for the samples with the highest content of Ag (5.3 Ag atoms per formula unit) showed, that a small fraction of Ag atoms is also found at the 24k site, in agreement with the findings of Johnsen et al. (Johnsen S. 2007). In the x-ray powder spectra the increasing content of Ag can be detected from the intensity ratio of the peaks indexed as (222), (320) and (321). This way of filling the vacancies explains the enlargement of the unit cell dimensions until at x = 4.8 all vacancies are filled by Ag. Consequently, also the interatomic distances increase slightly with increasing Ag content. The free parameter x of the 16i (x, x, x) site remains rather constant over the whole solubility range (Table V).
The atomic displacement parameters (ADPs) for both samples (namely $Ba_8Ag_xGe_{46-x-y}\square_y$ with x = 2.3 and 4.4) are consistent with features as usually observed for clathrates of type-I: Ba2-atoms in 6c sites give cause to a large anisotropy of electron densities, whereas Ba1-atoms in 2a sites behave like one of the framework atoms (see Table VI). Least square fits of the ADPs as a function of temperature (Figure 8) with the Einstein model of Eq.(1) for Ba2 and with the Debye model of Eq.(2) for the framework atoms

$$U_{ii} = \frac{\hbar^2}{2mk_B\Theta_{E,ii}} \coth\frac{\Theta_{E,ii}}{2T} + d^2 \qquad (1)$$

$$U_{iso} = \frac{3\hbar^2 T}{mk_B\Theta_D^2}\left[\frac{T}{\Theta_D}\int_0^{\Theta_D/T}\frac{x}{e^x-1}dx + \frac{\Theta_D}{4T}\right] + d^2 \qquad (2)$$

result in $\Theta_{E,11}$ = 88 K, $\Theta_{E,22}$ = 67 K and Θ_D = 269 K (x_{Ag} = 2.3) and $\Theta_{E,11}$ = 88 K, $\Theta_{E,22}$ = 68 K and Θ_D = 261 K (x_{Ag} = 4.4). Note that $\Theta_{E,\,ii}$ (ii is i.e. the direction or plane of the vibration).

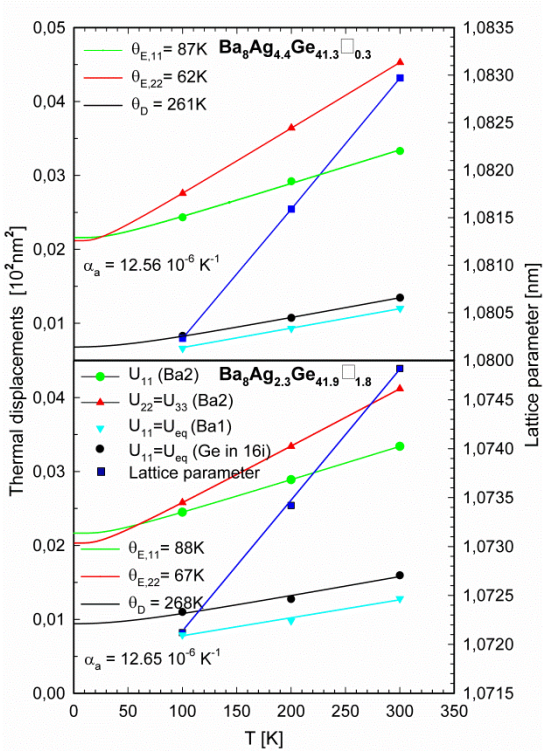

Figure 8: Temperature dependency of atom displacement and lattice parameters of $Ba_8Ag_{2.3}Ge_{41.9}\square_{1.8}$ and $Ba_8Ag_{4.4}Ge_{41.3}\square_{0.3}$.

The linear thermal expansion coefficient is defined as

$$\alpha_a = \frac{1}{a_{300K}}\left(\frac{\partial a_T}{\partial T}\right)_p \qquad (3)$$

in which a_{300K} is the lattice parameter at 300 K and a_T is the lattice parameter at temperature T. The present study yields values of $\alpha_a = 12.65 \cdot 10^{-6}$ K^{-1} ($x_{Ag} = 2.3$) and $\alpha_a = 12.56 \cdot 10^{-6}$ K^{-1} ($x_{Ag} = 4.4$) in very good agreement with a recent compilation of clathrate type I thermal expansion data (R. G. Falmbigl M. 2010).

5.2.1.3 Phase relations at 800°C and at 600°C

The combined data as obtained from XPD, SEM (Fig.4) and EPMA (see Table VII) are the basis for the phase triangulation in the isothermal sections at 800°C (Figure 10) and 600°C (Figure 11).

Table VII: Phase equilibria and composition from EPMA, X-ray phase analysis and lattice parameter for alloys Ba-Ag-Ge annealed at 800°C and annealed at 600°C; a, b, c, d, e, f refer to EPMA images shown in Figure 9.

Nominal composition (at%)			X-ray phase analysis	Structure type	Lattice parameter (nm)			Composition EDX (at%)		
Ag	Ba	Ge			a	b	c	Ag	Ba	Ge
800°C										
1.85	14.81	83.34	κI	K_4Ge_{23-x}	1.0688(2)	1.0688(2)	1.0688(2)	1.8	15.2	83.0
	a)		κIX	Ba_6Ge_{25}	-	-	-	1.0	18.7	80.3
7.41	14.81	77.78	κI	K_4Ge_{23-x}	1.0819(4)	1.0819(4)	1.0819(4)	7.4	14.1	78.5
			$BaGe_2$	$BaSi_2$	-	-	-	-	-	-
			κIX	Ba_6Ge_{25}	-	-	-	1.5	18.3	80.2
11.12	14.81	74.07	κI	K_4Ge_{23-x}	1.0844(6)	1.0844(6)	1.0844(6)	9.8	14.6	75.6
			τ_2	$ThCr_2Si_2$	-	-	-	30.7	19.3	80.2
23.53	5.88	70.59	κI	K_4Ge_{23-x}	1.0842(6)	1.0842(6)	1.0842(6)	9.7	14.5	76.8
			(Ge)	C_{diam}	0.5659(7)	0.5659(7)	0.5659(7)	0.1	0.4	99.5
	b)		Liquid	-	-	-	-	83.7	0.7	15.6
16.16	33.33	50.51	τ_1	AlB_2	0.4425(3)	0.4425(3)	0.4880(1)	15.2	32.5	52.3
			τ_2	$ThCr_2Si_2$	-	-	-	29.4	23.8	46.8
			$BaGe_2$	$BaSi_2$	-	-	-	-	-	-
36	24	40	τ_1	AlB_2	0.4427(1)	0.4427(1)	0.4882(8)	18.8	29.6	51.6
			τ_2	$ThCr_2Si_2$	0.4610(7)	0.4610(7)	1.069(8)	34.2	20.1	45.7
	c)		(Ag)	Cu	-	-	-	0.2	0.3	99.5
25	33	42	τ_1	AlB_2	0.4485(1)	0.4485(1)	0.4814(3)	21.8	33.0	45.2
			Liquid	-	-	-	-	81.2	16.6	2.2
49.54	10.34	40.12	κI	K_4Ge_{23-x}	1.0842(4)	1.0842(4)	1.0842(4)	9.7	14.7	75.6
			τ_2	$ThCr_2Si_2$	0.4628(5)	0.4628(5)	1.064(6)	30.0	20.0	50.0
	d)		Liquid	-	-	-	-	87.6	0.7	11.7
74.8	15.5	9.7	τ_1	AlB_2	0.4438(6)	0.4438(6)	0.4868(8)	17.2	33.1	49.7
			Liquid	-	-	-	-	82.1	14.8	3.1
			(Ag)	Cu	0.4086(7)	0.4086(7)	0.4086(7)	96.4	3.1	0.5
600°C										
1.85	14.81	83.34	κI	K_4Ge_{23-x}	1.0805(3)	1.0805(3)	1.0805(3)	6.6	15.4	78.0
			κIX	Ba_6Ge_{25}	1.4560(1)	1.4560(1)	1.4560(1)	1.6	18.9	79.5
			(Ge)	C_{diam}	0.5654(6)	0.5654(6)	0.5654(6)	0.2	0.3	99.5
7.41	14.81	77.78	κI	K_4Ge_{23-x}	1.0819(2)	1.0819(2)	1.0819(2)	7.4	14.1	78.5
			$BaGe_2$	$BaSi_2$	-	-	-	0.5	30.7	68.8
	e)		κIX	Ba_6Ge_{25}	-	-	-	1.5	18.3	80.2
16.16	33.33	50.51	τ_1	AlB_2	0.4425(3)	0.4425(3)	0.4880(1)	15.2	32.5	52.3
			τ_2	$ThCr_2Si_2$	-	-	-	29.4	23.8	46.8
			$BaGe_2$	$BaSi_2$	-	-	-	-	-	-
14.82	14.82	70.37	κI	K_4Ge_{23-x}	1.0844(5)	1.0844(5)	1.0844(5)	9.7	14.8	75.5
			τ_2	$ThCr_2Si_2$	-	-	-	29.4	18.9	51.7
25	33	42	τ_1	AlB_2	0.4488(8)	0.4488(8)	0.4808(8)	22.7	32.4	44.9

			$Ba(AgGe)_5$	$CaCu_5$	0.5819(0)	0.5819(0)	0.4599(5)	79.5	16.5	4.0
29.75	13.67	56.58	κI	K_4Ge_{23-x}	1.0840(3)	1.0840(3)	1.0840(3)	8.6	15.2	76.1
			τ_2	$ThCr_2Si_2$	0.4614(0)	0.4614(0)	1.068(0)	29.4	20.8	49.8
			(Ag)	Cu	-	-	-	93.6	0.2	6.2
36	24	40	τ_1	AlB_2	0.4427(2)	0.4427(2)	0.4882(3)	18.2	32.7	49.1
			τ_2	$ThCr_2Si_2$	0.4605(5)	0.4605(5)	1.0711(6)	32.0	21.1	46.9
			(Ag)	Cu	0.4089(1)	0.4089(1)	0.4089(1)	95.6	0.0	4.4
23.53	5.88	70.59	κI	K_4Ge_{23-x}	1.0842(2)	1.0842(2)	1.0842(2)	9.7	41.1	76.2
	f)		(Ge)	C_{diam}	0.5659(7)	0.5659(7)	0.5659(7)	0.3	0.4	99.3
			(Ag)	Cu	-	-	-	88.6	0.3	1.1

κI: clathrate type-I; κIX: clathrate type-XI; τ_1: $BaAg_xGe_{1-x}$; τ_2: $BaAg_{2-x}Ge_{2+x}$

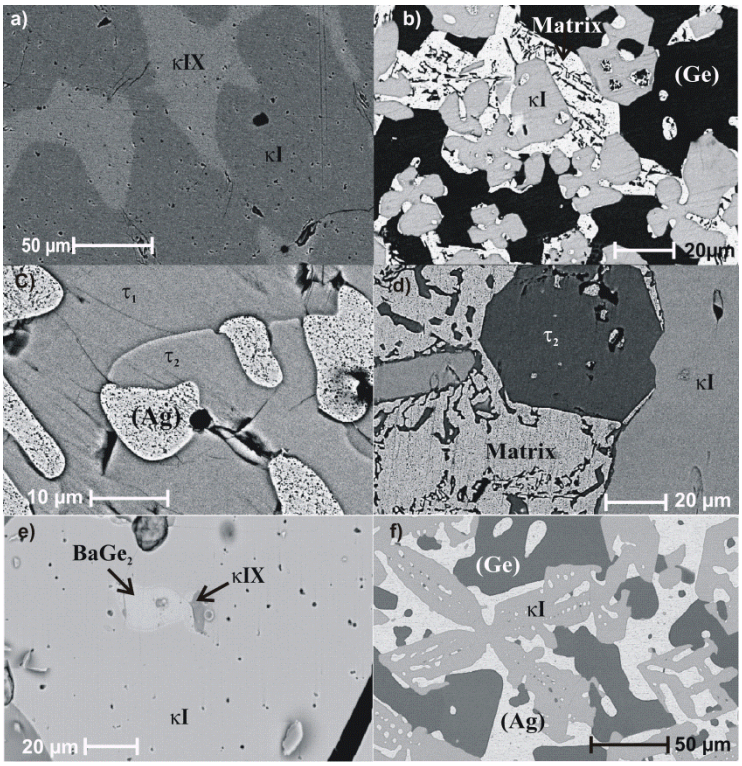

Figure 9: Microstructures of several Ba – Ag – Ge alloys annealed at 800°C: a), b), c), d) and annealed at 600°C: e), f). Nominal composition, atomic percent from EPMA and X-ray phase analysis are given in Table IV.

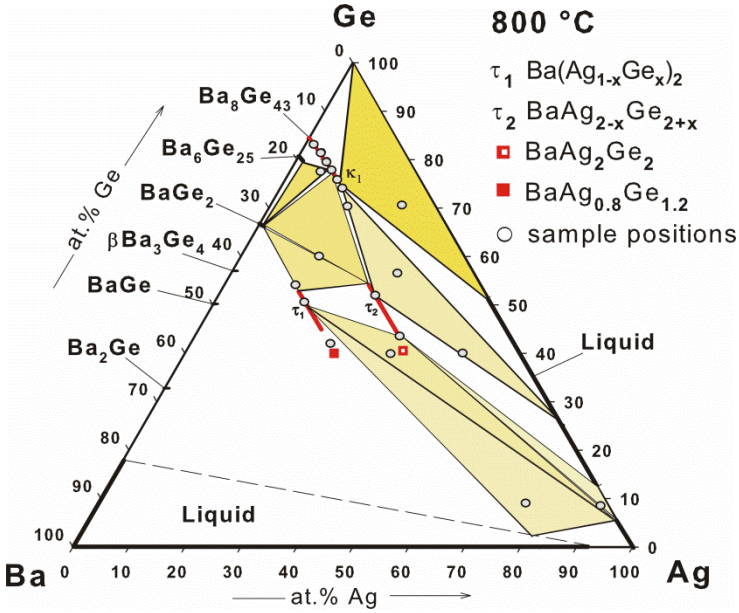

Figure 10: Partial isothermal section at 800°C for the ternary system Ba-Ag-Ge.

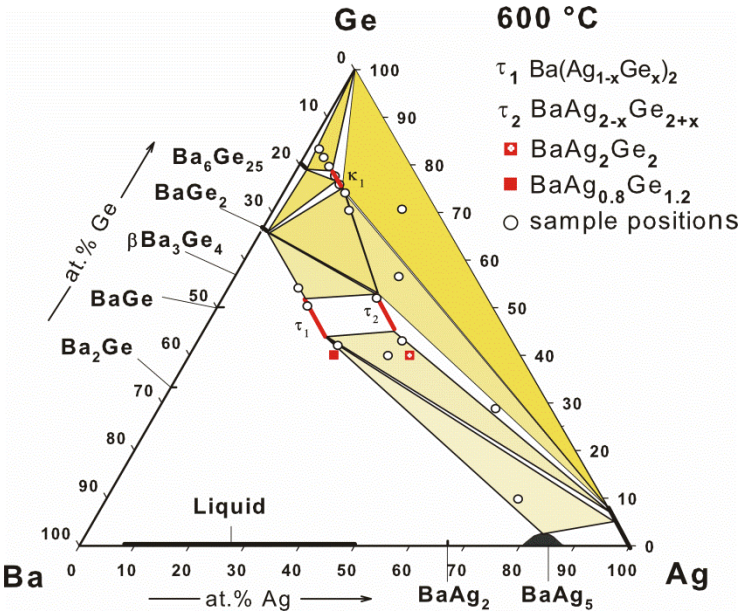

Figure 11: Partial isothermal section at 600°C for the ternary system Ba-Ag-Ge.

At 800°C the type-I clathrate is in equilibrium with the clathrate type-IX (Ba_6Ge_{25} type), which contains a maximum amount of 1.5 at% Ag and has a lattice parameter of a = 1.4561(7) nm. Alloys containing the moisture sensitive compound $BaGe_2$ ($BaSi_2$ type), quickly decompose on air. At the solubility limit of silver (x_{Ag} = 5.3), the clathrate I phase forms a two-phase equilibrium with $BaAg_{2-x}Ge_{2+x}$ ($ThCr_2Si_2$ type). At 800°C the EPMA data indicate a quite large homogeneity region of about 10 at% ranging from $BaAg_{1.3}Ge_{2.7}$ (x = 0.7, a = 0.4652(9), c = 1.0606(2) nm) to $BaAg_{1.8}Ge_{2.2}$ (x = 0.2, a = 0.4610(7), c =

1.0697(9) nm). The homogeneity region does not include the stoichiometric composition for full atomic ordering in contrast to an earlier report by Eisenmann et al. (M. N. Eisenmann B. 1970) on the existence of $BaAg_2Ge_2$, for which single crystals were obtained from alloys reacted at 1250°C (no further details were given). The Rietveld refinement data for a sample in the Ge-rich part of the homogeneity region of $BaAg_{2-x}Ge_{2+x}$ are collected in Figure 12.

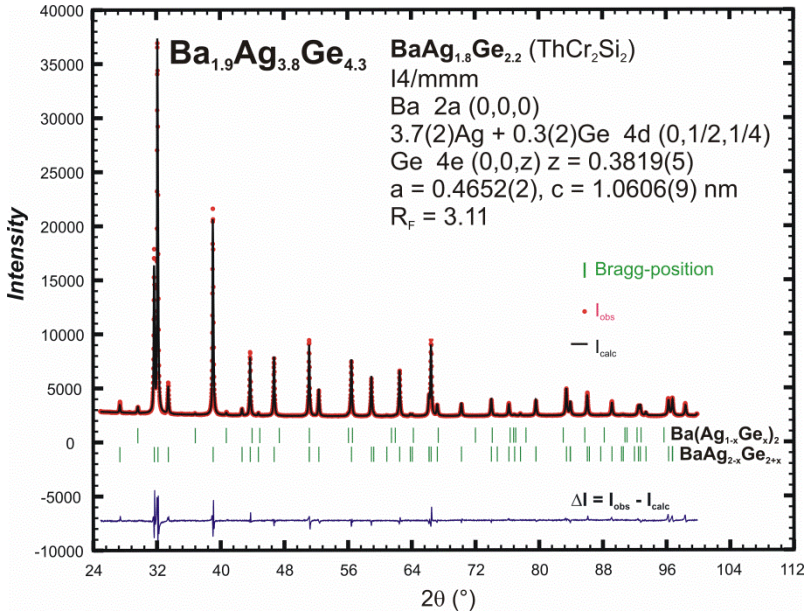

Figure 12: Rietveld refinement for $BaAg_{2-x}Ge_{2+x}$ (x = 0.2, $ThCr_2Si_2$ type).

They confirm the $ThCr_2Si_2$ structure type with a random substitution of Ag atoms for Ge atoms at the 4d site of space group *I4/mmm* (z_{4e} = 0.3819(5)). The second phase in the refinement is $Ba(Ag_{1-x}Ge_x)_2$ with the AlB_2 type structure. Merlo et al. (P. M. Merlo F. 1996) indicated a solid solubility range for $Ba(Ag_{1-x}Ge_x)_2$ at 550°C, however, no details on the extension of the single phase region were presented. At 800°C we observe only a quite small homogeneity region extending from $BaAg_{0.5}Ge_{1.5}$ (x = 0.75; a = 0.4427(1), c = 0.4882(8) nm) to $BaAg_{0.7}Ge_{1.3}$ (x = 0.65; a = 0.4485(1), c = 0.4814(3) nm). The Rietveld refinement for a sample containing $Ba(Ag_{1-x}Ge_x)_2$ as the main phase is shown in Figure 13 containing $BaGe_2$ and $BaAg_{2-x}Ge_{2+x}$ (<10%) as minor secondary phases. Because the binary Ba_8Ge_{43} phase only exists between 770 and 810°C (B. S. Carrillo-Cabrera W. 2004), the partial isothermal section at 600°C was investigated to define the stability range of the clathrate I phase of $Ba_8Ag_xGe_{46-x}$ (Figure 11), which at 600°C is rather limited and extends from about ~6.6 to ~9.8 at% Ag ($3.4 \leq x \leq 5.3$). The results of EPMA measurements and X-ray phase analysis are summarized in Table VII. The solubility

range for the $BaAg_{2-x}Ge_{2+x}$ and $Ba(Ag_{1-x}Ge_x)_2$ phase is only slightly smaller than at 800°C (from 1.45 to 1.7 Ag atoms per unit cell for $BaAg_{2-x}Ge_{2+x}$; $0.55 \leq x \leq 0.3$). The compound $BaAg_5$ solves about 4 at% germanium at 600°C.

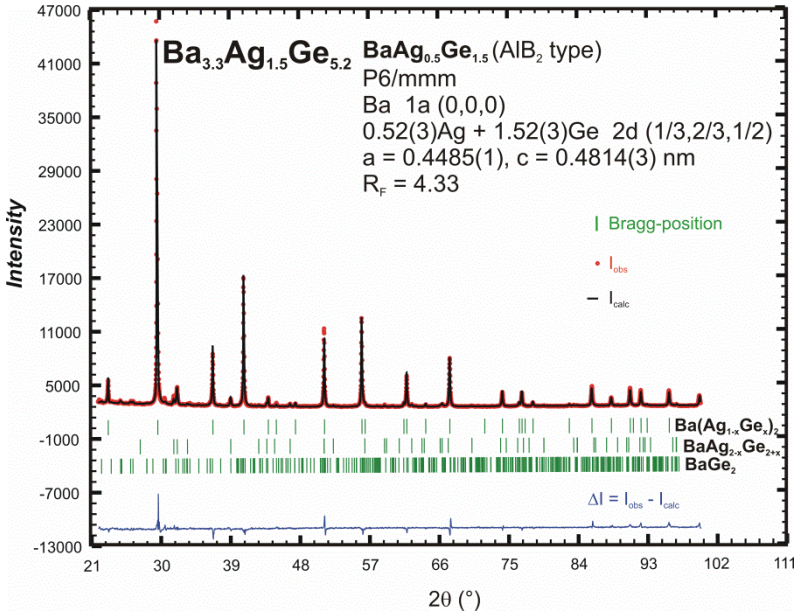

Figure 13: Rietveld refinement for $Ba(Ag_{1-x}Ge_x)_2$ (AlB_2 structure type, x = 0.75).

5.2.1.4 Liquidus and solidus projection and invariant reactions

The liquidus surface, derived for the germanium and silver rich part of the Ag-Ba-Ge system (see Figure 14), is based on the microstructures of about 30 samples, which were analyzed in their as cast state as well as after slow cooling in the DSC.

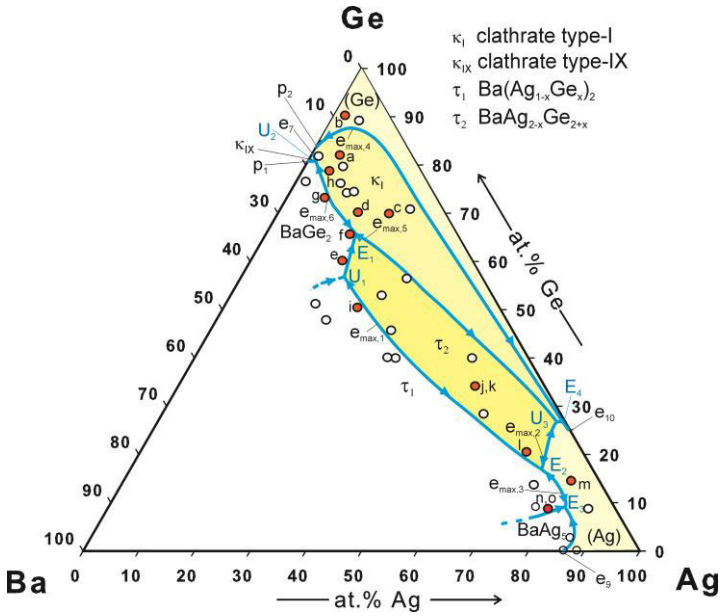

Figure 14: **Partial liquidus projection of the Ag-Ba-Ge system; the microstructures of the alloys marked in red (filled circles) and labeled as (a) to (o) are shown in Figure 15.**

The microstructures of the alloys marked in red and denoted with a, b, c etc. in Figure 14 are presented in Figure 15. Alloys annealed at 800°C (600°C, depending on the part of the isothermal section) were used to define the phase equilibria at sub-solidus temperature (Figure 16) and the corresponding solidus temperatures have been determined with DSC. The crystallographic data for all the binary and ternary solid phases are summarized in Table IV. The primary crystallization field of the clathrate type-I $Ba_8Ge_{43}\square_3$ in the binary Ba-Ge system is very limited (~ 1 at.%) and the phase exists only in a small temperature range between 808 and 770°C (B. S. Carrillo-Cabrera W. 2004). As a consequence of the strong stabilization by Ag of the clathrate type-I solid solution $Ba_8Ag_xGe_{46-x-y}\square_y$ (κ_I) in the ternary system, the primary crystallization field of κ_I enlarges considerably and extends up to the ternary eutectic E_4 (66.6 at.% Ag, 0.5 at.% Ba, 32.9 at.% Ge) close to the binary Ag-Ge system (see Figure 14). The melting temperature of the clathrate increases from 808°C in the binary system to 873°C in the ternary for $Ba_8Ag_5Ge_{41}$. The ternary clathrate type-I melts congruently and forms quasi-binary eutectics with (Ge), $BaGe_2$ and τ_2 ($BaAg_{2-x}Ge_{2+x}$).

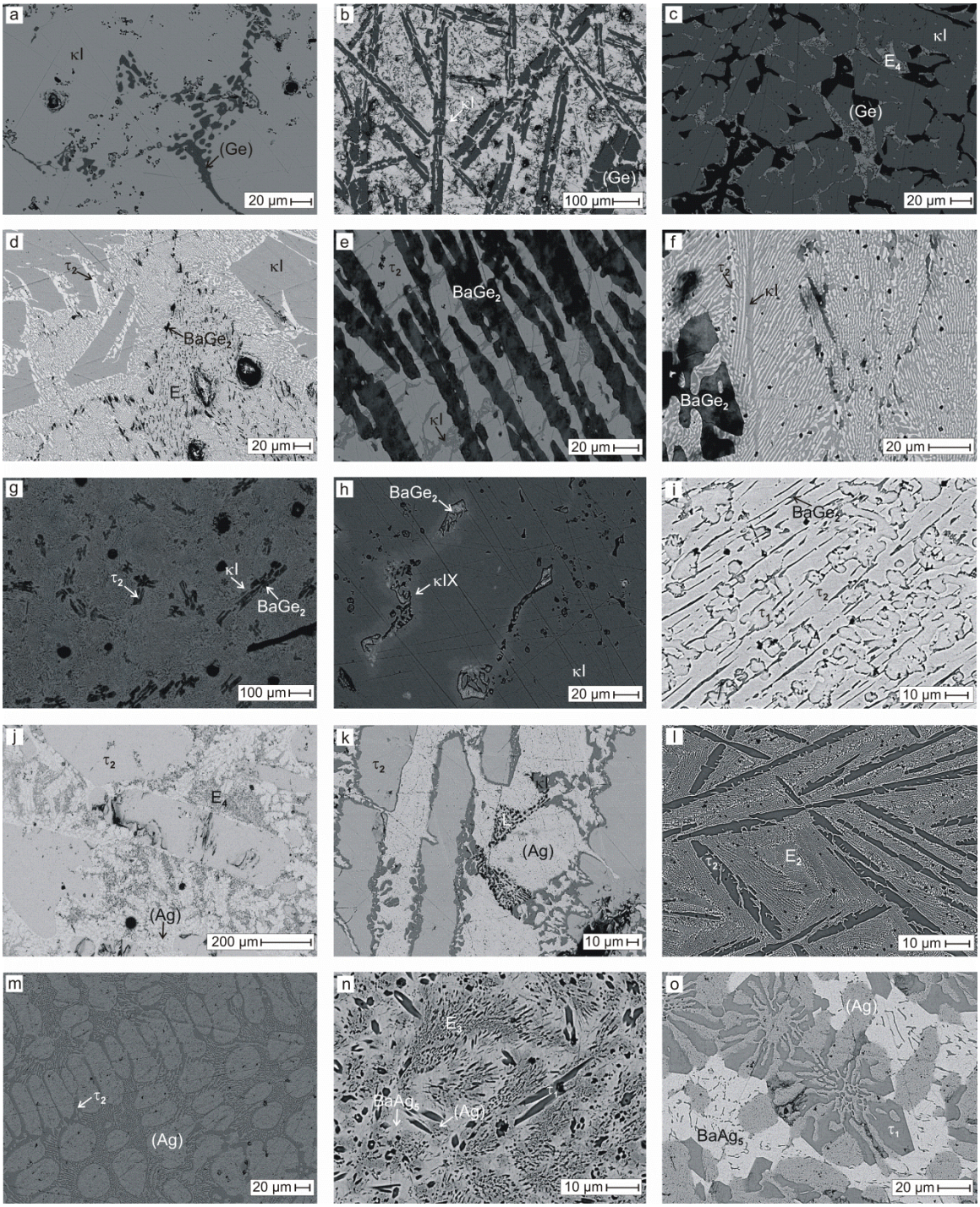

Figure 15: Microstructures of several Ag-Ba-Ge alloys in as cast and annealed state and after DSC measurements. The sample positions can be seen in Table VII (marked in red and labeled as (a) to (o)); κ_I…clathrate type-I; κ_{IX}…clathrate type-IX; τ_1…$Ba(Ag_{1-x}Ge_x)_2$, τ_2…$BaAg_{2-x}Ge_{2+x}$.

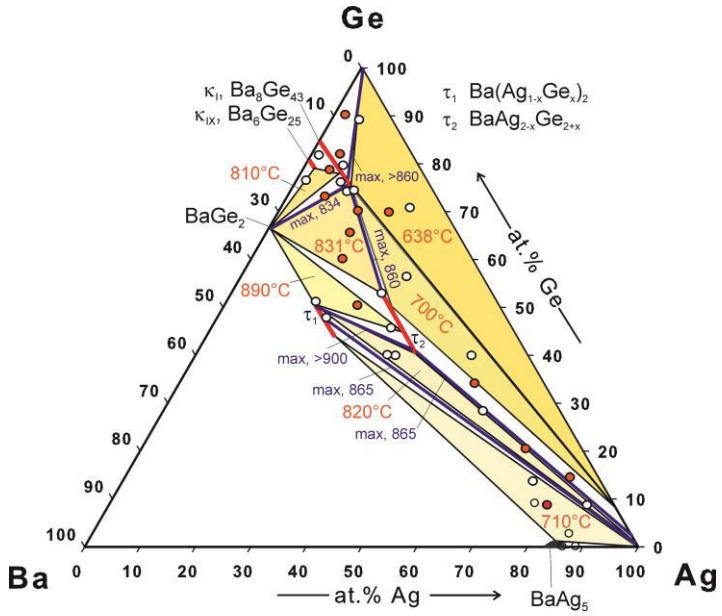

Figure 16: Solidus surface of the partial Ag-Ba-Ge system up to 33.33 at.% Ba and tie lines of the quasi binary sections; all temperatures are in °C.

Alloy $Ba_{13.7}Ag_{5.6}Ge_{80.7}$ is an almost single-phase clathrate with small amounts of (Ge), which formed during the monovariant reaction L ↔ κ_I + (Ge) (microstructure after the DSC measurement, Figure 15a). The microstructure of the sample $Ba_8Ag_2Ge_{90}$ in as cast state (Figure 15b) shows primary crystallization of (Ge) followed by crystallization of (Ge) and κ_I during the same monovariant reaction. Alloy $Ba_{10}Ag_{20}Ge_{70}$ (as cast) contains large grains of κ_I and (Ge) and liquid, which finally crystallizes in form of the ternary eutectic E_4: L ↔ κ_I + (Ge) + (Ag) (Figure 15c) at 633°C. In the as cast alloy with composition $Ba_{14.8}Ag_{14.8}Ge_{70.4}$, large primary grains of κ_I are present and a mixture of 2 eutectics (see Figure 15d). First we observe the crystallization of the liquid along the monovariant line L ↔ κ_I + τ_2 and then the formation of $BaGe_2$ through the invariant reaction E_1 (L ↔ κ_I + τ_2 + $BaGe_2$) at 831°C. The as-cast alloy $Ba_{23}Ag_{17}Ge_{60}$ is very close to the line of joint crystallization of $BaGe_2$ and τ_2 (Figure 15e) and contains also small quantities of κ_I. The microstructure of the as-cast alloy $Ba_{20}Ag_{15}Ge_{65}$, (Figure 15f) from the same three-phase region but with slightly higher Ge content, represents the primary crystallization of $BaGe_2$ followed by the crystallization of liquid along the monovariant line L ↔ κ_I + τ_2 and the formation of smaller grains of $BaGe_2$ in the invariant eutectic E_1 (κ_I + τ_2 + $BaGe_2$) with composition $Ba_{18.2}Ag_{16.7}Ge_{65.1}$. The sample with composition $Ba_{20}Ag_7Ge_{73}$ is very close to the monovariant line L ↔ $BaGe_2$ + κ_I (Figure 15g), which contains a maximum $e_{max,6}$. Figure 15g also shows the formation of very fine grains of τ_2

at the invariant point E_1. However, alloy $Ba_{16}Ag_5Ge_{79}$ (Figure 15h, after DSC measurement), which is located on the other side of the quasi-binary section $BaGe_2 + \kappa_I$, shows primary grains of κ_I followed by the peritectic formation of clathrate type-IX (κ_{IX}) and finally the crystallization of $BaGe_2$. Such crystallization behaviour and a solidus temperature of 810°C indicate an invariant reaction U_2: $L + BaGe_2 \leftrightarrow \kappa_{IX} + \kappa_I$.

The ternary phases τ_1- $Ba(Ag_{1-x}Ge_x)_2$ and τ_2 form also congruently from the melt. Thus the alloy $Ba_{15}Ag_{24}Ge_{51}$ is very close to the line of joint crystallization of τ_1 and τ_2 (Figure 15i) and $BaGe_2$ crystallizes from the last portion of liquid. These three phases coexist in the invariant transition equilibrium U_1: $L + \tau_1 \leftrightarrow \tau_2 + BaGe_2$ at 887°C. The phase τ_2 like κ_I exhibits a huge primary crystallization field, which extends up to 78 at % Ag. The microstructure of the alloy $Ba_{13}Ag_{53}Ge_{34}$ (Figure 15j) annealed at 800°C shows large primary grains of τ_2, which were grown in equilibrium with a liquid with composition $Ba_{1.3}Ag_{71.7}Ge_{27.0}$. After slow DSC cooling (5 K/min), the alloy contains large amount of κ_I (see Figure 15k), which formed around τ_2 during the transition reaction U_3: $L + \tau_2 \leftrightarrow \kappa_I$ + (Ag) at 700°C. Both invariant equilibria E_4 and U_3 are located close to the binary eutectic $L \leftrightarrow$ (Ag) + (Ge). However, samples with higher Ba content result in the crystallization of a eutectic structure E_2: $L \leftrightarrow \tau_1 + \tau_2$ + (Ag) at 820°C with composition $Ba_{8.8}Ag_{73.4}Ge_{17.8}$. Thus, primary grains of τ_2 together with large amounts of a fine eutectic structure (E_2) can be seen from the microstructure of the alloy $Ba_9Ag_{69}Ge_{22}$ in Figure 15. The homogeneity region of τ_2 includes stoichiometric $BaAg_2Ge_2$, which has been reported by Eisenmann (M. N. Eisenmann B. 1970) to exist at high temperatures. Due to the very fine eutectic structure, it was not possible to measure the composition of the eutectic constituents, but the presence of τ_1, τ_2 and (Ag) has been confirmed via Rietveld refinement of the XPD pattern. The composition of a quasi-binary eutectic $e_{max,2}$ has been well defined from the as-cast alloy $Ba_5Ag_{80}Ge_{15}$, which contains primary grains of (Ag), followed by the crystallization with τ_2 during the monovariant reaction $L \rightarrow$ (Ag) + τ_2 (Figure 15m) and the formation of fine grains of τ_1 in the ternary eutectic E_2. The presence of τ_1 has been confirmed by XPD. Another quasi-binary section with a maximum point $e_{max,3}$ is formed by τ_1 and (Ag) and therefore the crystallization of alloys with higher Ba content finishes in the invariant eutectic E_3. The alloy $Ba_{12}Ag_{79}Ge_9$ (Figure 15n) is close to the line of joint crystallization of τ_1 and $BaAg_5$. The microstructure also shows a fine eutectic structure E_3: $L \leftrightarrow \tau_1 + BaAg_5$ + (Ag). However,

after the DSC experiment, the microstructure of the same alloy changed completely as can be seen in Figure 15o. Large grains of τ_1 and (Ag) are present together with large areas of $BaAg_5$.

From the microstructures and DSC measurements, the Schulz-Scheil reaction scheme shown in Figure 17 has been constructed.

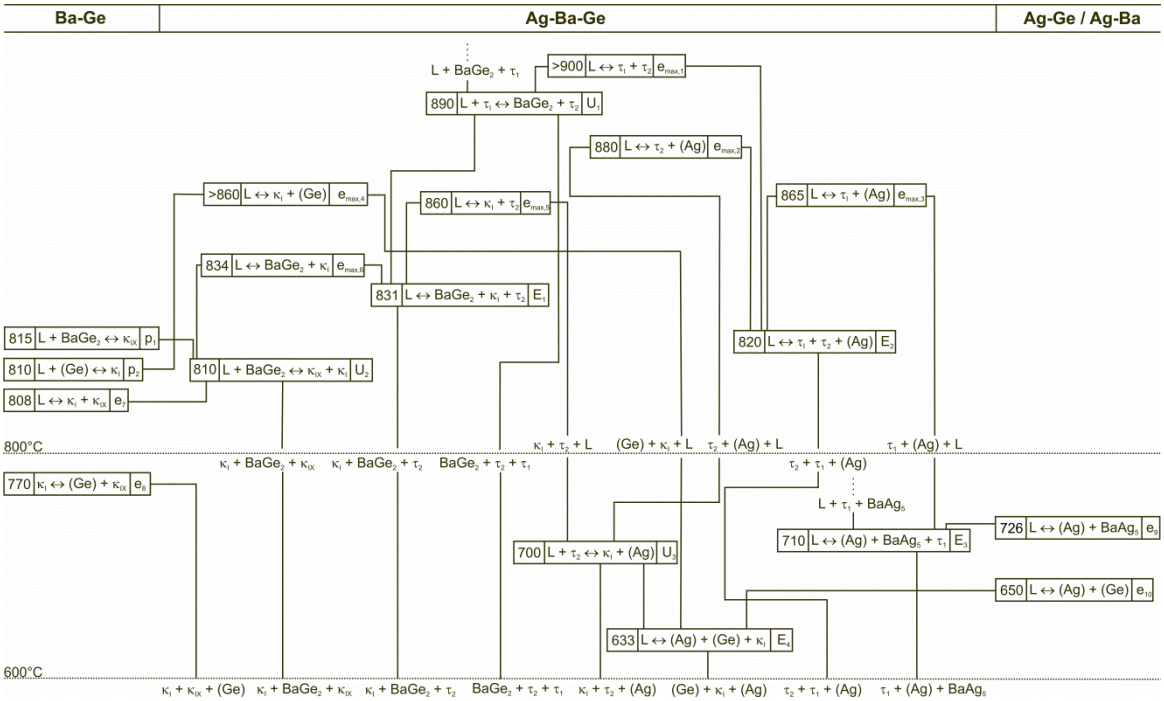

Figure 17: Schultz-Scheil diagram of the ternary Ag-Ba-Ge system investigated up to 33.33 at.% Ba, all temperatures are given in °C.

Four invariant eutectic reactions (Class I reaction, see Figure 17 and Table VIII), 6 quasi-binary eutectics and 3 transition reactions (Class II reaction) are present in the investigated part of the ternary phase diagram.

Table VIII: Monovariant and invariant equilibria.

Reaction	Reaction type	T, °C	Phase	Composition in at.%		
				Ag	Ba	Ge
$L \leftrightarrow \tau_1 + \tau_2$	$e_{max,1}$	> 900	L	-	-	-
			τ_1	-	-	-
			τ_2	-	-	-
$L + \tau_1 \leftrightarrow BaGe_2 + \tau_2$	U_1	890	L	-	-	-
			$BaGe_2$	-	-	-
			τ_1	14.6	33.0	52.4
			τ_2	32.7	19.7	47.6

$L \leftrightarrow \tau_2 + (Ag)$	$e_{max,2}$	880	L	73.8	8.2	18.0
			τ_2	38.2	20.0	41.8
			(Ag)	98.5	-	1.5
$L \leftrightarrow \tau_1 + (Ag)$	$e_{max,3}$	865	L	77.8	8.5	13.7
			τ_1	21.8	33.7	44.5
			(Ag)	98.9	-	1.1
$L \leftrightarrow \kappa_I + (Ge)$	$e_{max,4}$	> 860	L	-	-	-
			κ_I	5.4	14.9	79.7
			(Ge)	-	-	100.0
$L \leftrightarrow \kappa_I + \tau_2$	$e_{max,5}$	860	L	17.7	17.0	65.3
			κ_I	10.2	14.9	74.8
			τ_2	26.1	20.2	53.7
$L \leftrightarrow \kappa_I + BaGe_2$	$e_{max,6}$	834	L	7.1	19.4	73.5
			κ_I	9.7	14.9	75.4
			$BaGe_2$	-	32.5	67.5
$L \leftrightarrow BaGe_2 + \kappa_I + \tau_2$	E_1	831	L	16.7	18.2	65.1
			$BaGe_2$	-	32.0	68.0
			κ_I	10.3	14.9	74.8
			τ_2	28.2	20.0	51.8
$L \leftrightarrow \tau_1 + \tau_2 + (Ag)$	E_2	820	L	73.4	8.8	17.8
			τ_1	-	-	-
			τ_2	40.0	40.1	19.9
			(Ag)	-	-	-
$L + BaGe_2 \leftrightarrow \kappa_I + \kappa_{IX}$	U_2	810	L	-	-	-
			$BaGe_2$	-	32.3	67.7
			κ_I	6.4	15.0	78.6
			κ_{IX}	1.4	19.2	79.4
$L \leftrightarrow (Ag) + BaAg_5 + \tau_1$	E_3	710	L	81.9	8.5	9.6
			(Ag)	99.0	-	1.0
			$BaAg_5$	85.6	12.7	1.7
			τ_1	21.8	33.7	44.5
$L + \tau_2 \leftrightarrow \kappa_I + (Ag)$	U_3	700	L	60.0	-	40.0
			τ_2	33.5	19.5	47.0
			κ_I	10.5	15.0	74.5
			(Ag)	92.3	-	7.7
$L \leftrightarrow (Ag) + (Ge) + \kappa_I$	E_4	633	L	66.6	0.5	32.9
			(Ag)	95.5	-	5.5
			(Ge)	-	-	100
			κ_I	9.8	14.9	75.3

5.2.1.5 Melting points of clathrate type-I compounds

Table IX combines the melting points for the ternary clathrates of type-I measured during this work and literature data: $A_8T_xM_{46-x}$ (A = Sr, Ba, Eu; T = Ni, Pd, Pt, Cu, Ag, Au, Zn, Cd, B, Al, Ga, In; M = Si, Ge, Sn), quaternary compounds and several inverse clathrate type-I.

Table IX: Melting points of several ternary $A_8T_xM_{46-x}$ and quaternary (A = Sr, Ba, Eu; T = Ni, Pd, Pt, Cu, Ag, Au, Zn, Cd, B, Al, Ga,; M = Si, Ge, Sn) clathrates type-I compounds and decomposition temperatures of the inverse clathrate type-I $Ge_{38}\{P,As,Sb\}_8\{Cl,Br,I\}_8$, $Si_{46-x}P_xTe_y$ and tin based compounds.

Compound	Lattice parameter (nm)	Ref.	Melting point (°C)	Ref.
$Ba_8Al_{16}Ge_{30}$	1.08533(1)	-	958	(Christensen M. 2010)
	1.0835(1)	-	971±5	(S.H. Eisenmann B. 1986)
$Ba_8Al_{16}Si_{30}$	1.05772(2)	-	1190	(Christensen M. 2010)
	1.0607(3)	-	1084±5	(S.H. Eisenmann B. 1986)
$Ba_8Al_{14}Si_{31}$	1.0625(10)	-	1143	(M. J. Condron C.L. 2006)
$Ba_8Al_{12}Si_{34}$	1.05656	-	1150	(Tsujii N. 2011)
$Ba_8Al_{14}Si_{32}$	1.059840(14)	(Tsujii N. 2011)	1135	(K. S. Condron C.L. 2008)
$Ba_8Al_{15}Si_{31}$	1.063220(9)	-	1132.6	(Tsujii N. 2011)
$Ba_8B_{0.17}Al_{14.3}Si_{31.4}$	1.06248(4)	-	~1145	(K. S. Condron C.L. 2007)
$Ba_8B_{0.32}Al_{14.2}Si_{30.5}$	1.06140(4)	-	~1151	(K. S. Condron C.L. 2007)
$Ba_{7.3}Sr_{0.7}Al_{14}Si_{31}$	1.05962(12)	-	1140	(K. S. Condron C.L. 2007)
$Ba_{7.7}Eu_{0.3}Al_{14}Si_{31}$	1.06306(12)	-	1142	(K. S. Condron C.L. 2007)
$Ba_7EuAl_{13}Si_{33}$	1.06143(4)	-	~1300	(K. S. Condron C.L. 2006)
$Sr_8Ga_{16}Ge_{30}$	1.0719(5)	-	774±5	(Kuznetsov V.L. 2000)
	1.0734(1)	-	764±5	(S. H. Eisenmann B. 1986)
	-	-	777	(Cai K.F. 2007)
	1.072	-	770±5	(Sales B.C. 2001)
$Sr_8Ga_{16}Si_{30}$	1.0459(4)	-	1038±5	(S. H. Eisenmann B. 1986)
$Ba_8Ga_{16}Ge_{30}$	1.08030(3)	-	967	(Christensen M. 2010)
	1.0739(6)	-	974±5	(Kuznetsov V.L. 2000)
	1.07668(8)	-	957±5	(S. H. Eisenmann B. 1986)
	-	-	982	(Cai K.F. 2007)
	1.078	-	963±5	(Sales B.C. 2001)
$Ba_{8.06}Ga_{15.59}Si_{4.54}Ge_{25.71}$	1.0750	-	963	(Martin J. 2007)
$Ba_{8.05}Ga_{15.78}Si_{5.05}Ge_{25.11}$	1.0744	-	968	(Martin J. 2007)
$Ba_{8.07}Ga_{15.66}Si_{7.47}Ge_{22.80}$	1.0726	-	985	(Martin J. 2007)

$Ba_{8.06}Ga_{15.74}Si_{9.05}Ge_{21.16}$	1.0715	-	997	(Martin J. 2007)
$Ba_{8.08}Ga_{15.76}Si_{10.72}Ge_{19.44}$	1.0705	-	1005	(Martin J. 2007)
$Ba_{8.10}Ga_{15.84}Si_{13.38}Ge_{16.68}$	1.0687	-	1016	(Martin J. 2007)
$Ba_8Ga_{16}Si_{30}$	1.05259(2)	-	1187	(Christensen M. 2010)
	1.0509(3)	-	1197±7	(Kuznetsov V.L. 2000)
	1.05300(9)	-	1111±5	(S. H. Eisenmann B. 1986)
$Ba_8Ga_{16}Sn_{30}$	1.1683(7)	-	511±4[a]	(Kuznetsov V.L. 2000)
	1.1680(1)	-	500[a]	(Schäfer M.C. 2011)
$Eu_8Ga_{16}Ge_{30}$	1.070	-	688±5	(Sales B.C. 2001)
	1.07056(2)	-	699	(C.-C. W. Paschen S. 2001)
$Ba_8Zn_8Ge_{38}$	1.07534(1)	-	940	(Christensen M. 2010)
$Ba_8Cd_8Ge_{38}$	1.09609(2)	(B. S. Koblyuk-M. N. 2007)	813	*
$Ba_8Cu_6Ge_{40}$	1.07492(5)	(G. A. Koblyuk-M. N. 2009)	907	(Christensen M. 2010)
$Sr_8Cu_{5.3}Ge_{40.7}$	1.06368 (2)	*	~750	*
$Ba_8Cu_{4.7}Si_{41.3}$	1.03331(2)	(Yan X. 2010)	1180	*
$Ba_8Ag_5Ge_{41}$	1.0843(3)	*	873(3)	*
$Ba_8Ag_5Si_{41}$	1.04613(5)	*	1140(1)	*
$Ba_8Au_6Ge_{40}$	1.07979(1)	*	926(1)	*
$Ba_8Au_{5.3}Ge_{40.7}$	1.079891(8)	-	931(1)	(Zhang H. 2011)
$Ba_8Au_{5.1}Si_{40.9}$	1.04130(2)	*	~1230	*
$Ba_8Ni_6Ge_{40}$	1.06891(2)	-	823	(Christensen M. 2010)
$Ba_8Ni_{3.3}Si_{42.7}$	1.02893(3)	(C. M. Falmbigl M. 2012)	1100	*
$Ba_8Pd_{3.8}Ge_{42.2}$	1.07710(2)	(G. A. Koblyuk-M. N. 2007)	834	*
$Ba_8Pd_4Si_{42}$	1.03629(1)	(G. A. Koblyuk-M. N. 2008)	1140	*
$Ba_8Pt_{3.5}Ge_{42.5}$	1.07520(2)	(R. M. Koblyuk-M. N. 2007)	847	*
$Ba_8Pt_{3.8}Si_{42.2}$	1.03629(1)	(G. A. Koblyuk-M. N. 2008)	1210	*
Inverse clathrate type-I				
$Si_{46-x}P_xTe_y$ (x~2y)	y=8;	(K. S. Condron C.L. 2006)	950[b]	(K. T. Kishimoto K. 2007)
	0.996457(9)		1100[b]	(K. T. Kishimoto K. 2007)
	y=7	-	1170[b]	(Philipp F. 2008)
	y=7.4; 0.997168(8)	-	1220[b]	(Philipp F. 2008)

	y=6.7; 0.99789(2)			
$Ge_{38}P_8Cl_8$	1.03514(3)	-	630-760[b]	(Zaikina J.V. 2009)
$Ge_{38}P_8Br_8$	1.04074(4)	-	690-775[b]	(Zaikina J.V. 2009)
$Ge_{38}P_8I_8$	1.05067(6)	-	600-750[b]	(Zaikina J.V. 2009)
$Ge_{38}As_8Br_8$	1.05161(5)	-	670-810[b]	(Zaikina J.V. 2009)
$Ge_{38}As_8I_8$	1.06158(4)	-	670-800[b]	(Zaikina J.V. 2009)
$Ge_{38}Sb_8I_8$	1.08697(6)	-	515-675[b]	(Zaikina J.V. 2009)
$Ge_{43.3}I_{2.7}I_8$	1.0814(3)	-	510[b]	(Menke H. 1972)
$Sn_{19.3}Cu_{4.7}As_{22}I_8$	1.11736(3)	(Nesper R. 1986)	575[b]	(Kovnir K.A. 2005)
$Sn_{20.5}\square_{3.5}As_{22}I_8$	1.1092(1)	(Zaikina J. V. 2008)	525[b]	(Kovnir K.A. 2005)

*this work; [a] Liquidus temperature; [b] Decomposition temperature from thermogravimetry

For a better overview of the available data, the melting points for the ternary $A_8T_xM_{46-x}$ compounds are summarized in the histogram in Figure 18. As can be seen from Table IX and Figure 18, Si-based clathrates generally have much higher melting points compared with their Ge-based homologues and all investigated compounds melt congruently beside $Ba_8Ga_{16}Sn_{30}$ (clathrate VIII and I), which forms through a peritectic reaction.

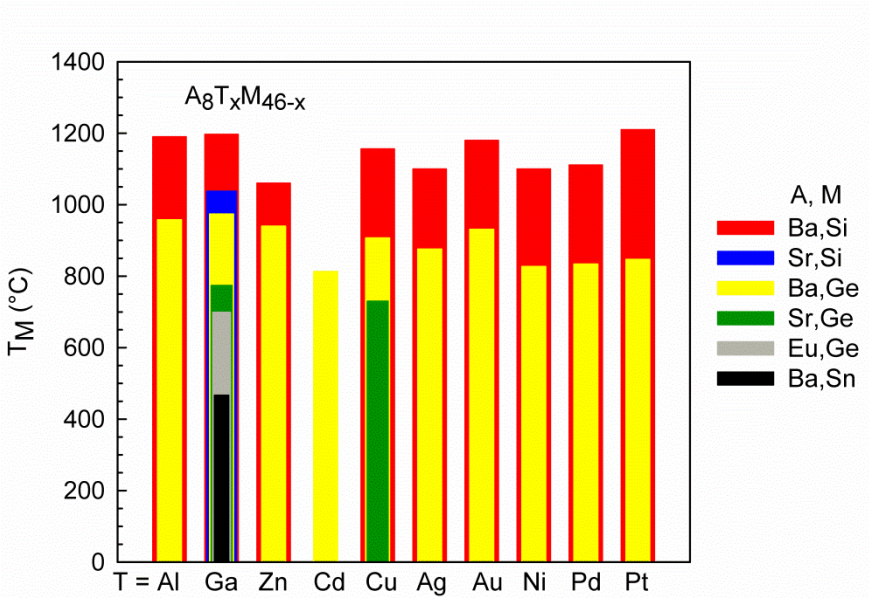

Figure 18: Melting points of type-I clathrates $A_8T_xM_{46-x}$ (A = Sr, Ba, Eu; T = Ni, Pd, Pt, Cu, Ag, Au, Zn, Cd, Al, Ga; M = Si, Ge, Sn); the exact compositions for the investigated compounds and references are given in Table IX.

The thermal stability data for various inverse clathrate type-I $Ge_{38}\{P,As,Sb\}_8\{Cl,Br,I\}_8$,

$Si_{46-x}P_xTe_y$ and tin based compounds are summarized at the end of Table IX. A single step decomposition has been found for $Ge_{38}\{P,As,Sb\}_8\{Cl,Br,I\}_8$ (Zaikina J.V. 2009) and $Si_{46-x}P_xTe_y$ ((K. T. Kishimoto K. 2007), (Zaikina J.V. 2009)) and the Si-based compounds exhibit the highest thermal stability compared with the Ge and Sn-based inverse clathrates. Details concerning synthesis, crystal structures, thermal stability, thermoelectric properties, magnetic properties and mechanical stability of inverse clathrates can be found in a comprehensive review article by M. Falmbigl and P. Rogl (M. Falmbigl 2012).

5.2.1.6 Physical properties of the clathrates $Ba_8Ag_xGe_{46-x-y}\square_y$

5.2.1.6.1 Specific Heat

Results of the temperature dependent heat capacity C_p of the $Ba_8Ag_{3.4}Ge_{41.5}\square_{1.1}$ phase are studied in detail because it is representative for the type I clathrate series $Ba_8Ag_xGe_{46-x-y}\square_y$. The data are displayed in Figure 19. A standard analysis of C_p(T) [Sommerfeld value γ = 15 mJ/molK^2, Debye temperature θ_D^{LT} = 260 K, inset Figure 19 (a)] works only for a very limited temperature range (T < 5 K).The Debye function in general reveals a global maximum $(Cp/T)^{max}$ at $\theta_D/T \approx 3.6$.

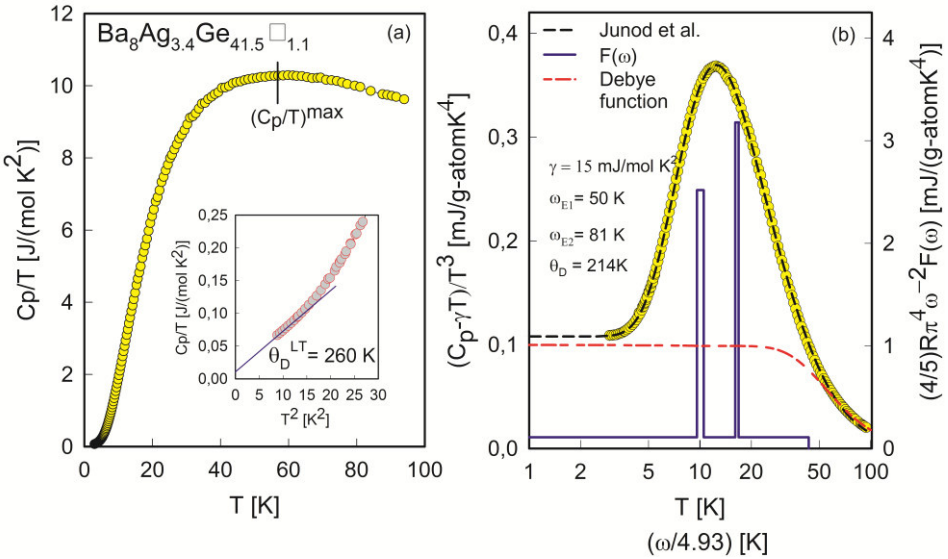

Figure 19: Temperature dependent specific heat C_p of $Ba_8Ag_{3.4}Ge_{41.5}\square_{1.1}$, plotted as C_p/T vs. T (a) and $(C_p - \gamma T)/T^3$ vs. ln$T$ (b). The dashed line is a least squares fit of the experimental data using the model described in the text with two Einstein-like modes (Θ_D^{Junod} = 214 K, ω_{E1} = 49.6 with a total width of 8.8 K and ω_{E2} = 81.2 with a total width of 7.2 K). The red dashed line is a Debye function with Θ_D = 214 K. The solid line refers to the right axis and sketches the phonon spectral function $F(\omega)$ plotted as $\omega/4.93$ vs. $(4/5)R\pi^4\omega^{-2}F(\omega)$ for which ω is given in Kelvin.

Thus, the experimental results of $(Cp/T)^{max}$ observed at 60 K (see vertical bar in Figure 19(a)) yields a Debye temperature of $\theta_D \approx 60 \times 3.6$ K = 216 K. A substantial deviation of the low temperature specific heat from the Debye model (T > 5 K) indicates a rather complex phonon spectrum. The loosely bound electropositive Ba atoms located in the framework cages vibrate in rattling modes which may be modelled by Einstein modes arising above the background of Debye-like vibrations of the clathrate host atoms. An advancement of this ansatz was suggested by Junod et al. (B. D. Junod A. 1979) by introducing optical phonon branches with a finite width in frequency. A least squares fit of Junod's model to the present experimental data results in two Einstein branches with frequencies $\omega_{E1} = 49.6 \pm 4.4$ K and $\omega_{E2} = 81.2 \pm 3.6$ K and a cut-off frequency at $\theta_D^{Junod} =$ 214 K (dashed line in Figure 19(b)). The temperature of 214 K compares well with the Debye temperature as extracted from the maximum of C_p/T(T). The corresponding spectral function F(ω) obtained out of the fit is shown as a solid line, and its values can be read from the right axis of Figure 19(b). The dash-dotted line represents the Debye function for the specific heat with θ_D = 214 K. It should be noted that Einstein-like and cut-off frequencies derived for $Ba_8Ag_{3.4}Ge_{41.5}\square_{1.1}$, correspond to the range of values as observed for the Ge-based type I clathrates $Ba_8M_xGe_{46-x-y}\square_y$ (M = Cu, Zn, Cd, Pd, Pt) [(G. A. Koblyuk-M. N. 2009), (G. A. Koblyuk-M. N. 2007), (B. S. Koblyuk-M. N. 2007), (G. A. Koblyuk-M. N. 2007), (R. M. Koblyuk-M. N. 2007)]. This is in fair agreement with the data extracted from the X-ray ADP-results. On the basis of these results we conclude that the substitution of Ge by a metal M does not significantly change the vibrational dynamics of the atoms of the host lattice.

5.2.1.6.2 Electrical Resistivity

In Figure 20 the experimental results for the electrical resistivity (ρ) are plotted for the Ag – substituted type I clathrates including estimated error bars, being of the order of a few percent.

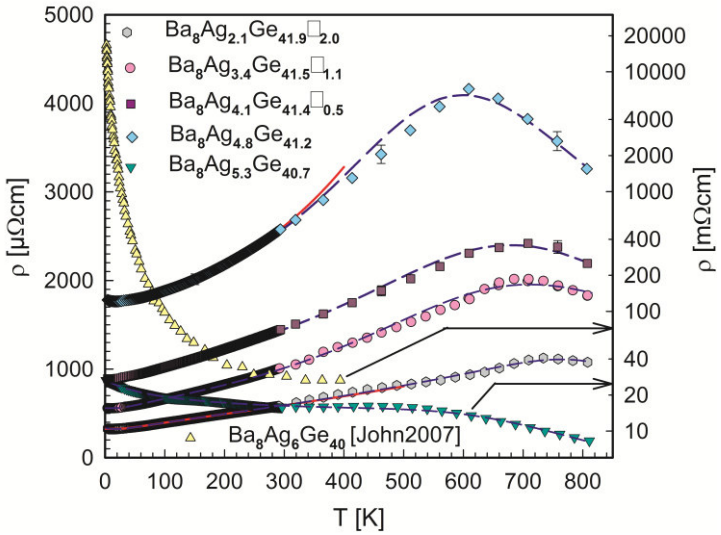

Figure 20: Temperature dependent resistivity ρ of $Ba_8Ag_xGe_{46-x-y}\square_y$; data of $Ba_8Ag_6Ge_{40}$ are taken from Ref. (Johnsen S. 2007)and refer to the right axis. The red solid lines are least squares fits based on the Bloch-Grüneisen model including a Mott-Jones term. The dashed lines are fits according to a model described in the text.

At low temperatures - except for $Ba_8Ag_6Ge_{40}$ and $Ba_8Ag_{5.3}Ge_{40.7}$ – the resistivity ρ(T) exhibits a metallic behaviour, which gradually changes at high temperatures and at increased Ag content towards a more insulating character. Focusing on the compound $Ba_8Ag_{2.1}Ge_{41.9}\square_{2.0}$, the metallic behaviour becomes evident, because ρ(T) can be fitted bythe Bloch-Grüneisen model. The fit is shown as a solid line in Figure 20, revealing a Debye temperature of $\theta_D = 210$ K, which is typical for type I clathrates.

At low temperatures for increasing content of Ag the behaviour of ρ(T) becomes qualitatively and quantitatively modified: i) the overall absolute resistivity increases and ii) the almost linear ρ(T) dependence steadily changes, resulting in a significant deviation from linearity. Such behaviour is rather rarely found in the literature. According to Chiu (Chiu J.C.H. 1976), such deviations can be described within the theory of Mott and Jones (Berger S., PhD Thesis 2003) taking into account an additional T^3 term. In this model the resistivity is governed by processes, in which electrons are scattered into unoccupied states present in the type I clathrates. The probability of such a scattering event is proportional to the DOS and its first derivative with respect to energy. For systems with Fermi energy near to a maximum in the DOS, a negative deviation of the resistivity from linearity (= saturation effect) might be observed. Conversely, for a system with the Fermi energy near to a minimum of the DOS, ρ(T) is expected to positively deviate from linearity. Following these arguments, one may conclude that the substitution of Ge by Ag drives the metallic state as ascribed to $Ba_8Ge_{43}\square_3$ towards a state with a gap. In fact, the

compounds $Ba_8Ag_{5.3}Ge_{40.7}$ and "$Ba_8Ag_6Ge_{40}$" (see Figure 20) behave like semiconductors for which the resistivity decreases by 4 orders of magnitude (Johnsen S. 2007) when changing the temperature from 4 K to room temperature. The experimentally observed Mott-Jones contribution, becoming more pronounced with increasing Ag content, documents that the Fermi level approaches the gap (solid lines, Figure 20). The evolution towards an insulating state upon the Ge/Ag substitution becomes evident in ρ(T) also above room temperature. Increasing Ag content causes a maximum to appear which becomes more pronounced and shifts towards lower temperature for increasing Ag content.

For modelling ρ(T) in the entire temperature range up to 800 K we combine the metallic low temperature behaviour (Bloch-Grüneisen formula including the Mott-Jones term) with the gap-related features at higher temperatures using a rectangular DOS. It should be noted, that we place the Fermi energy E_F is slightly above an appearing band gap, which results in a distinctly temperature dependent charge carrier density *n*. For more details we refer to Ref. (Fornasari L. 2006). Reasonable least squares fits yield a band gap width Δ ranging from about 8300 K for $Ba_8Ag_{4.1}Ge_{41.4}\square_{0.5}$ to 6900 K for $Ba_8Ag_{4.8}Ge_{41.2}$.

5.2.1.6.3 Thermal Conductivity

In Figure 21 the data for the temperature dependent thermal conductivity λ(T) of the Ag-based clathrates are summarised.

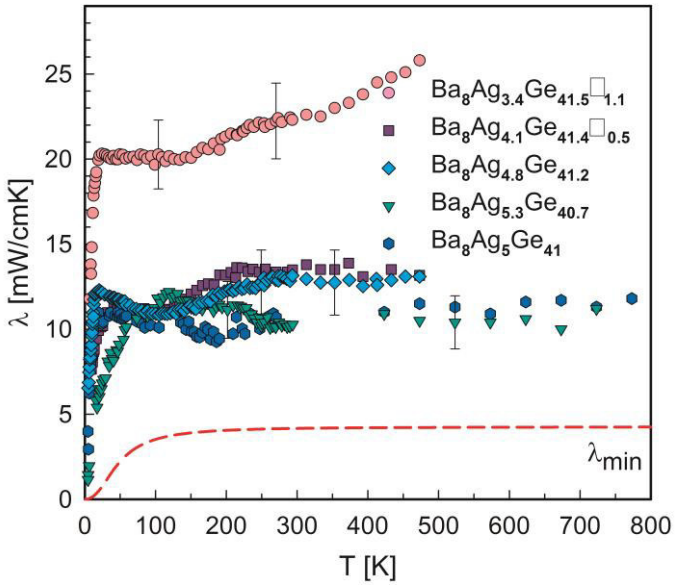

Figure 21: Temperature dependent thermal conductivity λ of $Ba_8Ag_xGe_{46-x-y}\square_y$. The dashed line represents the minimum thermal conductivity of type I clathrates.

The quite large error bars (measurement errors in the range of 10-15%) follow from two distinctly different measurement methods. In order to compare the low temperature measurements (4 to 300 K) with the measurements above room temperature, a T^3 term, representing radiation losses in the low temperature steady-state heat flow measurement was subtracted. Overall, the thermal conductivities are small, being of the order of the minimum thermal conductivity λ_{min}, as estimated by the model of Cahill and Pohl ((Cahill D. 1989), dashed line, Figure 21). The values of $\lambda(T)$ within the studied series of alloys are similar, only $Ba_8Ag_{3.4}Ge_{41.5}\square_{1.1}$ exhibits a larger thermal conductivity, partly caused from the higher electronic contribution λ_e, reaching 10 mW/cmK at 300 K. Assuming the applicability of the Wiedemann Franz law, λ_e can be derived from the electrical resistivity data as shown in Figure 20. A common feature of all clathrates $Ba_8Ag_xGe_{46-x-y}\square_y$ is the absence of a pronounced low temperature maximum, characterizing, in general, simple metals and insulators with sufficiently low defect/impurity concentrations. Scattering of both, electrons and phonons on impurities, vacancies, grain boundaries or other static defects significantly suppress the initial rise of $\lambda(T)$, resulting in a practically featureless temperature dependency. In order to reveal the principal scattering mechanism, the total thermal conductivity $\lambda(T)$ is separated into contributions from the electrons (λ_e) and the lattice (λ_{ph}). An example of this procedure is shown in Figure 22 for $Ba_8Ag_{4.1}Ge_{41.4}\square_{0.5}$, yielding $\lambda_e \sim 5$ mW/cmK and $\lambda_{ph} \sim 9$ mW/cmK at room temperature in relation to $\lambda_{min} \sim 5$ mW/cmK.

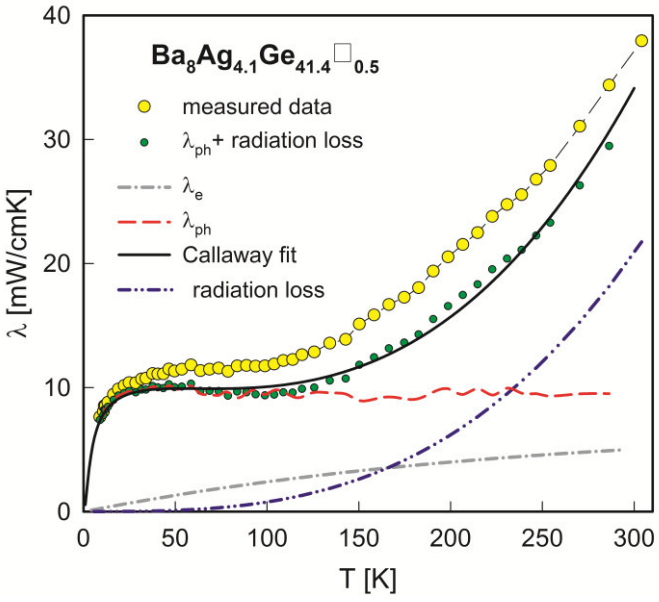

Figure 22: Temperature dependent thermal conductivity λ of $Ba_8Ag_{4.1}Ge_{41.4}\square_{0.5}$. The solid line is a least squares fit according to the model of Callaway (v. B. Callaway J. 1969) as described in the text.

The dashed, the dashed-doted and the dashed-dot-dot lines represent the phonon part, the electronic contribution and the radiation losses, respectively.

A detailed analysis based on the model of Callaway (v. B. Callaway J. 1969) allows to account for λ_{ph} taking into account individual scattering processes by appropriate relaxation times, i.e. τ_c: $\tau_c^{-1} = \tau_B^{-1} + \tau_D^{-1} + \tau_e^{-1} + \tau_U^{-1}$, where the subscripts B, D, e and U refer to scattering of the phonons on boundaries, defects, electrons and include Umklapp processes U, respectively. A least squares fit of this model is shown in Figure 22 as a solid line, revealing a Debye temperature θ_D = 202 K and emphasizes the importance of defect and boundary scattering. At higher temperatures, Umklapp scattering as the dominant scattering process causes a decrease of $\lambda_{ph}(T)$ (see Figure 22).

5.2.1.6.4 Thermopower and Hall effect

The temperature dependent Seebeck coefficient *S(T)* for various concentrations *x* of $Ba_8Ag_xGe_{46-x-y}\square_y$ is displayed in Figure 23, including data for "$Ba_8Ag_6Ge_{40}$" from Ref. (Johnsen S. 2007).

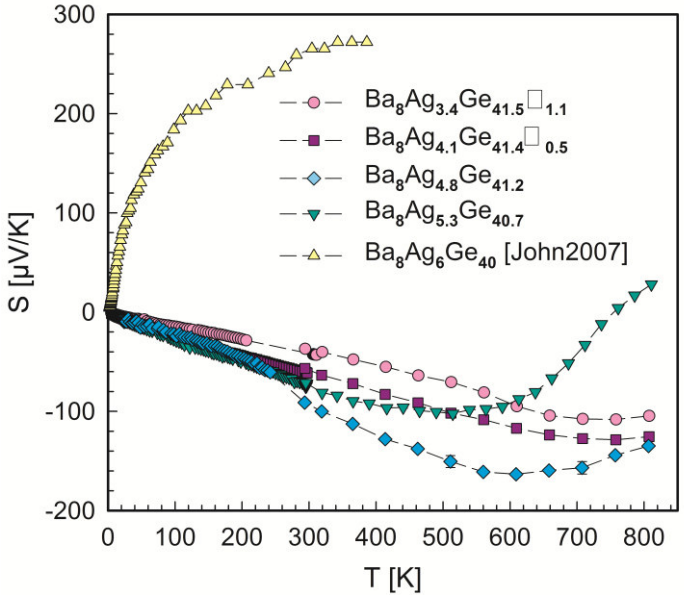

Figure 23: Temperature dependent thermopower S of $Ba_8Ag_xGe_{46-x-y}\square_y$; data for $Ba_8Ag_6Ge_{40}$ are taken from Ref. (Johnsen S. 2007).

The measurement error is about 4%, which is already implied in the symbol size. While samples with Ag content x < 6 exhibit negative Seebeck coefficients in the entire temperature range as a signature of electrons as the key charge carriers, the compound "$Ba_8Ag_6Ge_{40}$" shows large and positive *S(T)* values. This might be interpreted as a hole dominated transport. Thus, the substitution of Ge by Ag drives the electron dominated

transport via charge compensation into a hole dominated transport regime for the maximum of the substitution. In the proximity of compensation, very large *S(T)* values arise due to the depletion of charge carriers and this, consequently, results in a large electrical resistivity (compare Figure 20).

Below about 600 K, *S(T)* behaves almost linearly for x < 6, before reaching a minimum at higher temperatures. Employing Mott's formula (Blatt F.J. 1968),

$$S_d\left(T > \Theta_D\right) = \frac{\pi^2 k_B^2 2m}{e\hbar^2\left(3n\pi^2\right)^{\frac{2}{3}}}T \qquad (8)$$

(*m* being the mass of the carriers and e the respective charge) allows the derivation of the charge carrier density *n*. It is accepted, that Eq.(8) is valid for systems without significant electronic correlations. Based on Eq.(8), the charge carrier density *n* can be evaluated, ranging from $n = 0.54\text{x}10^{21}$ cm^{-3} for $x_{Ag} = 4.8$, $n = 1.1\text{x}10^{21}$ cm^{-3} for $x_{Ag} = 4.1$ and $n = 1.9\text{x}10^{21}$ cm^{-3} for $x_{Ag} = 3.4$ (electrons in all three cases), whilst in case of $x_{Ag} = 6$, $n = 0.36\text{x}10^{19}$ cm^{-3} (holes). Note that in the latter case a linear *S(T)* dependence has been chosen at low temperatures (below 50 K). Consequently, Eq.(8) needs to be modified by an additional pre-factor of 1/3 (Blatt F.J. 1968). To check the reliability of the charge carrier estimation done from analysing the slopes of *S(T)* according to Eq.(8), we performed Hall measurements on the $Ba_8Ag_{3.4}Ge_{41.2}\square_{1.4}$, and $Ba_8Ag_{5.3}Ge_{40.7}$ compounds. While the former turned out to behave more metallic-like, the latter clearly evidenced semiconducting-like features of $\rho(T)$ (compare Figure 20). In fact, our Hall data reveal that the charge carrier density in the $Ag_{3.4}$ sample is about 5 times larger than for the $Ag_{5.3}$ compound (Figure 24).

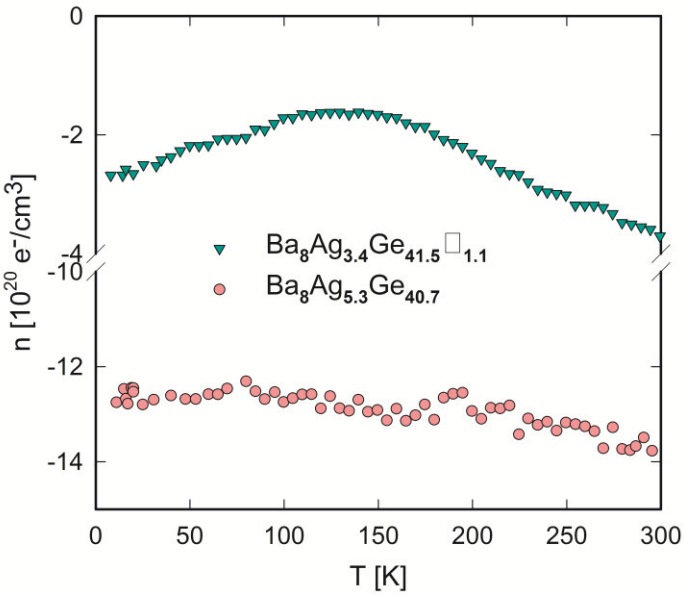

Figure 24: Temperature dependent charge carrier concentration n of two alloys of $Ba_8Ag_xGe_{46-x-y}\square_y$.

As already concluded from the Seebeck data, electrons are the dominating charge carriers in these Ag-based materials. We also note that *n* derived from *S(T)* is in good agreement with *n* obtained from the Hall data. Moreover, the more pronounced temperature dependence of *n(T)* in the case of $Ba_8Ag_{5.3}Ge_{40.7}$ reflects its more semiconducting nature when compared to metallic $Ba_8Ag_{3.4}Ge_{41.2}\square_{1.4}$.

Minima observed in *S(T)* of $Ba_8Ag_xGe_{46-x-y}\square_y$ for x < 6 can be explained considering the more general expression

$$S(T) \propto \frac{1}{N(T)} \frac{\partial N(E)}{\partial E}_{E_F}, \qquad (9)$$

which contains a temperature dependent variation of $[1/N(E)]dN(E)/dE$.

A comparison of *S(T)* and $\rho(T)$ for various x reveals a natural correspondence among the absolute values of $|S(T)|$ rising with increasing $\rho(T)$ as well as a striking correspondence among the maxima in $\rho(T)$ and the maxima in $|S(T)|$. The decrease of resistivity at high temperatures beyond the maximum in $\rho(T)$ implies an increase of the charge carrier density as a consequence of thermal excitations across the band gap. Such an increase of *n* concomitantly reduces *S(T)* (compare Eq.(8)). This effect is a consequence of the band gap, which shrinks with increasing content of Ag.

5.2.1.6.5 Thermoelectric Figure of Merit

The temperature dependent figure of merit, $ZT = S^2T/(\rho\lambda)$, characterises the thermoelectric ability of a single material concerning power generation or cooling. In general, technical applicability requests a ZT above 1. ZT values derived from the present study are documented in Figure 25. Although, the Seebeck coefficients reach absolute values well above 100 µV/K and the thermal conductivity is smaller than 20 mW/cmK, the ZT values suffer from large electrical resistivities and thus reach only a maximum of ~ 0.42 for $Ba_8Ag_{4.1}Ge_{41.4}\square_{0.5}$ at 800 K. It should be noted that this is not found at the Zintl limit of x_{Ag} = 5.3, but at slightly lower Ag concentrations due to a more reasonable value of the electrical resistivity. Future attempts to improve ZT will focus on an enhancement of the electrical conductivity.

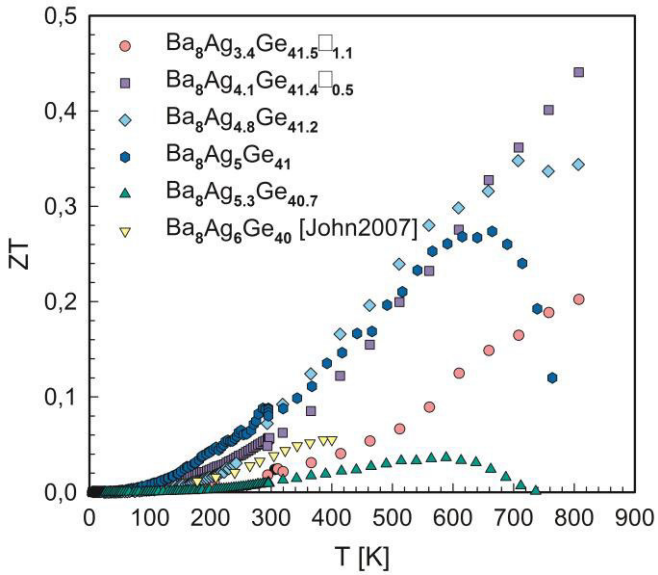

Figure 25: Temperature dependent figure of Merit ZT of $Ba_8Ag_xGe_{46-x-y}\square_y$ including literature data (Johnsen S. 2007).

5.2.1.7 Summary

The isothermal sections at 800°C and 600°C were investigated up to 33.33 at% Ba in the Ba – Ag – Ge system. For the clathrate phase $Ba_8Ag_xGe_{46-x-y}\square_y$ the cubic primitive symmetry (space group $Pm\bar{3}n$, a~1.1nm) was confirmed by x-ray powder diffraction assisted by x-ray single crystal analyses. From EPMA, XRD and DSC/DTA measurements, the liquidus and solidus projection of the Ba-Ag-Ge system has been constructed up to 33.33 at.% Ba. Eight different primary crystallization regions were found: (Ge), $Ba_8Ag_xGe_{46-x-y}\square_y$ (κ_I, clathrate type-I), $Ba_6Ag_xGe_{25-x}$ (κ_{IX}, clathrate type-IX),

$BaGe_2$, $Ba(Ag_{1-x}Ge_x)_2$ (τ_1), $BaAg_{2-x}Ge_{2+x}$ (τ_2), $BaAg_5$ and (Ag). κ_I forms quasi-binary sections with (Ge), $BaGe_2$ and τ_2. Three further quasi binary sections can be found between τ_1 and τ_2, τ_1 and (Ag) and τ_2 and (Ag). All the ternary compounds form congruently from the melt. The ternary invariant reactions (4 eutectic and 3 transition reactions) have been determined for the region investigated and are the basis for a Schulz-Scheil diagram. At 800°C the clathrate type I solid solution ranges from binary $Ba_8Ge_{43}\square_3$ to $Ba_8Ag_{5.3}Ge_{40.7}$ and at 600°C the clathrate solution $Ba_8Ag_xGe_{46-x-y}\square_y$ separates from the Ba-Ge boundary and extends from about 6.6 to 9.8 at% Ag. The clathrate type-IX Ba_6Ge_{25} phase has a maximum solubility of 1.5 at% Ag at both temperatures. The homogeneity region of the two ternary compounds, that were already reported in literature, have been found to extend from x = 0.7-0.2 for $BaAg_{2-x}Ge_{2+x}$ ($ThCr_2Si_2$ -type) and x = 0.5-0.7 for $BaAg_xGe_{2-x}$ (AlB_2-type) at 800°C. Both homogeneity regions do not change significantly at 600°C. Five single phase samples with compositions $Ba_8Ag_xGe_{46-x}$ (x = 3.4, 4.1, 4.8, 5, 5.3) were prepared in a different way to reach a higher relative density for measuring its physical properties. Large values of the Seebeck coefficient have been measured for all compounds and the figure of merit reaches about 0.5 for $Ba_8Ag_{4.1}Ge_{41.4}\square_{0.5}$. Due to the very high values of the electrical resistivity very near to compensation, the largest values of the figure of merit are found for compounds exhibiting a residual metallic state.

5.3 THE TERNARY SYSTEM Ba-Ag-Si

Despite superconductivity, discovered in Na and Ba doped silicon clathrates, ((Kawai H. 1995), (Yamanaka S. 2000)) triggered intense studies of clathrate type I compounds $Ba_8Ag_xSi_{46-x}$ ((Tse J. S. 2005), (Kamakura N. 2005), (Herrmann R.F.W., Superconductivity in silicon based barium-inclusion clathrates 1998)), there is still little known about phase equilibria in the Ba – Ag – Si system and about the homogeneity region of clathrates at a defined temperature. Kamakura et al. (Kamakura N. 2005) combined electronic band structure calculations of Ba_8Si_{46} and $Ba_8Ag_6Si_{40}$ with photoemission experiments performed on arc melted alloys $Ba_8Ag_xSi_{46-x}$ (x = 0, 1, 3, 6),

which were ground and compressed at 3 GPa and 800 °C in an h-BN container. Single crystal X-ray data of $Ba_8Ag_{3.8}Si_{42.2}$ confirmed Ag-atoms in the 6c-site of the clathrate type I structure (Cordier G. 1991). Beside the clathrate type-I phase, Dörrscheidt and Schäfer (S. H. Dörrscheidt W., Beiträge zu den Stabilitätskriterien der AlB2-Struktur 1981) mentioned a compound without a large homogeneity region derived from nominal compositions $BaAg_xSi_{2-x}$ ($0.5 \leq x \leq 1.0$, space group C222, presumably $Sr_8Ag_5Si_9$-type, as a derivative of the AlB_2-type). A more recent reinvestigation by R. Cardoso Gil et al. (Cardoso Gil R. 1999) arrived at a formula Ba_2AgSi_3 with a different space group ($Ba_4Li_2Si_6$ structure type, Fddd, a = 0.862, b = 1.493 and c = 1.965 nm) and a superstructure of the AlB_2-type according to $a = 2a_{AlB2}$, $b = 2\sqrt{3}a_{AlB2}$, $c = 4c_{AlB2}$. Single crystal X-ray intensity refinements by Merlo et al. (P. M. Merlo F. 1996) prompted a compound $Ba_{32}Ag_{21.54}Si_{30.2}$ with $Ba_3Ag_2Si_3$ structure type (space group C222).

This chapter compiles consistent information on the phase relations in the isothermal section at 800°C for the region with Ba-contents less than 33.3 at.%, provides details on the homogeneity regions of ternary compounds in combination with atomic ordering in the corresponding crystal structures and thermoelectric data on the clathrate type I as a function of temperature.

5.3.1 Results and Discussion

5.3.1.1 The solid solution for clathrate type-I $Ba_8Ag_xSi_{46-x}$

The solubility range of the ternary type-I clathrate at 800 °C was studied by X-ray powder diffraction (XRPD) and electron probe microanalysis (EPMA) on a series of samples with nominal composition $Ba_8Ag_xSi_{46-x}$ (x = 3 to 7). Table X shows a comparison of the EPMA data with the results of Rietveld refinements of the X-ray spectra.

Table X: Results from EPMA and Rietveld refinement for $Ba_8Ag_xSi_{46-x}$.

Nominal composition	EPMA (at.%)			Accepted composition[a]	Latt. Par. [nm]	Si2 in 16i x	Si3 in 24k y, z
	Ba	Ag	Si				
$Ba_8Ag_3Si_{43}$	15.3	8.4	76.3	$Ba_8Ag_{4.3}Si_{41.7}$	1.04309(3)	0.1832(4)	0.1170(2), 0.3058(3)
$Ba_8Ag_5Si_{41}$	15.8	10.0	74.2	$Ba_8Ag_5Si_{41}$	1.04585(1)	0.1833(2)	0.1153(3), 0.3050(3)
$Ba_8Ag_6Si_{40}$	15.2	10.3	74.5	$Ba_8Ag_{5.4}Si_{40.6}$	1.04613(5)	0.1842(2)	0.1149(4), 0.3049(5)

[a]from Rietveld refinement

In all cases the spectra could be fully indexed in the basis of a cubic clathrate type I lattice (space group $Pm\bar{3}n$) with minor amounts of Si and/or $BaSi_2$. As no binary clathrate type I exists under normal pressure, the ternary homogeneity region is very limited at 800°C and was found to extend from $Ba_8Ag_{4.3}Si_{41.7}$ to $Ba_8Ag_{5.4}Si_{40.6}$ (Figure 26).

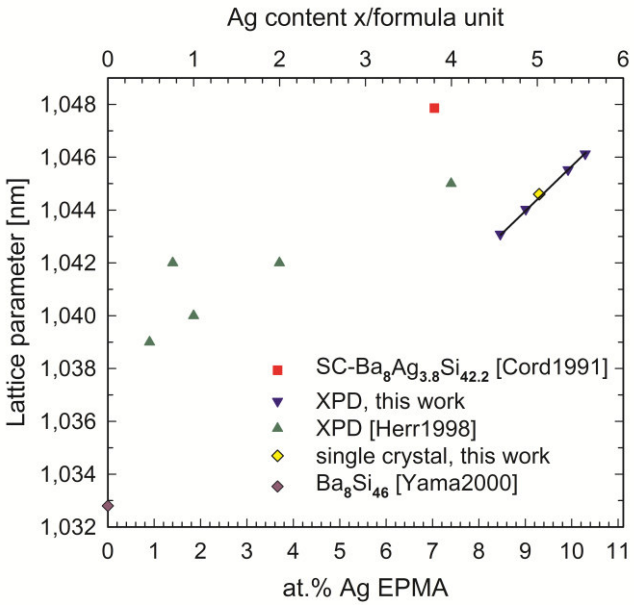

Figure 26: Lattice parameters versus silver content for alloys $Ba_8Ag_xSi_{46-x}$ quenched from 800°C and literature data.

The lattice parameters show a linear increase with increasing silver content but differ quite strongly from those reported earlier by Cordier at al. ((Cordier G. 1991), (X-ray single crystal data, a = 1.0478(6) nm for $Ba_8Ag_{3.8}Si_{42.2}$)) and from those of Herrmann et al. ((Herrmann R.F.W. 1998), XRPD for $Ba_8Ag_xSi_{46-x}$, x = 4,2,1,0.8,0.5). Our refinement unambiguously located the Ba atoms in the sites 2a (0,0,0) and 6c (¼,0,½), whereas Ag and Si atoms share the 6d (¼,½,0) site. Silicon occupies the sites 16i (x,x,x) and 24k (0,y,z). No vacancies were encountered. Substitution of silicon by silver atoms in the crystal lattice does not strongly affect positional parameters of Si in the 16i site and the 24k site. X-ray single crystal data for $Ba_8Ag_{4.9}Si_{41.1}$ (see Table XI) confirm the general atom distribution on the lattice sites.

Table XI: X-Ray single crystal data at RT ([a]nominal composition).

Parameter/compound	**$Ba_8Ag_5Si_{41}$[a]**
Space Group	$Pm\bar{3}n$
Formula of refinement	$Ba_8Ag_{4.9}Si_{41.1}$
a [nm]	1.0446(2)
μ_{abs} [mm^{-1}]	39.9
V (nm^3)	1.1398
ρ_x (gcm^{-3})	4.05
Reflections in refinement	$388 \geq 4\sigma(F_o)$ of 480
Number of variables	17
$R_F^2 = \Sigma\|F_0^2-F_c^2\|/\Sigma F_0^2$	0.018
R_{Int}	0.0134
wR2	0.0486
GOF	1.046
Extinction (Zachariasen)	0.0023(2)
Residual density $e^-/Å^3$; max; min	0.81; -1.44
Ba1 in 2a(0, 0, 0); occ.	1.00
$U_{11}= U_{22}=U_{33}$	0.0108(1)
Ba2 in 6c(1/4, 0, 1/2);occ.	1.00
$U_{11}= U_{22}$; U_{33}	0.0247(2); 0.0326(2)
M in 6d(1/4, 0, 1/2); occ.	0.816(2)Ag + 0.184Si
$U_{11}= U_{22}$; U_{33}	0.0143(2); 0.0112(2)
Si2 in 16i(x, x, x); occ.	1.00
x	0.18432(4)
$U_{11}=U_{22}=U_{33}$	0.0113(2)
Si3 in 24k(0,y,z); occ.	1.001(1)
y, z	0.11720(6), 0.30405(5)
U_{11}; U_{22};	0.0111(3); 0.0121(3);
U_{33}	0.0114(3)

Atomic displacement parameters (ADP) in the crystal are consistent with features generally observed for clathrates of type-I: Ba2-atoms in the 6c sites show a large anisotropy of the electron densities, whereas Ba1-atoms in 2a behave like framework atoms (see Table XI). Least squares fits of the ADPs as a function of temperature (Figure 27) with the Einstein model (see Figure 27) for Ba2 and with the Debye model for the framework atoms, results in $\Theta_{E,11}$ = 108 K, $\Theta_{E,22}$ = 81 K and Θ_D = 427 K (Θ_E, Θ_D Einstein- and Debye temperature). The linear thermal expansion coefficient (Formula see

Figure 27; a_{300K}: lattice parameter at 300 K; a_T: lattice parameter at temperature T) yields $\alpha_a = 9 \cdot 10^{-6}\ K^{-1}$, which is perfectly consistent with a recent compilation of clathrate type I thermal expansion data (R. G. Falmbigl M. 2010). The deviation of the linearity in all cases (lattice parameter a(T), ADPs U(T)) may be explained by a slight uncertainty in the temperature measurement at 200 K.

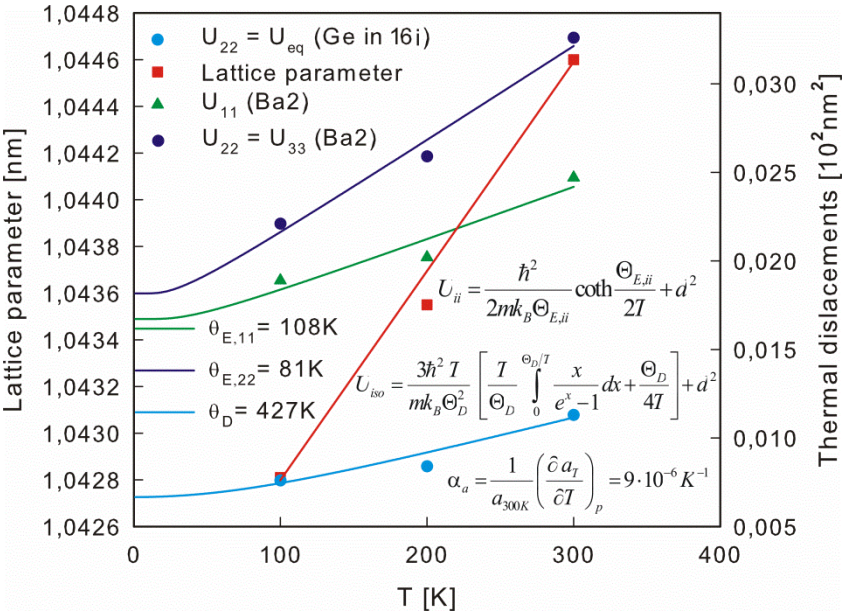

Figure 27: Temperature dependency of atom displacement parameters and lattice parameter of $Ba_8Ag_{4.9}Si_{41.1}$.

5.3.1.2 Phase equilibria in the system Ba – Ag – Si for 0 to 33.3 at.% Ba

The isothermal section at 800°C for the silicon and silver rich part is shown in Figure 28.

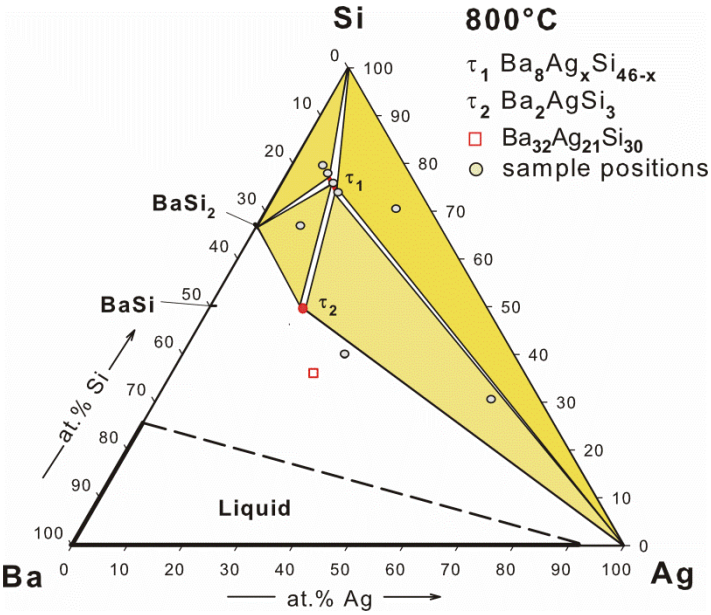

Figure 28: Partial isothermal section for the ternary system Ba – Ag – Si at 800°C.

At low Ag content, clathrate I is in equilibrium with silicon and $BaSi_2$. At higher silver content, the equilibrium phase was identified as τ_2-Ba_2AgSi_3 ($Ba_4Li_2Si_6$ structure type), which does not show a homogeneity range at 800 °C but oxidizes on air. Structural details can be found in (Cardoso Gil R. 1999). Figure 29 shows the SEM images of samples documenting the four three-phase equilibria at 800°C.

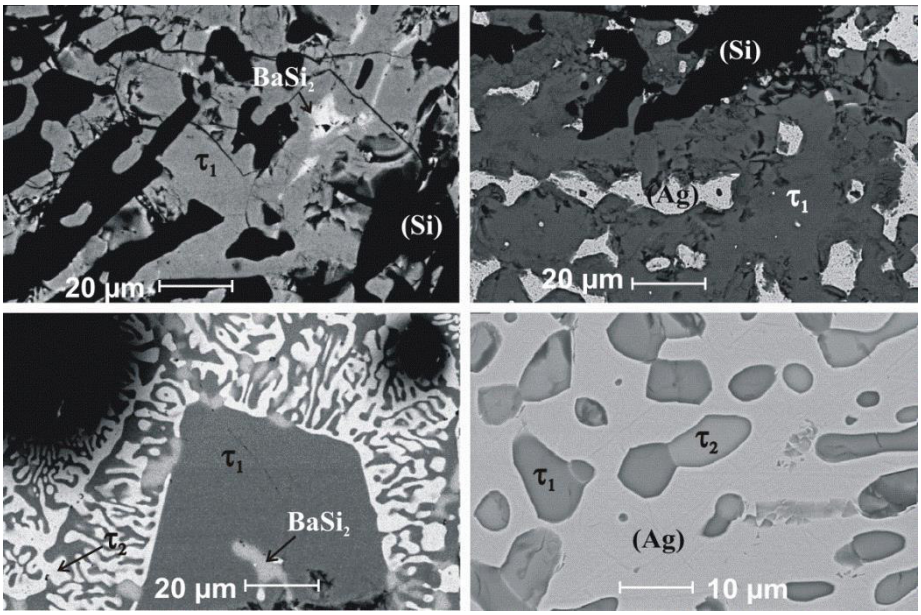

Figure 29: SEM images showing the microstructures of the four three-phase equilibria of Figure 28 (τ_1: clathrate-I; τ_2: Ba_2AgSi_3).

It is interesting to note that high pressure synthesis at 3 GPa and 800°C yields a

continuous clathrate type I solid solution starting from binary Ba_8Si_{46} up to $Ba_8Ag_6Si_{40}$ at surprising and significantly larger unit cell parameters (a = 1.0560 nm).

5.3.1.3 Temperature dependent thermal conductivity

The temperature dependent thermal conductivity was measured for $Ba_8Ag_5Si_{41}$ in the low temperature range between 10 K and about 300 K. A pronounced low temperature maximum, which in general characterises crystalline solids, is obvious from Figure 30.

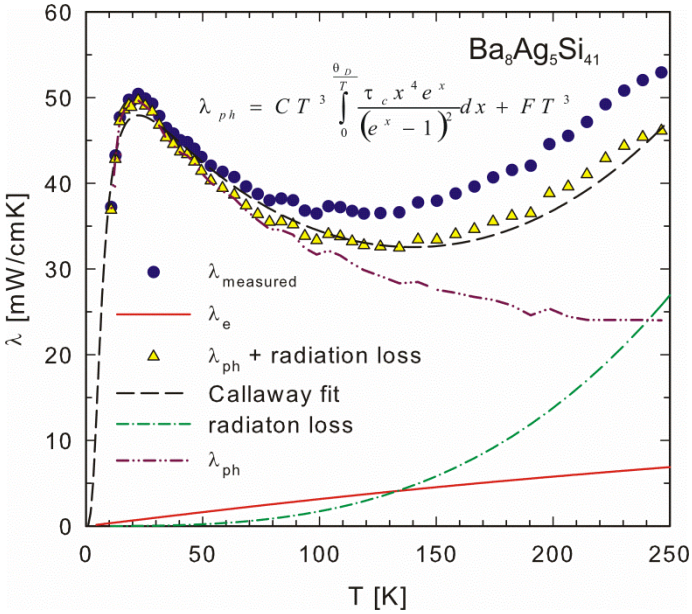

Figure 30: λ(T) of Ba8Ag5Si41. The black dashed line is a least squares fit to the model of Callaway (v. B. Callaway J. 1969) as described in the text. The violet dashed-dotted-dotted line, the red solid line and the green dashed dotted line represent the phonon part, the electronic contribution and the radiation losses, respectively.

For a more detailed consideration, the thermal conductivity can be separated into the lattice thermal conductivity (λ_{ph}) and the electronic contribution to the thermal conductivity (λ_e): $\lambda = \lambda_{ph} + \lambda_e$. (10)

The electronic contribution to the thermal conductivity can be calculated using the Wiedemann-Franz law:

$\lambda = (L_0 T)/\rho$ (11)

using the electrical resistivity (ρ) and assuming a temperature independent Lorentz number ($L_0 = 2.45 \cdot 10^{-8}$ WΩ/K^2). The lattice thermal conductivity according to Callaway (v. B. Callaway J. 1969), together with a radiation loss term (FT^3) is drawn in Figure 30. The overall relaxation time for scattering processes (τ_c) is expressed as the sum of various scattering processes (scattering on boundaries, point defect scattering, "Umklapp" processes, scattering on electrons).

5.3.1.4 Thermopower, resistivity and figure of merit

The results of the electrical resistivity and thermopower measurements at low (4.2-300 K) and high (300-800 K) temperatures are shown in Figure 31. The thermopower values S(T) are negative over the whole temperature range, indicating electrons as dominant charge carries, with a quite moderate maximum of -76 µV/K at about 760 K. Below about 400 K, S(T) behaves almost linearly, before reaching a minimum at higher temperatures. Employing Mott's formula (Blatt F. J. 1968) (see Figure 31) where m is the mass of the carriers and e is the respective charge, allows to derive the charge carrier density n (n = $6.2 \cdot 10^{20}$ cm^{-3}).

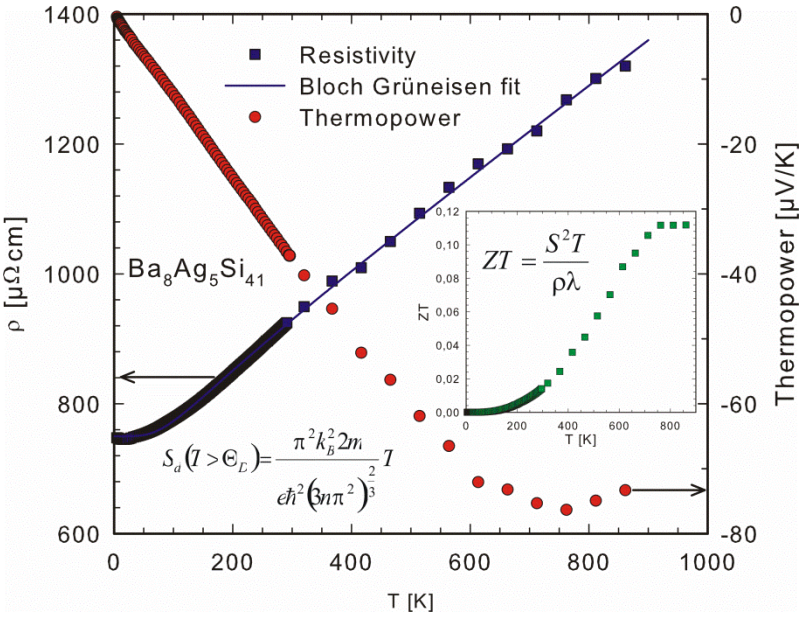

Figure 31: Temperature dependent resistivity (ρ), thermopower (S) and calculated figure of merit (ZT) for $Ba_8Ag_5Si_{41}$. The blue solid line is a least squares fit based on the Bloch-Grüneisen model.

The Equation in Figure 31 is valid for systems without significant electronic correlations. The temperature dependent electrical resistivity exhibits a simple metallic behaviour, which can be described with the Bloch-Grüneisen model. A least squares fit is shown as a blue solid line in Figure 31, revealing a Debye temperature Θ_D = 474 K, in quite good agreement with the value extracted from a least squares fit to the ADPs. The calculated temperature dependent dimensionless figure of merit can be found in the inset of Figure 31. As any application requires ZT above 1, the derived highest ZT value of about 0.12 at 800 K, caused by a quite low thermopower and high thermal conductivity, may be improved by fine-tuning the composition.

5.5 THE TERNARY SYSTEM Ba-Au-Si

Single crystal X-ray refinements proved isotypism with the clathrate type I structure for three alloys $Ba_8Au_xSi_{46-x}$, x = 5.4, 5.9 (Jaussaud N. 2005) and 6.0 (Cordier G. 1991). In contrast to the X-ray single crystal structure determination by Cordier (Cordier G. 1991) suggesting full atom order with Au atoms in the 6c sites, the X-ray analysis by Jaussaud et al. (Jaussaud N. 2005) revealed a lower gold content within the 6c sites, but a small random substitution of Au for Si within the 24k sites. Both groups of authors ((Jaussaud N. 2005), (Cordier G. 1991)) agree on a defect free Si, Au framework. The maximum superconducting fraction in the clathrate solution $Ba_8Au_xSi_{46-x}$ ($0.2 \leq x \leq 6$) prepared at 800°C and 3 GPa was found at x = 1 (Herrmann R.F.W. 1998). Thermoelectric properties, measured for two compounds x = 5.4, 5.9, yielded either n-type or p-type behaviour, respectively, but Seebeck coefficients were rather small in both alloys (Jaussaud N. 2005). ^{29}Si MAS NMR (Magic Angle Spinning Nuclear Magnetic Resonance) spectroscopy indicated a strong contribution of the Si-3s orbital to the band at the Fermi level (Jaussaud N. 2005). Investigations of the electronic structure revealed a metallic character for $Ba_8Au_6Si_{40}$ and TEM studies confirmed a simple type I unit cell (space group $Pm\bar{3}n$) (Herrmann RFW 1999). Vibrational dynamics and electronic structure have been analyzed for $Ba_8Au_xSi_{46-x}$ (x = 1 to 6) by means of first principles calculations assisted by Raman spectroscopy (Tse J.S. 2005). It was demonstrated that Au substitution within the Si-framework of "Ba_8Si_{46}" significantly reduced the electron density at the Fermi-level leaving behind a poor metal for $BaAu_6Si_{40}$ (Tse J.S. 2005). High pressure Raman spectroscopy experiments (up to 27 GPa) have been carried out on $Ba_8Au_6Si_{40}$ (Kume T. 2007) in order to find an isostructural phase transition similar to Ba_8Si_{46} under high pressure. Besides the type I clathrate, the high temperature and high pressure synthesis of $BaAu_2Si_2$ ($ThCr_2Si_2$ type, a = 0.45331(6) and c = 1.0297(1) nm) has been reported (Takahashi S. 2001).

The present chapter presents information on the phase relations in the isothermal section at 800 °C for the region with Ba-contents less than 33.33 at.% and gives details on the crystal structures and homogeneity regions of binary and ternary compounds. Additionally, temperature dependent thermoelectric data are provided for $Ba_8Au_{5.1}Si_{40.9}$,

as part of the clathrate type-I homogeneity region, and low temperature resistivity measurements for the new superconducting compound $BaAu_3Si$.

5.4.1 Results and discussion

5.4.1.1 The clathrate type-I solid solution $Ba_8Au_xSi_{46-x}$

The solubility range of the ternary type-I clathrate at 800 °C was studied by XRD and EPMA on a series of samples with nominal composition $Ba_8Au_xSi_{46-x}$ (x = 3,4,5,6). Table XII shows a comparison of the EPMA data with the results of Rietveld refinement of the X-ray spectra.

Table XII: Results from EPMA and Rietveld refinement for type-I clathrates $Ba_8Au_xSi_{46-x}$.

Nominal composition	EPMA (in at.%)			Accepted composition	Lattice parameter [nm]	Si2 in 16i(x,x,x)	Si3 in 24k (0,y,z)
	Au	Ba	Si				
$Ba_8Au_3Si_{43}$	7.4	14.2	78.4	$Ba_8Au_{4.0}Si_{42}$	1.03963(4)	0.1825(2)	0.1195(2), 0.3079(2)
$Ba_8Au_5Si_{41}$	10.0	14.6	75.4	$Ba_8Au_{5.1}Si_{40.9}$	1.04130(2)	0.1834(1)	0.1164(1), 0.3047(1)
$Ba_8Au_6Si_{40}$	11.3	15.1	73.6	$Ba_8Au_6Si_{40}$	1.04191(2)	0.1852(1)	0.1168(1), 0.3063(1)*

*Au+Si

In all cases the spectra could be fully indexed on the basis of a cubic clathrate type I lattice (space group $Pm\bar{3}n$) with minor amounts of Si in some cases. As no binary Si-based type I clathrate exists at normal pressure the ternary homogeneity region is limited at 800°C and was found to extend from 7.4 to 11.3 at.% Au (i.e. $4 \leq x \leq 6.0$). The lattice parameters for the clathrate series increase linearly with increasing gold content and are in perfect agreement with single crystal data reported by Cordier et al. (a = 1.0422(2) nm for $Ba_8Au_6Si_{40}$ (Cordier G. 1991)) and single crystal data of Jaussaud et al. (a = 1.0414(1) nm for $Ba_8Au_{5.43}Si_{40.57}$ and a = 1.0419(1) nm for $Ba_8Au_{5.89}Si_{40.11}$ (Jaussaud N. 2005)) (see Figure 32).

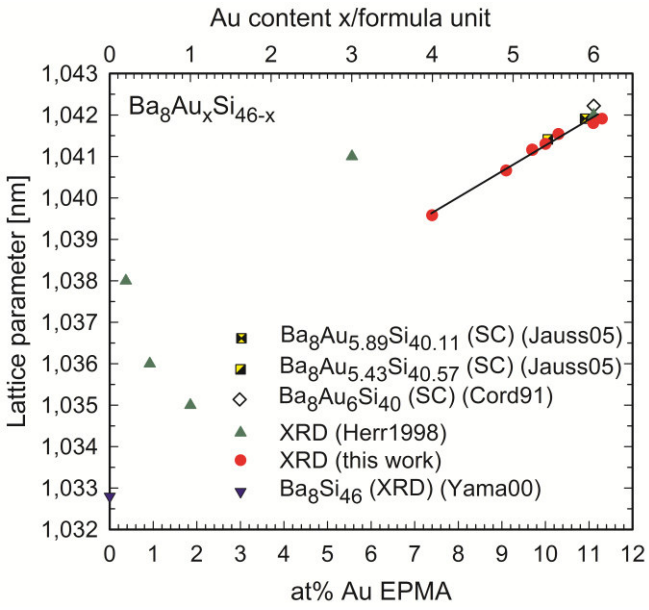

Figure 32: Lattice parameters versus gold content for the alloys $Ba_8Au_xSi_{46-x}$, quenched from 800°C including literature data. The dashed line is a guide for the eye.

Our refinement of the XRD spectra unambiguously located the Ba atoms in the sites 2a (0, 0, 0) and 6c (¼,0,½), Au and Si atoms were found to randomly share the 6d site (¼,½,0), and silicon atoms occupy the sites 16i (x, x, x) and 24k (0, y, z). Cordier et al. (Cordier G. 1991) reported that Au preferentially occupies the 6c site but our XRD refinements are in good agreement with the results of Jaussaud et al. (Jaussaud N. 2005), who reported for 2 single crystals, that minor amounts of Au also occupy the 24k site. No vacancies were encountered. Substitution of silicon by gold atoms in the crystal lattice over the limited homogeneity range leads to Au-dependent atom parameters for x_{Si} in 16i (x, x, x) and y_{Si}, z_{Si} for Si3 atoms in 24k (0, y, z). The results obtained for the clathrate-I series from Rietveld refinement and EPMA are summarized in Table XII.

5.4.1.2 Phase equilibria in the system Ba – Au – Si for 0 to 33.3 at.% Ba

The partial isothermal section at 800°C, evaluated from XRD and EPMA on about 35 alloys, is shown in Figure 33.

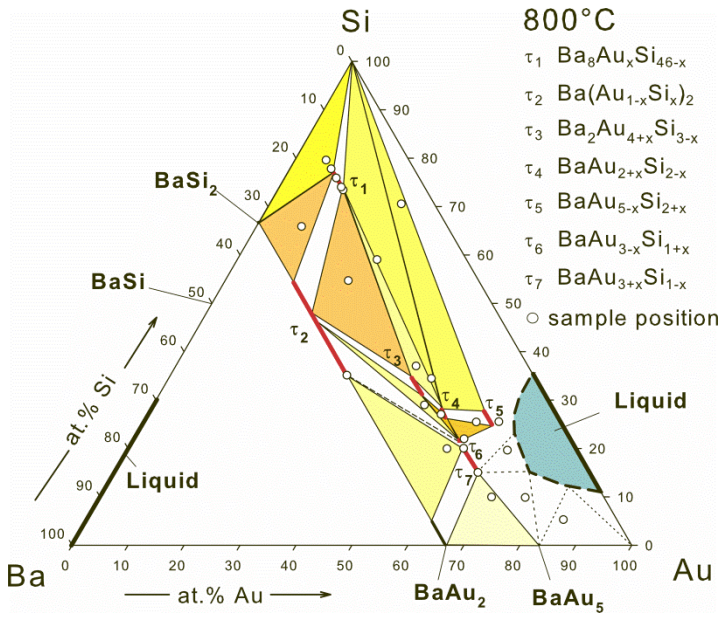

Figure 33: Partial isothermal section for the ternary system Ba - Au - Si at 800°C.

The information concerning the binary phase diagrams Ba-Si and Au-Si is taken von Massalski (Massalski T.B. 1990) and a summary of all the appearing phases at 800°C is given in Table XIII.

Table XIII: Crystallographic data on all solid phases of the ternary system Ba-Au-Si at 800°C.

	Space group	Structure type	Lattice parameter [nm]			Ref.
			a	b	c	
(Si)	$Fd\bar{3}m$	C_{diam}	0.54303	-	-	(Massalski T.B. 1990)
(Au)	$Fm\bar{3}n$	Cu	0.40773(1)	-	-	(Massalski T.B. 1990)
$BaSi_2$	*Pnma*	$BaSi_2$	0.8942(4)	0.6733(3)	1.1555(5)	(Massalski T.B. 1990)
BaSi	*Cmcm*	TlI	0.5042(5)	1.197(1)	0.4142(2)	(Massalski T.B. 1990)
$BaAu_2$	*P6/mmm*	AlB_2	0.4804	-	0.4119	(Bruzzone G. 1970)
$BaAu_5$	*P6/mmm*	$CaCu_5$	0.5690	-	0.4542	(Palenzona A. 1967)
τ_1-$Ba_8Au_xSi_{46-x}$ ($4 \leq x \leq 6$)	$Pm\bar{3}n$	K_4Ge_{23-x}	1.0396(3)-1.0419(1)	-	-	*
τ_2-$BaAu_xSi_{2-x}$ ($0.4 \leq x < 1$)	*P6/mmm*	AlB_2	0.4193(2)-0.4305(1)	-	0.5032(2)-0.490(1)	*

τ_3-$BaAu_{4+x}Si_{3-x}$	oI	unknown	0.65097(4)	0.82267(5)	2.38516(13)	*
τ_4-$BaAu_{2+x}Si_{2-x}$	tP	unknown	1.053	1.053	0.845	*
τ_5-$BaAu_{5-x}Si_{2+x}$	*Pnma*	$BaAu_5Si_2$	0.8935(2)	0.6939(2)	1.0365(2)	*
τ_6-$BaAu_{3-x}Si_{1+x}$	unknown	unknown	-	-	-	*
τ_7-$BaAu_{3+x}Si_{1-x}$	*P*4/*nmm*	$BaAu_3Ge$	0.6488(2)	-	0.5305(2)	*

* This work

At low gold content, τ_1-$Ba_8Au_xSi_{46-x}$ is in equilibrium with silicon and $BaSi_2$ (see Figure 34a).

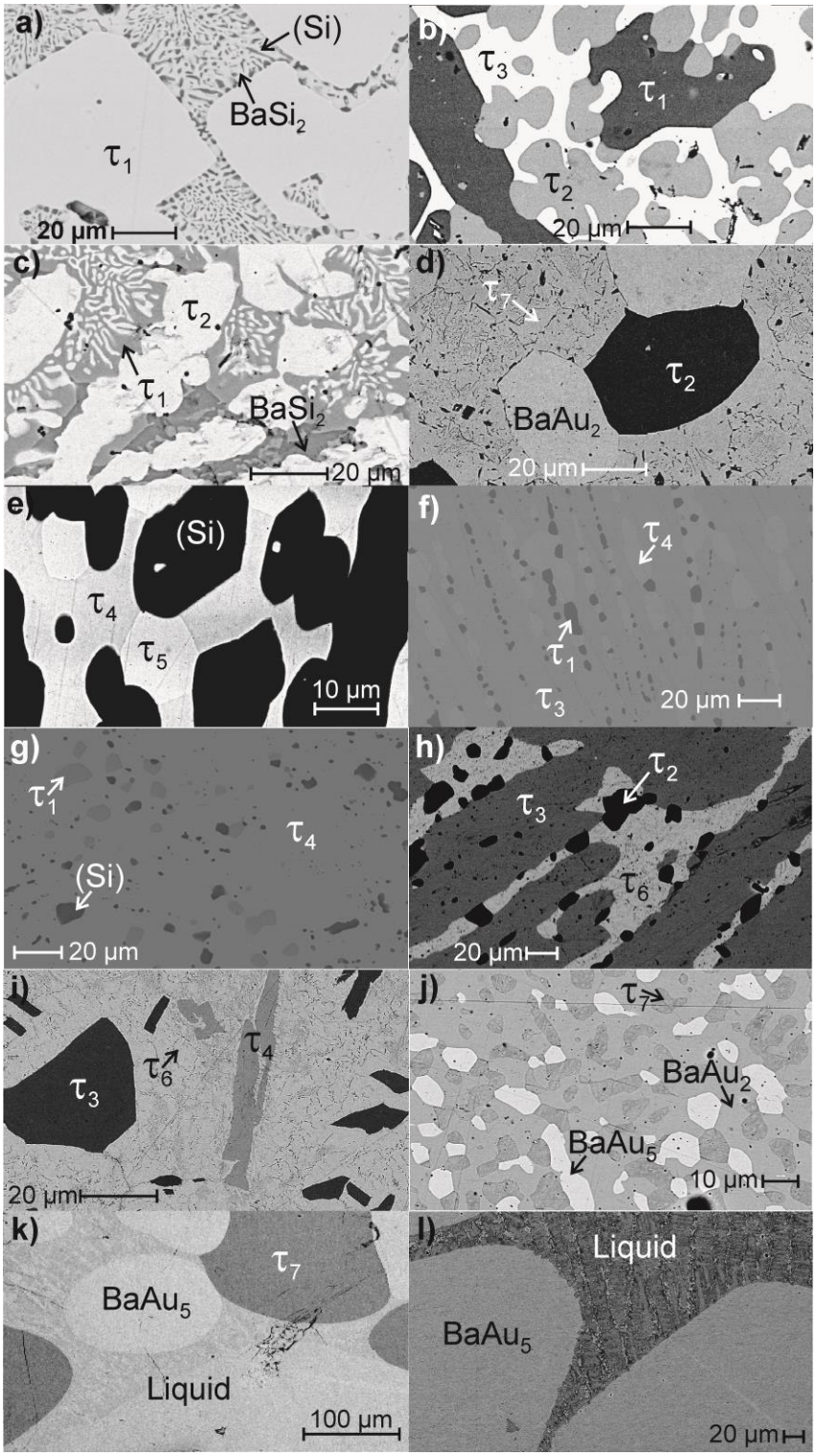

Figure 34: SEM (backscatter detector) images of Ba-Au-Si alloys annealed at 800°C revealing phase equilibria; composition of the phases a, b, c, d, e, f refer to Table XIV (τ_1-clathrate I; τ_2-$Ba(Au_{1-x}Si_x)_2$; τ_3-$Ba_2Au_{4+x}Si_{3-x}$; τ_4-$BaAu_{2+x}Si_{2-x}$; τ_5-$BaAu_{5-x}Si_{2+x}$; τ_6-$BaAu_{3-x}Si_{1+x}$; τ_7-$BaAu_{3+x}Si_{1-x}$).

At higher gold content, a three-phase equilibrium between τ_1, $BaSi_2$ and τ_2-$Ba(Au_{1-x}Si_x)_2$ (AlB_2 type) is formed (see Figure 34c). τ_2 exhibits a quite large homogeneity region, extending from $BaAu_{0.4}Si_{1.6}$ (a = 0.4193(2) and c = 0.5032(0) nm) to $BaAu_{0.9}Si_{1.1}$ (a =

0.4353(4) and c = 0.4853(0) nm), in all cases with c/a~1.1. The Rietveld refinement for $BaAu_{0.9}Si_{1.1}$ as the main phase is shown in Figure 35.

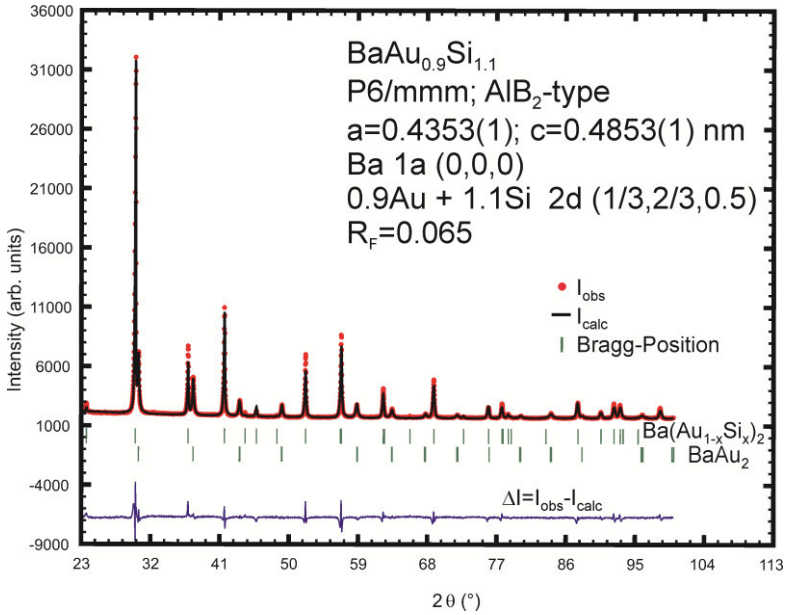

Figure 35: Rietveld refinement for τ_2-$Ba(Au_{1-x}Six)_2$ (AlB_2 type, x = 0.55) as the main phase with less than 3% of $BaAu_2$.

Besides $BaAu_{0.9}Si_{1.1}$, small amounts of $BaAu_2$ (< 2%) and traces of τ_7-$BaAu_{3+x}Si_{1-x}$ (as seen in EPMA, but no additional peaks present in the XRD spectra) can be found in the sample. The SEM picture of a sample (20.8 at.% Ba, 56.2 at.% Au, 23 at.% Si) representing this three-phase equilibrium is shown in Figure 34d. $BaAu_2$ (c/a~0.88, AlB_2 type) solves about 7.5 at.% Si at 800°C. Both compounds with 33.3 at.% Ba, $BaAu_2$ and τ_2, oxidize on air. Five further new ternary phases were encountered in the Au-Ba-Si system at 800°C. τ_3-$Ba_2Au_{4+x}Si_{3-x}$ (formula derived from EPMA measurements) exhibits a homogeneity range of only a few atomic percent of gold at 800°C with hitherto unknown structure type. At the gold-rich end of the solubility range of τ_3, a three-phase equilibrium exists among τ_3, τ_4-$BaAu_{2+x}Si_{2-x}$ (structure unknown) and τ_6-$BaAu_{3-x}Si_{1+x}$ with also unknown structure type. Figure 34e shows the three-phase equilibrium between (Si), τ_4 and τ_5-$BaAu_{5+x}Si_{2-x}$ (own structure type), which has a small homogeneity region at 800°C. Binary $BaAu_5$, τ_5 and τ_7 were found to be in equilibrium with liquid at 800°C. The crystal structure of

τ_7-$BaAu_{3+x}Si_{1-x}$ ($BaAu_3Ge$ type) has been determined from single crystal analysis. The crystal structures of the new ternary phases τ_5 and τ_7 will be discussed in detail in the next chapter. The results received from EPMA and X-ray phase analysis are summarized in

Table XIV and the SEM pictures representing all the three-phase equilibria are shown in Figure 34.

Table XIV: EPMA and X-ray phase analysis data for ternary three phase alloys (quenched from 800°C) in the system Au-Ba-Si; a, b, c, d, e and f correspond to the SEM images of Figure 34.

Nominal composition (at.%)			X-ray phase analysis	Structure type	Lattice parameter [nm]			Composition EPMA (at.%)		
Au	Ba	Si			a	b	c	Au	Ba	Si
5.6	14.8	79.6	(Si)	C_{diam}	0.5429(2)	0.5429(2)	0.5429(2)	0.0	0.0	100.0
			τ_1	K_4Ge_{23-x}	1.03963(2)	1.03963(2)	1.03963(2)	8.3	14.2	77.5
	a)		$BaSi_2$	$BaSi_2$	-	-	-	1.0	31.5	67.5
22.0	23.2	54.8	τ_1	K_4Ge_{23-x}	1.04178(2)	1.04178(2)	1.04178(2)	11.5	15.6	72.9
			τ_2	AlB_2	0.42370(3)	0.42370(3)	0.49653(5)	17.8	33.6	48.6
	b)		τ_3	-	-	-	-	43.3	21.7	35
8.0	26.0	66.0	τ_2	AlB_2	0.4193(2)	0.4193(2)	0.50320(4)	12.7	32.3	55.0
			τ_1	K_4Ge_{23-x}	1.04066(2)	1.04066(2)	1.04066(2)	8.6	14.9	76.5
	c)		$BaSi_2$	$BaSi_2$	-	-	-	0.0	32.2	67.8
57.0	20.0	23.0	τ_2	AlB_2	0.43051(6)	0.43051(6)	0.4901(1)	32.3	31.8	35.9
			τ_7	$BaAu_3Ge$	0.64588(6)	0.64588(6)	0.52989(4)	60.3	19.2	20.5
	d)		$BaAu_2$	AlB_2	-	-	-	62.0	31.3	6.7
23.5	5.9	70.6	(Si)	C_{diam}	0.54340(7)	0.54340(7)	0.54340(7)	0.0	0.0	100.0
			τ_5	$BaAu_5Si_2$	-	-	-	60.0	12.5	27.5
	e)		τ_4	unknown	-	-	-	54.5	17.1	28.4
43.0	20.0	37.0	τ_1	K_4Ge_{23-x}	-	-	-	11.3	15.5	72.2
			τ_3	unknown	-	-	-	43.4	22.0	34.6
	f)		τ_4	unknown	-	-	-	52.0	19.7	28.3
47.0	18.5	34.5	(Si)	C_{diam}	-	-	-	0.0	0.0	100.0
			τ_1	K_4Ge_{23-x}	-	-	-	11.3	15.8	72.9
	g)		τ_4	unknown	-	-	-	51.9	20.0	28.1
49.5	22.3	28.2	τ_2	AlB_2	-	-	-	19.6	33.3	47.1
			τ_3	unknown	-	-	-	47.5	21.4	31.1
	h)		τ_6	unknown	-	-	-	58.9	20.2	20.9
52.3	20.7	27.0	τ_3	unknown	-	-	-	46.9	22.1	31.0
			τ_4	unknown	-	-	-	53.5	20.0	26.5
	i)		τ_6	unknown	-	-	-	58.7	20.8	20.5
70.0	20.0	10.0	$BaAu_5$	$CaCu_5$	-	-	-	83.5	16.5	0.0
			$BaAu_2$	AlB_2	-	-	-	67.2	32.8	0.0
	j)		τ_7	$BaAu_3Ge$	-	-	-	65.0	19.0	16.0
76.0	14.0	10.0	$BaAu_5$	$CaCu_5$	-	-	-	84.9	15.1	-

k)			τ_7	$BaAu_3Ge$	-	-	-	65.7	19.1	15.2
			Liquid	-	-	-	-	73.9	11.7	14.4
85.0	9.7	5.3	$BaAu_5$	$CaCu_5$	0.57252(3)	0.57252(3)	0.45333(6)	83.6	16.4	-
l)			Liquid	-	-	-	-	75.7	12.8	11.5
			Au	(Cu)	-	-	-	100	-	-

τ_1-clathrate I; τ_2-$Ba(Au_{1-x}Si_x)_2$; τ_3-$Ba_2Au_{4+x}Si_{3-x}$; τ_4-$BaAu_{2+x}Si_{2-x}$; τ_5-$BaAu_{5-x}Si_{2+x}$; τ_6-$BaAu_{3-x}Si_{1+x}$; τ_7-$BaAu_{3+x}Si_{1-x}$

5.4.1.3 Crystal structure of the new ternary compounds

5.4.1.3.1 τ_5-$BaAu_5Si_2$ ($BaAu_5Si_2$-type)

The crystal structure of τ_4-$BaAu_5Si_2$ was solved by direct methods and refined to R = 0.029 with residual electron densities smaller than ± 4.4 $e^-/Å^3$, yielding a completely ordered atom arrangement (see Table XV).

Table XV: X-Ray single crystal data for τ_5-$BaAu_5Si_2$ at RT (Anisotropic displacement parameters in $[10^{-2}nm^2]$).

Parameter/compound	
Space Group	*Pnma*
Composition from EPMA	$Au_{63.5}Ba_{12.9}Si_{23.6}$ (at.%)
Formula from refinement	$BaAu_5Si_2$
a, b, c [nm]	0.8935(2), 0.6939(2), 1.0365(2)
μ_{abs} $[mm^{-1}]$	119.97
V (nm^3)	0.6427
ρ_x (gcm^{-3})	12.18
Reflections in refinement	$1355 \geq 4\sigma(F_o)$ of 1512
Number of variables	44
$R_F^2 = \Sigma\|F_0^2-F_c^2\|/\Sigma F_0^2$	0.029
R_{Int}	0.065
wR2	0.066
GOF	1.131
Extinction (Zachariasen)	0.00080(6)
Residual density $e^-/Å^3$; max; min	4.44; -4.08
Atomic parameters	
Au1 in 8d (*x,y,z*); occ.	1.011(4)
x, y, z	0.09011(3), 0.04489(4), 0.60857(2)
U_{11}; U_{22}; U_{33}	0.0102(2); 0.0122(1); 0.0139(1)
Au2 in 8d (*x,y,z*); occ.	1.004(4)

x, y, z			0.09919(3), 0.03388(4), 0.16865(3)		
U_{11}; U_{22}; U_{33}			0.0118(1); 0.0131(1); 0.0184(1)		
Au3 in 4c (*x*,1/4,*z*); occ.			1.002(4)		
x, z			0.33198(5), 0.31754(4)		
U_{11}; U_{22}; U_{33}			0.0090(2); 0.0163(2); 0.0154(2)		
Ba in 4c (*x*,1/4,*z*); occ.			0.991(4)		
x, *z*			0.22133(8), 0.89391(5)		
U_{11}; U_{22}; U_{33}			0.0122(3); 0.0137(3); 0.0134(2)		
Si1 in 4c (*x*,1/4,*z*); occ.			1.09(2)		
x, *z*			0.0613(4), 0.3804(2)		
U_{11}; U_{22}; U_{33}			0.008(1); 0.009(1); 0.015(1)		
Si2 in 4c (*x*,1/4,*z*); occ.			1.03(2)		
x, *z*			0.3238(3), 0.5516(3)		
U_{11}; U_{22}; U_{33}			0.009(1); 0.011(1); 0.015(1)		
Interatomic distances [nm]; standard deviations < 0.0001					
Ba –	2Au2	0.3398	Au2	1Au3	0.2993
	–2Au2	0.3450		–1Au2	0.2999
	–2Au1	0.3461		–1Ba	0.3398
	–2Au1	0.3485		–1Ba	0.3450
	–2Au2	0.3536		–1Ba	0.3536
	–2Au1	0.3589	Au3	1Si2	0.2428
	-2Au3	0.3591		–1Si1	0.2505
	–1Si2	0.3596		–2Au2	0.2823
Au1	1Si1	0.2456		–1Si1	0.2899
	–1Si2	0.2595		–2Au2	0.2993
	–1Si1	0.2772		–2Au1	0.3060
	–1Au1	0.2837		–2Ba	0.3591
	–1Au1	0.2847	Si1	2Au1	0.2456
	–1Au2	0.2897		–1Au3	0.2505
	–1Au2	0.2914		–2Au2	0.2680
	–1Au3	0.3060		–2Au1	0.2772
	–1Ba	0.3461		–1Si1	0.2899
	–1Ba1	0.3485		–1Ba	0.2942
	–1Ba1	0.3589	Si2	2Au2	0.2413
Au2	1Si2	0.2413		–1Au3	0.2428
	–1Si1	0.2680		–2Au1	0.2595
	–1Au3	0.2823		–1Si1	0.2942

–1Au1	0.2897	–1Ba	0.3596
–1Au1	0.2914		

The crystal structure of τ_4-$BaAu_5Si_2$ adopts the orthorhombic primitive space group *Pnma* as the highest possible crystal symmetry (a = 0.8935(2), b = 0.6939(2) and c = 1.0365(2) nm), revealing Ba, Au and Si atoms in the crystallographic site 4c (x,¼,z) and Au atoms in the site 8d (x,y,z). Refinement of the occupancy of all atom sites and anisotropic atomic displacement parameters show full occupation in all Wyckoff positions (see Table XV). The structure in a three-dimensional view is shown in Figure 36a emphasizing on the Ba and Au3 polyhedra.

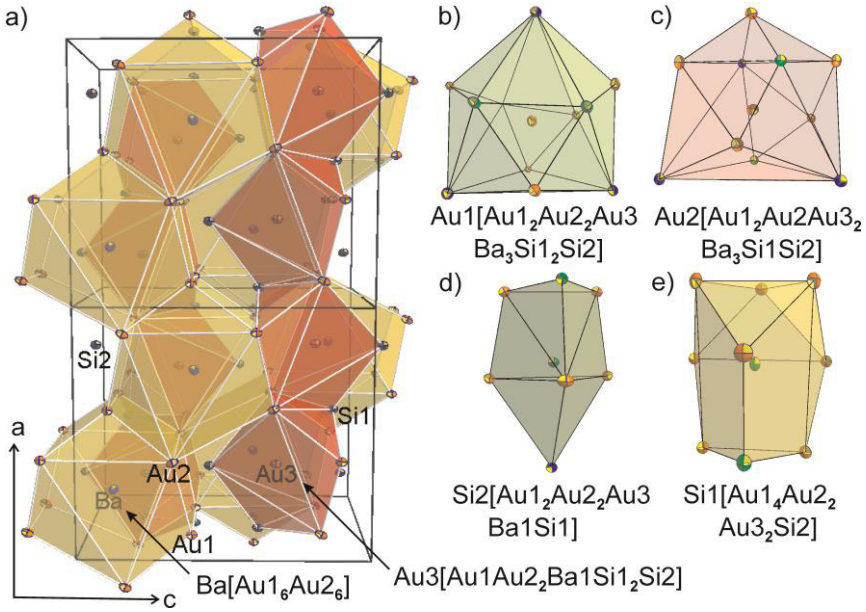

Figure 36: **Crystal structure of τ_5-$BaAu_5Si_2$ (own structure type) (a) three dimensional view (2 unit cells in x direction) with anisotropic displacement parameters from single crystal refinement and polyhedra around the Ba and Au3 atoms; coordination polyhedra around Au1 (b), Au2 (c), Si1 (d) and Si2 (e).**

Each Ba-atom is surrounded by 12 gold atoms and these Ba-polyhedra are interconnected sharing rectangular faces to form chains along the x-direction. The Au3 atoms are surrounded by 3 Si and 6 Au atoms and share triangular faces to build up chains in the same direction. The whole structure can be described by alternating layering of these two chains. The other coordination polyhedra of this structure type are shown in Figure 36b, c, d, e.

5.4.1.3.2 τ_7-$BaAu_3Si$ ($BaAu_3Ge$-type)

The crystal structure of $BaAu_3Si$ was solved employing direct methods and was found to be isotypic with the structure type of $BaAu_3Ge$ (space group *P4/nmm)*. The lattice of this structure type is fully ordered with Ba-atoms occupying the crystallographic site 2b (¾,¼,½), Au-atoms in sites 4d (0,0,0) and 2c (¼,¼,z) and Si-atoms in site 2c (Table XVI).

Table XVI: X-Ray single crystal data for τ_7-$BaAu_3Si$ at RT (anisotropic displacement parameters in [10^2nm^2]).

Parameter/compound	
Space Group	*P4/nmm*
Composition from EPMA	$Au_{60.1}Ba_{21.0}Si_{18.9\ (at.\%)}$
Formula from refinement	$BaAu_3Si$
a; c [nm]	0.6488(2); 0.5305(2)
μ_{abs} [mm^{-1}]	106.99
V (nm^3)	0.2233
ρ_x (gcm^{-3})	11.25
Reflections in refinement	290 ≥ 4σ (F_o) of 311
Number of variables	16
$R_F^2 = \Sigma\|F_0^2-F_c^2\|/\Sigma F_0^2$	0.023
R_{Int}	0.042
wR2	0.062
GOF	1.324
Extinction (Zachariasen)	0.0049(5)
Residual density e$^-$/Å^3 max; min	4.85; -2.85
Atomic Parameters	
Ba in 2b(3/4,1/4,1/2); occ.	1.009(7)
U_{11}; $U_{22}=U_{33}$	0.0113(3); 0.0202(5)
Au1 in 4d(0, 0, 0); occ	0.993(9)
U_{11}; $U_{22}=U_{33}$	0.0235(2); 0.0148(3)
Au2 in 2c(1/4,1/4,*z*); occ.	0.997(5)
z	0.6613 (1)
$U_{11}=U_{22}$; U_{33}	0.0134(2); 0.0158(3)
Si in 2c(1/4,1/4,*z*); occ.	0.995(6)
z	0.2012(6)
$U_{11}= U_{22}$; U_{33}	0.0039(6); 0.0049(5)
Interatomic distances [nm];Standard deviations < 0.0001	

Ba –	4Au2	0.3355
	–8Au1	0.3507
	–4Si	0.3611
Au2 –	1Si	0.2441
	–1Si	0.2864
	–4Au1	0.2914
Au1 –	2Si	0.2530
	–2Au2	0.2914
	– 4Au1	0.3244
Si –	1Au2	0.2441
	–4Au1	0.2530
	–1Au2	0.2864

Although the Au-Si distances are rather short (~ 0.25 nm), full occupancy in all Wyckoff positions was proven during the refinement. Characteristic polyhedra in this structure are a square pyramid around the silicon atoms in 2c (Figure 37a), a distorted "rectangle" around the gold atoms Au1 in 4d (Figure 37c) and a 16-atom coordination polyhedron around the Ba-atoms (Figure 37b).

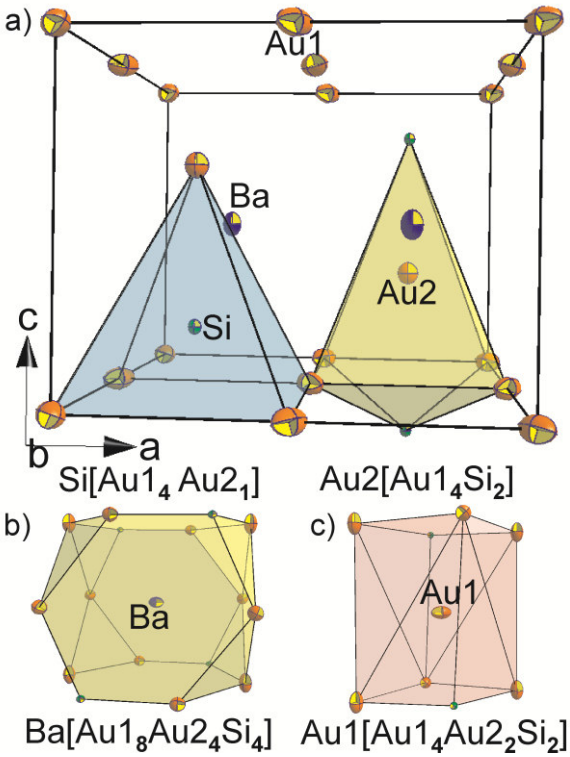

Figure 37: Crystal structure of τ_7-$BaAu_3Si$ ($BaAu_3Ge$ type); (a) three dimensional view of the unit cell with anisotropic displacement parameters from single crystal refinement and the corresponding coordination.

The polyhedra around the Au2 atoms are very similar to those of the isotypic compound $BaAu_3Ge$ with exception of one additional Si atom of the quite short Au-Si distances.

5.4.1.3.2.1 Electrical resistivity of $BaAu_3Si$

Low temperature resistivity measurements (see Figure 38) reveal a rather metallic behavior with a superconducting transition at T_c ~ 1.5 K. An external magnetic field reduces the critical temperature T_c. The upper critical magnetic field is reached by T_c =0. External magnetic fields of ~ 0.25 T suppress superconductivity completely.

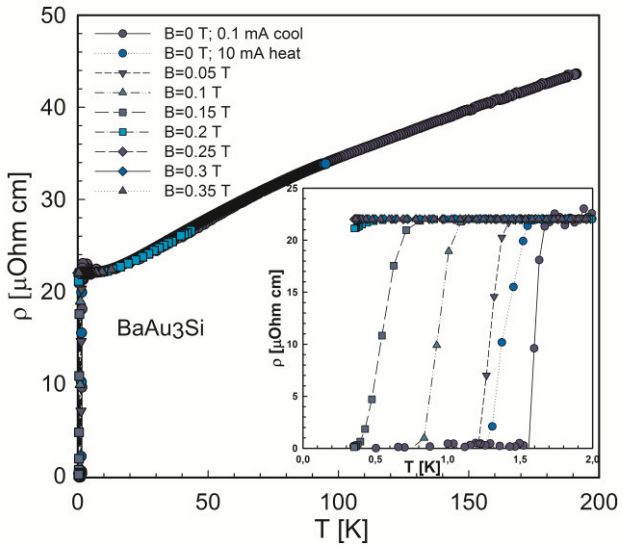

Figure 38: Temperature dependent resistivity of $BaAu_3Si$ for various externally applied magnetic fields.

5.4.1.4 Physical properties of $Ba_8Au_{5.1}Si_{40.9}$

5.4.1.4.1 Temperature dependent thermal conductivity

The temperature dependent thermal conductivity of $Ba_8Au_{5.1}Si_{40.9}$ is shown in Figure 39.

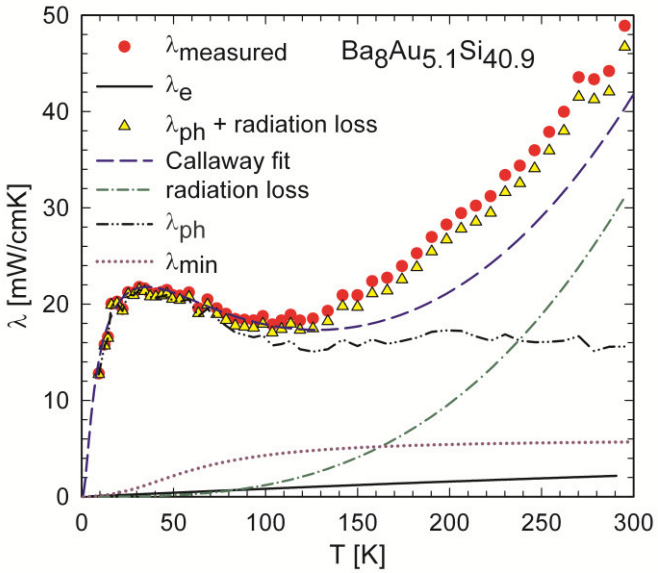

Figure 39: Measured thermal conductivity (red circles), electronic contribution (black solid line) and phonon part (dashed-dotted-dotted black line) of the total thermal conductivity. The blue dashed line is a least squares fit described in the text, the green dashed dotted line is the radiation loss and the dark pink dotted line is the minimum thermal conductivity.

The "glass-like" temperature dependency of λ(T) without a peak at very low temperatures is related to the scattering of both, electrons and heat-carrying phonons on impurities, vacancies, grain boundaries and static defects. The overall values are rather small with the lattice thermal conductivity (λ_{ph}) being the dominant contribution to the overall thermal conductivity.

The electronic contribution to the total thermal conductivity (λ_e, Figure 39) can be derived from the electrical resistivity (Figure 38) using the Wiedemann-Franz law. This, in general, is valid only for free electron systems but used often also for clathrates and other complex materials. The temperature dependency of the lattice thermal conductivity can be modelled according to Callaway (v. B. Callaway J. 1969). A least squares fit to the data is shown in Figure 39. The minimum thermal conductivity in Figure 39 (dark pink dotted line) has been calculated using a formula derived by Cahill and Pohl (Cahill D. 1989)

$$\lambda_{\min} = \left(\frac{3n}{4\pi}\right)^{1/3} \frac{k_B^2 T^2}{h\theta_D} \int_0^{\theta_D/T} \frac{x^3 e^x}{\left(e^x - 1\right)^2} dx \qquad (12)$$

The Debye temperature (θ_D = 290 K) has been taken from a recent publication (R. G. Falmbigl M. 2010) dealing with the thermal expansion of several Si and Ge based clathrate compounds. The number of atoms per unit cell volume, n = 4.8x10^{28}/m^3. The measured thermal conductivity is about 3 times larger than the minimum thermal conductivity.

5.4.1.4.2 Electrical resistivity

The temperature dependency of the electrical resistivity in the temperature range between 4.5 and 1000 K is shown in Figure 40 including literature data for $Ba_8Au_{5.4}Si_{40.6}$ and $Ba_8Au_{5.9}Si_{40.1}$ (Jaussaud N. 2005) in the low temperature range.

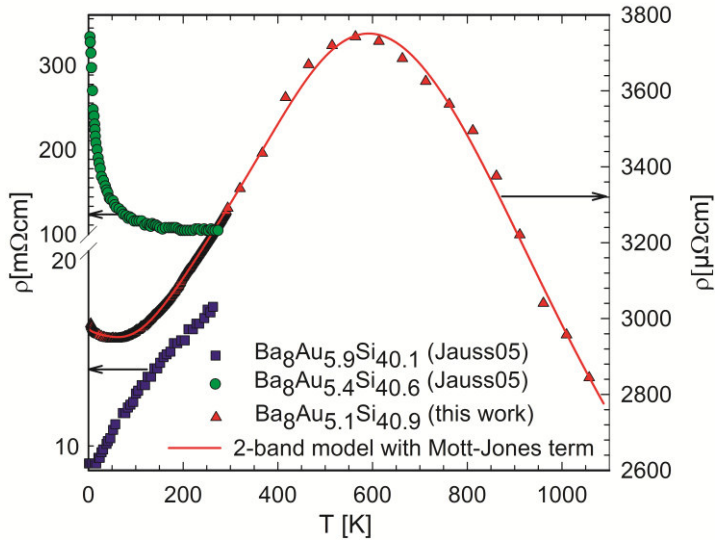

Figure 40: **Temperature dependency of the electrical resistivity (ρ) and literature data. The red solid line is the least squares fit explained in the text.**

$Ba_8Au_{5.4}Si_{40.6}$ is a semiconductor and $Ba_8Au_{5.9}Si_{40.1}$ shows a simple metal-like behaviour in the temperature range up to 300 K with an about 6 times larger resistivity compared to $Ba_8Au_{5.1}Si_{40.9}$.

The electrical resistivity of $Ba_8Au_{5.1}Si_{40.9}$ is characterized by a distinct minimum at very low temperatures and a broad maximum at high temperatures. Such a complex behavior can never be described by the standard Bloch-Grüneisen equation. We adopted a model (Berger S., PhD Thesis 2003) containing the Bloch-Grüneisen formula to account for the electron phonon interaction, but allowing for a temperature dependent charge carrier density $n(T)$. A Mott-Jones term, AT^3, was added to specify scattering of electrons in narrow states (in general, *d*-like) near to the Fermi energy (Berger S., PhD Thesis 2003),

$$\rho_{ph} = R\left(\frac{T}{\theta_D}\right)^5 \int \frac{z^5}{\left(e^z-1\right)\left(1-e^{-z}\right)} \qquad (13)$$

and

$$\rho(T) = \frac{\rho_0 n_0 + \rho_{ph}}{n(T)} + \frac{AT^3}{n(T)} \quad . \qquad (14)$$

In equations (13) and (14), ρ_0 is the residual resistivity (T→0), n_0 the residual charge carrier density, R the electron-phonon interaction constant and θ_D is the Debye

temperature. The high temperature maximum can be described quite well with this model (see fit in Figure 40). The decrease of the resistivity beyond the maximum implies an increase of the charge carrier density caused by thermal excitations across the band gap.

5.4.1.4.3 Thermopower, Hall Effect and dimensionless Figure of Merit

The thermopower of $Ba_8Au_{5.1}Si_{40.9}$ has been measured in the temperature range between 4.5 and 1000 K. The measurement results are shown in Figure 41a including literature data (Jaussaud N. 2005) for $Ba_8Au_{5.4}Si_{40.6}$ and $Ba_8Au_{5.9}Si_{40.1}$.

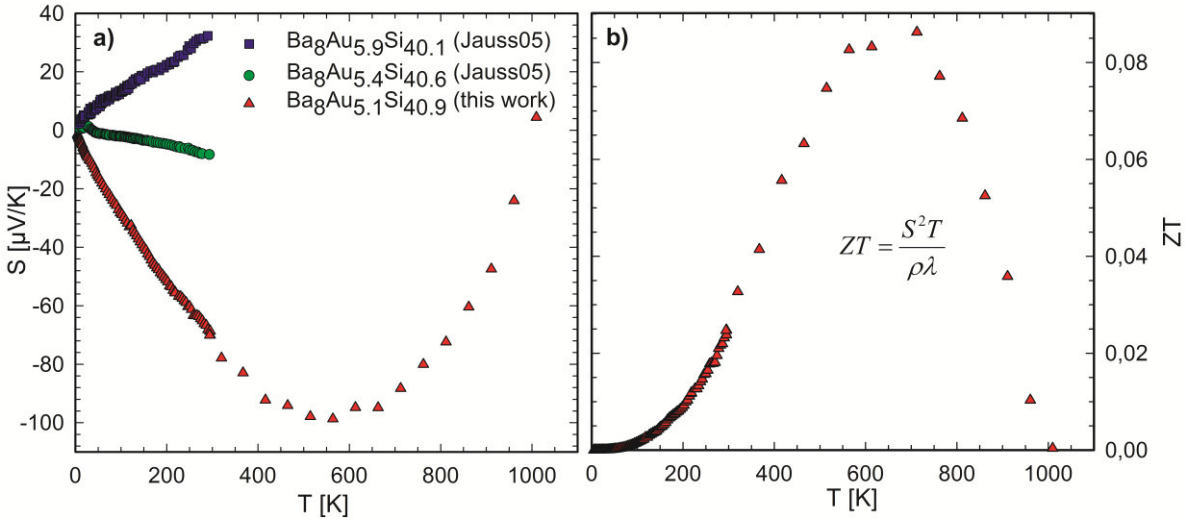

Figure 41: a) Temperature dependency of the thermopower (S) and literature data b) Shows the calculated temperature dependency of the dimensionless figure of merit ZT for $Ba_8Au_{5.1}Si_{40.9}$.

The thermopower values of $Ba_8Au_{5.4}Si_{40.6}$ are very small and negative over the whole temperature range (see Figure 41a; S_{max}(300 K) ~ -10 µV/K) whereas the measured thermopower values of $Ba_8Au_{5.9}Si_{40.1}$ are slightly larger and positive (S_{max}(300 K) ~ 35 µV/K), indicating a hole dominated transport. $Ba_8Au_{5.1}Si_{40.9}$ is also an n-type material, in which electrons are the main charge carriers, but its thermopower value at 300 K is about 6 times larger than that of $Ba_8Au_{5.4}Si_{40.6}$. For temperatures well below 500 K, S(T) behaves almost linearly before reaching a maximum at higher temperatures. Using Mott's formula,

the charge carrier density n = 1.65×10^{20} cm^{-3} can be calculated. At high temperatures, however, charge carriers are excited across the gap in the electronic density of states, hence, *n(T)* increases. As a consequence S(T) starts to decrease. Note, the maximum in S(T) coincides with the maximum in ρ(T), suggesting the very same physical origin.

In order to confirm the obtained charge carrier concentration, Hall measurements were done in the temperature range from 4.5 to 350 K (9 and 5 T) on a Physical Property Measurement System (PPMS). The charge carrier concentration (electrons) has been calculated from the Hall coefficient $n = -1/eR_H$ (Figure 42b) and has been found to be in perfect agreement with the estimation from the slope of the $S(T)$ curve.

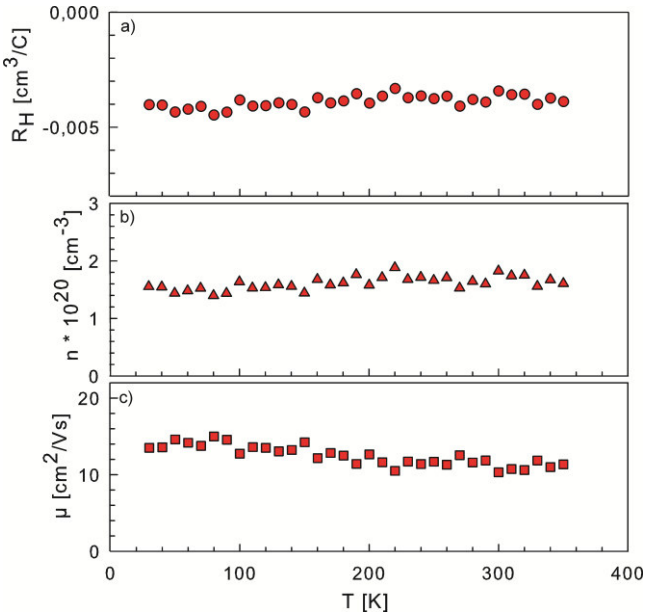

Figure 42: **a) Hall coefficient (RH), b) charge carrier concentration (n) and c) Hall mobility (μ) for $Ba_8Au_{5.1}Si_{40.9}$.**

The negative values of the Hall coefficients (Figure 42a) are also in good agreement with the Seebeck coefficient. From the Hall coefficient and the electrical resistivity we also calculated the Hall mobility $\mu = R_H / \rho$, which is about 12 cm^2/Vs at room temperature (Figure 42c).

The calculated temperature dependency of the figure of merit can be seen in Figure 41b. As a high ZT (>>1) requires large thermopower, good electrical conductivity and low thermal conductivity, the maximum ZT value of 0.09 at 800°C is currently too low for any thermoelectric applications. The low ZT results from the quite high electrical resistivity and a small thermopower.

5.4.1.5 Summary

Phase relations at 800°C within the ternary system Ba-Au-Si up to 33.3 at.% Ba have been derived. Equilibria are characterized by the clathrate type-I solid solution, $Ba_8Au_xSi_{46-x}$, extending at 800°C from $Ba_8Au_4Si_{42}$ (a=1.039 nm) to $Ba_8Au_6Si_{40}$ (a=1.042

nm). Cubic primitive symmetry (space group $Pm\bar{3}n$) was confirmed for the entire clathrate solution by x-ray powder diffraction. Consistent with a monotonous almost linear rise of the lattice parameters with increasing gold content, atom site preferences from X-ray refinement define that gold atoms preferably occupy the 6d site in random mixture with Si atoms.

The phase equilibria at 800°C reveal a total of seven ternary phases in the investigated region up to 33.3 at.% barium. The homogeneity range has been established for $Ba(Au_{1-x}Si_x)_2$ (AlB_2-type; extends from $BaAu_{0.4}Si_{1.6}$ to $BaAu_{0.9}Si_{1.1}$). $BaAu_{2+x}Si_{2-x}$ exhibits a very small homogeneity range (x = 0.6-0.7) and two other ternary phases exist at about 22 at.% Ba, 52 at.% Au and 28 at.% Si and 20 at.% Ba, 58 at.% Au and 22 at.% Si. The crystal structures of two further novel phases in the gold-rich part have been determined from single crystal X-ray data: $BaAu_{3+x}Si_{1-x}$ with $BaAu_3Ge$-type (space group *P4/nmm,* x=0: a=0.6448(2), c=0.5305(2) nm) and $BaAu_{5+x}Si_{2-x}$ (own structure type, space group *Pnma*, x=0: a=0.8981(2), b=0.7106(2) and c=1.0363(2) nm). $BaAu_3Si$ has been found to be superconducting from resistivity measurements with $T_c \sim 1.5$ K.

5.5 THE TERNARY SYSTEM Ba-Au-Ge

Although several research groups have dealt with compounds from the Ba - Au - Ge system ((Cordier G. 1991), (Johnsen S. 2007), (H. M. Anno H. 2005), (Herrmann RFW 1999), (Zhang H. 2011)) there is still a lack not only on the phase equilibria in the ternary system but also on the homogeneity range of the type I clathrate solid solution $Ba_8Au_xGe_{46-x-y}\square_y$ at a defined temperature. Electrical resistivity, magnetic susceptibilities, the density of states at the Fermi level as well as the band gap have been elucidated for $Ba_8Au_6Ge_{40}$ (Herrmann RFW 1999), for which X-ray data seem to confirm a full atom order ((Cordier G. 1991), (Johnsen S. 2007)) without superstructure formation in contrast to binary $Ba_8Ge_{43}\square_3$ with an 8-fold enlargement of the basic clathrate type I unit cell ((C. J. Carrillo-Cabrera W. 2000), (B. S. Carrillo-Cabrera W. 2004), (N.L.

Okamoto 2006)). However no information on vacancy/atom distribution for x<6 has hitherto been reported. Resistivity, thermopower and Hall effect have been studied in detail for alloys $3 \leq x \leq 6$ revealing n- and p-type behavior (*n*-type for *x*=3 to 5, *p*-type for *x*=5 to 6) (H. M. Anno H. 2005). Besides the clathrate type I a ternary compound $BaAu_{3.16}Ge_{0.84}$ was synthesized by melting the elements in Al_2O_3 crucibles under an argon atmosphere at about 1300°C and reported to be isotypic with the $ThCr_2Si_2$ structure type, a = 0.465 and c = 1.056 nm (May N. 1972).

Details on the vacancy/atom distribution throughout the homogeneity region of the clathrate-I phase are given in this part together with the derived phase equilibria at 800°C for the composition range from 0 to 33.3 at.% barium. The crystal structures and homogeneity ranges of ternary phases in the range from 0 to 33.3 at.% Ba have been determined. Furthermore thermoelectric performance of $Ba_8Au_6Ge_{40}$ has been tested for the temperature range from 4.2 to 800 K and resistivity has been measured for the new compound $BaAu_3Ge$.

5.5.1 Results and discussion

5.5.1.1 The clathrate type I solid solution $Ba_8Au_xGe_{43-x-y}\square_y$ at 800°C

The solubility range of the ternary type I clathrate was studied by XPD and EPMA (Table XVII) on a series of samples with nominal composition $Ba_8Au_xGe_{46-x}$ (x = 1, 2, 3, 4, 5, 6, 8).

Table XVII: Composition and crystallographic data from combined EPMA and Rietveld analyses for the clathrate type I solid solution $Ba_8Au_xGe_{43-x-y}\square_y$.

Nominal composition	EPMA (at.%) Ba	Au	Ge	Accepted composition[a]	Lattice parameter [nm]	Ge2 in 16i (x,x,x)	Ge31 in 24k (0,y,z); occ.	Ge32 24k (0,y,z); occ.
$Ba_8Au_1Ge_{45}$	15.2	2.4	82.4	$Ba_8Au_{1.3}Ge_{42}\square_{2.7}$	1.06820(2)	0.1837(1)	0.1118(5), 0.3062(5); 0.540(5)	0.1312(8), 0.3331(7); 0.460(5)
$Ba_8Au_2Ge_{44}$	15.6	4.3	80.1	$Ba_8Au_{2.2}Ge_{41.4}\square_{2.4}$	1.07081(2)	0.1830(1)	0.1115(8), 0.3033(9); 0.54(1)	0.1260(8), 0.3269(7); 0.46(1)
$Ba_8Au_{3.5}Ge_{42.5}$	15.3	7.2	77.5	$Ba_8Au_{3.8}Ge_{40.8}\square_{1.4}$	1.07550(3)	0.1831(1)	0.118(1), 0304(1); 0.54(1)	0.122(1), 0.321(1); 0.46(1)

$Ba_8Au_4Ge_{42}$	15.1	8.4	76.5	$Ba_8Au_{4.4}Ge_{40.3}\square_{1.3}$	1.07726(2)	0.1835(2)	0.113(2), 0.304(2); 0.53(1)	0.123(2), 0.314(2); 0.47(1)
$Ba_8Au_{5.5}Ge_{40.5}$	15.1	10.7	74.2	$Ba_8Au_{5.6}Ge_{40}\square_{0.4}$	1.07965(2)	0.1829(2)	0.112(1), 0.296(2); 0.58(2)	0.126(2), 0.315(1); 0.42(2)
$Ba_8Au_6Ge_{40}$	14.8	11.1	74.1	$Ba_8Au_6Ge_{40}$	1.07979(1)	0.1828(2)	0.1171(3), 0.3092(3)	-

[a] from Rietveld refinement introducing the Au content in the 6d site from the corresponding EPMA data

In all cases the spectra could be fully indexed on the basis of a cubic clathrate type I lattice (a ≈ 1.07 nm) with minor amounts of Ge (< 2.2%). No extra reflections for a larger unit cell such as a' = 2a as reported for $Ba_8Ge_{43}\square_3$ ((B. S. Carrillo-Cabrera W. 2004), (N.L. Okamoto 2006)) were observed in $Ba_8Au_xGe_{46-x}$ for $1 \leq x \leq 6$ by XPD and XSCD. Starting from binary $Ba_8Ge_{43}\square_3$ the maximal solubility for gold at 800°C was found to be 6 gold atoms per formula unit (Figure 43).

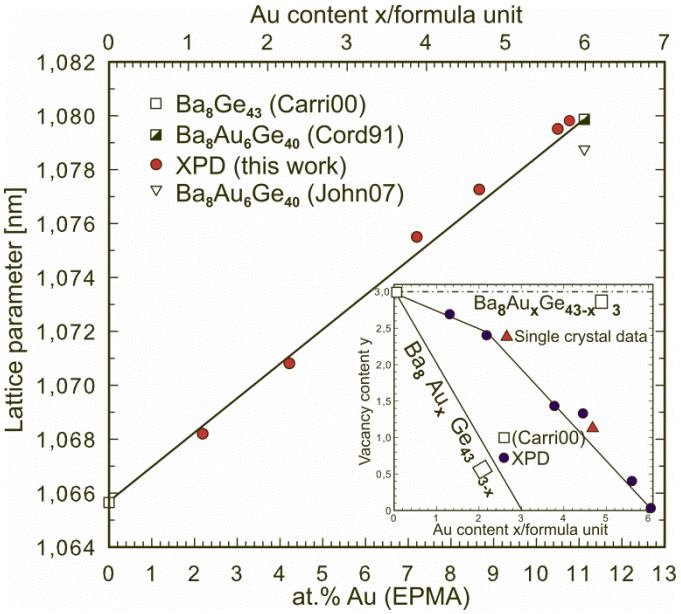

Figure 43: Lattice parameters vs. Au-content for the clathrate type I solid solution $Ba_8Au_xGe_{46-x-y}\square_y$; the inset shows the filling of vacancies with increasing gold content derived from X-ray Rietveld refinement and single crystal data.

The lattice parameters show a linear increase with increasing gold content with some small positive deviation at higher gold contents. Samples close to the solubility limit, yield lattice parameters, which are close to that reported by Cordier and Woll (Cordier G. 1991) for a single crystal of stoichiometric $Ba_8Au_6Ge_{40}$ (melted at 1300°C and cooled at

100 K/hr; a = 1.07987(7) nm). Structure analyses by Cordier et al.((Cordier G. 1991) XSCD) and Johnsen et al. ((Johnsen S. 2007) XPD) agree on the fact that Au preferentially occupies the 6d site in $Ba_8Au_6Ge_{40}$. X-ray single crystal data for $Ba_8Au_{4.6}Ge_{40.3}\square_{1.1}$ (Table XVIII) show a full occupancy of both Ba sites whereas a random mixture of Au, Ge atoms and vacancies occupies the 6d site (¼,½,0).

Table XVIII: X-Ray single crystal data for κ_1-$Ba_8Au_xGe_{46-x-y}\square_y$ (x=4.6, y=1.1) at RT, (Anisotropic displacement parameters in [$10^{-2}nm^2$]).

Parameter/compound	
Space group	$Pm\bar{3}n$
Structure type	K_4Ge_{23-x}
Formula from refinement	$Ba_8Au_{4.6}Ge_{40.3}\square_{1.1}$
a [nm]	1.0791(2)
μ_{abs} [mm^{-1}]	44.74
V (nm^3)	1.2566
ρ_x (gcm^{-3})	6.52
Reflections in refinement	$460 \geq 4\sigma(F_o)$ of 575
Number of variables	24
$R_F^2 = \Sigma\|F_0^2-F_c^2\|/\Sigma F_0^2$	0.022
R_{Int}	0.027
wR2	0.039
GOF	1.068
Extinction (Zachariasen)	0.0006(5)
Residual density $e^-/Å^3$; max; min	1.07; -0.77
Atom parameters	
Ba1 in 2a (0,0,0); occ.	1.01(1)
$U_{11}= U_{22}=U_{33}$	0.0125(2)
Ba2 in 6c (1/4,0,1/2); occ.	1.02(1)
$U_{11}= U_{22}$; U_{33}	0.0303(4); 0.0461(4)
M in 6d (1/4,0,1/2); occ.	0.77Au* + 0.05Ge + 0.18(1)□
$U_{11}= U_{22}$; U_{33}	0.0238(2); 0.0122(1)
Ge2 in 16i (*x*,*x*,*x*); occ.; *x*	1.00; 0.1834(1)
$U_{11}=U_{22}=U_{33}$	0.0131(1)
Ge31 in 24k (0,*y*,*z*); occ.	0.831(3)
y, *z*	0.1171(1), 0.3062(1)
U_{11}; U_{22}; U_{33}	0.0147(2); 0.0152(5); 0.009(1)
Ge32 in 24k (0,*y*,*z*); occ.	0.169(3)
y, *z*	0.1276(7), 0.3315(6)
U_{11}; $U_{22}=U_{33}$	0.0147(2); 0.0152(5); 0.009(1)
Interatomic distances with standard deviations < 0.0004	

Ba1 –	8Ge2	0.3429	Ge2–	–3Ge32	0.2571
	–12Ge31	0.3521		–1Ba1	0.3430
	–12Ge32	0.3713	Ge31–	1Ge32	0.0194
Ba2 –	8Ge32	0.3560		–1Ge31	0.2531
	–8Ge31	0.3651		–2Ge2	0.2477
	–4M	0.3815		–1M	0.2551
	–8Ge2	0.4013		–1Ba1	0.3521
	–4Ge31	0.4158		–2Ba2	0.3651
	–4Ge32	0.4174	Ge32–	1Ge31	0.0352
M –	4Ge32	0.2371		–1M	0.2371
	–4Ge31	0.2551		–2Ge2	0.2571
	–4Ba2	0.3815		–1Ge31	0.2579
	–8Ge2	0.4013		–1Ge32	0.2614
Ge2–	3Ge31	0.2477		–2Ba2	0.3560
	–1Ge2	0.2486		–1Ba1	0.3713

*Au content was fixed after EPMA

Because refinement of occupancies for three species in one site is not reliable, the Au content was fixed from EPMA measurements. The occurrence of vacancies in 6d leads to a disturbance in the neighbouring 24k site (occupied by Ge3 atoms): the atomic displacement parameters (ADPs) reveal strong anisotropy, which disappears with vanishing 6d defects. A Difference Fourier calculated for the clathrate structure without the 24k Ge atoms (see Figure 44a) documents a splitting of the Ge3 atom into two positions (Ge31 and Ge32) with slightly different coordinates. It should be noted that the occupancy of Ge32 (occ.=0.17, Table XVIII) directly correlates with the amount of vacancies in the 6d site (occ.=0.18). The variation of the free parameters y and z for the site 24k (0, y, z) for Ge31 and Ge32 with increasing Au content is shown in Figure 44b.

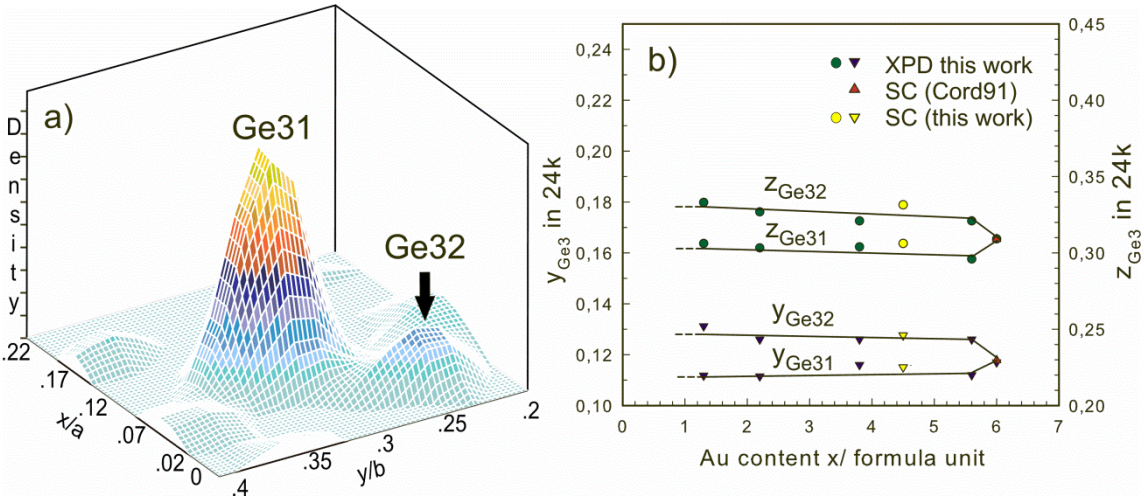

Figure 44: a) Three dimensional view of the contour plot of the electron density (Ge in 24k) from a difference Fourier map for $Ba_8Au_{4.6}Ge_{40.3}\square_{1.1}$; b) Au content x per formula unit vs. compositional parameters y and z for the split Ge3 site (0, y, z) in $Ba_8Au_xGe_{46-x-y}\square_y$.

This structural model was successfully used for Rietveld refinement of the X-ray diffraction spectra of several clathrate compositions $Ba_8Au_xGe_{46-x}$ (x = 1, 2, 3.5, 4, 5.5, 6). The XPD refinement in all cases confirmed the Ba atoms in sites 2a (0, 0, 0) and 6c (¼,0,½), Ge atoms in the sites 16i (x, x, x) and 24k (0, y, z), whereas Au, Ge atoms and vacancies can be found at 6d (¼,½,0). The refinement of XPD intensities for the sample with x=6 showed, that a small amount of gold (~1.5%) also enters the 24k site in agreement with the findings of Johnsen et al. (Johnsen S. 2007). Table XVII summarizes EPMA data and the results of Rietveld refinements. The higher Ba-content in mass %, as derived from EPMA, is related to the occurrence of vacancies in the crystal lattice. The amount of vacancies does not decrease linearly with the increasing gold content but all voids vanish at a composition of 6 atoms of gold per unit cell (Figure 43). The experimental data concerning gold atoms filling the voids are clearly in between two substitution models drawn in Figure 43: (i) substitution of germanium atoms and no filling of vacancies according to $Ba_8Au_xGe_{43-x}\square_3$, and (ii) first all the vacancies are filled prior to Ge/Au exchange. This means that filling vacancies and substitution of Ge by Au atoms takes place simultaneously in quite good agreement with the results reported for other ternary clathrates such as Ba-Zn-Ge (G. A. Koblyuk-M. N. 2007), Ba-Cu-Ge (G. A. Koblyuk-M. N. 2009), Ba-Cd-Ge (B. S. Koblyuk-M. N. 2007), Ba-Ag-Ge.

5.5.1.2 Phase equilibria in the ternary system Ba – Au – Ge for 0 to 33.3 at.% Ba

The partial isothermal section at 800°C is presented in Figure 45 and microstructures of alloys representing the three-phase equilibria are shown in Figure 46.

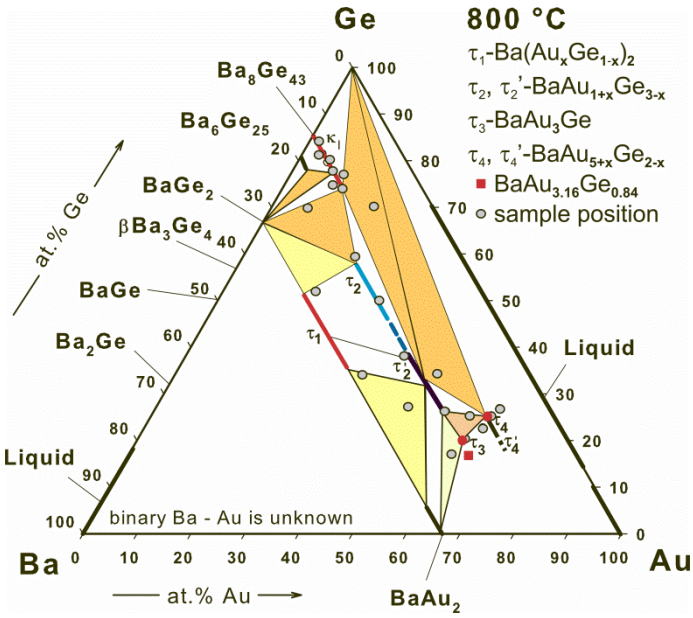

Figure 45: Partial isothermal section at 800°C of the ternary system Ba – Au – Ge.

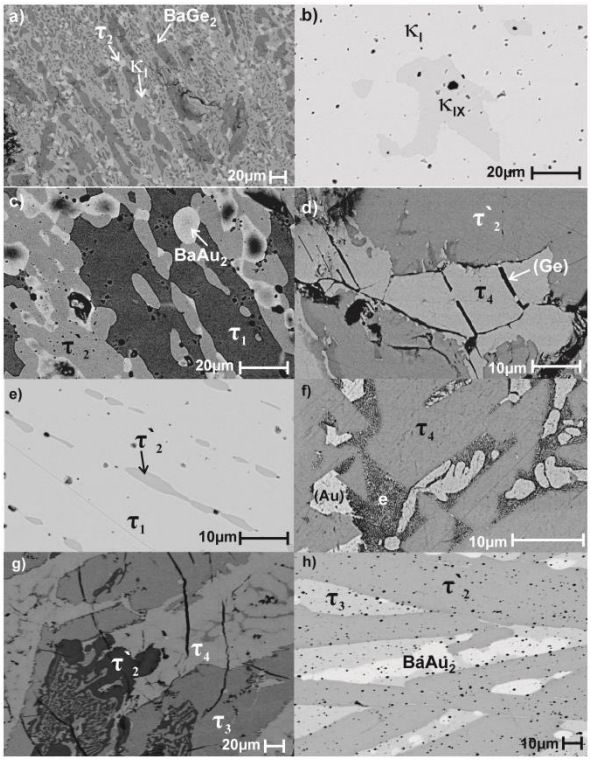

Figure 46: Microstructures of several Ba – Au – Ge alloys (annealed at 800°C) revealing binary or ternary phase equilibria; the composition of the phases in a, b, c, d, e, f, g, h can be found in Table

XIX (κ_I: clathrate I; κ_{IX}: clathrate IX; τ_1: $Ba(Au_{1-x}Ge_x)_2$; τ_2: $BaAu_{1+x}Ge_{3-x}$ ($BaNiSn_3$ type); $\tau`_2$: $BaAu_{1+x}Ge_{3-x}$ ($Ce(Ni,Sb)_4$ type); τ_3: $BaAu_3Ge$; τ_4: $BaAu_{5+x}Ge_{2-x}$; e: eutectic).

The corresponding EPMA data and results from X-ray phase analysis are summarized in Table XIX.

Table XIX: X-ray phase analysis, lattice parameters and phase composition from EPMA (EDX) for Ba-Au-Ge alloys annealed at 800°C; a, b, c, d, e and f refer to the SEM images of Figure 46.

Nominal composition (at.%)			Phase	Structure type	Lattice parameter (nm)			Composition from EPMA (at.%)		
Au	Ba	Ge			a	b	c	Au	Ba	Ge
1.9	14.8	83.3	(Ge)	C_{diam}	0.5658(1)	0.5658(1)	0.5658(1)	0.1	0.2	99.7
			κ_I	K_4Ge_{23-x}	1.06820(2)	1.06820(2)	1.06820(2)	2.4	15.2	82.4
6.9	23.4	69.7	τ_2	$BaNiSn_3$	-	-	-	22.4	20.5	57.1
a)			κ_I	K_4Ge_{23-x}	1.0797(1)	1.0797(1)	1.0797(1)	11.3	15.4	73.4
			$BaGe_2$	$BaSi_2$	0.9072(2)	0.6808(1)	1.1636(4)	0.3	33.0	66.7
5.6	15.0	79.4	κ_{IX}	Ba_6Ge_{25}	1.45598(3)	1.45598(3)	1.45598(3)	2.2	18.0	79.8
b)			κ_I	K_4Ge_{23-x}	1.07550(3)	1.07550(3)	1.07550(3)	7.2	15.3	77.5
17.2	30.9	51.9	τ_2	$BaNiSn_3$	0.4647(1)	0.4647(1)	1.0346(1)	23.1	18.3	58.6
			τ_1	AlB_2	0.4381(1)	0.4381(1)	0.4929(1)	16.2	30.0	53.7
35.0	31.0	34.	τ_2'	$Ce(Ni,Sb)_4$	-	-	-	47.1	20.0	32.9
			τ_1	AlB_2	0.44870(4)	0.44870(4)	0.4754(1)	31.7	32.1	36.2
c)			$BaAu_2$	AlB_2	0.47689(5)	0.47689(5)	0.41867(8)	61.4	33.0	5.4
48.6	17.0	34.4	τ_2'	$Ce(Ni,Sb)_4$	-	-	-	45.7	19.6	34.7
			(Ge)	C_{diam}	-	-	-	0.3	0.2	99.5
d)			τ_4	$BaAu_5Si_2$	-	-	-	62.8	11.8	25.4
39.5	21	39.5	τ_2'	$Ce(Ni,Sb)_4$	0.4575(2)	0.4654(2)	1.0553(5)	40.8	19.4	39.8
e)			τ_1	AlB_2	-	-	-	29.1	31.1	39.8
21.0	19.0	60.0	τ_2	$BaNiSn_3$	0.4650(4)	0.4650(4)	1.033(3)	23.7	19.3	57.0
			κ_I	K_4Ge_{23-x}	1.0796(2)	1.0796(2)	1.0796(2)	11.1	15.1	73.8
63.9	9.2	26.9	τ_4	$BaAu_5Si_2$	0.8981(2)	0.7106(1)	1.0363(2)	61.3	13.0	25.4
			(Au)	Cu	0.4075(1)	0.4075(1)	0.4075(1)	97.5	0.0	2.5
f)			Eutectic	-	-	-	-	65.8	0.0	34.2
58.8	15.2	26.0	τ_2'	$Ce(Ni,Sb)_4$	-	-	-	51.8	19.7	28.6
			τ_3	$BaAu_3Ge$	-	-	-	61.2	19.2	19.6
g)			τ_4	$BaAu_5Si_2$	-	-	-	63.0	11.9	25.1
57.6	22.0	20.4	τ_3	$BaAu_3Ge$	0.6457(2)	0.6457(2)	0.5485(2)	61.1	19.4	19.6
			τ_2'	$Ce(Ni,Sb)_4$	-	-	-	53.3	19.5	27.2
h)			$BaAu_2$	AlB_2	-	-	-	67.0	31.6	1.4

Details on the crystal structure of the ternary compounds observed are discussed in the next chapter. At low gold content, type I clathrate (κ_I) is in equilibrium with clathrate type IX (κ_{IX}, Ba_6Ge_{25} type). The microstructure of an alloy proving the corresponding tie line

is shown in Figure 46b. The maximum solubility of gold in clathrate type-IX at 800°C is 2.7 at.% (a = 1.4559(8) nm). Alloys containing moisture sensitive $BaGe_2$ ($BaSi_2$ type) quickly decompose on air and were therefore polished under glycerin. At the solubility limit of gold in clathrate I, a three-phase equilibrium exists between κ_I, $BaGe_2$ and τ_2-$BaAu_{1+x}Ge_{3-x}$ (for the corresponding microstructure see Figure 46a). The homogeneity region of τ_2 does not include stoichiometric $BaAuGe_3$ ($x \geq 0.1$). At low gold contents, the Rietveld refinement for τ_2 (x=0.6) indicates the $BaNiSn_3$ structure type (a = 0.4615(3) and c = 1.0492(5) nm) (Figure 47) at 800°C.

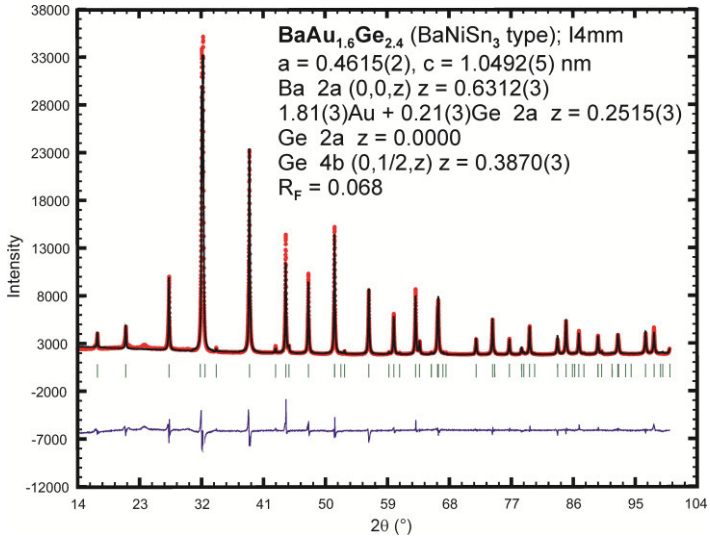

Figure 47: Rietveld refinement for τ_2-$BaAu_{1+x}Ge_{3-x}$ (x = 0.6, $BaNiSn_3$ structure type).

With increasing gold content, the tetragonal structure undergoes a structural transformation into the orthorhombic phase labeled τ_2'. As this structural transformation is supposed to occur between x=0.8 and x=1, this part of the phase region is dotted in Figure 45. Samples with higher gold content close to $BaAu_2Ge_2$, contain both structures, but no correspondence was found to a $ThCr_2Si_2$ type phase, which was reported by N. May and H. Schäfer (May N. 1972) for $BaAu_{3.16}Ge_{0.84}$. From X-ray single crystal analysis it was possible to determine the structure type of the orthorhombic phase τ_2'. It is a new representative of the $Ce(Ni,Sb)_4$ type with a homogeneity region ranging at 800°C for $1 \leq x \leq 1.7$. A two-phase equilibrium exists between τ_2' and τ_1 at 800 °C (Figure 46e). τ_1-$Ba(Au_{1-x}Ge_x)_2$ exhibits a quite large homogeneity range extending from $BaAu_{0.5}Ge_{1.5}$ (a = 0.4381(0) and c = 0.4929(7) nm) to $BaAu_{0.9}Ge_{1.1}$ (a = 0.4656(3) and c = 0.4979(5) nm) with $\frac{c}{a} \sim 1.1$ in all cases. The Rietveld refinement (Figure 48) and the SEM picture

(Figure 46c) for the sample with nominal composition $Ba_{3.45}Au_{3.1}Ge_{3.45}$ proves the three-phase equilibrium between τ_1-$Ba(Au_{1-x}Ge_x)_2$, τ_2'-$BaAu_{1+x}Ge_{3-x}$ and $BaAu_2$ (AlB_2 type).

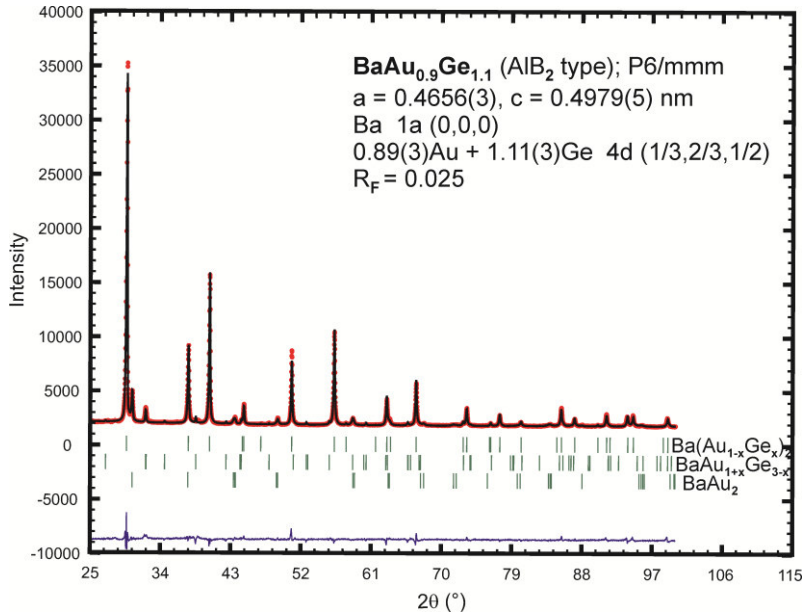

Figure 48: Rietveld refinement for a sample with nominal composition $Ba_{3.45}Au_{3.1}Ge_{3.45}$.

The simple AlB_2 type was confirmed for $Ba(Au_{1-x}Ge_x)_2$ as no unindexed X-ray reflections are observed in the samples on both ends of the homogeneity range. A second phase with AlB_2-type extends at 800°C from binary $BaAu_2$ (a = 0.4804 and c = 0.4119 nm (B. G. Bruzzone G. 1970)) to a solubility limit of about 5.4 at.% Ge (from EPMA, $BaAu_{1.8}Ge_{0.2}$ with a = 0.4983(4), c = 0.4346(3) nm and $\frac{c}{a}$ ~ 0.9). $BaAu_2$ oxidizes on air as can be seen from the microstructure in Figure 46c. Two further new ternary phases were located in the Au-Ba-Ge system at 800°C: τ_3-$BaAu_3Ge$ is in equilibrium with τ_2' and τ_4-$BaAu_{5+x}Ge_{2-x}$ (x = 0, $BaAu_5Si_2$ type). With higher gold content $BaAu_{5+x}Ge_{2-x}$ undergoes a structural transformation into a closely related derivative structure type with the lattice geometry: $a = a_{BaAu_5Si_2}, b = b_{BaAu_5Si_2}, c = 2c_{BaAu_5Si_2}$. The sample with nominal composition $Ba_{0.94}Au_{6.45}Ge_{2.61}$ (annealed at 800°C) was found to be in equilibrium with a gold-rich liquid and contains three phases in solid state (Figure 49).

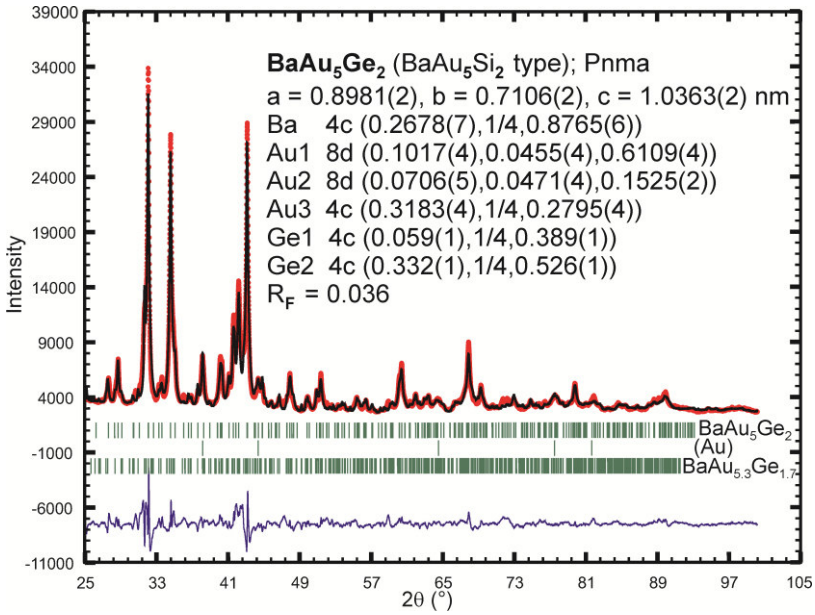

Figure 49: Rietveld refinement for an alloy with nominal composition $Ba_{0.94}Au_{6.45}Ge_{2.61}$ revealing τ_4-$BaAu_5Ge_2$, τ_4'-$BaAu_{5.3}Ge_{1.7}$ and small amounts of (Au).

No further attempts have been made to establish the entire gold-rich part of the isothermal section.

5.5.1.3 Crystal structure of the ternary compounds

The ternary compounds of the Ba – Au – Ge system mainly belong to three different structural families: AlB_2 type, derivatives of the $BaAl_4$ type, derivatives of Cu_3Au type.

5.5.1.3.1 Derivatives of the $BaAl_4$ structure type

The classification of $BaAl_4$ derivative structures relies on the type of coordination polyhedron around the transition metal, which can either be a tetrahedron or a square pyramid. The Ba-atom is located at the center of an almost regular 16-vertex coordination polyhedron. The atomic framework of the ternary derivatives $RT_{2-x}M_{2+x}$ (R: alkaline earth, rare earth element, T: transition element, M: metal) can also be expressed as a sequence of layers of atoms of the same element perpendicular to the c-axis (Bazela W. 2007). The sequence of atom layers in the structure types of $ThCr_2Si_2$, $BaNiSn_3$ and $Ce(Ni,Sb)_4$ can thus be written as:

R-M-T-M-R-M-T-M-R ($ThCr_2Si_2$)

M-R-T-M-M-R-T-M-M ($BaNiSn_3$)

R-M/T-M/T-M/T-R-M/T-M/T-M/T-R ($Ce(NiSb)_4$-type, with a statistical distribution of Ni and Sb in all 8 Al sites)

5.5.1.3.1.1 Tetragonal derivatives: τ_2-$BaAu_{1+x}Ge_{3-x}$ ($BaNiSn_3$ type)

The $BaNiSn_3$ structure type was confirmed by X-ray Rietveld refinement (Figure 47) of a single-phase sample $BaAu_{1.6}Ge_{2.4}$. The non-stoichiometric composition was proven with EPMA and shows a homogeneity range $0.1 \leq x \leq 1.7$. At higher gold content ($x \approx 2$) a structural transformation occurs into an orthorhombic phase τ_2' with the closely related $Ce(Ni,Sb)_4$ type.

5.5.1.3.1.2 Orthorhombic derivative: τ_2'- $BaAu_{1+x}Ge_{3-x}$ ($Ce(Ni,Sb)_4$ type)

Although the $Ce(Ni,Sb)_4$ type (space group *Immm*) was already described by Percharskii et al. (Percharskij V.K. 1982) in 1982, only a few isotypic compounds have hitherto been reported in the literature.

A single crystal taken from an alloy with composition $BaAu_2Ge_2$ revealed a body-centered orthorhombic unit cell (a = 0.4577(2), b = 0.4656(2), c = 1.0558(5) nm). Structural solution was achieved by direct methods in the highest possible space group *Immm* prompting three independent atomic positions. Barium adopts the crystallographic 2a sites and germanium and gold the 4i and 4j sites (details can be found in Table XX and Figure 50).

Table XX: X-Ray single crystal data for τ_2'-$BaAu_{1+x}Ge_{3-x}$ (x=1) at RT (Anisotropic displacement parameters in [$10^{-2}nm^2$]).

Parameter/compound	
Space group	*Immm*
Structure type	$Ce(Ni,Sb)_4$
Formula from refinement	$BaAu_2Ge_2$
a; b; c [nm]	0.4577(2); 0.4656(2); 1.0558(5)
μ_{abs} [mm^{-1}]	86.60
V (nm^3)	0.225
ρ_x (gcm^{-3})	9.986
Reflections in refinement	$282 \geq 4\sigma(F_o)$ of 314
Number of variables	15
$R_F^2 = \Sigma\|F_0^2-F_c^2\|/\Sigma F_0^2$	0.047
R_{Int}	0.029
wR2	0.099

GOF	1.164
Extinction (Zachariasen)	0.0026(5)
Residual density $e^-/Å^3$; max; min	6.54; -5.81
Atom parameters	
Ba in 2a (0,0,0); occ.	1.00
U_{11}; U_{22}; U_{33}	0.0125(7); 0.0127(8); 0.0143(7)
M1 in 4j (1/2,0,*z*); occ.	0.507Au + 0.493(8)Ge
z	0.2549(1)
U_{11}; U_{22}; U_{33}	0.0202(6); 0.055(1); 0.0234(7)
M2 in 4i (0,0,*z*); occ.	0.500Au + 0.500(8)Ge
z	0.3738(1)
U_{11}; U_{22}; U_{33}	0.0154(5); 0.0192(6); 0.0205(6)
Interatomic distances [nm] with standard deviations < 0.0001	
Ba – 4M1	0.3480
–8M2	0.3526
–4M1	0.3533
–2M2	0.3947
M1 – 2M2	0.2610
–2M2	0.2696
M2– 2M1	0.2610
1M2	0.2663
2M2	0.2663

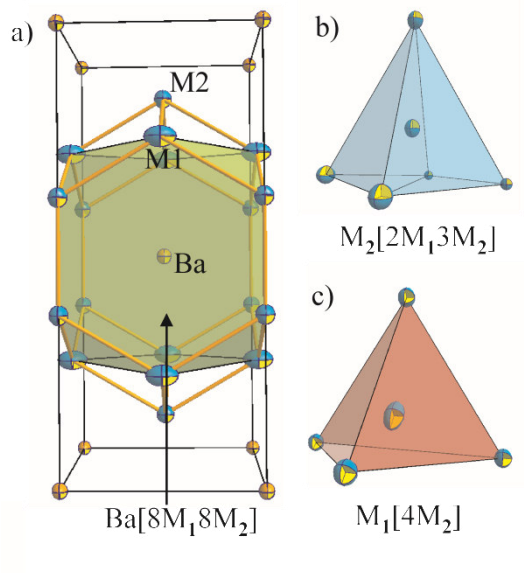

Figure 50: Crystal structure of τ_2'-$BaAu_2Ge_2$ ($Ce(Ni,Sb)_4$ type); (a) three dimensional view with anisotropic displacement parameters from single crystal refinement with Ba-polyhedra; (b) polyhedra around M2 (~50%Au and ~50%Ge), (c) M1 (~50%Au and ~50%Ge).

As both 4-fold crystallographic sites (4i, 4j) are statistically occupied by gold and germanium atoms in a ratio of about 1:1 (Table XX) and as these sites show elongation of ADP ellipsoids along the b-axis, structural refinements were also performed in the lower symmetry space groups *Imm*2 and *I*222. However, attempts to separate germanium and gold atoms geometrically were unsuccessful. The only improvement achieved from the lower symmetry refinements came from small off-center positions of the atoms.

5.5.1.3.2 Tetragonal derivative of Cu_3Au type: τ_3-$BaAu_3Ge$ (own structure type)

An X-ray powder diffraction spectrum similar to the already known $BaAl_4$ derivatives was observed for a single phase alloy $BaAu_3Ge$ (τ_3), but the profile contained various reflections which do not belong to any of the known derivative structure types. Analyses of the extinctions of a single crystal - isolated from an alloy $BaAu_3Ge$ - yield the primitive space group *P4/nmm* as the highest possible crystal symmetry. The structure was solved with direct methods revealing Ba-atoms in site 2b (¾,¼,½), Au-atoms the crystallographic sites 4d (0,0,0) and 2c (¼,¼,z) and Ge-atoms in site 2c (Table XXI).

Table XXI: X-Ray single crystal data for τ_3-$BaAu_3Ge$ at RT(Anisotropic displacement parameters in [$10^{-2}nm^2$]).

Parameter/compound	
Space group	*P*4/*nmm*
Structure type	$BaAu_3Ge$
Formula from refinement	$BaAu_3Ge$
a; c [nm]	0.6459(2); 0.5487(2)
μ_{abs} [mm^{-1}]	110.55
V (nm^3)	0.2289
ρ_x (gcm^{-3})	11.62
Reflections in refinement	288 ≥ 4σ (F_o) of 316
Number of variables	14
$R_F^2 = \Sigma\|F_0^2-F_c^2\|/\Sigma F_0^2$	0.029
R_{Int}	0.034
wR2	0.079
GOF	1.173
Extinction (Zachariasen)	0.0011(4)
Residual density $e^-/Å^3$ max; min	6.78; -5.46
Atom parameters	

Ba in 2b (3/4,1/4,1/2); occ.		1.015(6)
U_{11}= U_{22}; U_{33}		0.0103(3); 0.0166(5)
Au1 in 4d (0, 0, 0); occ		0.999(5)
U_{11}=U_{22}; U_{33}		0.0222(2); 0.0142(2)
Au2 in 2c (1/4,1/4,*z*); occ.		0.989(5)
z		0.6795(1)
U_{11}= U_{22}=U_{33}		0.0139(3)
Ge in 2c (1/4,1/4,*z*); occ.		1.06(3)
z		0.2185(3)
U_{11}= U_{22}; U_{33}		0.0112(4); 0.0126(5)
Interatomic distances [nm] with standard deviations < 0.0001		
Ba –	4Au2	0.3376
	–8Au1	0.3569
	–4Ge	0.3580
Au2 –	1Ge	0.2530
	–4Au1	0.2882
Au1 –	2Ge	0.2579
	2Au2	0.2882
	4Au1	0.3229
Ge–	1Au2	0.2530
	4Au1	0.2882

Refinement of the individual occupancies of all Wyckoff positions proved full occupation and full atom order. The polyhedron around the gold and germanium atoms (Figure 51b, c) in the 2c site is a square pyramid and the Ba-atoms can be found inside the characteristic 16-atom coordination polyhedron (12 Au and 4 Ge atoms, see Figure 51a).

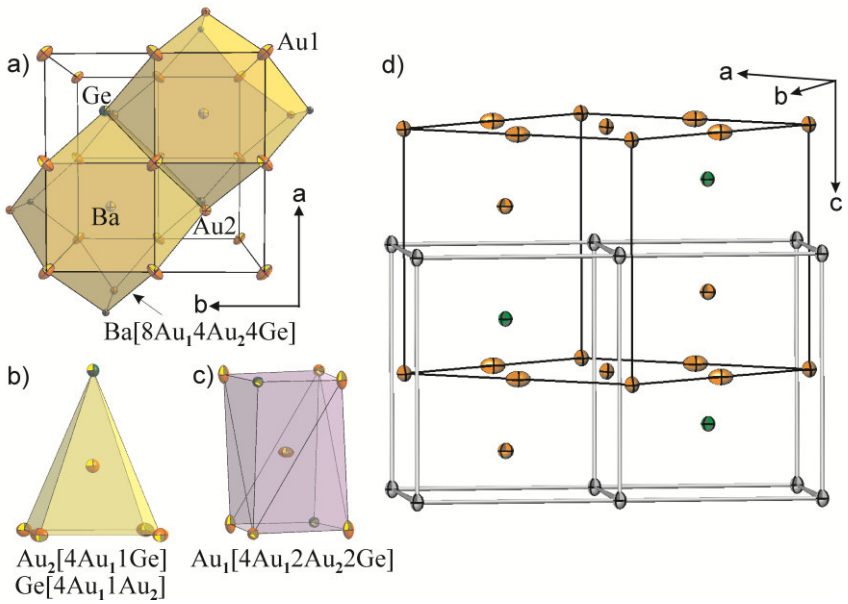

Figure 51: Crystal structure of τ_3-$BaAu_3Ge$ (own structure type); (a) three dimensional view of the unit cell with anisotropic displacement parameters from single crystal refinement and Ba-polyhedra; (b) coordination polyhedron of Au2, the polyhedron around the Ge-atom is also a square pyramid; (c) polyhedron around Au1; (d) geometrical relation of the unit cell of τ_3-$BaAu_3Ge$ (solid frame) and subunits of $CePt_3B$ type (unit cell outlined by grey hollow frame).

The structure of τ_3-$BaAu_3Ge$ shows a close relation to the $BaAl_4$ type ($a = \sqrt{2}a_{BaAl_4}$ = 0.6459(2), $c = \frac{c_{BaAl_4}}{2}$ = 0.5487(2) nm) concerning the lattice geometry and coordination polyhedra, however, an even better description of the structure can be found as a stacking variant of the $CePt_3B$ type (Figure 51d). In this case τ_3-$BaAu_3Ge$ is a tetragonal filled derivative of the cubic Cu_3Au type ($a \cong a_{CePt_3B}\sqrt{2}$, $c \cong c_{CePt_3B}$).

5.5.1.3.2.1 Electrical resistivity of $BaAu_3Ge$

A superconducting transition at T_c ~ 2.2 K is obvious from the temperature dependent resistivity measurements (see Figure 52). With increasing external magnetic fields, the superconducting transition is broadened and shifted to lower values (see inset Figure 52).

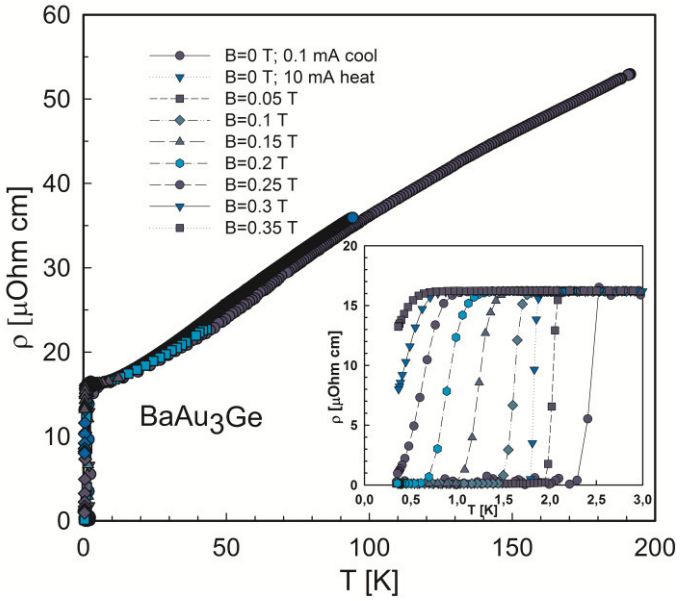

Figure 52: Temperature dependent resistivity measurements under various external magnetic fields.

5.5.1.3.3 Crystal structure of τ_4-$BaAu_5Ge_2$ and τ_4'- $BaAu_{5.3}Ge_{1.7}$

The crystal structure of τ_4'-$BaAu_{5.3}Ge_{1.7}$ was solved with direct methods in the orthorhombic primitive space group *Pnma* (a = 0.8895(3), b = 0.7175(3) and c = 2.0658(3) nm). Refinement of the occupancy of all atom sites and anisotropic atomic displacement parameters show a statistical distribution of Au and Ge atoms in three of eight sites 4c (x,¼,z) (Table XXII).

Table XXII: X-Ray single crystal data for τ_4'-$BaAu_{5.3}Ge_{1.7}$ at RT (Anisotropic displacement parameters in [$10^{-2}nm^2$]).

Parameter/compound	
Space group	*Pnma*
Structure type	$BaAu_{5.3}Ge_{1.7}$
Formula from refinement	$BaAu_{5.3}Ge_{1.7}$
a, b, c [nm]	0.8895(3), 0.7175(3) 2.0658(3)
μ_{abs} [mm^{-1}]	121.07
V (nm^3)	1.318
ρ_x (gcm^{-3})	13.15
Reflections in refinement	1937≥4σ(F_o) of 3075
Number of variables	93
$R_F^2 = \Sigma\|F_0^2-F_c^2\|/\Sigma F_0^2$	0.047
R_{Int}	0.105
wR2	0.128
GOF	1.007
Extinction (Zachariasen)	0.00020(2)

Residual density $e^-/Å^3$; max; min	4.62; -4.68
Atom parameters	
Au1 in 8d (*x,y,z*); occ.	1.00
x, y, z	0.05934(7), 0.04464(8), 0.30245(3)
U_{11}; U_{22}; U_{33}	0.0222(3); 0.0168(2); 0.0196(3)
Au2 in 8d (*x,y,z*); occ.	1.00
x, y, z	0.06457(8), 0.05213(9), 0.56295(3)
U_{11}; U_{22}; U_{33}	0.0183(3); 0.0197(3); 0.0230(3)
Au3 in 8d (*x,y,z*); occ.	1.00
x, y, z	0.10835(8), 0.03676(9), 0.05818(3)
U_{11}; U_{22}; U_{33}	0.0201(3); 0.0190(2); 0.0258(3)
Au4 in 8d (*x,y,z*); occ.	1.00
x, y, z	0.39812(8), 0.55433(8), 0.32436(3)
U_{11}; U_{22}; U_{33}	0.0325(4); 0.0148(3); 0.0230(3)
M1 in 4c (*x*,1/4,*z*); occ.	0.533Au + 0.467(3)Ge
x, *z*	0.0853(2), 0.17923(8)
U_{11}; U_{22}; U_{33}	0.0365(1); 0.0221(7); 0.0314(8)
Ba1 in 4c (*x*,1/4,*z*); occ.	1.00
x, *z*	0.2471(2), 0.43519(6)
U_{11}; U_{22}=U_{33}	0.0219(7); 0.0188(6); 0.0150(6)
Ba2 in 4c (*x*,1/4,*z*); occ.	1.00
x, *z*	0.2564(2), 0.68865(6)
U_{11}; U_{22}=U_{33}	0.0171(6); 0.0242(6); 0.0139(6)
M2 in 4c (*x*,1/4,*z*); occ.	0.573Au + 0.427(3)Ge
x, *z*	0.3154(2), 0.25333(7)
U_{11}; U_{22}; U_{33}	0.0289(7); 0.0229(6); 0.0260(7)
M3 in 4c (*x*,1/4,*z*); occ.	0.418Au + 0.582(3)Ge
x, *z*	0.3356(2), 0.12039(8)
U_{11}; U_{22}; U_{33}	0.0284(8); 0.0177(6); 0.0253(7)
Ge1 in 4c (*x*,1/4,*z*); occ.	1.00
x, *z*	0.3565(3), 0.8582(1)
U_{11}; U_{22}; U_{33}	0.019(1); 0.014(1); 0.015(1)
Ge2 in 4c (*x*,1/4,*z*); occ.	0.976(7)
x, *z*	0.5470(3), 0.5648(1)
U_{11}; U_{22}; U_{33}	0.013(1); 0.015(1); 0.019(1)
Au5 in 4c (*x*,1/4,*z*); occ.	1.00
x, *z*	0.8112(1), 0.51876(4)
U_{11}; U_{22}; U_{33}	0.0160(4); 0.0208(4); 0.0163(4)
Interatomic distances [nm] with standard deviations < 0.0001	

Ba1 –	2Au2	0.3408	Au4–	1Au4	0.2810
	–2Au4	0.3437		–1Au1	0.2809
	–2Au3	0.3514		–1Au1	0.3070
	–2Au2	0.3519		–1Au3	0.3129
	–2Au1	0.3532		–1Ba2	0.3390
	–2Au3	0.3562		–1Ba2	0.3423
Ba2 –	2Au4	0.3390		–1Ba1	0.3437
	–2Au2	0.3417	M1–	1M3	0.2535
	–2Au4	0.3423		–1M2	0.2554
	–2Au1	0.3520		–2Au4	0.2747
	–2Au1	0.3561		–1M2	0.2776
	–2Au3	0.3599		–2Au3	0.2939
Au1 –	1Ge4	0.2521		–2Au1	0.2950
	–1M2	0.2864	M2–	1M1	0.2554
	–1M2	0.2897		–2Au4	0.2731
	–1M3	0.2944		–1M3	0.2752
	–1Au1	0.2947		–1M1	0.2776
	–1M1	0.2950		–2Au1	0.2864
	–1Au4	0.3069		–2Au1	0.2897
	–1Au2	0.3070		–1Ba1	0.3806
	–1Au4	0.3129		–2Ba2	0.3881
	–1Ba2	0.3520	M3–	1M1	0.2535
	–1Ba1	0.3532		–2Au2	0.2626
	–1Ba2	0.3561		–1M2	0.2752
Au2–	1M3	0.2626		–2Au3	0.2842
	–1Au5	0.2817		–1Au5	0.2883
	–1Au2	0.2841		–2Au1	0.2945
	–1Ge4	0.2844		–1Ba1	0.3836
	–1Au2	0.2940		–2Ba2	0.3941
	–1Au5	0.2961	G1–	2Au2	0.2521
	–1Au3	0.2980		–1Au5	0.2756
	–1Au1	0.3070		–2Au4	0.2844
	–1Ba1	0.3408		–2Au2	0.3181
	–1Ba2	0.3417		–1Ge2	0.3615
	–1Ba1	0.3519		–2Ba2	0.3686
Au3–	1Ge2	0.2482	Ge2–	2Au3	0.2482
	–1M3	0.2842		–1Au5	0.2563

	–1Au5	0.2849		–2Au4	0.2730
	–1M1	0.2939		–2Au3	0.3016
	–1Au2	0.2980		–1Ge1	0.3181
	–1Ge2	0.3016		–1Ba1	0.3636
	–1Au3	0.3058		–1Ba2	0.3780
	–1Au3	0.3126	Au5–	1Ge2	0.2536
	–1Au4	0.3133		–1Ge1	0.2573
	–1Ba1	0.3514		–2Au2	0.2817
	–1Ba1	0.3562		–2Au3	0.2849
	–1Ba2	0.3600		–1M3	0.2883
Au4–	1Ge2	0.2730		–2Au2	0.2961
	–1M2	0.2731		–2Ba1	0.3747
	–1M1	0.2747		–2Au4	0.3993
	–1Ge1	0.2756			

All other sites are fully ordered among Au, Ge or Ba-atoms. The structure in three-dimensional view is shown in Figure 53 emphasizing on the Ba-polyhedra.

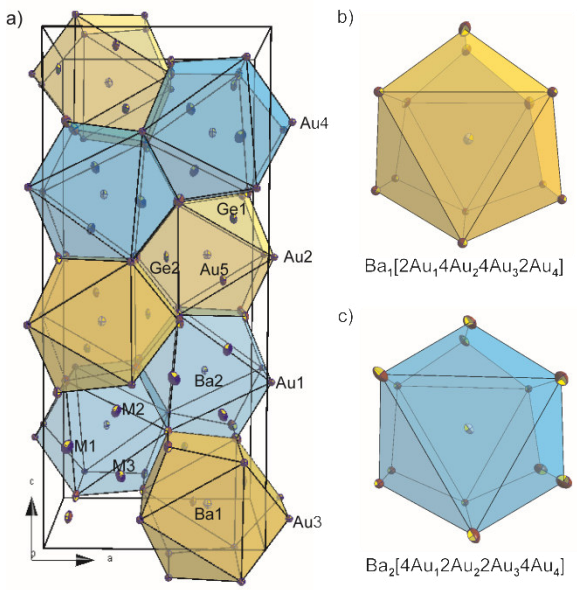

Figure 53: Crystal structure of τ_4'-$BaAu_{5.3}Ge_{1.7}$ (own structure type), M are mixed sites (~50%Au and 50%Ge); (a) three dimensional view with anisotropic displacement parameters from single crystal refinement; polyhedra around Ba1 (b), Ba2 (c).

Each Ba-atom is surrounded by 12 gold atoms and these Ba-polyhedra are interconnected sharing edges or rectangular faces to form a three dimensional framework. The structure

is closely related to τ_4-$BaAu_5Ge_2$ (Figure 54), which crystallizes in the $BaAu_5Si_2$ structure type.

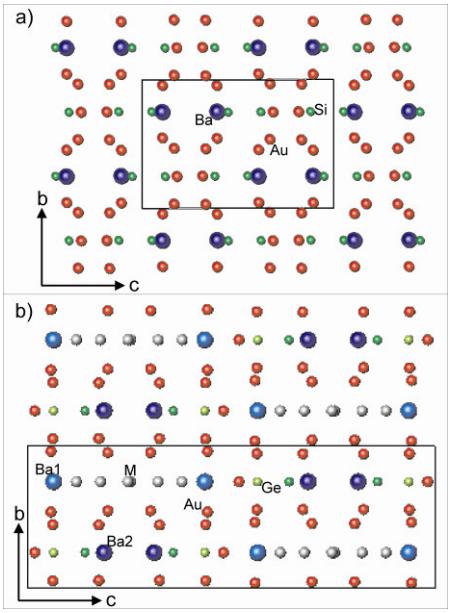

Figure 54: Crystal structure of a) $BaAu_5Ge_2$ ($BaAu_5Si_2$ type) and b) $BaAu_{5.3}Ge_{1.7}$ (own structure type); blue atoms are barium, red atoms are gold, green atoms are germanium or silicon and mixed positions (~ 50%Au and 50%Ge) are grey.

Rietveld refinement for a sample containing both structure types is shown in Figure 49. The primitive orthorhombic unit cell of τ_4-$BaAu_5Ge_2$ (space group *Pnma*; a = 0.8981(2), b = 0.7106(2) and c = 1.0363(2) nm) contains half of the atoms with respect to the unit cell of $BaAu_{5.3}Ge_{1.7}$. Atoms in the six different atomic sites of $BaAu_5Ge_2$ are fully ordered and the structure shows dense packing of Ba-polyhedra similar to $BaAu_{5.3}Ge_{1.7}$.

5.5.1.4 Physical properties of $Ba_8Au_6Ge_{40}$

Although intensive investigations concerning the thermoelectric properties (thermopower, electrical resistivity or conductivity) of $BaAu_xGe_{46-x}$ (x = 3-6) have been carried out by Anno et al. (H. M. Anno H. 2005) in the high temperature region (300 - 900 K), for $BaAu_6Ge_{40}$ by Johnsen et al. (Johnsen S. 2007) in the low temperature regime (2 – 400 K) and for $BaAu_{\sim 5.3}Ge_{40.7}$ (Zhang H. 2011), the aim of this work was to provide detailed information on thermal conductivity, thermopower and electrical resistivity at the solubility limit of gold in the Ge-based clathrate lattice $Ba_8Au_6Ge_{40}$.

5.5.1.4.1 Temperature dependent thermal conductivity

The temperature dependent thermal conductivity (λ) was measured in the low temperature range between 10 K and room temperature for $Ba_8Au_6Ge_{40}$ (Figure 55).

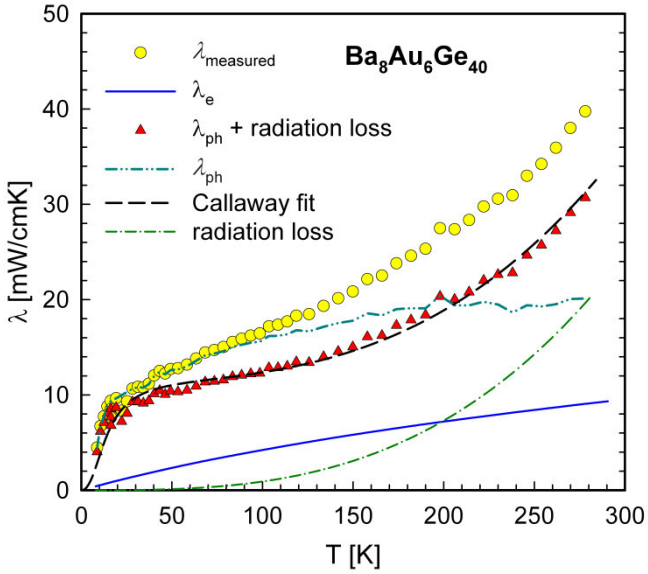

Figure 55: Temperature dependency of the thermal conductivity. The black dashed line is a least squares fit according to the model of Callaway (v. B. Callaway J. 1969). The blue dashed-dotted-dotted line, the dark blue solid line and the green dashed dotted line represent the phonon part, the electronic contribution and the radiation loss, respectively.

As assumed for clathrates, the overall values of λ(T) are small and strongly dominated by the lattice thermal conductivity (λ_{ph}) at low temperatures. A suppression of the pronounced maximum of λ(T) at low temperatures is a common feature of many Ge-based clathrates. Scattering of both, electrons and heat-carrying phonons on impurities, vacancies, grain boundaries or other static defects inhibits the initial rise of λ(T), resulting in a "glass-like" temperature dependency. The decomposition of the total thermal conductivity into phononic and electronic contributions is shown in Figure 55. The phonon contribution is still about 4 times the minimal thermal lattice conductivity as estimated from the equation after Cahill and Pohl (Cahill D. 1989).

5.5.1.4.2 Thermopower, electrical resistivity and figure of merit

The results of the electrical resistivity measurements and thermopower measurements in the temperature range between 4.2 and 800 K are shown in Figure 56.

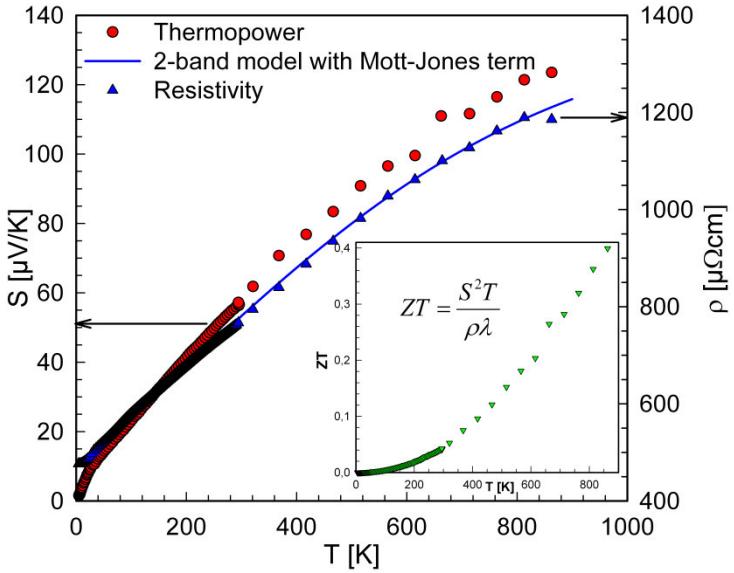

Figure 56: Temperature dependent electric resistivity (ρ), thermopower (S) and calculated figure of merit (ZT) for $Ba_8Au_6Ge_{40}$. The blue solid line is a least squares fit explained in the text.

As has been shown by Anno et al. (H. M. Anno H. 2005), n- and p-type clathrates can be received within the $BaAu_xGe_{46-x}$ solid solution through changing the gold content. For $Ba_8Au_6Ge_{40}$, the thermopower values are positive over the whole temperature range (highest value: 120 µV/K at about 800 K) and are in good agreement with the results reported in the literature ((H. M. Anno H. 2005), (Johnsen S. 2007)). Positive thermopower values can be related to a hole dominated transport and the charge carrier density (n = 1.2×10^{21} cm^{-3} (holes)) has been estimated from the linear range at high temperatures (Blatt F. J. 1968), which is in perfect agreement with the result reported from Hall measurements (H. M. Anno H. 2005).

The simplest way to describe the metal-like behavior of the electrical resistivity is to apply the Bloch-Grüneisen formula for the phonon part,

$$\rho_{ph} = \frac{C}{\Theta_D}\left(\frac{T}{\Theta_D}\right)^5 \int_0^{\Theta_D/T} \frac{z^5 dz}{\left(e^z - 1\right)\left(1 - e^{-z}\right)} \qquad (15)$$

C is a temperature independent electron-phonon interaction constant and Θ_D is the Debye temperature. This equation reveals a T^5 dependency at very low temperatures whereas at higher temperatures ρ(T) should show a linear behavior. As the measured temperature dependent electrical resistivity ρ(T) of $Ba_8Au_6Ge_{40}$ exhibits a distinct positive deviation from linearity, ρ(T) can be described only, taking into account an additional T^3 term (Chiu J.C.H. 1976) and a temperature dependent charge carrier density (blue solid line Figure 56, compare e.g. Ref. (Berger S. 2003)). There, the resistivity is governed by

scattering processes, in which electrons are scattered into unoccupied states present in the type I clathrates. The probability of such scattering is proportional to the density of states and its derivative with respect to energy.

For the calculation of the temperature dependent figure of merit (ZT) above room temperature, the room temperature value of the radiation corrected thermal conductivity has been taken, assuming that it should be constant. As any thermoelectric application requires a ZT above 1, the highest ZT value of about 0.4 derived at 800 K is too low but can be improved to 0.9 by working in the region between 5.3-5.4 gold atoms per formula unit as has been shown by Zhang et al. (Zhang H. 2011).

5.5.1.5 Summary

The isothermal section at 800°C has been investigated up to 33.33% Ba in the Ba-Au-Ge system. The homogeneity range of the clathrate type I solid solution (K_4Ge_{23-x} type, space group $Pm\bar{3}n$) $Ba_8Au_xGe_{46-x-y}\square_y$ (□ is a vacancy) ranges from binary $Ba_8Ge_{43}\square_3$ (a ≅1.066 nm) to $Ba_8Au_6Ge_{40}$ (a ≅1.079 nm). Another clathrate type (clathrate type IX, Ba_6Ge_{25} type, a ≅ 1.456 nm) can be found at 800°C with a small solubility of gold (~2.7%). Furthermore four new ternary phases have been found in the investigated region. A homogeneity range of the phases τ_1-$Ba(Au_{1-x}Ge_x)_2$ ($0.55 \le x \le 0.75$, AlB_2-type), τ_2-$BaAu_{1+x}Ge_{3-x}$ ($0.1 \le x < 1$, $BaNiSn_3$ type) and τ_2'-$BaAu_{1+x}Ge_{3-x}$ ($1 < x < 1.7$, $Ce(Ni,Sb)_4$-type) could be established. The crystal structures of two phases in the gold-rich part have been determined from single crystal X-ray data and were found to form new structure types: τ_3-$BaAu_3Ge$ with $BaAu_3Ge$-type (space group *P4/nmm,* a=0.6459(2), c=0.5487(2) nm) and τ_4-$BaAu_{5+x}Ge_{2-x}$ (x=0, $BaAu_5Si_2$-type, space group *Pnma*, a=0.8981(2), b=0.7106(2) and c=1.0363(2) nm), the latter revealing with increasing gold content a closely related derivative structure type τ_4' ($BaAu_{5.3}Ge_{1.7}$, $a = a_{BaAu_5Si_2}, b = b_{BaAu_5Si_2}, c = 2c_{BaAu_5Si_2}$).

Resistivity measurements of the new compound $BaAu_3Ge$ showed metallic behavior with a superconducting transition at 2.2 K. Physical properties (resistivity, thermopower, thermal conductivity) were measured for $Ba_8Au_6Ge_{40}$ in the high and low temperature range. $Ba_8Au_6Ge_{40}$ shows p-type behavior over the whole temperature range and a rather low temperature dependent thermal conductivity and resistivity. The evaluated maximum figure of merit ZT_{max} ~ 0.4 at 800 K.

5.6 THE TERNARY SYSTEM Sr-Cu-Ge

In contrast to the large number of known intermetallic clathrates of type-I with barium as an electropositive guest atom inside the cages, the number of representatives reported with strontium is rather limited. Eisenmann et al. (S. H. Eisenmann B. 1986) were the first to report on the formation and crystal structure of the compounds $Sr_8Al_{16}Si_{30}$, $Sr_8Ga_{16}Si_{30}$ and $Sr_8Ga_{16}Ge_{30}$. Besides these examples, the only further Sr-based ternary clathrate type-I compound, which has been found so far, is $Sr_8Zn_8Ge_{38}$ (Qiu L. 2004). Additionally, several investigations have been published dealing with the substitution of a forth element (a) either in the framework (e.g., $Sr_8Ga_{16}Ge_{30-x}Sn_x$ ($0 \leq x \leq 12$) (Li D.C. 2012) and $Sr_8Al_xGa_{16-x}Si_{30}$ (clathrate type-I, $0 \leq x \leq 7$ and type-VIII, $8 \leq x \leq 13$) (I. N. Kishimoto K. 2008)) or (b) as a second guest inside the cages (f. e. $Ba_{8-x}Sr_xAu_6Ge_{46-x}$ ($0 \leq x \leq 4$) (F. H. Anno H. 2006) and $Ba_{8-x}Sr_xAl_{14}Si_{32}$ ($0.6 \leq x \leq 1.3$) (Roudebush J.H. 2011)).

This chapter focuses on (I) the formation and crystal structure of type-I clathrates in the systems Sr-Cu-Ge and Ba-Sr-Cu-Ge; (II) on phase relations in the Ge-rich part of the Sr-Cu-Ge system at 700°C and (III) on low temperature physical properties (electrical resistivity and specific heat) of $Sr_8Cu_{5.3}Ge_{40.7}$. The investigations will rely on single crystal X-ray diffraction at different temperatures (300, 200, 100 K), X-ray powder diffraction, differential thermal analysis and electron probe micro analysis.

5.6.1 Results and Discussion

5.6.1.1 Clathrates type-I in the systems Sr-Cu-Ge(Si,Sn) and Ba-Sr-Cu-Ge

In the ternary system Sr-Cu-Ge, a clathrate type-I phase (κ_I) was found to exist in only a very small temperature interval below melting with an almost point composition close to the Zintl limit $Sr_8Cu_{5.3}Ge_{40.7}$ (a = 1.06311(3) nm, Ge standard). The κ_I-phase decomposes eutectoidally already at 730±3°C (from DTA measurements) according to the isothermal reaction: $\kappa_I \Leftrightarrow$ (Ge) + $SrGe_2$ + $SrCu_{2-x}Ge_{2+x}$ (for crystallographic details on the phases see Table XXIII).

Table XXIII: Crystallographic data on the solid phases of the binary systems Sr-Ge and Cu-Ge and the ternary system Sr-Cu-Ge.

Phase	Space group	Structure type	Lattice parameter [nm]			Ref.
			a	b	c	
(Ge)	$Fd\bar{3}m$	C_{diam}	0.56574	-	-	(Massalski T.B. 1990)
(Sr) hT	$Im\bar{3}m$	W	0.485(1)	-	-	(Sheldon E.A. 1953)
(Sr) rT	$Fm\bar{3}m$	Cu	0.60849(5)	-	-	(Sheldon E.A. 1953)
(Cu)	$Fm\bar{3}m$	Cu	0.36416	-	-	(Massalski T.B. 1990)
$SrGe_2$	*Pnma*	$BaSi_2$	0.874	0.665	1.124	(S. H. Betz A. 1968)
SrGe	*Cmcm*	TlI	0.486(1)	1.140(1)	0.419(1)	(S. H. Betz A. 1967)
$SrGe_{0.76}$ rT	*Immm*	SrSi	0.484	1.338	1.852	(S. H. Eisenmann B. 1975)
Sr_2Ge	*Pnma*	$PbCl_2$	0.813(2)	0.520(6)	0.958(2)	(S. H. Eisenmann B. 1974)
$Cu_{2.5}Ge$ hT	$Fm\bar{3}m$	BiF_3	0.5906	-	-	(Lenz J. 1971)
Cu_3Ge hT	*P6₃/mmc*	$IrAl_3$	0.4169	-	0.7499	(Lenz J. 1971)
Cu_3Ge rT	*Pmmn*	Cu_3Ti	0.455	0.529	0.420	(B. H. Schubert K. 1957)
$Cu_{0.85}Ge_{0.15}$	*P6₃/mmc*	Mg	0.2612	-	0.4232	(B. G. Schubert K. 1952)
$Sr_8Cu_xGe_{46-x}$	$Pm\bar{3}n$	Na_4Si_{23}	1.06311(3)	-	-	x=5.3*
$SrCu_{0.67}Ge_{1.33}$	*P6/mmm*	AlB_2	0.4230	-	0.4619	(Rieger W. 1969)
$SrCu_9Ge_4$	*I4/mcm*	$CeNi_{8.5}Si_{4.5}$	0.8273(2)	-	1.1909(5)	(Kranenberg C. 2003)
$SrCu_{2-x}Ge_{2+x}$	*I4/mmm*	$ThCr_2Si_2$	0.4270(6)	-	1.0258(10)	x=0 (Parthé E. 1969)
			0.4256(2)	-	1.0205(8)	x=0 (Schäfer M.C. 2012)
			0.428(1)	-	1.031(2)	x=0 (N. N. Dörrscheidt W. 1976)
			0.42850(4)	-	1.0370(1)	x=0.4*

* This work

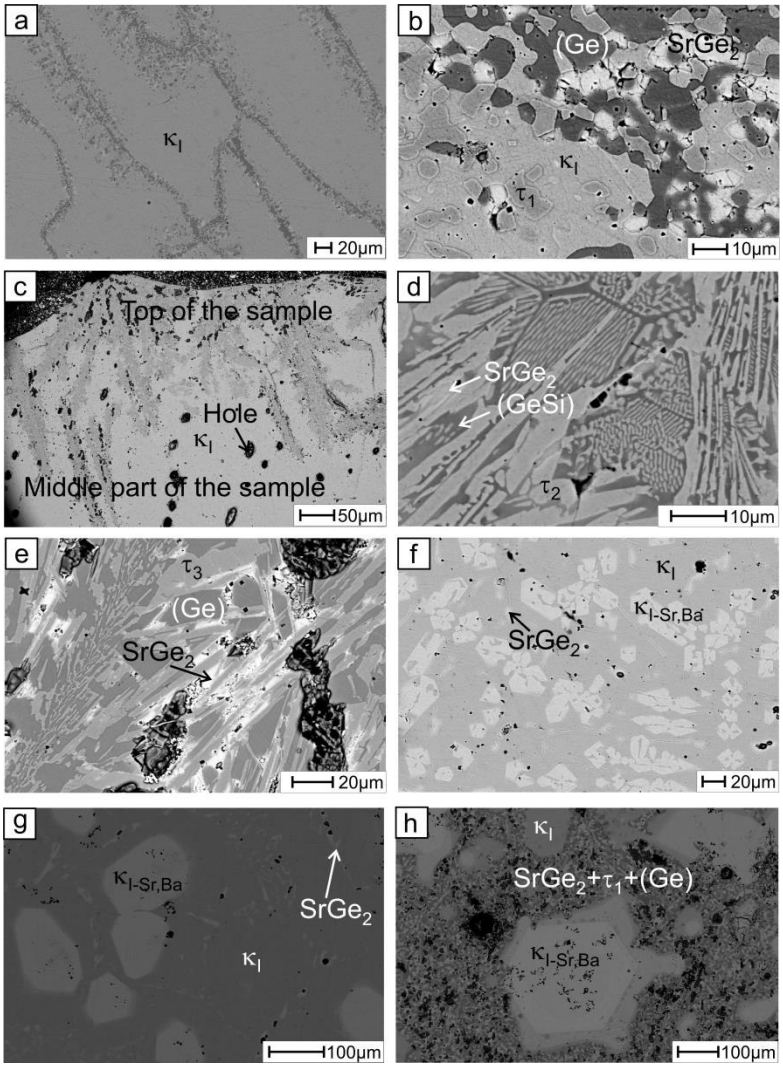

Figure 57: EPMA images of alloys with nominal composition $Sr_8Cu_{5.3}Ge_{40.7}$ (a) annealed at 600°C, (b) partial decomposition and (c) in as cast state, (d) of $Sr_8Cu_5Ge_{41}Si_5$ in as cast state, (e) of $Sr_8Cu_5Ge_{44}Sn_2$ in as cast state and (f) of $Ba_{0.5}Sr_{7.5}Cu_{5.3}Ge_{40.7}$ in as cast state, (g) annealed at 760°C and (h) 700°C. Compositions of all phases from EPMA measurements can be found in Table XXIV.

Figure 57a shows this decomposition, starting at the grain boundaries of an as cast sample annealed at 600°C; Figure 57b is a close-up with a higher magnification. Although it was possible to receive a major amount of the clathrate phase in small (and thus rapidly quenched) arc-melted buttons (< 0.25 g), the decomposition of the clathrate phase is already visible at the top of the samples due to slower cooling (see Figure 57c). All other attempts to produce larger single-phase samples of the ternary clathrate by quenching from high temperatures, including from liquid state, failed. Due to the presence of $SrGe_2$, multiphase alloys decompose rather quickly on air.

We further investigated the substitution of κ_I via a forth element as a possible stabilizer either as a guest or a framework atom, as it was observed for the binary clathrate type-I $Ba_8Ge_{43}\square_3$,

where the substitution with transition metals like silver leads to a strong stabilization (DFT calculations in (C. M. Zeiringer I. 2011)). Concerning the framework, a partial substitution of Ge by Si or Sn proved unsuccessful by analyzing alloys with nominal composition $Sr_8Cu_5Si_xGe_{46-x}$ (x = 5, 10, 20, 30) and $Sr_8Cu_5Sn_2Ge_{44}$ in as cast state and after annealing at 750°C. Figure 57d shows the microstructure of the alloy $Sr_8Cu_5Si_5Ge_{41}$ in as cast state. The main phase is (Ge,Si), with a rather inhomogeneous distribution of Si. A small amount of silicon is solved in the ternary compound τ_2. The alloy $Sr_8Cu_5Sn_2Ge_{44}$ in as cast state (see Figure 57e) also contains three phases, namely (Ge), $SrGe_2$ and a ternary phase τ_3. A small amount of tin solves in (Ge) and $SrGe_2$. Crystallographic details and EPMA data for these alloys are compiled in Table XXIV.

Table XXIV: EPMA and X-ray phase analysis data corresponding to the microstructures of the alloys shown in Figure 57, for the alloys used for the lattice parameter determination shown in Figure 58 and for the alloys in the partial isothermal section in Figure 61.

Alloy (Nominal composition)	X-ray phase analysis	Structure type	Lattice parameter [nm]			Composition EPMA (at.%)			
			a	b	c	Sr	Ba Si Sn	Cu	Ge
$Sr_8Cu_{5.3}Ge_{40.7}$ a) and b) 600°C	(Ge)	C_{diam}	0.56579(5)	-	-	0.0	-	1.6	98.4
	κ_I	Na_4Si_{23}	1.06307(2)	-	-	14.3	-	9.8	75.9
	$SrGe_2$	$BaSi_2$	-	-	-	31.7	-	1.2	67.1
	τ_1	$ThCr_2Si_2$	0.4287(2)	-	1.0370(1)	19.3	-	31.4	49.3
$Sr_8Cu_{5.3}Ge_{40.7}$ c) as cast	(Ge)	C_{diam}	0.56569(5)	-	-	0.0	-	1.6	98.4
	κ_I	Na_4Si_{23}	1.06288(4)	-	-	14.2	-	9.5	76.3
	$SrGe_2$	$BaSi_2$	-	-	-	31.1	-	1.5	67.4
	τ_1	-	-	-	-	19.2	-	20.9	59.9
$Sr_8Cu_5Ge_{41}Si_5$ d) as cast	(GeSi)	C_{diam}	-	-	-	-	6-30	~1.7	94-70
	τ_2	-	-	-	-	23.3	2.6	20.9	53.2
	$SrGe_2$	$BaSi_2$	-	-	-	30.8	-	1.9	67.3
$Sr_8Cu_5Ge_{44}Sn_2$ e) as cast	(Ge)	C_{diam}	-	-	-	-	1.2	1.7	97.1
	τ_3	-	-	-	-	21.9	21.8	0.9	55.4
	$SrGe_2$	$BaSi_2$	-	-	-	32.1	1.3	1.7	64.9
$Ba_{0.5}Sr_{7.5}Cu_{5.3}Ge_{40.7}$ f) as cast	κ_I	Na_4Si_{23}	1.06277(3)	-	-	14.6	-	9.4	75.9
	$\kappa_{I\text{-}Sr,Ba}$	Na_4Si_{23}	1.0648(1)	-	-	9.9	4.3	9.5	76.3
	$SrGe_2$	$BaSi_2$	-	-	-	31.6	-	1.4	67.0
$Ba_{0.5}Sr_{7.5}Cu_{5.3}Ge_{40.7}$ g) 760°C	κ_I	Na_4Si_{23}	1.06315(3)	-	-	14.6	-	9.6	75.9
	$\kappa_{I\text{-}Sr,Ba}$	Na_4Si_{23}	1.0658(1)	-	-	8.8	6.0	9.7	75.6
	$SrGe_2$	$BaSi_2$	-	-	-	32.0	-	1.6	66.4

	κ_I	Na_4Si_{23}	-	-	-	14.4	-	9.9	75.7
	$\kappa_{I\text{-}Sr,Ba}$	Na_4Si_{23}	1.06588(6)	-	-	7.4	7.2	9.9	75.5
$Ba_{0.5}Sr_{7.5}Cu_{5.3}Ge_{40.7}$			-	-	-	9.6	4.9	9.8	75.7
h) 700°C	(Ge)	C_{diam}	0.56574(3)	-	-	0.1	-	1.3	98.6
	$SrGe_2$	$BaSi_2$	-	-	-	32.0	-	1.1	66.9
	τ_1	$ThCr_2Si_2$	-	-	-	19.5	-	30.8	49.7
$SrCuGe_3$	(Ge)	C_{diam}	0.56579(3)	-	-	0.0	-	0.5	99.5
i) 700°C	$SrGe_2$	$BaSi_2$	-	-	-	31.9	-	1.3	66.8
	τ_1	$ThCr_2Si_2$	0.42850(4)	-	1.0370(1)	19.9	-	31.4	48.7
$SrCu_4Ge_{12}$	(Ge)	C_{diam}	0.56568(5)	-	-	0.0	-	0.7	99.3
j) 700°C	τ_1	$ThCr_2Si_2$	0.42700(5)	-	1.0376(1)	20.0	-	34.9	45.1
	eutectic	-	-	-	-	0.9	-	57.8	41.3
	κ_I	Na_4Si_{23}	-	-	-	14.7	-	9.7	75.6
$Ba_{5.5}Sr_{2.5}Cu_{5.5}Ge_{40.5}$	$\kappa_{I\text{-}Sr,Ba}$	Na_4Si_{23}	1.06813(2)	-	-	1.3	13.5	9.6	75.6
as cast	$SrGe_2$	$BaSi_2$	-	-	-	32.5	-	1.2	66.3
	τ_1	-	-	-	-	22.6	-	20.7	56.7
$Ba_{4.5}Sr_{3.5}Cu_{5.2}Ge_{40.8}$	κ_I	Na_4Si_{23}	1.06281(2)	-	-	5.0	9.4	9.6	76.0
as cast	$\kappa_{I\text{-}Sr,Ba}$	Na_4Si_{23}	1.06648(2)	-	-	14.6	-	9.5	76.9

Replacement of Sr by Ba, however, leads to the formation of a quaternary solution of clathrate type-I $Ba_{8-y}Sr_yCu_xGe_{46-x}$ ($0 \le y \le \sim 5.6$; $5.2 \le x \le 5.4$), which is confined to the Ba-rich side and does not cover the region near $Sr_8Cu_{5.3}Ge_{40.7}$. Our present investigations of the clathrate type-I solid solution $Ba_{8-y}Sr_yCu_xGe_{46-x}$ are focused on the region with approximately five copper atoms (x = 5.2 - 5.4) per formula unit and strontium contents y between 0.5 and 8. In as cast state, all prepared samples showed a mixture of two clathrate type-I phases, namely $Sr_8Cu_xGe_{46-x}$ (κ_I) and $Ba_{8-y}Sr_yCu_xGe_{46-x}$ ($\kappa_{I\text{-}Sr,Ba}$) with clearly defined phase boundaries in between. Figure 57f shows the microstructure of an alloy with nominal composition $Ba_{0.5}Sr_{7.5}Cu_{5.3}Ge_{40.7}$ in as cast state, indicating primary crystallization of $\kappa_{I\text{-}Sr,Ba}$ with composition $Ba_{2.4}Sr_{5.6}Cu_{5.3}Ge_{40.7}$ (from EPMA) followed by the crystallization of small amounts of $SrGe_2$ and κ_I with composition $Sr_8Cu_{5.2}Ge_{40.8}$. After annealing at 760°C (Figure 57g), large grains of both clathrate phases can be seen ($\kappa_{I\text{-}Sr,Ba}$ with composition $Ba_{4.8}Sr_{3.2}Cu_{5.2}Ge_{40.8}$ and κ_I), whereas after annealing at 700°C, κ_I already decomposes and mainly large crystallites of $\kappa_{I\text{-}Sr,Ba}$ remain with different Sr/Ba ratios from the center ($Ba_{3.9}Sr_{4.1}Cu_{5.4}Ge_{40.6}$) to the edge ($Ba_{2.7}Sr_{5.3}Cu_{5.4}Ge_{40.6}$) of the grain (see Figure 57h). The homogeneity region of the clathrate solid solution $Ba_{8-y}Sr_yCu_{\sim 5.3}Ge_{40.7}$ extends from y = 0 to y ~ 5.6 in as cast state. No measurable Ba content has been found in the Sr-clathrate κ_I. The

dependency of the lattice parameter with increasing Sr content from y = 0 to y = 8 is shown in Figure 58.

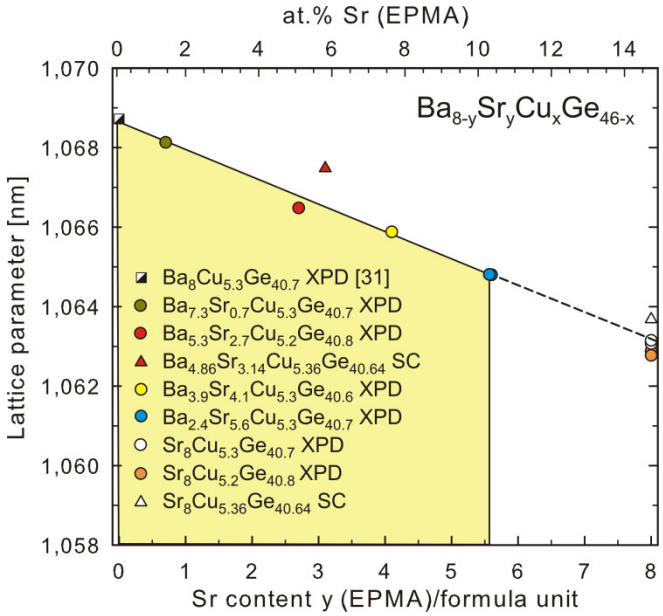

Figure 58: Dependency of the lattice parameter with increasing Sr-content for the clathrate type-I solid solution $Ba_{8-y}Sr_yCu_xGe_{46-x}$ with $5.2 \leq x \leq 5.4$; the lattice parameters (at RT, composition and exact values are given in Table XXIV) were obtained either from single crystal X-ray diffraction (SC) or from X-ray powder diffraction (XPD) using Ge as internal standard; the yellow area indicates the solubility limit of Sr determined by EPMA in as cast state.

The exact composition has been determined with EPMA. As can be seen, the lattice parameters almost linearly decrease with increasing Sr-content and the observed deviations are probably due to the slightly different Cu-content. Detailed information on the crystal structure of the clathrates type-I $Sr_8Cu_xGe_{46-x}$ and $Ba_{8-y}Sr_yCu_xGe_{46-x}$ is given in the next chapter. Table XXIV summarizes the results from EPMA and XPD for the alloys in Figure 57 (they are correspondingly labeled from a) to h)), for the samples used for lattice parameter determination in Figure 58 and for the alloy marked in red in Figure 61.

5.6.1.2 Crystal structure of the clathrates type-I $Sr_8Cu_xGe_{46-x}$ and $Ba_{8-y}Sr_yCu_xGe_{46-x}$

Crystal specimens suitable for X-ray single crystal diffraction were isolated from mechanically crushed samples with nominal composition $Sr_8Cu_{5.3}Ge_{40.7}$ in as cast state and $Ba_4Sr_4Cu_5Ge_{41}$ annealed at 800°C. The crystal structure was successfully solved for both compounds in the cubic primitive space group $Pm\bar{3}n$, as typical for the clathrate type-I crystal structure. The refinements for both crystals revealed full occupation of the crystallographic sites 16i and 24k by germanium. The mixed occupancy in the 6d site has been refined in two different ways. First, the Cu content has been fixed according to the

result from EPMA (5.3) and only the Ge content has been refined. For both crystals, a fully occupied 6d site results from this strategy. Additionally, a possible split of the 24k site occupied by germanium has been investigated (Difference Fourier synthesis), which is generally correlated with the appearance of vacancies in the 6d site (see also f.e. clathrates type-I $Ba_8Ag_xGe_{46-x}$, $Ba_8Cu_xGe_{46-x}$ (G. A. Koblyuk-M. N. 2009), $Ba_8Cd_xGe_{46-x}$ (G. A. Koblyuk-M. N. 2007). After excluding vacancies in the crystal structure, the Cu/Ge ratio has been refined and resulted in the reported value of x_{Cu}=5.36 close to the value from EPMA. In case of $Ba_{4.9}Sr_{3.1}Cu_{5.3}Ge_{40.7}$, the refinement furthermore revealed a mixed occupancy of Ba and Sr in the crystallographic sites 2a and 6c (atoms AE1 and AE2). Final refinements for both crystals were carried out introducing anisotropic atom displacement parameters (ADP's) and converged to R-values lower than $R_F \leq 0.022$ and residual electron densities below 1.5 $e^-/Å^3$. The chemical formulae derived from these X-ray refinements ($Ba_{4.86}Sr_{3.14}Cu_{5.36}Ge_{40.64}$ and $Sr_8Cu_{5.36}Ge_{40.64}$) are in good agreement with the composition obtained from EPMA ($Ba_{4.2}Sr_{3.8}Cu_{5.3}Ge_{40.8}$ and $Sr_8Cu_{5.3}Ge_{40.7}$). Details of the structure refinement at 300 K can be found in Table XXV. X-ray powder diffraction intensities collected from polycrystalline samples are in good agreement with the intensities calculated from the structural models obtained from the single crystal studies. The atom site distribution among Ba, Sr in $Ba_{4.86}Sr_{3.14}Cu_{5.36}Ge_{40.64}$, clearly shows that Ba, Sr atoms are sharing both centers of the cages, however, the smaller Sr-atoms reveal preference for the 2a-site in the smaller pentagondodecahedral cage (occ.=0.805) with respect to a much lower Sr-occupancy of the 6c site (standardized setting) at the center of the larger tetrakaidekahedral cage (occ.=0.255). A mixed occupancy of both sites has also been found for $Eu_4Sr_4Ga_{16}Ge_{30}$ by synchrotron X-ray powder diffraction studies (Zhang Y. 2002), whereas full atom order with the smaller atom in the pentagon dodecahedron has been reported for $K_6Eu_2Ga_{10}Ge_{36}$ (B. S. Paschen S. 2006), $K_6Eu_2Zn_5Ge_{41}$ (B. S. Paschen S. 2006), $K_6Eu_2Cd_5Ge_{41}$ (B. S. Paschen S. 2006) and $Eu_2Ba_6M_xSi_{46-x}$ (M=Cu, Al, Ga) (Mudryk Y. 2002) from X-ray single crystal data. The anisotropic displacement parameters (ADP) of the guest atoms inside the large tetrakaidecahedron are usually 2 times larger than those of the guests inside the smaller pentagondodecahedron (U_{11}=0.028(1); $U_{22}=U_{33}$=0.043(1) $Å^2$, see Table XXV and Table XXVI) but for $Sr_8Cu_{5.36}Ge_{40.64}$, the ADP's of Sr2-atoms were about 4 times larger (U_{11}=0.0422(7); $U_{22}=U_{33}$=0.0802(7) $Å^2$) applying the same structure model. Figure 59 shows a plot of the electron density of the Sr2-atoms in the 6c site at 300 K (difference

Fourier synthesis) illustrating a rather unitary round shape in case of $Ba_{4.86}Sr_{3.14}Cu_{5.36}Ge_{40.64}$ (Figure 59b), whereas clear hints are visible for an off-center position in $Sr_8Cu_{5.36}Ge_{40.64}$ (Figure 59a).

Table XXV: X-Ray single crystal data for $Ba_{4.9}Sr_{3.1}Cu_{5.3}Ge_{40.7}$ at 300 K (Anisotropic displacement parameters U_{ij} in [$10^{-2}nm^2$]).

Parameter/compound	**$Ba_{4.9}Sr_{3.1}Cu_{5.3}Ge_{40.7}$**
Space Group	$Pm\bar{3}n$
Formula from EPMA	$Ba_{4.2(1)}Sr_{3.8(1)}Cu_{5.3(1)}Ge_{40.7(1)}$
Formula from refinement	$Ba_{4.86(3)}Sr_{3.14(3)}Cu_{5.36(4)}Ge_{40.64(10)}$
a [nm]	1.06748(2)
μ_{abs} [mm^{-1}]	34.52
V (nm^3)	1.216
ρ_x (gcm^{-3})	5.7
Reflections in refinement	$439 \geq 4\sigma(F_o)$ of 561
Number of variables	20
$R_F = \Sigma\|F_0-F_c\|/\Sigma F_0$	0.022
R_{Int}	0.057
wR2	0.043
GOF	1.152
Extinction (Zachariasen)	0.00109(9)
Residual density $e^-/Å^3$; max; min	1.539; -1.391
Atom parameters	
AE1 in 2a (0,0,0); occ.	0.195(4) Ba + 0.805 Sr
$U_{11}= U_{22}=U_{33}$	0.0125(3)
AE2 in 6c (1/4,0,1/2); occ.	0.745(3) Ba + 0.255 Sr
U_{11}; $U_{22} = U_{33}$	0.0239(4); 0.0431(3)
M in 6d (1/4,1/2,0); occ.	0.107(4) Ge + 0.893 Cu
U_{11}; $U_{22} = U_{33}$	0.0145(5); 0.0102(3)
Ge2 in 16i (*x*, *x*, *x*); occ.	1.000(2)
x	0.18296(3)
$U_{11}=U_{22}=U_{33}$	0.0096(1)
Ge3 in 24k (0,*y*,*z*); occ.	0.999(2)
y, *z*	0.11941(4), 0.31410(4)
U_{11}; U_{22}; U_{33}	0.0110(2); 0.0114(2); 0.0114(2)
Interatomic distances [nm]; Standard deviation < 0.0001	
AE1 – 8 Ge2 0.3383	–3 Ge3 0.2497

	–12Ge3	0.3587		–1 AE1	0.3383
AE2 –	8 Ge3	0.3562		–3 Ge2	0.3906
	–4 M	0.3774		–3 AE2	0.3972
	–8 Ge2	0.3972	Ge3–	1 Ge3	0.2549
M –	4 Ge3	0.2425		–2 Ge2	0.2497
	–4 AE2	0.3774		–1 M	0.2425
	–8 Ge2	0.3972		–2 AE2	0.3561
Ge2–	1 Ge2	0.2479		–1 AE1	0.3587

Table XXVI: X-Ray single crystal data for $Sr_8Cu_{5.3}Ge_{40.7}$ at 300 K (the non-standardized setting is used for an easier comparison; Anisotropic displacement parameters U_{ij} in [10^{-2}nm^2]).

Parameter/compound	**$Sr_8Cu_{5.3}Ge_{40.7}$**
Space Group	$Pm\bar{3}n$
Formula from EPMA	$Sr_{8.0(1)}Cu_{5.3(1)}Ge_{40.7(1)}$
Formula from refinement	$Sr_{8.0(1)}Cu_{5.36(2)}Ge_{40.64(10)}$
a [nm]	1.06368(2)
μ_{abs} [mm^{-1}]	36.07
V (nm^3)	1.203
ρ_x (gcm^{-3})	5.5
Reflections in refinement	423≥4σ(F_o) of 548
Number of variables	22
$R_F = \Sigma\|F_0-F_c\|/\Sigma F_0$	0.020
R_{Int}	0.029
wR2	0.041
GOF	1.076
Extinction (Zachariasen)	0.0013(1)
Residual density e$^-$/Å^3; max; min	1.029; -1.228
Atom parameters	
Sr1 in 2a (0,0,0); occ.	0.989(4)
$U_{11}= U_{22}=U_{33}$	0.0135(3)
Sr2 in 24k (0,y,z); occ.	0.248(1)
y, z	0.4771(7), 0.2405(6)
U_{11}; $U_{22} = U_{33}$	0.028(1); 0.043(1)
M in 6d (1/4,1/2,0); occ.	0.106(3) Ge + 0.894 Cu
U_{11}; $U_{22} = U_{33}$	0.0155(4); 0.0108(2)
Ge2 in 16i (x, x, x); occ.	1.003(2)
x	0.1828(2)
$U_{11}=U_{22}=U_{33}$	0.0104(1)

Ge3 in 24k (0,*y*,*z*); occ.		0.998(2)			
y, *z*		0.1187(5), 0.3148(4)			
U_{11}; U_{22}; U_{33}		0.0119(1); 0.0115(1); 0.0122(1)			
Interatomic distances [nm]; Standard deviation < 0.0001					
Sr1 –	8Ge2	0.3369	M –	4Ge3	0.2414
	–12Ge3	0.3579		–4Sr2	0.3667
Sr2 –	2Ge3	0.3335		–8Sr2	0.3698
	– 2Ge3	0.3541		–8Ge2	0.3959
	– 2Ge3	0.3661		–4Sr2	0.4005
	– 1M	0.3668	Ge2–	1Ge2	0.2474
	– 2M	0.3698		–3Ge3	0.2494
	– 2Ge3	0.3710		–Sr1	0.3369
	– 2Ge2	0.3736		–3Sr2	0.3796
	– 2Ge2	0.3865		–3Sr2	0.3865
	– 1Ge3	0.3893		–3Ge2	0.3890
	– 1M	0.4005	Ge3–	1M	0.2414
	– 2Ge2	0.4102		–2Ge2	0.2494
	– 2Ge3	0.4105		–1Ge3	0.2526
	– 1Ge3	0.4370		–2Sr2	0.3335

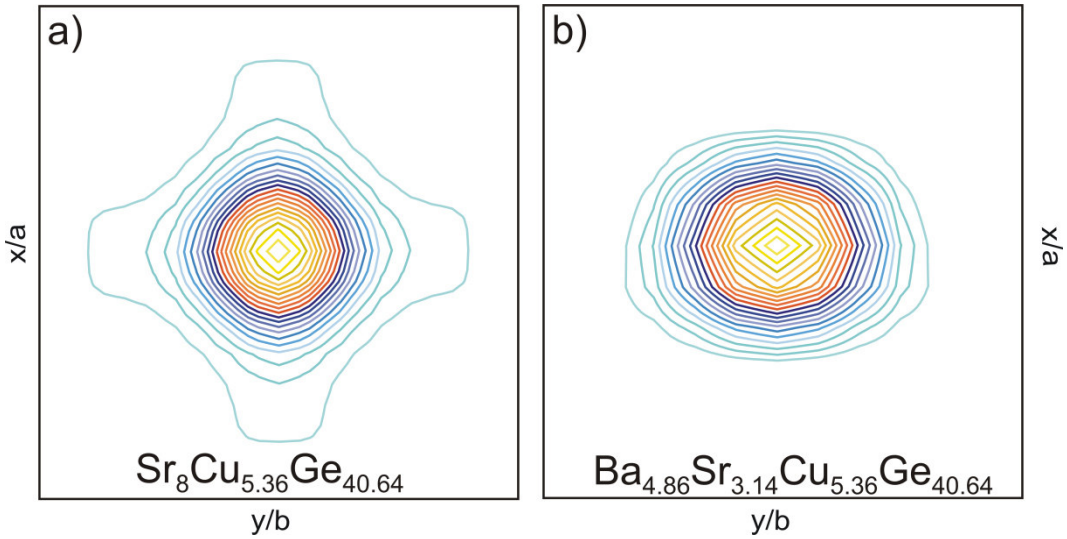

Figure 59: Contour plot of the electron density at 300 K of the Sr2-atoms in the 6c-site for (a) $Sr_8Cu_{5.36}Ge_{40.64}$ and (b) $Ba_{4.86}Sr_{3.14}Cu_{5.36}Ge_{40.64}$ from difference Fourier synthesis; negative electron density was omitted.

This off-centering could be described by placing the strontium atoms (Sr2-atoms) in a 24 k site with an occupation of ~1/4. Off-centering has already been successfully applied to

other ternary type-I clathrates with Sr as guest ions like $Sr_8Zn_8Ge_{38}$ or $Sr_8Ga_{16}Ge_{30}$ (Qiu L. 2004). For $Sr_8Cu_{5.36}Ge_{40.64}$ the distances between the off-center Sr2 atoms at 300 K are 0.0398 nm and 0.0486 nm and decrease only slightly with decreasing temperature (100 K: Sr2-Sr2 0.0371 nm and Sr2-Sr2 0.0421 nm); they are in good agreement with those in $Sr_8Zn_8Ge_{38}$. The results of the crystal structure refinement at 300 K are summarized in Table XXVI.

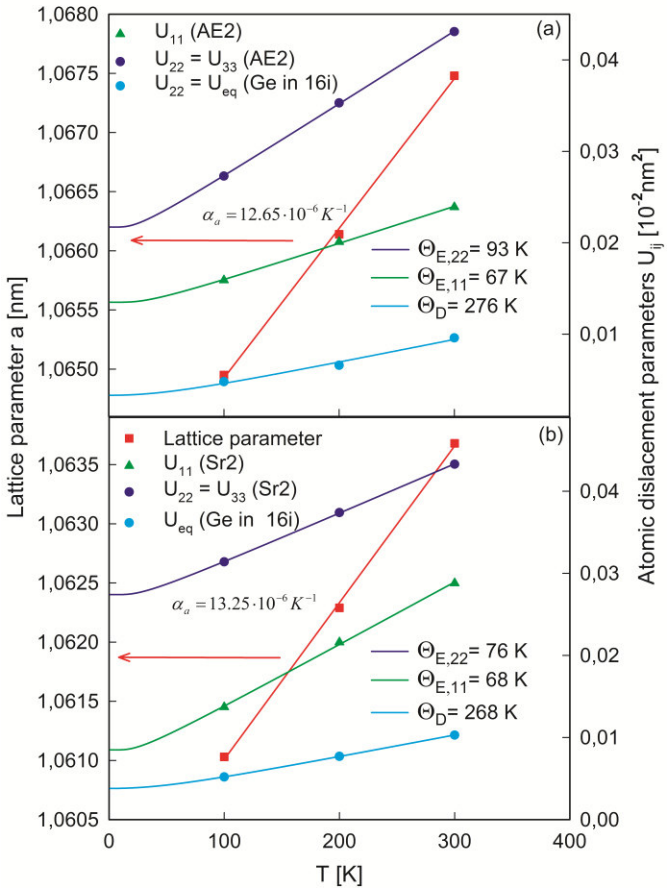

Figure 60: Temperature dependent lattice parameter and atomic displacement parameters of (a) $Ba_{4.86}Sr_{3.14}Cu_{5.36}Ge_{40.64}$ and (b) $Sr_8Cu_{5.36}Ge_{40.64}$.

Least squares fits as a function of temperature of the ADP's (see Figure 60) for AE2 or Sr2 (off-center model) for both crystals employing the Einstein model (Eq.(16)) and the Debye model (Eq.(17) for the framework atoms)

$$U_{ii} = \frac{\hbar^2}{2mk_B\Theta_{E,ii}}\coth\frac{\Theta_{E,ii}}{2T} + d^2 \qquad (16)$$

$$U_{iso} = \frac{3\hbar^2 T}{mk_B\Theta_D^2}\left[\frac{T}{\Theta_D}\int_0^{\Theta_D/T}\frac{x}{e^x-1}dx + \frac{\Theta_D}{4T}\right] + d^2 \qquad (17)$$

(where $\Theta_{E,ii}$ is the Einstein temperature; ii refers to the direction or plane of the vibration; m is the mean atomic mass; k_B is the Boltzmann constant; $\hbar$ is the reduced Planck constant and

Θ_D is the Debye temperature) result in $\Theta_{E,11}$ = 67 K, $\Theta_{E,22}$ = 93 K and Θ_D = 276 K for $Ba_{4.86}Sr_{3.14}Cu_{5.36}Ge_{40.64}$ and $\Theta_{E,11}$ = 68 K, $\Theta_{E,22}$ = 76 K and Θ_D = 268 K for $Sr_8Cu_{5.36}Ge_{40.64}$, respectively.

The linear thermal expansion coefficient, i.e.,

$$\alpha_a = \frac{1}{a_{300K}}\left(\frac{\partial a_T}{\partial T}\right)_p \quad , \tag{18}$$

where a_{300K} is the lattice parameter at 300 K and a_T is the lattice parameter at temperature T, is $\alpha_a = 12.65\times10^{-6}$ K^{-1} ($Ba_{4.86}Sr_{3.14}Cu_{5.36}Ge_{40.64}$) and $\alpha_a = 13.25\times10^{-6}$ K^{-1} ($Sr_8Cu_{5.36}Ge_{40.64}$).

The speed of sound (υ) can be estimated from

$$\upsilon \approx \frac{2\pi\Theta_D k_B}{h} / \left(6\pi^2 n\right)^{1/3} \quad , \tag{19}$$

where n is the number of atoms per unit volume (Qiu L. 2004). The calculated speed of sound according to equation (19) is 2500 m/s for $Sr_8Cu_{5.36}Ge_{40.64}$ and 2600 m/s for $Ba_{4.86}Sr_{3.14}Cu_{5.36}Ge_{40.64}$. These values range in the same order of magnitude as reported by Qiu et al. (Qiu L. 2004) for $Sr_8Zn_8Ge_{38}$ (2600 m/s) or $Sr_8Ga_{16}Ge_{30}$ (2800 m/s).

5.6.1.3 Phase relations at 700°C

Information on the pertinent binary phase diagrams Sr-Ge and Cu-Ge is taken from Massalski (Massalski T.B. 1990). Crystallographic data on the solid phases of the binary systems Sr-Ge and Cu-Ge and the ternary system Sr-Cu-Ge are summarized in Table XXIII.

The phase equilibria in the Ge-rich part of the Sr-Cu-Ge system have been studied below the decomposition temperature of the clathrate type I at 700°C. Only two three-phase equilibria exist in the region investigated (see Figure 61).

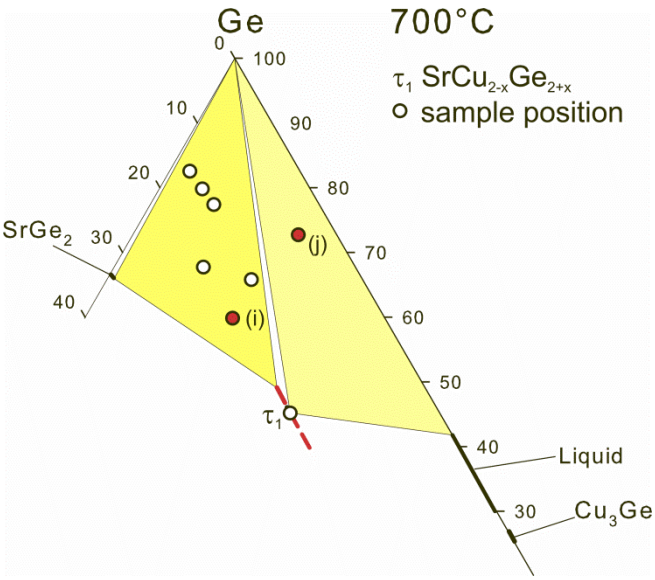

Figure 61: Partial isothermal section of the Sr-Cu-Ge system at 700°C in the Ge-rich corner. Results from EPMA and XPD for the alloys marked in red and labeled with (i) and (j) are given in Table XXIV.

(Ge) is in equilibrium with $SrGe_2$ and $SrCu_{2-x}Ge_{2+x}$ (τ_1) and with τ_1 and liquid. τ_1 crystallizes in the $ThCr_2Si_2$ structure type (XPD) at this temperature and its homogeneity range extends to higher Ge-contents of 48.7 at.% Ge (x=0.4; EPMA). The results of EPMA measurements and XPD are summarized in Table XXIV (i and j).

5.6.1.4 Physical properties

A small single crystal specimen of $Sr_8Cu_{5.3}Ge_{40.7}$ (~ 20mg, with < 1.5% (Ge) as secondary phase) for physical properties measurements (from 2 K to room temperature (RT)) was gained from an arc melted sample (~100 mg), kept on air for some days to decompose due to the presence of $SrGe_2$. The remaining pieces were washed afterwards with diluted H_2SO_4 to remove secondary phases and/or decomposition products. Figure 62 shows the Rietveld refinement of the sample used for physical properties measurements in comparison with the XPD pattern of the as cast alloy and the alloy annealed at 700°C.

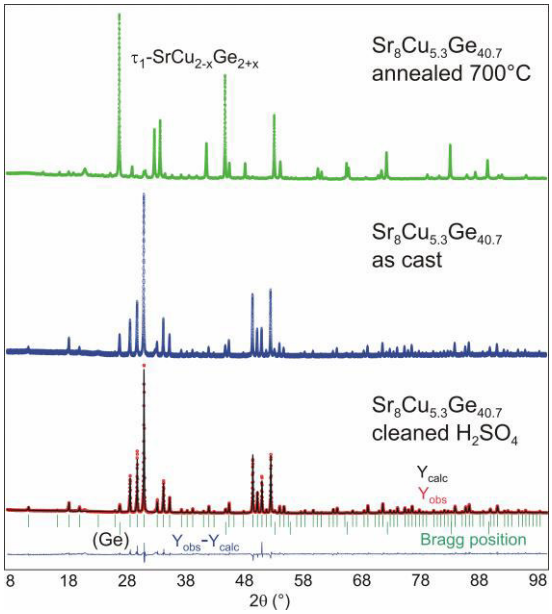

Figure 62: Rietveld refinement of the alloy used for physical properties measurements and XPD pattern of the as cast and annealed (700 °C) alloy.

5.6.1.4.1 Electrical resistivity

The electrical resistivity was measured on bar-shaped pieces of around 1.2 mm length, 0.5 mm height and 0.5 mm width. A study of the temperature dependent electrical resistivity, ρ, performed for $Sr_8Cu_{5.3}Ge_{40.7}$, revealed a simple metallic behavior as deduced from the constant slope of ρ(T) above 80 K (see Figure 63).

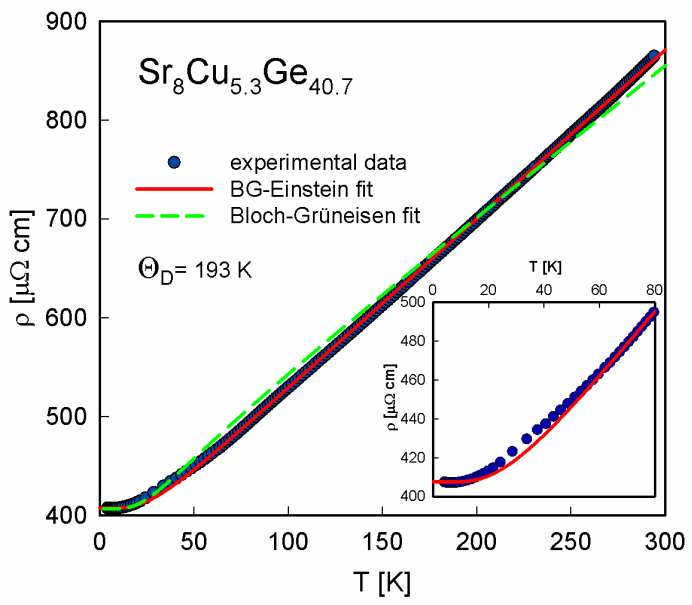

Figure 63: Temperature dependent electrical resistivity, ρ, of $SrCu_{5.3}Ge_{40.7}$; the red solid line corresponds to a least squares fit (Bloch Grüneisen-Einstein fit) as explained in the text and the green dashed line to the simple Bloch Grüneisen fit. The inset shows the temperature range between 2 and 80 K with a larger magnification.

At lower temperatures, a combination of electron scattering on thermally activated acoustic phonons and scattering on low lying optical phonon branches allow to fairly well describe ρ(T), i.e.

$$\rho_{el}(T) = \rho_0 + 4A \cdot \left(\frac{T}{\Theta_D}\right)^5 \int_0^{\Theta_D/T} \left[\frac{x^5}{(e^x - 1)(1 - e^{-x})} dx\right] + B \cdot \left(\Theta_{E,11} - \Theta_{E,22} + T \cdot \ln\left(\frac{e^{\frac{\Theta_{E,22}}{T}} - 1}{e^{\frac{\Theta_{E,11}}{T}} - 1}\right)\right). \quad (20)$$

The first two terms refer to the conventional Bloch Grüneisen (BG) law (BG-fit is shown as a green dashed line in Figure 63), while the far right terms of Eqn. (20) represent the temperature dependence of ρ(T) originated from scattering of conduction electrons on optical phonons (Engquist H.L. 1980). Employing the Einstein temperatures as derived above ($\Theta_{E,11}$ = 68 K and $\Theta_{E,22}$ = 76 K), reveals a reasonable fit to the data for a Debye temperature Θ_D = 193 K, a residual resistivity ρ_0 = 407 μΩcm and two material dependent parameters A = 75.3 μΩcm and B = 11.8 μΩcm/K. The Debye temperature from this procedure is smaller than that extracted from the ADP data. The resulting residual resistivity ratio (RRR) is 2.12. The rather high overall resistivity might be explained from a reduced charge carrier density due to the closeness of the material to a metal-insulator transition. A composition with x_{Cu}=5.333 would actually be at the Zintl limit and locate the alloy in the band gap. However, the experimental uncertainty from EPMA with a Δx_{Cu}~±0.2 might infer a carrier concentration Δn<±0.2 e^-(holes)/f.u. explaining the observed resistivities.

5.6.1.4.2 Heat Capacity

Specific heat measurements of $Sr_8Cu_{5.3}Ge_{40.7}$, taken from 2 K to 200 K, are plotted as C_p/T vs T in Figure 64a.

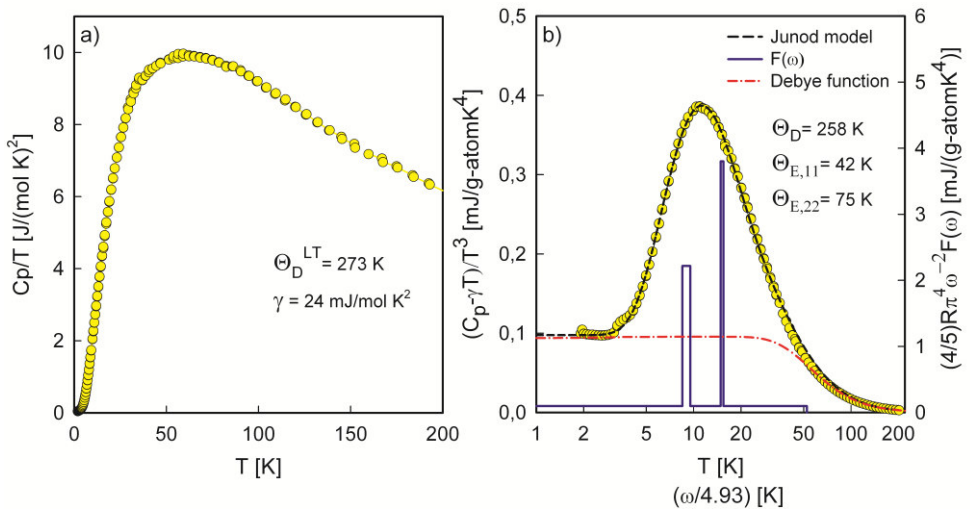

Figure 64: Temperature dependent specific heat, C_p, of $Sr_8Cu_{5.3}Ge_{40.7}$ plotted as C_p/T vs T (a), and $(C_p-\gamma T)/T^3$ vs lnT (b); the dashed line corresponds to the Junod fit as explained in section 3.4.2. The spectral function, F(ω), plotted as $(4/5)R\pi^4\omega^{-2}F(\omega)$ vs. ω/4.93, is shown as a solid line (referring to the right axis); the dashed dotted line is the calculated Debye function.

A standard low temperature fit $Cp(T) = \gamma T + \beta T^3$ was applied, resulting in a Debye temperature Θ_D^{LT} = 273 K that is close to the value obtained from the ADP calculations. The relatively large Sommerfeld value, γ = 24 mJ/molK^2, can be attributed to an electronic density of states at the Fermi energy of about 10 states/eV/f.u. if the electron-phonon enhancement factor is small. The lattice dynamics of $Sr_8Cu_{5.3}Ge_{40.7}$ can be derived, employing a model proposed by Junod et al. ((B. D. Junod A. 1979), (Junod A. 1983)). A comparison between a simple Debye model (red dashed line) and the Junod model (black dashed line) is presented in Figure 64b. The heat capacity data obtained apparently deviate from the simple Debye scenario. As a consequence, an inclusion of Einstein modes with certain finite spectral widths is required to arrive at a proper description of $C_p(T)$. Such a fit renders a Debye temperature Θ_D = 258 K and two Einstein modes, $\Theta_{E,11}$ = 42 K and $\Theta_{E,22}$ = 75 K with a width of 1 K and 3 K, respectively. The resulting spectral function F(ω) is shown as a blue solid line in Figure 64b, referring to the right axis. This analysis clarifies the contribution and backs the importance of Einstein modes in the present clathrate. A more detailed explanation of the models used can be found e.g. in Ref. (G. A. Koblyuk-M. N. 2007).

5.6.1.5 Summary

In the Sr-Cu-Ge system, the clathrate type-I forms in a very small temperature range below melting with a very limited solubility close to the Zintl limit $Sr_8Cu_{5.3}Ge_{40.7}$ and decomposes at about 730 °C eutectoidally into (Ge), $SrGe_2$ and τ_1-$SrCu_{2-x}Ge_{2+x}$. At 700°C, a three phase equilibrium exists between (Ge), $SrGe_2$ and τ_1. The ternary compound τ_1-$SrCu_{2-x}Ge_{2+x}$ exhibits a homogeneity range in the Ge rich part to x=0.4 (a = 0.42850(4) nm, c = 1.0370(1) nm; $ThCr_2Si_2$ type). Lattice parameters of the clathrate type-I solid solution $Ba_{8-y}Sr_yCu_xGe_{46-x}$ ($0 \leq y \leq \sim 5.6$; $5.2 \leq x \leq 5.4$) decrease linearly with increasing Sr content reaching the maximum solubility of strontium at about 10 at%. The clathrate type-I crystal structure has been proven by X-ray single crystal diffraction on two single crystals with composition $Sr_8Cu_{5.3}Ge_{40.7}$ (a(Sr) = 1.06368(2) nm) and $Ba_{4.9}Sr_{3.1}Cu_{5.3}Ge_{40.7}$ (a(mix) = 1.06748(2) nm) measured at 300, 200 and 100 K. For the pure Sr compound an off-center model has been applied for the Sr atom inside the larger cage, whereas in case of the mixed compound the guests take almost center positions in the cages. From the temperature dependency of the lattice parameter and the atomic displacement parameters, the thermal expansion coefficient (α(Sr) = 13.25×10^{-6} and α(mix) = 12.65×10^{-6} K), the Debye (Θ_D(Sr) = 268 and Θ_D(mix) = 276 K) and Einstein temperatures ($\Theta_{E,22}$(Sr) = 76, $\Theta_{E,11}$(Sr) = 68 and $\Theta_{E,22}$(mix) = 93, $\Theta_{E,11}$(mix) = 67 K) and the speed of sound (ν(Sr) = 2500 ν(mix) = 2600 m/s) have been determined. A detailed analysis of the heat capacity data of $Sr_8Cu_{5.3}Ge_{40.7}$ corroborates fairly well these Debye and Einstein temperatures. From these investigations, one might expect a very low and glass-like thermal conductivity as it has been reported for other Sr or Eu based clathrates type-I (see e.g. Ref. (Bridges F. 2004)).

5.7 THE TERNARY SYSTEMS Sr-{Ag,Au}-{Si,Ge}

In a series of previous reports, we have systematically studied the ternary systems Ba-TM-{Si,Ge} (TM = Mn (Grytsiv A. 2009), Fe (Grytsiv A. 2009), Co (Grytsiv A. 2009), Rh [(G. A. Falmbigl M. 2013), (K. F. Falmbigl M. 2013)], Ir (G. A. Falmbigl M. 2013), Ni (C. M. Falmbigl M. 2012), Pd [(G. A. Koblyuk-M. N. 2008), (G. A. Koblyuk-M. N. 2007)], Pt [(G. A. Koblyuk-M. N. 2008), (G. A. Koblyuk-M. N. 2007)], Cu [(G. A. Koblyuk-M. N. 2009), (Yan X. 2010)], Ag [(B. E. Zeiringer I. 2011), (C. M. Zeiringer I. 2011), (G. A. Zeiringer I. 2012)], Au [(C. M. Zeiringer I. 2012), (M.-K. N. Zeiringer I. 2011)], Zn [(G. A. Koblyuk-M. N. 2007), (G. A.-K. Nasir N. 2009)] and Cd [(G. A.-K. Nasir N. 2009), (Koblyuk-M. N. 2007)]) and Sr-TM-{Si,Ge} (TM = Ni [(Falmbigl M. 2014), (Nasir N. 2010)], Cu [(Falmbigl M. 2014), (Nasir N. 2010), (Zeiringer I. 2014)], Pd (Romaka V.V. 2015), Pt (Romaka V.V. 2015), Zn [(Falmbigl M. 2014), (Romaka V.V. 2012)]) concerning the phase relations, formation and properties of thermoelectric clathrates, BCS-type superconducting skutterudites (f.e. $\{Ba,Sr\}Pt_4Ge_{12}$ (Bauer E. 2007)) and other new ternary intermetallic compounds (f.e. $BaPt_5Si_{12}$ (Grytsiv A.V. 2010)) or ternary compounds EpT_xX_{4-x} (Ep=Sr, Ba; T = Ni, Pd, Pt, Ag, Au; X = Si, Ge, Sn; (F. Kneidinger 2014)) among which noncentrosymmetric representatives exhibit unconventional superconductivity. Sequel to these studies, the present work is devoted to the investigation of the ternary systems Sr-{Ag,Au}-Si and Sr-{Ag,Au}-Ge in as cast state and after annealing at 700°C (Ge systems) or 800°C (Si systems). Hitherto, only a few ternary phases from these Sr-systems have been reported in the literature. Common to all these is a phase with 122 stoichiometry and $ThCr_2Si_2$ structure type (space group *I*4/*mmm*): $SrAg_2Ge_2$ (Eisenmann B. 1970), $SrAg_2Si_2$ (May N. 1972), $SrAu_2Ge_2$ ((Lin Q. 2012), (May N. 1972)) and $SrAu_2Si_2$ (N. N. Dörrscheidt W. 1976). The off-stoichiometric compounds $SrAu_{1.6}Ge_{2.4}$ ($CeBe_2Ge_2$ type, space group *P*4/*nmm*) and $SrAu_{1.9}Ge_{2.1}$ ($BaCu_2Sb_2$ type, space group *I*4/*mmm*) have been reported in our paper on ternary compounds EpT_xX_{4-x} (F. Kneidinger 2014). $SrAu_3Ge$ ($BaAu_3Ge$ type, space group *P*4/*nmm*) has recently been described by Lin and Corbett (Lin Q. 2012). Merlo et al. (Merlo F. 1996) investigated RMX compounds with R=alkaline earth, Eu or Yb, M=Ag and X=Si, Ge, Sn or Pb and among them characterized the compounds $SrAg_{0.9}Ge_{1.1}$ (AlB_2 type, space group *P*6/*mmm*), $Sr(Ag_{0.5}Ge_{0.5})_2$ (SrAgGe type, space group *C*2/*m*), $SrAg_{1.1}Ge_{0.9}$ (KHg_2 type, space group *Imma*). $Sr_8Ag_5Si_9$ ($Sr_8Ag_5Si_9$ type, space group *C*222) has been characterized by Dörrscheidt and Schäfer[38] from X-ray single crystal investigations.

The present paper is designed to explore the four ternary systems Sr-{Ag,Au}-{Si,Ge} in order to clarify two questions: (i) the existence of clathrate compounds, which may exhibit interesting thermoelectric properties, and (ii) the existence of compounds with noncentrosymmetric crystal structures and fully ordered atom arrangements, which may provide examples for unconventional superconductivity at low temperatures.

5.7.1 Results and Discussion

5.7.1.1 The binary systems Sr-Si, Sr-Ge, Sr-Ag, Sr-Au, Ag-Si, Ag-Ge, Au-Si and Au-Ge

Information on the binary phase diagrams Sr-Si and Sr-Ge are accepted from Palenzona and Pani ((Palenzona A. 2005), (Palenzona A. 2004)), whereas phase relations for the systems Sr-Ag, Sr-Au, Ag-Si, Ag-Ge, Au-Si and Au-Ge were taken from Massalski (Massalski T.B. 1990). Crystallographic details of all solid phases are summarized in Table XXVII.

Table XXVII: Crystallographic data on solid phases of the binary phase diagrams Sr-Ge, Sr-Si, Sr-Ag, Sr-Au, Ag-Ge, Ag-Si, Au-Ge and Au-Si and of the ternary systems Sr-{Ag,Au}-{Si,Ge}. The symbol □ denotes a vacancy.

Phase	Space group	Structure type	Lattice parameter [nm]			Reference/ Method
			a	b	c	
(βSr) hT (T > 547 °C)	$Im\bar{3}m$	W	0.485(1)	-	-	(Sheldon E.A. 1953)
(αSr) rT	$Fm\bar{3}m$	Cu	0.60849(5)	-	-	(Sheldon E.A. 1953)
(Si)	$Fd\bar{3}m$	C_{diam}	0.54303	-	-	(Massalski T.B. 1990)
(Ge)	$Fd\bar{3}m$	C_{diam}	0.56574	-	-	(Massalski T.B. 1990)
(Ag)	$Fm\bar{3}m$	Cu	0.40857	-	-	(Massalski T.B. 1990)
(Au)	$Fm\bar{3}m$	Cu	0.40773	-	-	(Massalski T.B. 1990)
Sr_2Si	*Pnma*	Co_2Si	0.811	0.515	0.954	(Widera A. 1976)
Sr_5Si_3	*I*4/*mcm*	Cr_5B_3	0.8089(4)	-	1.5733(8)	(Nesper R. 1999)
SrSi	*Cmcm*	TlI	0.483(1)	1.133(1)	0.404(1)	(Rocktäschel G. 1962)
β-$SrSi_2$ #	$I4_1/amd$	α-$ThSi_2$	0.4429(1)	-	1.3842(1)	(Palenzona A. 2004)
α-$SrSi_2$	$P4_332$	$SrSi_2$	0.6515	-	-	(Pringle G.E. 1972)
Sr_2Ge	*Pnma*	Co_2Si	0.813(2)	0.520(6)	0.958(2)	(S. H. Eisenmann B. 1975)
SrGe	*Cmcm*	TlI	0.486(1)	1.140(1)	0.419(1)	(S. H. Betz A. 1967)
$SrGe_{1.85}$	*P*6/*mmm*	AlB_2	0.4259(1)	-	0.4578(1)	(Palenzona A. 2005)
$SrGe_2$	*Pnma*	$BaSi_2$	0.874	0.665	1.124	(S. H. Betz A. 1968)

$SrAg_5$	*P6/mmm*	$CaCu_5$	0.5675	-	0.4619	(B. G. Palenzona A. 1967)
$SrAg_4$	unknown	unknown	-	-	-	(Massalski T.B. 1990)
$SrAg_2$	*Imma*	KHg_2	0.4817	0.7716	0.8263	(Köster W. 1965)
SrAg	*Pnma*	SrAg	1.6558(7)	0.4788(1)	0.6385(1)	(F. M. Merlo F. 1981)
Sr_3Ag_2	$R\bar{3}$	Er_3Ni_2	0.9962(3)	-	1.861(1)	(F. M. Merlo F. 1981)
$SrAu_5$	*P6/mmm*	$CaCu_5$	0.5627	-	0.4616	(Feller Kniepmeier M. 1960)
$SrAu_2$	*Imma*	KHg_2	0.4700	0.7489	0.8234	(Bruzzone G. 1970)
Sr_3Au_2	$R\bar{3}$	Er_3Ni_2	0.9604(4)	-	1.836(1)	(Fornasini M.L. 1985)
Sr_3Au_2 hT ($725 \leq T \leq 770$ °C)	unknown	unknown	-	-	-	(Massalski T.B. 1990)
Sr_7Au_3	$P6_3mc$	Th_7Fe_3	1.107(1)	-	0.7161(4)	(F. M. Merlo F. 1984)
Sr_9Au	unknown	unknown	-	-	-	(Massalski T.B. 1990)
Ternary Compounds						
$Sr_8Ag_5Si_9$	*C*222	$Sr_8Ag_5Si_9$	0.848(1)	1.469(2)	1.840(2)	(S. H. Dörrscheidt W. 1981), XSCD
τ_1-$Sr_2Ag_{1+x}Si_{3-x-y}\square_y$ x=0.17; y=0.43	*Fddd*	Sr_2LiSi_3	0.84488(2)	1.46376(2)	1.84018(2)	*, XSCD
τ_2-$SrAg_{2-x}Si_{2+x}$ x=0.1	*I4/mmm*	$ThCr_2Si_2$	0.437664(6)	-	1.04517(2)	*, XSCD
x=0			0.438(2)	-	1.048(2)	(May N. 1972), XSCD
τ_1-$Sr(Ag_xGe_{1-x})_2$ x=0.25	*P6/mmm*	AlB_2	0.43431(2)	-	0.45838(1)	*, XPD
x=0.45			0.4439(1)	-	0.4443(1)	(Merlo F. 1996), XPD
SrAgGe	*C2/m*	SrAgGe	1.1064(3)	0.4671(1) β=98.64(2)°	1.4171(2)	(Merlo F. 1996), XPD
$SrAg_{1.1}Ge_{0.9}$	*Imma*	KHg_2	0.4708(3)	0.7568(6)	0.8084(6)	(Merlo F. 1996), XPD
τ_2-$SrAg_{2-x}Ge_{2+x}$ x=0.2	*I4/mmm*	$ThCr_2Si_2$	0.44476(2)	-	1.0822(1)	*, XPD
x=0			0.445	-	1.085	(Eisenmann B. 1970), XSCD
τ_1-$Sr(Au_xSi_{1-x})_2$ x=0.375	*P6/mmm*	AlB_2	0.42241(2)	-	0.45799(3)	*, XPD
τ_1´-$Sr(Au_xSi_{1-x})_2$ x=0.25	*Fmmm*	Ca_2AgSi_3	0.83407(2)	1.44465(2)	0.92664(3)	*, XSCD
τ_2-$Sr(Au_{1-y}\square_y)(Si_{1-x}Au_x)_3$ x=0.59; y=0.64	*I4mm*	$BaNiSn_3$	0.44594(2)	-	1.01013(6)	*, XSCD
$SrAu_2Si_2$	*I4/mmm*	$ThCr_2Si_2$	0.437(1)	-	1.014(2)	(N. N. Dörrscheidt W. 1976), XSCD

τ_3-$SrAu_{3+x}Si_{1-x}$	-	unknown	-	-	-	*
τ_4-$SrAu_{5x}\square_xSi_2$ x=0.7	*Pnma*	$BaAu_5Si_2$	0.87557(3)	0.69945(2)	0.98873(3)	*, XSCD
τ_1-$Sr(Au_xGe_{1-x})_2$ x=0.25	*P6/mmm*	AlB_2	0.43263(2)	-	0.45852(7)	*, XPD
τ_2-$SrAu_{2-x}Ge_{2+x}$						
x=0	*I4/mmm*	$ThCr_2Si_2$	0.451(2)	-	1.035(2)	(May N. 1972), XSCD
x=0			0.4519(2)	-	1.0356(4)	(Lin Q. 2012), XSCD
x=0			0.45103(2)	-	1.0364(1)	*, XPD
x=0.2			0.45214(4)	-	1.0336(1)	*, XPD
x=0.35	*I4/mmm*	$BaCu_2Sb_2$	0.44866(2)	-	3.1808(1)	(F. Kneid. 2014), XSCD*
x=0.4			0.4477(2)	-	3.1694(2)	*, XPD
x=0.45	*P4/nmm*	$CaBe_2Ge_2$	0.44796(2)	-	1.06315(5)	(F. Kneid.2014), XSCD*
x=0.5			0.44930(4)	-	1.0578(2)	*, XPD
x=0.6			0.45131(3)	-	1.0496(2)	*, XPD
$SrAu_3Ge$	*P4/nmm*	$BaAu_3Ge$	0.6265(1)	-	0.55082	(Lin Q. 2012), XSCD

*This work; #temperature of the α-β transition is uncertain

5.7.1.2 The ternary systems Sr-{Ag,Au}-{Si,Ge}

The four ternary systems Sr-Ag-Si, Sr-Ag-Ge, Sr-Au-Si and Sr-Au-Ge have been investigated by EPMA and XPD in as cast state and after annealing at 700°C (Ge) or 800°C (Si) up to a maximum strontium content of 33.4 at.%. Crystallographic details of the solid ternary phases are given in Table XXVII.

5.7.1.2.1 The System Sr-Ag-Si

The partial isothermal section at 800°C of the Sr-Ag-Si system, shown in Figure 65, has been constructed basically on the results of XPD and EPMA of the annealed alloys marked in red and labelled with (a)-(d) (see Table XXVIII).

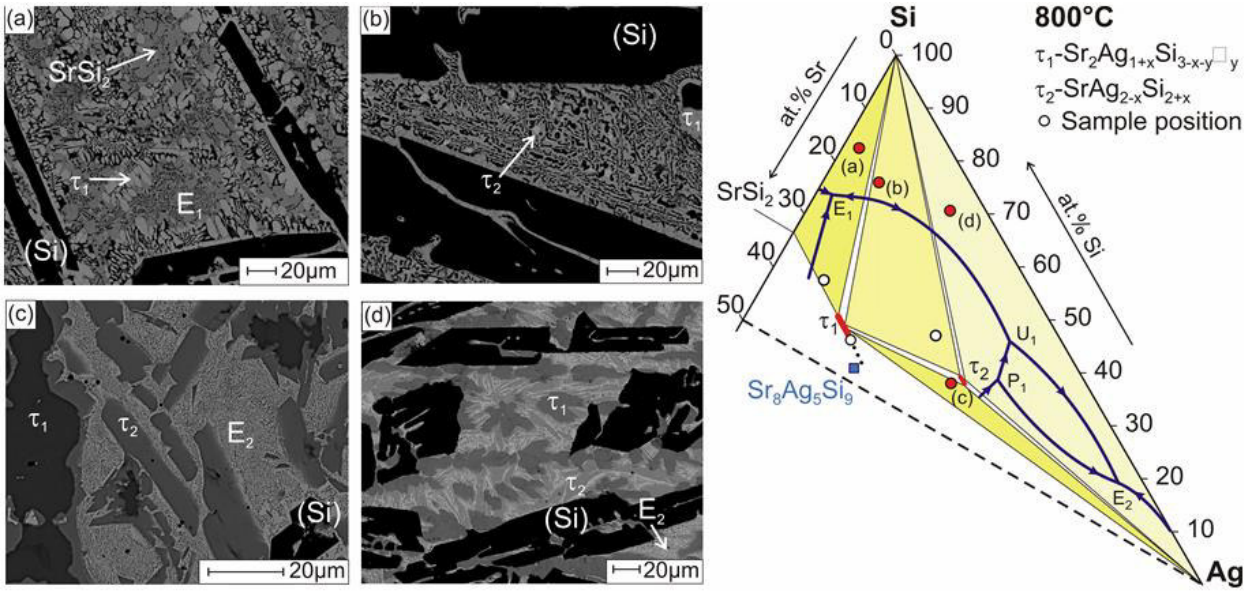

Figure 65: Isothermal section at 800°C and tentative liquidus projection (E: eutectic reaction, P: peritectic reaction, U: transition reaction) for the Sr-Ag-Si system up to 33.4 at.% Sr and microstructures in as cast state of the alloys marked in red and labelled with (a)-(d) in the isothermal section. The results from XPD and EPMA for these alloys annealed at 800°C are summarized in Table XXVIII.

Table XXVIII: Results from EPMA and XPD for alloys in as cast state or after annealing in the ternary systems Sr-Ag-{Ge,Si}.

Alloy (Nominal composition)	X-ray phase analysis	Structure type	Lattice parameter [nm]			Composition EPMA (at.%)		
			a	b	c	Sr	Ag	Ge Si
Sr-Ag-Si								
$Sr_{14.8}Ag_{2.8}Si_{82.4}$	(Si)	C_{diam}	0.54310(4)	-	-	-	-	100.0
800 °C (a)	α-$SrSi_2$	$SrSi_2$	0.65391(3)	-	-	33.0	-	67.0
	τ_1	Sr_2LiSi_3	0.83725(5)	1.4509(1)	1.8591(1)	33.6	14.7	51.7
$Sr_{14.8}Ag_{9.3}Si_{75.9}$	(Si)	C_{diam}	0.54301(3)	-	-	-	-	100.0
As cast (b)	τ_1	Sr_2LiSi_3	0.84547(5)	1.46521(1)	1.84266(2)	32.9	17.6	49.5
	τ_2	$ThCr_2Si_2$	-	-	-	-	-	-
$Sr_{20}Ag_{33}Si_{47}$	(Si)	C_{diam}	-	-	-	-	-	100.0
800 °C	τ_1	Sr_2LiSi_3	-	-	-	33.7	17.7	48.6
	τ_2	$ThCr_2Si_2$	0.43717(2)	-	1.0434(1)	20.1	39.2	40.7
$Sr_{22}Ag_{40}Si_{38}$	τ_1	Sr_2LiSi_3	-	-	-	33.8	17.5	48.7
800 °C (c)	τ_2	$ThCr_2Si_2$	0.43821(3)	-	1.0460(2)	20.6	40.2	39.2
	(Ag)	Cu	-	-	-	0.2	99.0	0.8

$Sr_{5.8}Ag_{23.6}Si_{70.6}$	(Si)	C_{diam}	-	-	-	-	-	100.0
800 °C (d)	τ_2	$ThCr_2Si_2$	0.43822(3)	-	1.0463(1)	19.9	41.9	38.2
	(Ag)	Cu	0.40830(3)	-	-	-	99.5	0.5
Sr-Ag-Ge								
$Sr_{14.8}Ag_{9.3}Ge_{75.9}$	(Ge)	C_{diam}	0.56594(5)	-	-	-	-	100.0
700 °C (e)	$SrGe_2$	$BaSi_2$	-	-	-	33.4	-	66.6
	τ_2	$ThCr_2Si_2$	0.44561(4)	-	1.0827(1)	19.8	33.7	46.5
$Sr_{32}Ag_{11}Ge_{57}$	$SrGe_2$	$BaSi_2$	0.8725(1)	0.6553(2)	1.1196(7)	32.7	-	67.3
700 °C (f)	τ_1	AlB_2	0.43343(3)	-	0.45837(5)	33.1	17.1	49.8
	τ_2	$ThCr_2Si_2$	-	-	-	19.5	34.1	46.4
$Sr_{5.9}Ag_{23.5}Ge_{70.6}$	(Ge)	C_{diam}	-	-	-	-	-	100.0
700 °C (g)	τ_2	$ThCr_2Si_2$	0.44531(2)	-	1.0823(1)	19.4	35.0	45.6
	(Ag)	Cu	-	-	-	-	85.1	14.9
$Sr_{22}Ag_{34}Ge_{44}$	τ_1	AlB_2	0.4341(1)	-	0.4587(1)	33.2	16.9	49.9
700 °C (h)	τ_2	$ThCr_2Si_2$	0.44476(2)	-	1.0822(1)	19.7	36.4	43.9

The microstructures of the silicon rich alloys in as cast state (Figure 65(a), (b)) are characterized by large (Si) dendrites and large amounts of eutectic matrix. In Figure 65(a), the solidification of liquid appears along the monovariant line L ↔ (Si)+τ_1 (τ_1-$Sr_2Ag_{1+x}Si_{3-x-y}\square_y$; Sr_2LiSi_3 type) finally ending with the crystallization of $SrSi_2$ ($SrSi_2$ type) in the invariant point E_1: L ↔ (Si)+$SrSi_2$+τ_1 (at ~ $Sr_{24}Ag_2Si_{74}$ in at.%) close to the binary eutectic L ↔ (Si)+$SrSi_2$ at 74 at.% Si. The eutectic structure of as cast alloy $Sr_{14.8}Ag_{9.3}Si_{75.9}$ in Figure 65(b) arises due to the crystallization of liquid along the same monovariant line. Very small quantities of τ_2 (τ_2-$SrAg_{2-x}Si_{2+x}$; $ThCr_2Si_2$ type) are also present in this alloy. The microstructure of the cast alloy with nominal composition $Sr_{22}Ag_{40}Si_{38}$ (Figure 65(c)) documents the peritectic reaction P_1: L+τ_1+(Si) ↔ τ_2 in which grains of τ_2 form around primary τ_1. Primary grains of (Si) together with τ_1, τ_2 and silver rich liquid in Figure 65(d) confirm this reaction. The position of a silver rich ternary eutectic E_2: L ↔ (Si)+(Ag)+τ_2 (at ~$Sr_4Ag_{79}Si_{17}$ in at.%) is near the binary one L ↔ (Si)+(Ag) (89 at.% Ag). Based on the analysis of the microstructures of all alloys, a tentative liquidus projection has been constructed, which is presented in Figure 65.

Phase equilibria at 800°C (see Figure 65) are characterized by the two ternary compounds τ_1-$Sr_2Ag_{1+x}Si_{3-x-y}\square_y$ and τ_2-$SrAg_{2-x}Si_{2+x}$. A liquid phase is not present anymore at 800°C in the

(Ag) rich part of the isothermal section. EPMA suggest a homogeneity region for τ_1 extending at 800°C from $Sr_{33.6}Ag_{14.7}Si_{51.7}$ in at.% but its Ag rich end has not been determined yet. A single crystal has been selected for this phase. τ_2 exhibits only a very limited homogeneity range at 800°C (x = ± 0.1). Details of the single crystal X-ray diffraction refinements are presented in the following chapters.

5.7.1.2.1.1 The crystal structure of τ_1- $Sr_2Ag_{1+x}Si_{3-x-y}\square_y$ (Sr_2LiSi_3-type)

In order to elucidate the precise atom distribution in the crystal structure of τ_1 at lower silver and strontium contents than in the stoichiometric compound $Sr_8Ag_5Si_9$ (quenched from 1000°C, XSCD, space group *C*222; a=0.848(1), b = 1.469(2), c=1.840(2) nm) previously reported by Dörrscheidt (S. H. Dörrscheidt W. 1981) a single crystal was selected from a single-phase sample with nominal composition $Sr_{33.3}Ag_{20}Si_{46.7}$ after annealing at 800°C. The observed extinctions were unambiguously consistent with the space group *Fddd* (Nr. 70; a=0.84488(2), b=1.46376(2), c=1.84018(3) nm). Crystal structure refinement was successful using the atomic positions of the Ba_2LiSi_3 structure (Von Schnering H.G. 1996), but refinement of the occupancies did not reveal full ordering in all positions. Whereas the Sr atoms fully occupy the crystallographic sites 16g (1/8,1/8,0.50010(2)) and 16g (1/8,1/8,-0.00026(1)), the Wyckoff positions 16f (1/8,0.45741(3),1/8) and 32h (0.37158(5),0.04132(4),0.12437(2)) are randomly shared by silver and silicon. However, the Wyckoff site 16f (1/8,0.2888(1),1/8) is only partially filled (58 %) by silicon resulting in the composition $Sr_2Ag_{1.17(1)}Si_{2.40}\square_{0.43}$. The partial occupancy of the 16-fold position significantly improves the R- value by ~ 1.5% and also reduces the anisotropy in the atom displacement parameters (ADPs) of all atoms. The refinement converged with R_F=0.041, with rather spherical ADPs and without any significant residual electron densities (± 1.5 e/Å^3). The smallest interatomic distances are $d_{Si\text{-}M(Ag+Si)}$=0.2390 nm, $d_{M\text{-}M(Ag+Si)}$=0.2450 nm, $d_{Sr\text{-}M(Ag+Si)}$=0.3332 nm, $d_{Sr\text{-}Si}$=0.3326 nm and $d_{Sr\text{-}Sr}$=0.4224 nm. Further details of the crystal structure refinement are listed in Table XXIX.

Table XXIX: X-Ray single crystal data for τ_1-$Sr_2Ag_{1+x}Si_{3-x-y}\square_y$ (Sr_2LiSi_3-type) at RT (anisotropic displacement parameters U_{ij} in [$10^{-2}nm^2$]). The symbol □ denotes a vacancy. In this case, the non-standardized setting is used for an easier comparison with isostructural and standardized Ba_2AgSi_3 (Cardoso Gil R. 1999).

Parameter/Compound	**$Sr_2Ag_{1+x}Si_{3-x-y}\square_y$; x=0.17, y=0.43**
Space Group	*Fddd*
Formula from EPMA (at.%)	$Sr_{33.4}Ag_{19}Si_{47.6}$
Composition from refinement	$Sr_2Ag_{1.17(1)}Si_{2.40}\square_{0.43} \equiv$ $^*Sr_{33.3}Ag_{21.85}Si_{44.82}$ at.%
a, b [nm]	0.84488(2), 1.46376(2)
c [nm]	1.84018(3)
μ_{abs} [mm^{-1}]	15.6
V (nm^3)	2.275
ρ_x (gcm^{-3})	4.31
Reflections in refinement	$831 \geq 4\sigma(F_o)$ of 831
Number of variables	34
$R_F = \Sigma\|F_0-F_c\|/\Sigma F_0$	0.041
R_{Int}	0.060
wR2	0.068
GOF	1.31
Extinction (Zachariasen)	0.00006(1)
Residual density $e^-/Å^3$; max; min	1.23; -1.54
Atom parameters	
Sr1 in 16g (1/8,1/8,z); occ.	0.999(2)
z	-0.00026(1)
U_{11}, U_{22}, U_{33}, $U_{12;}$ $U_{23}=U_{13}=0$	0.0097(3), 0.0098(2), 0.0091(3), -0.0040(2)
Sr2 in 16g (1/8,1/8,z); occ.	1.000(2)
z	0.50010(2)
U_{11}, U_{22}, U_{33}, $U_{12;}$ $U_{23}=U_{13}=0$	0.0093(3), 0.0097(7), 0.0082(3), -0.0037(2)
Si1 in 16f (1/8,y,1/8); occ.	0.58(1)
y	0.2888(1)
U_{11}, U_{22}, U_{33}, $U_{13;}$ $U_{12}=U_{23}=0$	0.014(1), 0.014(1), 0.016(2), -0.010(1)
M1 in 16f (1/8,y,1/8); occ.	0.560(2) Ag + 0.440 Si
y	0.45741(3)
U_{11}, U_{22}, U_{33}, $U_{13;}$ $U_{12}=U_{23}=0$	0.0090(3), 0.0079(2), 0.0124(3) 0.0014(2)
M2 in 32h (x,y,z); occ.	0.307(2) Ag + 0.693 Si
x, y, z	0.37158(5), 0.04132(4), 0.12437(2)
U_{11}, U_{22}, U_{33} U_{23}, U_{13}, U_{12}	0.0072(4), 0.0091(3), 0.0133(4) 0.0002(1), 0.0032(3), -0.0010(1)
Interatomic distances [nm]; Standard deviation < 0.0001	
Sr1 – 2M2 0.3343	–2Sr2 0.3365
–2M1 0.3349	–2Sr1 0.3369

	–2M1	0.3362	M1 –	1Si1	0.2468
	–2M2	0.3364		–2M2	0.2468
	–2Si1	0.3369		–2Sr2	0.3344
	–2M2	0.3380		–2Sr1	0.3349
	–2Sr2	0.4224	M2 –	1Si1	0.2391
Sr2 –	2Si2	0.3326		–1M2	0.2450
	–2M2	0.3332		–1M1	0.2468
	–2M1	0.3344		–1Sr2	0.3332
	–2M2	0.3348		–1Sr1	0.3343
	–2Si1	0.3365		–1Sr2	0.3348
	–2Sr1	0.4224		–1Sr2	0.3354
Si1 –	2M2	0.2390		–1Sr1	0.3364
	–1M1	0.2468		–1Sr1	0.3379
	–2Sr2	0.3326			

*Composition in at. %, normalised to 33.33 at.% Sr, as vacancies only appear in the Si positions

Detailed discussions of the Sr_2LiSi_3 structure type (filled ß-$K_4\square_2P_6$-type, superstructure of AlB_2-type based on 32 AlB_2-type subcells) and isotypic compounds as f.e. Eu_2AgSi_3, Ca_2AgSi_3 or Ba_2AgSi_3 can be found in the papers of Schnering et al. (Von Schnering H.G. 1996) and Cardoso et al. (Cardoso Gil R. 1999). Mixed site occupancies of silver and silicon in the crystallographic sites 16f and 32h have also been encountered for Eu_2AgSi_3 (Cardoso Gil R. 1999). The rather large anisotropic ADPs reported for the silicon atoms in the 16f site may also indicate the presence of vacancies in the crystal structure of Eu_2AgSi_3 (Cardoso Gil R. 1999). It should be mentioned that similar to Eu_2AgSi_3 (Cardoso Gil R. 1999) also $Sr_2Ag_{1+x}Si_{3-x-y}\square_y$ exhibits hexagonal pseudosymmetry (b/a = 1.7325 ~ √3). The possibility of intergrowth with domains of polymorphic modifications (such as α-$K_4\square_2P_6$-type) or stacking faults leading to the appearance of random substitutions and vacancies have already been discussed earlier (Cardoso Gil R. 1999).

As the Si-poor end and the phase width of the homogeneity range of τ_1 has not been investigated in this work, a symmetry reduction to space group *C*222, as has been reported earlier for $Sr_8Ag_5Si_9$ (S. H. Dörrscheidt W. 1981), cannot be excluded for Si-poor concentrations.

5.7.1.2.1.2 The crystal structure of τ_2-$SrAg_{2-x}Si_{2+x}$ ($ThCr_2Si_2$ type)

A single crystal suitable for X-ray single crystal structure determination was selected from a mechanically crashed alloy with nominal composition $Sr_{20}Ag_{33}Si_{47}$ annealed at 800°C. Analysis of the X-ray diffraction spots revealed a body centred tetragonal unit cell (a=0.437664(6) and c=1.04517(2) nm) and the crystal structure solution was performed in space group *I*4/*mmm* as the one with the highest possible symmetry consistent with systematic extinctions. Refinement of the occupancy of the atomic positions revealed full occupation of Sr in the 2a (0,0,0) and Si in the 4e (0,0,z) site. Refinement of the 4d (0,1/2,1/4) site leads to a mixed Si and Ag occupation resulting in a final composition $SrAg_{1.88}Si_{2.12}$ and R_F = 0.012. These results confirm the $ThCr_2Si_2$ structure type, earlier reported for $SrAg_2Si_2$ (May N. 1972). Details of the crystal structure refinement are given in Table XXX.

Table XXX: X-Ray single crystal data for τ_2-$SrAg_{2-x}Si_{2+x}$ ($ThCr_2Si_2$-type) at RT (anisotropic displacement parameters U_{ij} in [$10^{-2}nm^2$]).

Parameter/ Compound	**$SrAg_{2-x}Si_{2+x}$; x=0.1**
Space Group	*I* 4/*mmm*
Formula from EPMA (at.%)	$Sr_{20}Ag_{38}Si_{42}$
Formula from refinement	$SrAg_{1.88(2)}Si_{2.12} \equiv Sr_{20}Ag_{37.6}Si_{42.4}$
a, c [nm]	0.437664(6), 1.04517(2)
μ_{abs} [mm^{-1}]	35.0
V (nm^3)	0.2002
ρ_x (gcm^{-3})	5.80
Reflections in refinement	195≥4σ(F_o) of 195
Number of variables	11
$R_F = \Sigma\|F_0-F_c\|/\Sigma F_0$	0.012
R_{Int}	0.041
wR2	0.024
GOF	1.125
Extinction (Zachariasen)	0.0201(8)
Residual density $e^-/Å^3$; max; min	0.93; -1.44
Atom parameters	
Sr in 2a (0,0,0); occ.	1.006(5)
$U_{11}= U_{22}$, U_{33}; $U_{12}=U_{23}=U_{13}=0$	0.0078(1), 0.0081(2)
M in 4d (0,1/2,1/4); occ.	0.938(2) Ag+0.062 Si

U_{11}= U_{22}, U_{33}; U_{12}=U_{23}=U_{13}=0			0.01202(9), 0.0092(1)		
Si in 4e (0,0,z); occ.			0.993(5)		
z			0.38842(8)		
U_{11}= U_{22}, U_{33}; U_{12}=U_{23}=U_{13}=0			0.0102(3), 0.0079(4)		
Interatomic distances [nm]; Standard deviation < 0.0001					
Sr –	8Si	0.3327		–4Sr	0.3408
	–8M	0.3408	Si –	1Si	0.2332
M –	4Si	0.2623		–4M	0.2623
	–4M	0.3095		–4Sr	0.3307

5.7.1.2.2 The System Sr-Ag-Ge

The isothermal section has been constructed from the results of EPMA and XPD of alloys annealed at 700°C (see Figure 66 and Table XXVIII).

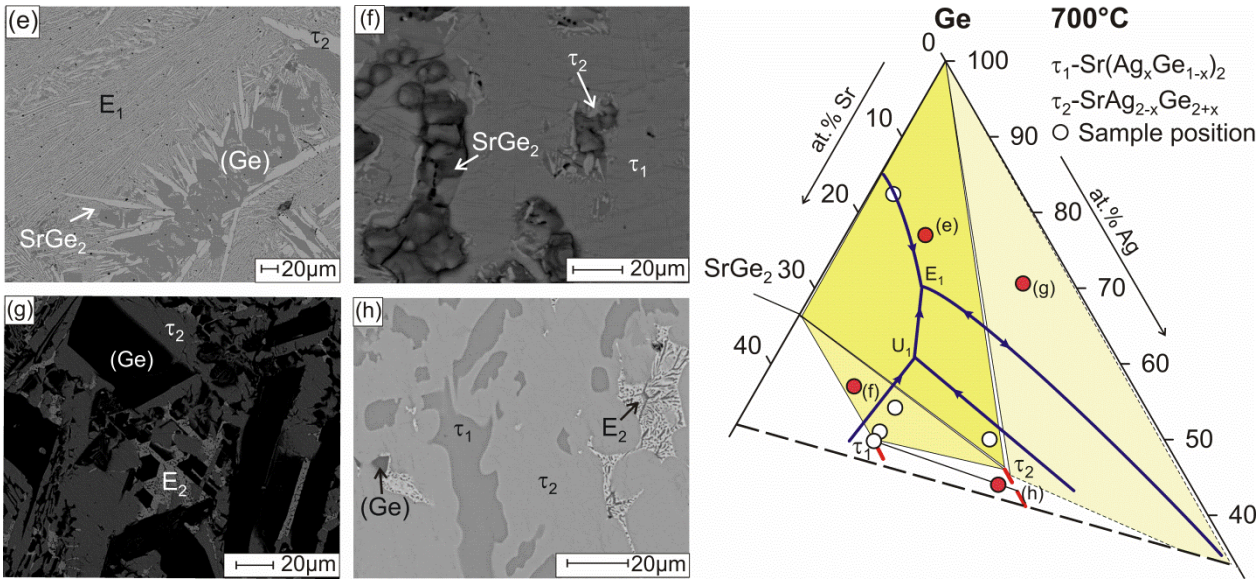

Figure 66: Isothermal section at 700°C and tentative partial liquidus projection (E: eutectic reaction, U: transition reaction) for the Ge-rich side of the Sr-Ag-Ge system and SEM images of the alloys marked in red and labelled with (e)-(h) in the isothermal section in as cast state. The results from XPD and EPMA for these alloys annealed at 700°C are summarized in Table XXVIII.

Figure 66(e) to 2(h) present the microstructures of as cast alloys, which are marked in red in the isothermal section in Figure 66. The microstructure of the alloy $Sr_{14.8}Ag_{9.3}Ge_{75.9}$ (Figure 66(e)) reveals primary grains of (Ge) together with needle like crystals of τ_2-$SrAg_{2-x}Ge_{2+x}$ ($ThCr_2Si_2$ type) and a rather fine eutectic structure. The composition of the ternary eutectic E_1: L ↔ (Ge)+$SrGe_2$+τ_2 ($SrGe_2$: $BaSi_2$ type) is ~$Sr_{19}Ag_{11}Ge_{70}$ (in at.%). As (Ge) is in equilibrium at 700°C with $SrGe_2$ and τ_2 (Figure 66), the invariant reaction

temperature is estimated to be within 700°C<T<755°C. The alloy with nominal composition $Sr_{32}Ag_{11}Ge_{57}$ contains primary grains of $SrGe_2$ (Figure 66(f)) followed by the peritectic formation of τ_2 and final crystallization of τ_1-$Sr(Ag_xGe_{1-x})_2$ (AlB_2 type). Figure 67 shows the Rietveld refinement of the X-ray powder pattern of the annealed alloy with nominal composition $Sr_{33}Ag_{17}Ge_{50}$ comprising τ_1 (AlB_2 type) as the main phase and small quantities of τ_2 and $SrGe_2$.

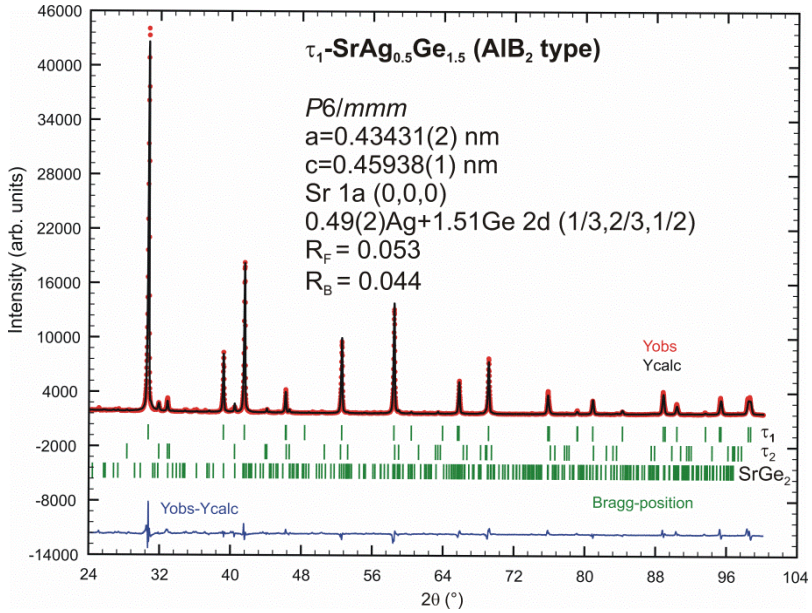

Figure 67: Rietveld refinement for an alloy with nominal composition $Sr_{33}Ag_{17}Ge_{50}$ annealed at 700°C containing τ_1-$Sr(Ag_xGe_{1-x})_2$ (AlB_2 type) as the main phase and small amounts of τ_2-$SrAg_2Ge_2$ ($ThCr_2Si_2$ type) and $SrGe_2$.

Alloy $Sr_{5.9}Ag_{23.5}Ge_{70.6}$ (Figure 66(g)) contains large grains of (Ge), τ_2 phase and liquid, which crystallizes finally in form of a ternary eutectic E_2: L ↔ (Ge)+(Ag)+τ_2. The position of the eutectic (~$Sr_2Ag_{65}Ge_{33}$ in at.%) is connected to the corresponding binary one L ↔ (Ge)+(Ag) at 75 at.% Ag. At 700°C, (Ge) and τ_2 are in equilibrium with liquid. The microstructure of the alloy $Sr_{22}Ag_{34}Ge_{44}$ in Figure 66(h) shows primary grains of τ_1 followed by the crystallization of τ_2 and liquid in form of eutectic E_2 (not shown in Figure 66). The Rietveld refinement of the X-ray powder pattern of the annealed alloy is presented in Figure 68: only two phases are present at 700°C namely τ_2 ($ThCr_2Si_2$ type) as main phase and τ_1. The refinement showed for τ_2 random site occupation of Ag and Ge in the crystallographic site 4d, whereas the 4e site is filled entirely with germanium.

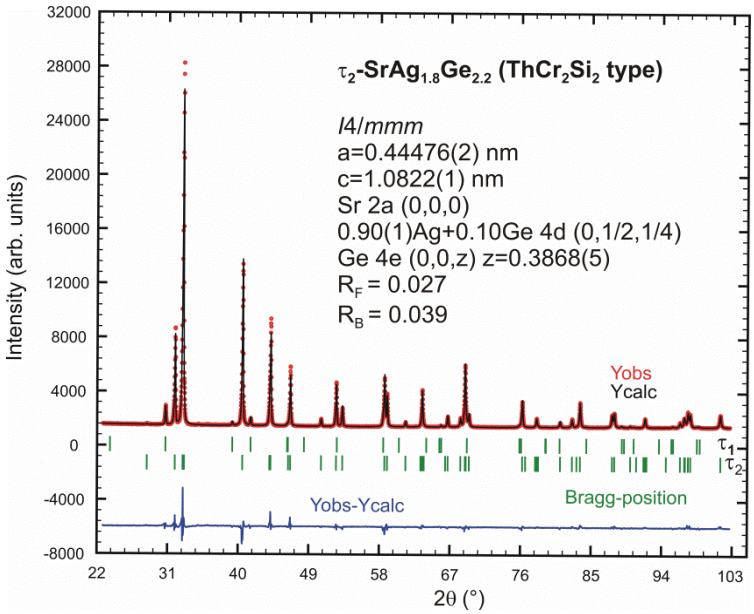

Figure 68: Rietveld refinement for an alloy with nominal composition $Sr_{22}Ag_{34}Ge_{44}$ annealed at 700°C containing τ_2-$SrAg_2Ge_2$ ($ThCr_2Si_2$ type) as the main phase and small amounts of τ_1-$Sr(Ag_xGe_{1-x})_2$ (AlB_2 type).

The Ge-poor ends of the homogeneity ranges of τ_1 and τ_2 at 700°C have not been investigated in this work. The partial tentative liquidus projection shown in Figure 66 has been constructed from the evaluations of the as cast microstructures.

5.7.1.2.3 The System Sr-Au-Si

The Sr-Au-Si system has been investigated up to 70 at.% gold and 33.3 at.% strontium on alloys in as cast state and after annealing at 800°C (650°C). Results from EPMA and XPD for the alloys marked in red in Figure 69 and annealed at 800°C (or at 650°C; see Figure 69g) are summarized in Table XXXI.

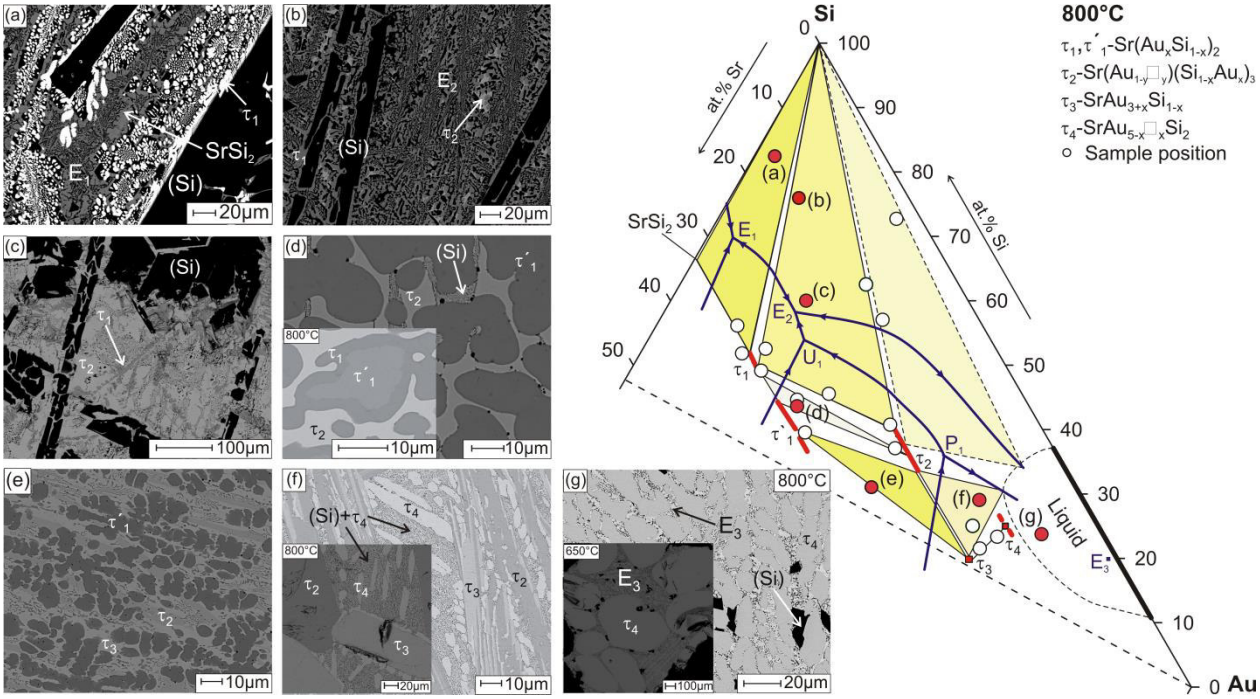

Figure 69: Partial isothermal section at 800°C and tentative liquidus projection (E: eutectic reaction, U: transition reaction, P: peritectic reaction) of the Sr-Au-Si system; microstructures are shown of the alloys marked in red and labelled with (a)-(g) in the isothermal section in as cast state or after annealing. The results from XPD and EPMA for these alloys annealed at 800°C (or 650°C (g)) are summarized in Table XXXI.

Table XXXI: Results from EPMA and XPD for alloys in as cast state or after annealing in the ternary systems Sr-Au-{Ge,Si}.

Alloy (Nominal composition)	X-ray phase analysis	Structure type	Lattice parameter [nm]			Composition EPMA (at.%)		
			a	b	c	Sr	Au	Ge Si
Sr-Au-Si								
$Sr_{14.8}Au_{2.8}Si_{82.4}$	(Si)	C_{diam}	0.54323(2)	-	-	-	-	100.0
800 °C (a)	α-$SrSi_2$	$SrSi_2$	0.65401(5)	-	-	32.4	-	68.6
	τ_1	Ca_2AgSi_3	0.82991(6)	-	0.93563(5)	32.1	14.3	53.6
$Sr_{14.8}Au_{9.3}Si_{75.9}$	(Si)	C_{diam}	0.54328(3)	-	-	-	-	100.0
800°C (b)	τ_1	Ca_2AgSi_3	-	-	-	32.6	17.6	49.8
	τ_2	$BaNiSn_3$	-	-	-	19.1	40.2	40.7
$Sr_{20}Au_{20}Si_{60}$	(Si)	C_{diam}	0.5429(3)	-	-	-	-	100.0
800 °C (c)	τ_1	Ca_2AgSi_3	-	-	-	33.0	15.9	51.1
	τ_2	$BaNiSn_3$	0.44059(3)	-	1.0109(1)	19.5	40.7	39.8

$Sr_{30.7}Au_{24}Si_{45.3}$	τ_2	$BaNiSn_3$	-	-	-	20.4	43.3	36.3
800 °C (d)	τ_1	Ca_2AgSi_3	-	-	-	32.8	17.8	49.4
	τ'_1	AlB_2	0.42162(4)	-	0.46026(7)	32.6	22.0	45.4
$Sr_{28}Au_{41}Si_{31}$	τ'_1	AlB_2	0.42388(1)	-	0.45815(3)	32.5	26.7	40.8
800 °C (e)	τ_3	-	-	-	-	20.9	60.4	18.7
$Sr_{13.5}Au_{56.5}Si_{30}$	(Si)	C_{diam}	-	-	-	-	-	100.0
800 °C (f)	τ_2	$BaNiSn_3$	0.44627(4)	-	1.01011(4)	20.3	47.3	32.4
	τ_3	-	-	-	-	20.8	60.6	18.6
	τ_4	$BaAu_5Si_2$	-	-	-	12.5	64.5	23.0
$Sr_{8.3}Au_{67.7}Si_{24}$	(Si)	C_{diam}	-	-	-	-	0.1	99.9
650 °C (g)	τ_4	$BaAu_5Si_2$	0.87715(5)	0.70034(6)	0.99301(5)	12.6	65.4	22.0
	(Au)	Cu	-	-	-	-	-	-
Sr-Au-Ge								
$Sr_{14.8}Au_{2.5}Ge_{82.7}$	(Ge)	C_{diam}	0.56586(6)	-	-	-	-	100.0
700 °C (h)	$SrGe_2$	$BaSi_2$	-	-	-	33.6	-	66.4
	τ_1	AlB_2	0.43102(2)	-	0.46182(3)	32.1	17.9	50.0
$Sr_{14.8}Au_{9.8}Ge_{75.4}$	(Ge)	C_{diam}	-	-	-	-	-	100.0
As cast (i)	τ_1	AlB_2	-	-	-	30.8	16.7	52.5
	τ_2	-	-	-	-	19.5	23.5	57.0
$Sr_{20}Au_{25}Ge_{55}$	(Ge)	C_{diam}	-	-	-	-	-	100.0
700 °C (j)	τ_1	AlB_2	0.43289(1)	-	0.45800(5)	32.8	19.0	48.2
	τ_2	$CaBe_2Ge_2$	0.45131(3)	-	1.0496(2)	18.9	29.3	51.8
$Sr_{5.9}Au_{23.5}Ge_{70.6}$	(Ge)	C_{diam}	0.56580(3)	-	-	-	-	100.0
700 °C (k)	τ_2	$ThCr_2Si_2$	0.45103(2)	-	1.0364(1)	19.1	39.1	41.8
	(Au)	Cu	-	-	-	-	85.1	14.9
	-	-	-	-	-	~16	~50	~34

Microstructures of these alloys in as cast state and for some of them after annealing at 800 or 650 °C are shown in Figure 69(a)-(g). The microstructure in Figure 69(a) for the alloy with nominal composition $Sr_{14.8}Au_{2.7}Si_{82.5}$ (in at.%) reveals primary grains of (Si) followed by the crystallization of liquid along the monovariant line L ↔ (Si)+τ_1 (τ_1-$Sr(Au_xSi_{1-x})_2$; structure type has not been determined in as cast state) and the crystallization of the last liquid at the invariant eutectic point E_1: L ↔ (Si)+$SrSi_2$+τ_1 (at ~$Sr_{19}Au_4Si_{77}$ in at.%) close to the binary eutectic at 74 at.% Si. At 800°C, (Si) is in equilibrium with $SrSi_2$ (α-$SrSi_2$ type) and τ_1-$Sr(Au_xSi_{1-x})_2$ (Ca_2AgSi_3 type); see Table XXXI(a)). An alloy with nominal composition $Sr_{14.8}Au_{9.3}Si_{75.9}$ is located in the same

primary crystallization field; thus large quantities of eutectic structures are present in the SEM image in Figure 69(b) resulting from the crystallization of the liquid along the same monovariant line, but with crystallization of τ_2 at the invariant point E_2: L ↔ (Si)+τ_1+τ_2 (at ~$Sr_{25}Au_{15}Si_{60}$, in at.%). The crystal structure of τ_2-$SrAu_{2+x}Si_{2-x}$ in as cast state, however, has not yet been analysed. Joint crystallization of (Si) and τ_1 is visible on the microstructure of the alloy with nominal composition $Sr_{20}Au_{20}Si_{60}$ (see Figure 69(c)). τ_1 is surrounded by τ_2 and the finally crystallized liquid corresponds to the monovariant crystallization of (Si) and τ_2. Equilibrium phases in this tie triangle at 800°C are (Si), τ_1 and τ_2 (τ_2-$Sr(Au_{1-y}\square_y)(Si_{1-x}Au_x)_3$; $BaNiSn_3$ structure type; see Table XXXI(c)). The alloy with nominal composition $Sr_{30.7}Au_{24}Si_{45.3}$ (Figure 69(d)) is located in the primary crystallization field of τ'_1. Annealing at 800°C (see inset in Figure 69(d)) leads to the formation of τ_1 around τ'_1. The microstructure of the alloy with composition $Sr_{28}Au_{41}Si_{31}$, presented in Figure 69(e), also reveals primary crystallization of τ'_1 followed by the crystallization of τ_2 ($BaNiSn_3$-type) and τ_3 (τ_3-$SrAu_{3+x}Si_{1-x}$; unknown structure type) and monovariant crystallization of τ'_1 and τ_3. After annealing at 800°C only 2 phases are present in this alloy namely τ'_1 and τ_3. Large grains of τ_2 and τ_3 are visible on the microstructure of the as cast alloy with nominal composition $Sr_{13.5}Au_{56.5}Si_{30}$ (see Figure 69(f)). The last liquid crystallizes in form of a two-phase eutectic microstructure (Si)+τ_4 (τ_4-$SrAu_{5-x}\square_xSi_2$; $BaAu_5Si_2$ type). Rather large crystals of τ_2 and τ_3 are grown in equilibrium with liquid at 800°C, as can be seen from the inset in Figure 69(f). The alloy with nominal composition $Sr_{8.3}Au_{67.7}Si_{24}$ is completely in the liquid state at 800°C. The microstructure of this alloy after quenching is shown in Figure 69(g). τ_4 is the primary crystallizing phase and the last liquid crystallizes in form of the eutectic E_3: L ↔ (Si)+(Au)+τ_4 with a composition (~$Sr_{0.5}Au_{80}Si_{\sim 19.5}$) very close to the binary Si/Au eutectic (at 81 at.% Au). Another part of this alloy was slowly cooled from 800 to 650 °C and annealed at this temperature for some days yielding large crystals of τ_4 (see inset Figure 69(g)). A possible partial liquidus projection for this system is also shown in Figure 69.

5.7.1.2.3.1 The crystal structures of τ_1-$Sr(Au_xSi_{1-x})_2$ (Ca_2AgSi_3 type) and τ'_1-$Sr(Au_xSi_{1-x})_2$ (AlB_2-type)

The crystal structures of τ_1- and τ'_1-$Sr(Au_xSi_{1-x})_2$ have been investigated on alloys annealed at 800°C by XPD and EPMA and of τ_1 also by XSCD. Rietveld refinement of the X-ray powder intensities of τ'_1-$Sr(Au_xSi_{1-x})_2$ for an alloy with nominal composition

$Sr_{31}Au_{30}Ge_{39}$ is shown in Figure 70 defining isotypism with the AlB_2 type (space group *P6/mmm*).

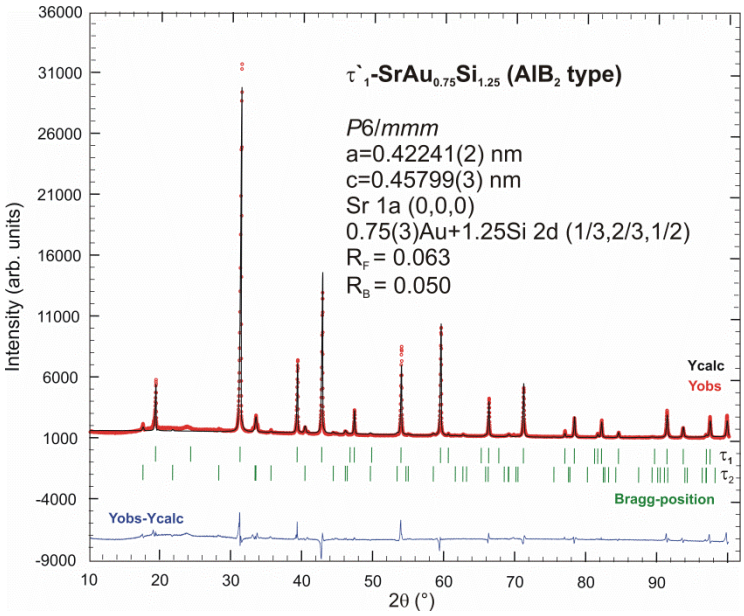

Figure 70: Rietveld refinement for the alloy with nominal composition $Sr_{31}Au_{30}Ge_{39}$ annealed at 800°C containing $\tau`_1$-$Sr(Au_xSi_{1-x})_2$ (AlB_2 type) as the main phase and traces of τ_2-$SrAu_{2+x}Si_{2-x}$ ($BaNiSn_3$ type).

As no unindexed reflections remain in the XPD patterns and the calculated intensities from Rietveld refinement agreed rather well with the experimentally observed ones (R_F = 0.063), no single crystal has been selected for this phase.

XPD patterns of annealed alloys close to τ_1-$Sr(Au_xSi_{1-x})_2$ at x=0.25, however, exhibit various strong superstructure reflections to the simple AlB_2 type. As an ordered superstructure can be expected with the stoichiometric composition Sr_2AuSi_3, a Rietveld refinement of the X-ray powder pattern was carried out using the crystallographic parameters of the Ca_2AgSi_3 structure ((Cardoso Gil R. 1999), see Figure 71*;* space group Fmmm; a=0.83504(4), b=1.4565(3) and c=0.9277(3) nm). For τ_1-$Sr(Au_xSi_{1-x})$ (x=0.25) the agreement between the calculated intensities from refinement with the experimentally observed spectrum was acceptable, but could be improved by a mixed occupation of Au and Si in one of the crystallographic sites 8h and by a defect in 16o.

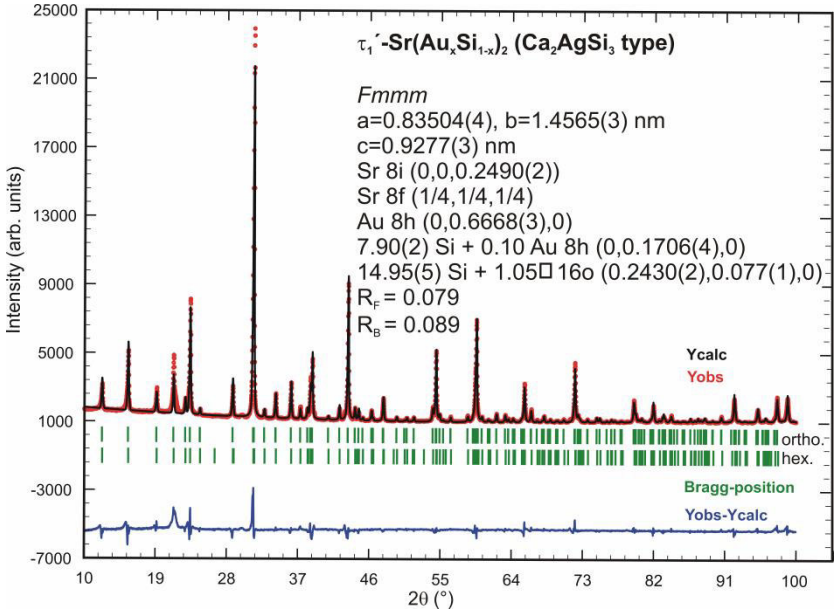

Figure 71: Rietveld refinement for an alloy with nominal composition $Sr_{33.3}Au_{16.7}Si_{50}$ (in at.%) applying the orthorhombic Ca_2AgSi_3 structure type (ortho.) and Bragg-reflections of the hexagonal $Ca_4Ag(Ag_{0.2}Si_{0.8})_3Si_{3.2}$ type (hex.).

In order to elucidate details of the superstructure, a single crystal specimen was mechanically isolated from an alloy with nominal composition $Sr_{32}Au_{19}Si_{49}$ after annealing at 800°C. Evaluation of the X-ray diffraction pattern prompted a hexagonal primitive unit cell (a=0.83407(2) and c=0.92664(3) nm) without systematic extinctions. Structure solution and refinement was carried out in space group $P\bar{6}m2$. Final refinement with ADPs converged to R_F=0.057 and highest residual electron densities +10.3 e/Å^3 located in the special position 1c (1/3,2/3,0), which is in the center of the Si_6 ring. Comparing unit cell dimensions, crystal symmetry and the atom site distribution, the crystal structure of "Sr_2AuSi_3" ($Sr_8Au_2(Au_{0.34}Si_{0.66})_3(Au_{0.21}Si_{0.79})_3Si_{7.62}Au_{0.38}$) would be isotypic with the crystal structure of $Ca_4Ag(Ag_{0.2}Si_{0.8})_3Si_{3.2}$ (labelled as "$Ca_5Ag_2Si_7$") reported by Merlo et al. (Merlo F. 1996). Detailed results of the crystal structure refinement are given in Table XXXII.

Table XXXII: X-Ray single crystal data for τ_1-$Sr(Au_xSi_{1-x})_2$ at RT (anisotropic displacement parameters U_{ij} in [10^{-2}nm^2]).

Parameter/ Compound	**$Sr(Au_xSi_{1-x})_2$; x=0.25**	
Space Group	$P\bar{6}m2$	*Fmmm*
Structure type	$Ca_4Ag(Ag_{0.2}Si_{0.8})_3Si_{3.2}$	Ca_2AgSi_3
Formula from EPMA	$Sr_{33.33}Au_{16.67}Si_{50}$ at.% ≡ $Sr_2Au_1Si_3$	$Sr_{33.33}Au_{16.67}Si_{50}$ at.% ≡ $Sr_2Au_1Si_3$
Formula from refinement	$Sr_8Au_2(Au_{0.34}Si_{0.66})_3(Au_{0.21}Si_{0.79})_3$ $Si_{7.62}Au_{0.38}$	$Sr_{16.00(1)}Au_{8.09(2)}Si_{22.6(1)}\square_{1.4}$ ≡ $Sr_{2.00}Au_{1.01}Si_{2.82}\square_{0.18}$

	$\equiv Sr_8Au_{4.03}Si_{11.97} \sim Sr_2Au_1Si_3$	
a, b, c [nm]	0.83407(2), 0.92664(3)	0.83407(2), 1.44465(2), 0.92664(3)
μ_{abs} [mm^{-1}]	68.6	68.6
V (nm^3)	0.55827	1.11654
ρ_x (gcm^{-3})	5.43	5.38
Reflections in refinement	$985 \geq 4\sigma(F_o)$ 1400	$709 \geq 4\sigma(F_o)$ 940
Number of variables	33	26
$R_F = \Sigma\|F_0-F_c\|/\Sigma F_0$	0.057	0.035
R_{Int}	0.050	0.071
wR2	0.143	0.063
GOF	1.066	0.930
Extinction (Zachariasen)	0.0072(7)	0.00010(3)
Residual density $e^-/Å^3$; max; min	10.3; -4.75	3.43; -3.11
Atom parameters		
Sr1 in	2h (1/3,2/3,z)	8f (1/4,1/4,1/4)
occ.	0.98(1)	1.007(5)
x, y, z	z = 0.2487(2)	-
$U_{11}=U_{22}=U_{12}$, U_{33}; $U_{23}=U_{13}=0$	0.0146(4), 0.0110(5)	U_{11}, U_{22}, U_{33}; $U_{12}=U_{23}=U_{13}=0$ 0.0083(4), 0.0084(4), 0.0075(3) -
Sr2 in	6n (x,-x,z)	8i(0,0,z)
occ.	0.96(6)	0.991(6)
x, y, z	0.8331, 0.1669(2), 0.2498(1)	0.24938(5)
$U_{11}=U_{22}$, U_{33}, U_{12}; $-U_{23}=U_{13}$	0.0150(3), 0.0120(4) 0.0075(3); -0.0005(4),	U_{11}, U_{22}, U_{33}; $U_{12}=U_{23}=U_{13}=0$ 0.0082(4), 0.0083(4), 0.0072(3) -
Au1 in	1a (0,0,0)	-
occ.	1.01(6)	-
$U_{11}=U_{22}=U_{12}$, U_{33}; $U_{23}=U_{13}=0$	0.0079(5), 0.0087(9)	-
Au2 in	1e (2/3,1/3,0)	-
occ.	1.002(3)	-
$U_{11}=U_{22}=U_{12}$, U_{33}; $U_{23}=U_{13}=0$	0.0059(5), 0.0062(8)	-
Si1 in	1f (2/3,1/3,1/2)	8h (0,y,0)
occ.	0.96(1)	0.84(1)
x, y, z	-	0.1646(1)
$U_{11}=U_{22}=U_{12}$, U_{33}; $U_{23}=U_{13}=0$	0.020(4), 0.032(9)	U_{11}, U_{22}, U_{33}; $U_{12}=U_{23}=U_{13}=0$ 0.010(1), 0.006(1), 0.012(1) -
Si2 in	3j (x,-x,0)	-
occ.	0.98(2)	-
x, y, z	0.1718, 0.8281(2)	-
$U_{11}=U_{22}$, U_{33}, U_{12}; $U_{23}=U_{13}=0$	0.031(2), 0.037(3) 0.012(1)	- -
Si3 in	3j (x,-x,0)	-
occ.	0.94(1)	-
x, y, z	0.4957, 0.5042(2)	-
$U_{11}=U_{22}$, U_{33}, U_{12}; $U_{23}=U_{13}=0$	0.021(2), 0.036(3) 0.006(2)	- -
M1 in	1b (0,0,1/2)	8h (0,y,0)

occ.			0.377(7) Au + 0.623 Si			0.703(2) Au + 0.297 Si		
x, *y*, *z*			-			0.66674(2)		
$U_{11}=U_{22}=U_{12}$, U_{33}; $U_{23}=U_{13}=0$			0.022(1), 0.025(1)			U_{11}, U_{22}, U_{33}; $U_{12}=U_{23}=U_{13}=0$ 0.0062(2), 0.0063(2), 0.0089(2) -		
M2 in			3k (x,y,1/2)			16o (x,y,0)		
occ.			0.215(4) Au + 0.785 Si			0.154(1) Au + 0.846 Si		
x, *y*, *z*			0.5024, 0.4976(8)			0.24878(5), 0.08293(5)		
$U_{11}=U_{22}$, U_{33}, U_{12}; $U_{23}=U_{13}=0$			0.012(1), 0.010(1) 0.007(1)			U_{11},U_{22}, U_{33} 0.0070(4), 0.0070(4), 0.0113(4) U_{12}=0.0002(1); $U_{23}=U_{13}=0$		
M3 in			3k (x,y,1/2)			-		
occ.			0.339(4) Au + 0.661 Si			-		
x, *y*, *z*			0.1691, 0.8309(1)			-		
$U_{11}=U_{22}$, U_{33}, U_{12}; $U_{23}=U_{13}=0$			0.0109(8), 0.015(1) 0.0048(8)			-		
Interatomic distances [nm]; Standard deviation < 0.0001 (only for the Ca_2AgSi_3 type)								
Sr1 –	2Si1	0.3316		–2Sr2	0.4170		–2Sr1	0.3346
	–4M2	0.3329	Si1 –	2M2	0.2387	M2 –	1Si1	0.2387
	–2M1	0.3346		–1M1	0.2437		–1M2	0.2396
	–4M2	0.3349		–2Sr1	0.3316		–1M1	0.2420
	–4Sr2	0.4170		–4Sr2	0.3352		–2Sr1	0.3329
Sr2 –	4M1	0.3341	M1 –	2M2	0.2420		–2Sr2	0.3345
	–4M2	0.3345		–1Si1	0.2437		–2Sr1	0.3350
	–4Si1	0.3352		–4Sr2	0.3341			

Due to the relatively high residual electron density, the gained R values and the result from Rietveld refinement, the crystal structure was inspected again. Final structure refinement after transformation to an orthorhombic unit cell ($a_{ortho}=a_{hex}$, $b_{ortho}=\sqrt{3}a_{hex}$ and $c_{ortho}=c_{hex}$, see Table XXXII) was successful in space group *Fmmm*. Full occupation by strontium atoms has been found for the Wyckoff positions 8f (1/4,1/4,1/4) and 8i (0,0, 0.24938(5)). A defect of ~ 15% appeared after refining the silicon content in the crystallographic site 8h (0,0.1646(1),0) and a mixed occupancy of gold and silicon in different ratios became obvious for the crystallographic sites 8h (0,0.66674(2),0) and 16o (0.24878(5),0.08293(5),0) leading to the composition $Sr_{2.00}Au_{1.01}Si_{2.82}\square_{0.18}$ for this crystal. After introduction of ADP´s the refinement now converged to acceptable low R values (R_F=0.035) and residual electron densities ≤ ±3.4 e/Å^3. Although the results from Rietveld refinement and single crystal refinement differ concerning the mixed sites and the position of the defect, the resulting composition is the same. It is worth to mention that it is not completely clear at this point, if there exists complete order for

stoichiometric Sr_2AuSi_3 with the fully ordered Ca_2AgSi_3 type and whether the mixed sites (defects) appear due to stacking faults or defects in this crystal specimen.

5.7.1.2.3.2 The crystal structure of τ_2- $Sr(Au_{1-y}\square_y)(Si_{1-x}Au_x)_3$ ($BaNiSn_3$-type)

Crystal structure and homogeneity range of τ_2-$SrAu_{2+x}Si_{2-x}$ have been investigated by EPMA and XPD after annealing at 800°C and by XSCD. The homogeneity range is rather limited at this temperature ranging from x=0 to x=0.35. Previously, a $ThCr_2Si_2$ type has been attributed to stoichiometric $SrAu_2Si_2$ (a=0.437(1), c=1.014(2) nm) by Dörrscheidt et al. (N. N. Dörrscheidt W. 1976). Although the Rietveld refinements for all X-ray powder patterns applying this structure type were acceptable and without unindexed reflections, one single crystal has been selected from an alloy at the gold rich end of the solid solution with nominal composition $Sr_{13.5}Au_{56.5}Si_{30}$ (SEM image of this alloy annealed at 800°C is shown in Figure 69(f)). Diffraction data for this crystal confirmed the tetragonal symmetry (a=0.44594(2) and c=1.01013(6) nm) and the analysis of the systematic extinctions arrived at the space groups *I*4/*mmm*, $I\bar{4}m2$, $I\bar{4}2m$, *I*4*mm*, *I*422, *I*4/*m*, $I\bar{4}$, *I*4. Crystal structure solution and subsequent refinement in the highest possible symmetric space group *I*4/*mmm* immediately revealed several electron densities with different peak heights close together along the c-axis, indicating a lower symmetry space group without a mirror plane perpendicular to the c-direction. Therefore, the space group *I*4*mm* was chosen and indeed crystal structure solution was successful within this space group. A first refinement showed strontium occupying the crystallographic site 2a (0,0,0.605(1)) and a random occupancy of gold and silicon (M) in the sites M1 2a (0,0,0.0), M2 2a (0,0,0.228(1)) and M3 4b (0,1/2,0.350(1)) in different ratios. Symmetry and atomic arrangement are consistent with the $BaNiSn_3$ type. Although the refinement yields a rather low R_F value (R_F=0.040), reasonable ADPs and small residual electron densities (< ± 4.5 e/Å³), the refined composition, $SrAu_2Si_2$, did not fit with EPMA (~$SrAu_{2.4}Si_{1.6}$) and also the interatomic bonding distance between the sites M1 and M2 was with d_{M1-M2}=0.2300 nm too short for fully occupied sites. Therefore, only the gold content was refined in the crystallographic site 2a (0,0,0.000) resulting in an occupation of 36%, as vacancies are only possible in this site. Refinement of the occupation of the other 2a site (0,0,0.228(1)) leads to an almost full occupation by silicon but a small amount of gold (1%) is still necessary for reasonably shaped ADPs. Furthermore, a mixed occupancy of

gold and silicon can be found also in Wyckoff position 4b. Details of the refinement are summarized in Table XXXIII.

Table XXXIII: X-Ray single crystal data for τ_2-$Sr(Au_{1-y}\square_y)(Si_{1-x}Au_x)_3$ ($BaNiSn_3$-type) at RT (anisotropic displacement parameters U_{ij} in [$10^{-2}nm^2$]). The symbol □ denotes a vacancy.

Parameter/Compound	**$Sr(Au_{1-y}\square_y)(Si_{1-x}Au_x)_3$; x=0.59, y=0.64**
Space Group	*I*4*mm*
Formula from EPMA	$Sr_{20}Au_{48}Si_{32}$ at.% ≡ $SrAu_{2.4}Si_{1.6}$
Formula from refinement	$SrAu_{2.13(5)}\square_{0.64}Si_{1.23}$ ≡ $Sr(Au_{0.36}\square_{0.64})(Si_{0.41}Au_{0.59})_3$
a, c [nm]	0.44594(2), 1.01013(6)
μ_{abs} [mm^{-1}]	104.5
V (nm^3)	0.20088
ρ_x (gcm^{-3})	8.91
Reflections in refinement	308≥4σ(F_o) of 330
Number of variables	17
$R_F = \Sigma\|F_0-F_c\|/\Sigma F_0$	0.043
R_{Int}	0.071
wR2	0.095
GOF	1.120
Extinction (Zachariasen)	0.0006(2)
Residual density $e^-/Å^3$; max; min	4.96; -3.21
Atom parameters	
Sr in 2a (0,0,z); occ.	1.0*
z	0.6049(5)
U_{11}, U_{22}, U_{33}	0.0094(8), 0.0094(8), 0.0144(7)
Au in 2a (0,0,z); occ.	0.36(1)
z	0.0000*
$U_{11}=U_{22}$, $U_{33;}$ $U_{12}=U_{23}=U_{13}=0$	0.012(1), 0.019(1)
M1 in 2a (0,0,z); occ.	0.011(8) Au + 0.989 Si
z	0.228(1)
$U_{11}=U_{22}$, $U_{33;}$ $U_{12}=U_{23}=U_{13}=0$	0.0044(8), 0.0025(9)
M2 in 4b (0,1/2,z); occ.	0.88(2) Au + 0.12 Si
z	0.3506(5)
U_{11}, U_{22}, $U_{33;}$ $U_{12}=U_{23}=U_{13}=0$	0.0246(6), 0.0133(5), 0.0202(4)
Interatomic distances [nm]; Standard deviation < 0.0001	

Sr –	4Au	0.3327	M1 –	1Au	0.2303
	–4M2	0.3336		–4M2	0.2551
	–4M1	0.3389		–4Sr	0.3389
	–4M2	0.3402		–1Sr	0.3808
	–1M1	0.3808	M2 –	2M1	0.2551
	–1Au1	0.3990		–2Au	0.2692
Au –	1M1	0.2303		–4M2	0.3153
	–4M2	0.2692		–2Sr	0.3336
	–4Sr	0.3327		–2Sr	0.3402
	–1Sr	0.3990			

*fixed during refinement

This model results in a final composition $Sr(Au_{1-y}\square_y)(Si_{1-x}Au_x)_3$ with x=0.59, y=0.64 i.e. $SrAu_{2.13(5)}Si_{1.23}\square_{0.64}$, R_F=0.043, residual electron densities < ± 5 e/Å^3 and rather spherical ADPs. Up to now, almost all known compounds crystallizing with $BaNiSn_3$ structure type exhibit a stoichiometric 1:1:3 composition or composition very close to it. Therefore, further investigations/calculations will be necessary to find the reason for the symmetry reduction and also to study this phase at other temperatures. The $ThCr_2Si_2$ structure type has been reported by Dörrscheidt et al. (Dörrscheidt W. 1976) for stoichiometric $SrAu_2Si_2$ samples, quenched from high temperatures (1250-1300°C). Therefore, a structure transformation with temperature and/or composition is conceivable. Furthermore, Isobe et al. (Isobe M. 2014) recently reported the formation of $SrAuSi_3$ with $BaNiSn_3$ type under high pressure conditions (6GPa, 1500°C).

5.7.1.2.3.3 The crystal structure of τ_3-$SrAu_{3+x}Si_{1-x}$

Although large crystals of τ_3-$SrAu_{3+x}Si_{1-x}$ were grown in equilibrium with liquid as can be seen from the SEM image in Figure 69(f) and from the drawn phase equilibria in the gold rich corner in Figure 69, no suitable single crystal for XSCD could be selected. All crystals had rather strong defects or diffuse reflections or crystal intergrowth. X-ray powder patterns of alloys with τ_3 as the main phase could be indexed with the $CeMg_2Si_2$ structure type ((Zmii O.F. 1971), space group P4/mmm; a= 0.44532, c= 0.52724 nm) but many small, unindexed reflections remained, which are probably due to a superstructure with a rather large unit cell.

5.7.1.2.3.4 The crystal structure of τ_4-$SrAu_{5-x}\square_xSi_2$ ($BaAu_5Si_2$ type)

A suitable single crystal of τ_4-$SrAu_{5-x}\square_xSi_2$ was selected from an alloy with nominal composition $Sr_{8.3}Au_{67.7}Si_{24}$ slowly cooled from 800 to 650°C and annealed at this temperature for 3 days. The microstructure of this alloy is presented in Figure 69(g) showing rather large crystals grown in equilibrium with the liquid. An orthorhombic primitive unit cell (a=0.87557(3), b=0.69945(2) and c=0.98873(3) nm) has been found from XSCD data and the crystal structure has been solved in space group *Pnma* as the highest possible symmetric one. Crystal structure refinement indicates isotypism with the $BaAu_5Ge_2$ structure type revealing an ordered arrangement of Sr atoms in the crystallographic site 4c (0.2524(1),1/4,0.8772(1)), Si atoms in the 4c sites (0.3390(4),1/4,0.5332(4)) and (0.0431(4),1/4,0.3770(4)) and Au atoms in two 8d sites (0.10065(4),0.05085(5),0.60759(4)) and (0.06462(4),0.03440(5),0.13680(4)). Refinement of the gold content in the Wyckoff position 4c (0.29942(5),0.25,0.28942(6)) leads to an occupation of only 32.5 %. Indeed, the same result could be achieved with a mixed occupation of gold and silicon (0.2Au + 0.8Si) in this site but would lead to a too high silicon content compared with the result from EPMA. Final refinement with ADPs concludes with the composition $SrAu_{4.3(1)}\square_{0.7}Si_2$, R_F=0.043 and residual electron densities ± 5.5 e/Å^3 close to the gold atoms. Further details of the crystal structure refinement are given in Table XXXIV.

Table XXXIV: X-Ray single crystal data for τ_4-$SrAu_{5-x}\square_xSi_2$ ($BaAu_5Si_2$-type) (anisotropic displacement parameters U_{ij} in [10^{-2}nm^2]). The symbol □ denotes a vacancy.

Parameter/ Compound	**$SrAu_{5-x}\square_xSi_2$; x=0.66**
Space Group	*Pnma*
Formula from EPMA	$Sr_{12.5}Au_{62.5}Si_{25}$ at.% ≡ $SrAu_5Si_2$
Formula from refinement	$SrAu_{4.3(1)}\square_{0.7}Si_2$
a, b, c [nm]	0.87557(3), 0.69945(2), 0.98873(3)
μ_{abs} [mm^{-1}]	162.4
V (nm^3)	0.60552
ρ_x (gcm^{-3})	10.91
Reflections in refinement	1515≥4σ(F_o) of 1779
Number of variables	52
$R_F = \Sigma\|F_0-F_c\|/\Sigma F_0$	0.044
R_{Int}	0.082

wR2			0.110		
GOF			1.111		
Extinction (Zachariasen)			0.00030(6)		
Residual density $e^-/Å^3$; max; min			5.50; -5.30		
Atom parameters					
Sr in 4c (x,1/4,z); occ.			1.013(8)		
x, z			0.2524(1), 0.8772(1)		
U_{11}, U_{33}, U_{22} U_{13}; U_{12}=U_{23}=0			0.0087(5), 0.0111(5), 0.0091(5), -0.0014(4)		
Au1 in 4c (x,1/4,z); occ.			0.325(2)		
x, z			0.29942(5), 0.28942(6)		
U_{11}, U_{33}, U_{22} U_{13}; U_{12}=U_{23}=0			0.0062(2), 0.0131(2), 0.0100(3) 0.0008(2)		
Au2 in 8d (x,y,z); occ.			0.984(7)		
x, y, z			0.10065(4), 0.05085(5), 0.60759(4)		
U_{11}, U_{22}, U_{33} U_{23}, U_{13}, U_{12}			0.0092(2), 0.0057(2), 0.0104(2) 0.0003(1), -0.0011(1), -0.0010(1)		
Au3 in 8d (x,y,z); occ.			0.982(7)		
x, y, z			0.06462(4), 0.03440(5), 0.13680(4)		
U_{11}, U_{22}, U_{33} U_{23}, U_{13}, U_{12}			0.0089(2), 0.0089(2), 0.0155(2) -0.0023(1), 0.0021(1), 0.0014(1)		
Si1 in 4c (x,1/4,z); occ.			1.015(7)		
x, z			0.3390(4), 0.5332(4)		
U_{11}, U_{33}, U_{22} U_{13}; U_{12}=U_{23}=0			0.008(1), 0.007(1), 0.012(1), -0.0005(3)		
Si2 in 4c (x,1/4,z); occ.			1.022(8)		
x, z			0.0431(4), 0.3770(4)		
U_{11}, U_{33}, U_{22} U_{13}; U_{12}=U_{23}=0			0.004(1), 0.006(1), 0.014(2) -0.001(1)		
Interatomic distances [nm]; Standard deviation < 0.0001					
Sr –	2Au2	0.3289		–2Au2	0.2903
	–2Au2	0.3355		–2Au3	0.2963
	–2Au2	0.3356		–2Sr	0.3632
	–2Au3	0.3400	Au2 –	1Si2	0.2457
	–2Au3	0.3418		–1Si1	0.2615
	–2Si1	0.3486		–1Si2	0.2719
	–2Au3	0.3490		–1Au2	0.2786
	–2Si2	0.3518		–1Au2	0.2853
Si1–	2Au3	0.2391		–1Au1	0.2903
	–1Au1	0.2435		–1Au3	0.2973
	–2Au2	0.2615		–1Au3	0.3005
	–2Au3	0.2700		–1Sr	0.3289
	–1Si2	0.3016		–1Sr	0.3355
	–1Sr	0.3486		–1Sr	0.3356
Si2 –	1Au1	0.2405	Au3 –	1Si1	0.2391

	–2Au2	0.2457	–1Si2	0.2820
	–2Au1	0.2695	–1Au1	0.2863
	–2Au2	0.2719	–1Au1	0.2962
	–2Au3	0.2820	–1Au3	0.2971
	–1Si1	0.3016	–1Au2	0.2973
	–1Sr	0.3518	–1Si1	0.2999
Au1 –	1Si2	0.2405	–1Au2	0.3005
	–1Si1	0.2435	–1Au3	0.3016
	–1Si2	0.2695	–1Sr	0.3400
	–2Au3	0.2863		

5.7.1.2.4 The System Sr-Au-Ge

Figure 72 presents the partial isothermal section at 700°C of the Sr-Au-Ge system together with the as cast microstructures of the alloys marked in red and labelled with (h)-(k).

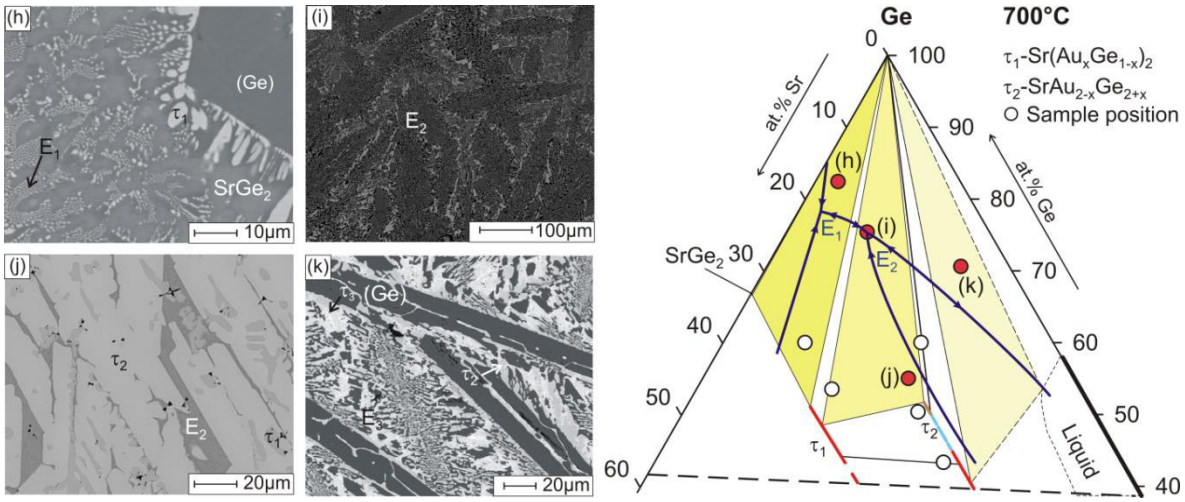

Figure 72: Germanium rich part of the isothermal section Sr-Au-Ge at 700°C, tentative partial liquidus projection (E: eutectic reaction) and microstructures of the alloys marked in red and labelled with (h)-(k) in the isothermal section in as cast state. The results from XPD and EPMA for these alloys annealed at 700°C are summarized in Table XXXI. The different structure types appearing for τ_2-$SrAu_{2-x}Ge_{2+x}$ are marked in brown: $CaBe_2Ge_2$ type; blue: $BaCu_2Sb_2$ type and red $ThCr_2Si_2$ type.

Results from XPD and EPMA of these alloys annealed at 700°C are summarized in Table XXXI. The microstructure of the as cast alloy $Sr_{14.8}Au_{2.5}Ge_{82.7}$ (Figure 72(h)) shows primary grains of (Ge) and a rather fine eutectic E_1: L ↔ (Ge)+$SrGe_2$+τ_1 (τ_1-$Sr(Au_xGe_{1-x})_2$; AlB_2 type) with composition $Sr_{20}Au_{1.5}Ge_{78.5}$ (in at.%), which is connected with the binary eutectic e: L ↔ (Ge)+$SrGe_2$ at 85 at.% Ge. The alloy with nominal composition

$Sr_{14.8}Au_{9.5}Ge_{75.7}$ is close to another ternary eutectic E_2: L ↔ (Ge)+τ_1+τ_2 (τ_2-$SrAu_{2-x}Ge_{2+x}$; $CaBe_2Ge_2$ type) with composition ~$Sr_{14}Au_{11}Ge_{75}$ (in at.%) (see Figure 72(i)). The microstructure in Figure 72(j) (alloy $Sr_{20}Au_{25}Ge_{55}$) reveals primary dendrites of τ_1 followed by the crystallization of τ_2 and a fine eutectic structure with composition E_2. Alloy $Sr_{5.9}Au_{23.5}Ge_{70.6}$ (Figure 72(k)) contains large primary grains of (Ge) and smaller grains of τ_2. A gold rich phase τ_3 with approximate composition $Sr_{16}Au_{50}Ge_{34}$ (in at. %; very small grains) forms peritectically around τ_2 but the final liquid crystallizes in form of a ternary eutectic E_3: L ↔ (Ge)+(Au)+τ_3 (at ~ $Sr_{10}Au_{54}Ge_{36}$ in at.%, not shown in Figure 72). From these observations, the tentative partial liquidus projection presented in Figure 72 has been constructed.

Phase equilibria at 700°C are characterized by the two ternary compounds τ_1 and τ_2 (see Figure 72). τ_1 crystallizes with AlB_2 type as defined by the Rietveld refinement in Figure 73 of the X-ray powder pattern of the alloy with nominal composition $Sr_{30}Au_{16.5}Ge_{53.5}$.

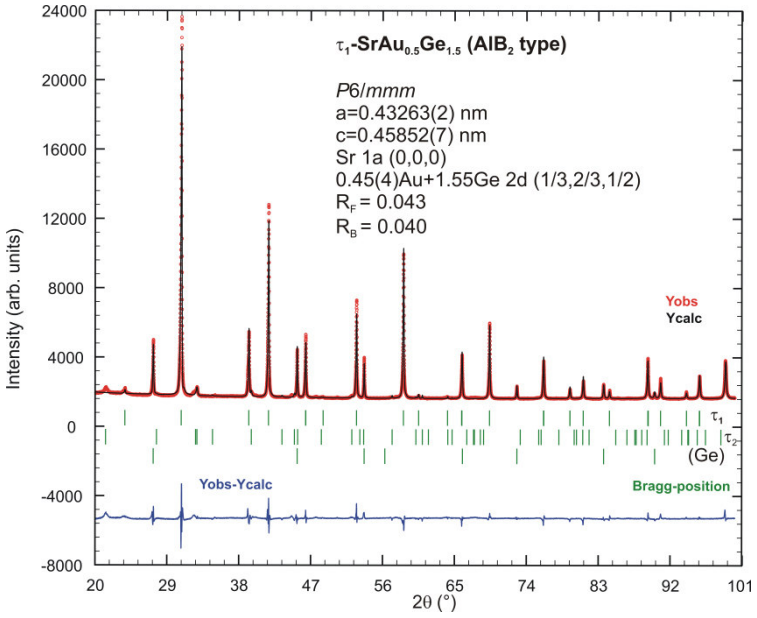

Figure 73: Rietveld refinement for an alloy with nominal composition $Sr_{30}Au_{16.5}Ge_{53.5}$ annealed at 700°C containing τ_1-$Sr(Au_xGe_{1-x})_2$ (AlB_2 type) as the main phase and small amounts of τ_2-$SrAu_{2-x}Ge_{2+x}$ ($CaBe_2Ge_2$ type) and (Ge).

Besides τ_1 the alloy also contains small quantities of τ_2 and (Ge) according to the location of the sample in the three-phase field. The crystal structures of τ_2 are discussed in more detail in the next chapter.

5.7.1.2.4.1 The crystal structure of τ_2-$SrAu_{2-x}Ge_{2+x}$

The crystal structure of τ_2-$SrAu_{2-x}Ge_{2+x}$ has been studied by XPD and XSCD in as cast state and after annealing at 700, 800 and 900°C. All diffraction patterns could be basically indexed within the $ThCr_2Si_2$ structure type but at the Ge-rich site of the solid solution some weak unindexed reflections remained and also the calculated intensities from Rietveld refinement did not fit well with the experimental observation. As these additional reflections appear also in as cast state but become less diffuse after annealing at higher temperatures, single crystals have been selected after annealing at 900°C from an alloy with nominal composition $SrAuGe_3$. Two different types of single crystals could be isolated from this alloy, namely one with a smaller tetragonal primitive unit cell ($CaBe_2Ge_2$ type, space group P4/nmm; a=0.44796(2), c=1.06315(5) nm) and another with a 3 times larger body centred tetragonal cell ($BaCu_2Sb_2$ type, space group I4/mmm; a=0.44866(2), c=3.1808(1) nm). The novel compound τ_2-$SrAu_{2-x}Ge_{2+x}$ (at x~0.5) and the two structure modifications have been briefly mentioned in a previous paper, which essentially focused on the superconducting properties of non-centrosymmetric compounds of stoichiometry 113 based on Sr and Ba in combination with 3d, 4d and 5d transition metals (F. Kneidinger 2014). Therefore a full account of the structure determination and results will be given here.

The $CaBe_2Ge_2$ structure type is perfectly consistent with the crystal structure refinement of the single crystal with the smaller unit cell with Sr occupying the crystallographic site 2c (1/4,1/4,0.74895(9)) and a mixed occupancy of gold and germanium in all other crystallographic sites 2c (1/4,1/4,0.13122(5)), 2c (1/4,1/4,0.36823(8)), 2b (3/4,1/4,1/2) and 2a (0,0,0). Detailed results of the structure analysis are presented in Table XXXV. The final refinement with anisotropic displacement parameters converged to an R-value R_F = 0.028, residual electron densities smaller than ±3 $Å^3$ and the composition $SrAu_{1.55(3)}Ge_{2.45}$.

Table XXXV: X-Ray single crystal data for τ_2-$SrAu_{2-x}Ge_{2+x}$ ($CaBe_2Ge_2$-type) at RT (anisotropic displacement parameters U_{ij} in [$10^{-2}nm^2$]).

Parameter/compound	**$SrAu_{2-x}Ge_{2+x}$; x=0.45**
Space Group	*P4/nmm*
Composition from EPMA	$Sr_{20}Au_{30}Ge_{50}$ at.% ≡ $SrAu_{1.5}Ge_{2.5}$
Formula from refinement	$SrAu_{1.55(3)}Ge_{2.45}$
a, c [nm]	0.44796(2), 1.06315(5)
μ_{abs} [mm^{-1}]	94.65

V (nm^3)		0.2133			
ρ_x (gcm^{-3})		9.76			
Reflections in refinement		$274 \geq 4\sigma(F_o)$ of 324			
Number of variables		21			
$R_F = \Sigma\|F_0-F_c\|/\Sigma F_0$		0.028			
R_{Int}		0.059			
wR2		0.084			
GOF		1.207			
Extinction (Zachariasen)		0.0015(1)			
Residual density $e^-/Å^3$; max; min		2.07; -2.98			
Atom parameters					
Sr1 in 2c(1/4,1/4,z); occ.		1.04(2)			
z		0.74895(9)			
$U_{11}=U_{22}$, U_{33}; $U_{12}=U_{23}=U_{13}=0$		0.0128(4), 0.0168(6)			
M1 in 2c(1/4,1/4,z); occ.		0.709(7) Au + 0.291 Ge			
z		0.13122(5)			
$U_{11}=U_{22}$, U_{33}; $U_{12}=U_{23}=U_{13}=0$		0.0151(2), 0.0169(3)			
M2 in 2c(1/4,1/4,z); occ.		0.252(5) Au + 0.748 Ge			
z		0.36823(8)			
$U_{11}=U_{22}$, U_{33}; $U_{12}=U_{23}=U_{13}=0$		0.0142(4), 0.0157(5)			
M3 in 2b(3/4,1/4,1/2); occ.		0.49(1) Au + 0.51 Ge			
$U_{11}=U_{22}$, U_{33}; $U_{12}=U_{23}=U_{13}=0$		0.0174(3), 0.0171(3)			
M4 in 2a(3/4,1/4,0); occ.		0.103(9) Au + 0.897 Ge			
$U_{11}=U_{22}$, U_{33}; $U_{12}=U_{23}=U_{13}=0$		0.0160(5), 0.0153(6)			
Interatomic distances [nm] with standard deviation ≤ 0.0001					
Sr1 –	4M2	0.3404		–4M3	0.2642
	–4M1	0.3414		–4Sr1	0.3404
	–4M3	0.3467	M3 –	4M2	0.2642
	–4M4	0.3484		–4M3	0.3168
M1 –	1M2	0.2520		–4Sr1	0.3467
	–4M4	0.2639	M4 –	–4M1	0.2639
	–4Sr1	0.3414		–4M4	0.3168
M2 –	1M1	0.2520		–4Sr1	0.3484

A new representative crystallizing with the $BaCu_2Sb_2$ structure type (DünnerJ. 1995) has been found with the other single crystal. According to Dünner (DünnerJ. 1995) the

$BaCu_2Sb_2$ structure type is an ordered stacking variant of two unit cells of $CaBe_2Ge_2$ alternating with one unit cell of $ThCr_2Si_2$ along the c-direction. Refinement for the bct crystal τ_2-$SrAu_{2-x}Ge_{2+x}$ revealed that strontium occupies the crystallographic sites 2a (0,0,0) and 4e (0,0,0.33436(5)), whereas a mixed occupancy of gold and germanium in different ratios fills the sites 4e (0,0,0.12895(5)), 4e (0,0,0.45948(3)) and 8g (0,1/2,0.08311(2)) (details can be found in Table XXXVI). The Wyckoff positions 4e (0,0,0.20623(2)) and 4d (0,1/2,1/4) are occupied either by gold (4e) or germanium (4d), but the refinement of the 4d site showed an occupation of only 80% germanium. This lower occupancy significantly improved the final refinement (R_F value lower by about 1% and smaller ADP's in all sites) and leads to the refined composition $SrAu_{1.65(4)}Ge_{2.15}\square_{0.2}$. As the $ThCr_2Si_2$ structure type has been reported for stoichiometric $SrAu_2Ge_2$ by May et al. (May N. 1972) and by Lin et al. (Lin Q. 2012) also at 700°C, another alloy richer in gold (nominal composition $Sr_{22}Au_{33}Ge_{45}$) closer to the 1:2:2 composition was investigated by XPD after annealing at 700°C. Indeed, no additional reflections were observed on the X-ray powder patterns and the Rietveld refinement endorses the $ThCr_2Si_2$ structure type (see Figure 74) for τ_2.

Table XXXVI: X-Ray single crystal data for τ_2-$SrAu_{2-x}Ge_{2+x}$ ($BaCu_2Sb_2$-type) at RT (anisotropic displacement parameters U_{ij} in [$10^{-2}nm^2$]). The symbol □ denotes a vacancy.

Parameter/compound	**$SrAu_{2-x}Ge_{2+x}$; x=0.35**
Space group	*I*4/*mmm*
Composition from EPMA	$Sr_{20}Au_{30}Ge_{50}$ at.% ≡ $SrAu_{1.5}Ge_{2.5}$
Formula from refinement	$SrAu_{1.65(4)}Ge_{2.15}\square_{0.2}$
a, c [nm]	0.44866(2), 3.18088(16)
μ_{abs} [mm^{-1}]	22.44
V (nm^3)	0.6403
ρ_x (gcm^{-3})	9.01
Reflections in refinement	429≥4σ(F_o) of 496
Number of variables	25
$R_F = \Sigma\|F_0-F_c\|/\Sigma F_0$	0.033
R_{Int}	0.057
wR2	0.097
GOF	0.976
Extinction (Zachariasen)	0.0005(1)
Residual density $e^-/Å^3$; max; min	3.48; -1.93
Atom parameters	

Sr1 in 2a(0,0,0); occ.			1.06(2)		
$U_{11}=U_{22}$, U_{33}; $U_{12}=U_{23}=U_{13}=0$			0.0143(7), 0.0150(9)		
Sr2 in 4e(0,0,*z*); occ.			1.09(1)		
z			0.33436(5)		
$U_{11}=U_{22}$, U_{33}; $U_{12}=U_{23}=U_{13}=0$			0.0153(6), 0.0141(8)		
Au1 in 4e(0,0,*z*); occ.			0.95(5)		
z			0.20623(2)		
$U_{11}=U_{22}$, U_{33}; $U_{12}=U_{23}=U_{13}=0$			0.0177(3), 0.0158(3)		
Ge1 in 4d(0,1/2,1/4); occ.			0.79(1)		
$U_{11}=U_{22}$, U_{33}; $U_{12}=U_{23}=U_{13}=0$			0.0209(9), 0.0158(1)		
M1 in 4e(0,0,*z*); occ.			0.100(9) Au + 0.900 Ge		
z			0.12895(5)		
$U_{11}=U_{22}$, U_{33}; $U_{12}=U_{23}=U_{13}=0$			0.0191(4), 0.0145(8)		
M2 in 4e(0,0,*z*); occ.			0.476(7) Au + 0.524 Ge		
z			0.45948(3)		
$U_{11}=U_{22}$, U_{33}; $U_{12}=U_{23}=U_{13}=0$			0.0149(4), 0.0102(4)		
M3 in 8g(0,1/2,*z*); occ.			0.477(7) Au + 0.523 Ge		
z			0.08311(2)		
U_{11}, U_{22}, U_{33}; $U_{12}=U_{23}=U_{13}=0$			0.0181(4), 0.0196(4), 0.0133(4)		
Interatomic distances [nm] with standard deviation ≤ 0.0001					
Sr1 –	8M2	0.3424	M1 –	1Au1	0.2458
	–8M3	0.3467		–4M3	0.2675
Sr2 –	4M1	0.3380		–4Sr2	0.3380
	–4Au1	0.3425	M2 –	1M2	0.2577
	–4M3	0.3453		–4M3	0.2621
	–4Ge1	0.3497		–4Sr1	0.3424
Au1 –	1M1	0.2458	M3 –	2M2	0.2621
	–4Ge1	0.2640		–2M1	0.2675
	–4Sr2	0.3425		–4M3	0.3172
Ge1 –	4Au1	0.2461		–2Sr2	0.3453
	–4Ge1	0.3172		–2Sr1	0.3467
	–4Sr2	0.3497			

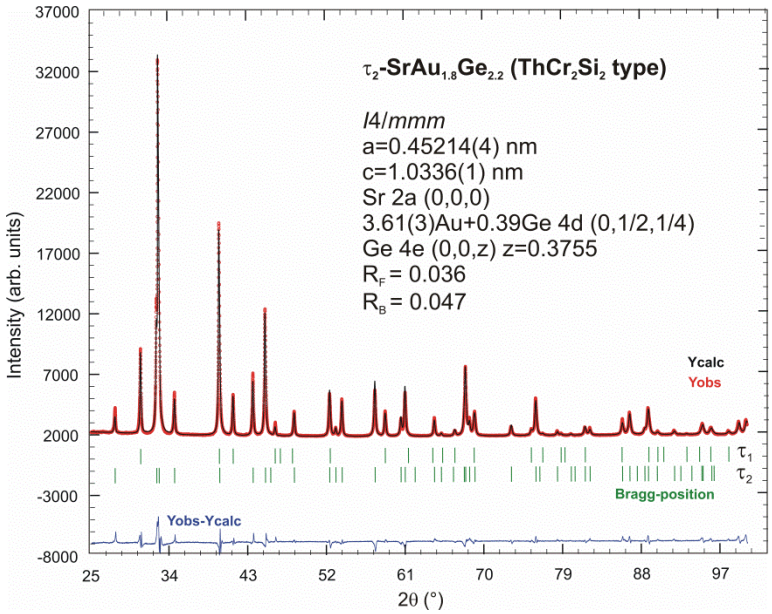

Figure 74: Rietveld refinement for an alloy with nominal composition $Sr_{22}Au_{33}Ge_{45}$ annealed at 700°C containing τ_2-$SrAu_{2-x}Ge_{2+x}$ ($ThCr_2Si_2$ type) as the main phase and small amounts τ_1-$Sr(Au_xGe_{1-x})_2$ (AlB_2 type).

The sample also contains small quantities of τ_1. Thus from the present investigation it is not clear if one can assume a continuous homogeneity field for τ_2-$SrAu_{2-x}Ge_{2+x}$ as the region near stoichiometric $SrAu_2Ge_2$ adopts the $ThCr_2Si_2$-type, whereas Ge-richer compositions crystallize with the $BaCu_2Sb_2$ structure. Lattice parameters (a and c in nm), c/a ratios and volume of the unit cells in dependence of the increasing germanium content x are shown in Figure 75(a)-(c). For the phase with the $BaCu_2Sb_2$ structure type we plotted the reduced lattice parameters $c=cBaCu_2Sb_2/3$ for x=0.35 and 0.4. The lattice parameter a changes only slightly over the whole investigated homogeneity range ($0.4477 \leq a \leq 0.4521$ nm, Figure 75(a)), whereas c strongly increases at the transition from the $ThCr_2Si_2$ type to the $BaCu_2Sb_2$ type and decreases afterwards again.

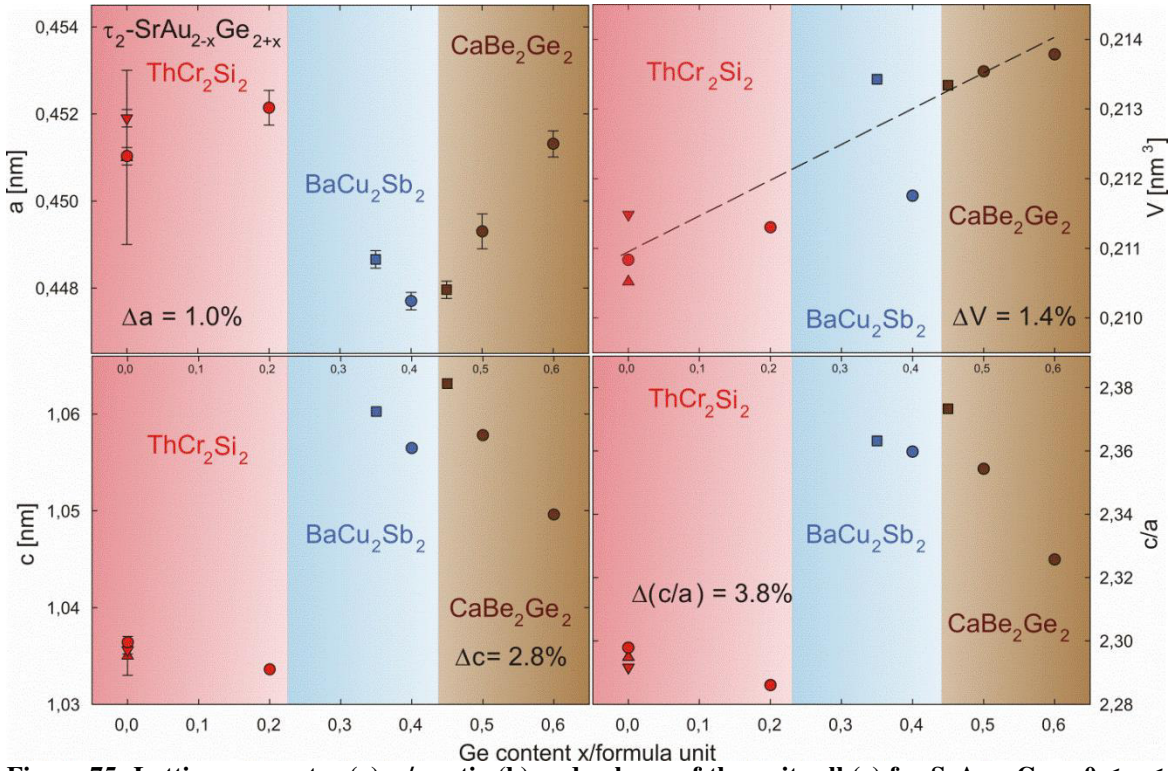

Figure 75: Lattice parameter (a), c/a ratio (b) and volume of the unit cell (c) for $SrAu_{2-x}Ge_{2+x}$ $0 \leq x \leq 0.6$; the reduced lattice parameters $c=c_{BaCu2Sb2}/3$ are shown for comparison with the smaller unit cells of the $ThCr_2Si_2$ and $CaBe_2Ge_2$ structure type. Circles represent the data of this work, squares - (F. Kneidinger 2014), triangle up – (May N. 1972), triangle down (Lin Q. 2012). Compositions and exact lattice parameters values of these alloys are also given in Table XXVII.

As can be seen from Figure 75(c), the volume of the unit cell increases with increasing germanium content, although gold has an atomic radius larger than covalent or metallic germanium radii (Taetum E. 1972). Group-subgroup relations in form of a Bärnighausen tree (Bärnighausen H. 1980) for the $BaAl_4$ family have been shown by Kussmann et al. (Kußmann D. 1999) and have been extended in our previous paper (F. Kneidinger 2014). Similar polymorphism has been reported recently for $BaCu_2Sb_2$ by Saparov and Sefat (Saparov B. 2012), who described an α-$BaCu_2Sb_2$ ($CaBe_2Ge_2$ type) to β-$BaCu_2Sb_2$ ($BaCu_2Sb_2$ type) transition and further polymorphs with the $ThCr_2Si_2$ structure type and possibly other metastable phases. Anand et al. (Anand V. K. 2012) found a further symmetry reduction for another $BaCu_2Sb_2$ modification for which he suggested a monoclinic structure (space group $P2_1/c$; a = 0.46414(3), b = 0.46418(3), c = 3.2680(2) nm and β= 90.616°).

5.7.1.3 Summary

Phase relations in the isothermal sections of the four ternary systems Sr-{Ag,Au}-{Si,Ge} have been established for the (Ge) or (Si) rich part up to 33.4 at.% strontium by X-ray powder diffraction and electron probe microanalysis of alloys in as cast state and after annealing at 700°C (Sr-{Ag,Au}-Ge) or 800°C (Sr-{Ag,Au}-Si). Phase equilibria in these systems are characterized by a series of ternary compounds, exhibiting in some cases extended homogeneity regions at a constant Sr-content. The existence of ternary compounds, reported earlier, has been confirmed: $SrAg_2Si_2$, $SrAg_2Ge_2$, $SrAg_{0.9}Ge_{1.1}$, $SrAu_2Ge_2$. For most of the novel compounds detected X-ray single crystal studies have been carried out: $Sr_2Ag_{1+x}Si_{3-x-y}\square_y$ (Sr_2LiSi_3 type; space group *Fddd;* x=0.17, y=0.43: a=0.84488(2), b=1.46376(2) and c=1.84018(2) nm), $SrAg_{2-x}Si_{2+x}$ ($ThCr_2Si_2$ type; space group *I*4/*mmm;* x=0.1: a=0.437664(6) and c=1.04517(2) nm), $Sr(Au_{1-y}\square_y)(Si_{1-x}Au_x)_3$ ($BaNiSn_3$ structure type; space group *I*4*mm*; x=0.59, y=0.64: a=0.44594(2) and c=1.01013(6) nm) and $SrAu_{5-x}\square_xSi_2$ ($BaAu_5Si_2$ type; space group *Pnma*; x=0.7: a=0.87557(3), b=0.69945(2) and c=0.98873(3) nm). The crystal structures of some of the compounds have been characterized by X-ray powder diffraction: $Sr(Ag_xGe_{1-x})_2$ (AlB_2 structure type; x=0.25: a=0.43431(2) and c=0.45838(1) nm), $SrAg_{2-x}Ge_{2+x}$ ($ThCr_2Si_2$ type; x=0.2: a=0.44476(2) and c=1.0822(1) nm) and $Sr(Au_xGe_{1-x})_2$ (AlB_2 structure type; x=0.25: a=0.43263(2) and c=0.45852(7) nm).

Polymorphism has been observed for $SrAu_{2-x}Ge_{2+x}$ (x=0.5: $CaBe_2Ge_2$ type; space group *P4/nmm;* a=0.44796(2) and c=1.06315(5); x=0.45: $BaCu_2Sb_2$ type; space group *I*4/*mmm*; *a*=0.44866(2) and c=3.1808(1) nm and x=0.2: $ThCr_2Si_2$ type; space group *I4/mmm*; a=0.45214(4) and c=1.0336(1) nm) and for $Sr(Au_xSi_{1-x})_2$ (x=0.25: Ca_2AgSi_3 type; space group *Fmmm*; a=0.83407(2) and c=0.92664(3) nm; x=0.375: AlB_2 type; space group *P6/mmm*; a=0.42241(2), c=0.45799(3) nm).

In summary, the exploration of the four ternary systems Sr-{Ag,Au}-{Si,Ge} resulted in a series of ternary compounds with various crystal structures mainly based on parent types such as $BaAl_4$ and AlB_2. Neither clathrate structures nor non-centrosymmetric structure types with full atom order have been encountered in the temperature range investigated.

References

Akazawa T., Hidaka H., Fujiwara T., Kobayashi T.C., Yamamoto E., Haga Y., Settai R., Onuki Y.,. "Pressure-induced superconductivity in ferromagnetic UIr without inversion symmetry." *J. Phys.: Cond. Mat.*, no. 16 (2004): L29.

Amano G., Akutagawa S., Muranaka T., Zenitani Y., Akimitsu J.,. "Superconductivity at 18 K in Yttrium Sesquicarbide System, Y2C3." *J. Phys. Soc. Jpn.*, no. 73 (2004): 530.

Anand V. K., Perera P. Kanchana, Abhishek Pandey, Goetsch R. J., Kreyssig A., Johnston D. C.,. "Crystal growth and physical properties of SrCu2As2, SrCu2Sb2, and BaCu2Sb2." *Physical Review B* 85, no. 21 (2012): 214523.

Anno H., Fukushima H., Koga K., Okiza K., Matsubara K.,. " Effect of Guest Substitution on Thermoelectric Properties of Clathrate Compounds." *Thermoelectrics, ICT*, 2006: 36-39.

Anno H., Hokazono M., Takakura H.,. "Thermoelectric properties of Ba8AuxGe46-x Clathrate Compounds." *Thermoelectrics, ICT 2005*, 2005: 102-105.

Anno H., Suzuki K., Koga K.,. "Effect of Au substitution on thermoelectric properties of silicon clathrate compounds." *Thermoelectrics ICT* , 2007: 226-229.

Aronsson B. "The Crystal Structure of RuB2, OsB2 and IrB1.35 and some general Comments on the Crystal Chemistry of Borides in the Composition Range MeB-MeB3." *Acta Chem. Scand.* 17 (1963): 2036-2050.

Aronsson B., Stenberg E., Aselius J.,. "Borides of Rhenium and the Platinum Metals. The Crystal Structure of Re7B3, ReB3, Rh7B3, RhB1.1 (approximate composition), IrB1.1 (approximate composition) and PtB." *Acta Chem. Scand.* 14 (1960): 733-741.

Aronsson B., Stenberg E., Åselius J.,. "„Borides of Ruthenium, Osmium and Iridium”." *Nature*, 1962: 377-378.

Aydemir U., Akselrud L., Carillo-Cabrera W., Candolfi C., Oeschler N., Baitinger M., Steglich F., Grin Y.,. "BaGe5: A New Type of Intermetallic Clathrate." *J. Am. Chem. Soc.* 32, no. 132 (2010): 10984–10985.

B. Eisenmann, H. Schäfer, K. Turban,. "Unknown." *Z. Naturforschung B*, 1974: 464.

Babizheztskyy V., Guerin R., Isnard O., Hiebl K. " Ternary rare-earth nickel arsenides R3Ni7As5 (R=La, Ce, Pr, Nd, Sm) with a new variant of the BaAl4-type: crystal structure and physical properties." *J. of Solid State Chem.*, no. 172 (2003): 265-276.

Badica P., Kondo T., Togano K.,. "Superconductivity in a New Pseudo-Binary Li2B(Pd1-xPtx)3 (x=0–1) Boride System." *J. Phys. Soc. Jpn.*, no. 74 (2005): 1014-1019.

Ban Z., Sikirica M.,. "The crystal structure of ternary silicides ThM2Si2(M = Cr, Mn, Fe, Co, Ni and Cu)." *Acta Crystallogr.*, no. 18 (1965): 594-599.

Bardeen J., Cooper L. N., Schrieffer J. R.,. "Theory of Superconductivity." *Phys. Rev.*, no. 108 (1957): 1175.

Bärnighausen H. "Group-subgroup relations between space groups: a useful tool in crystal chemistry." *Commun Math Chem*, no. 9 (1980): 139.

Bärnighausen H., Müller U.,. " Symmetriebeziehungen zwischen den Raumgruppen als Hilfsmittel zur straffen Darstellung von Strukturzusammenhängen in der Kristallchemie." University of Karlsruhe and University GH Kassel , 1996.

Bauer E., Hilscher G., Michor H., Paul Ch., Scheidt E. W., Gribanov A., Seropegin Yu., Noël H., Sigrist M., Rogl P.,. "Heavy Fermion Superconductivity and Magnetic Order in Noncentrosymmetric CePt3Si." *Phys. Rev. Lett.*, no. 92 (2004): 027003.

Bauer E., Khan R.T., Michor H., Royanian E., Grytsiv A., Melnychenko-Koblyuk N. , Rogl P., Reith D. , Podloucky R., Scheidt E.-W., Wolf W., Marsman M.,. " BaPtSi3: A noncentrosymmetric BCS-like superconductor." *Physi. Rev. B*, no. 80 (2009): 064504.

Bauer E., Rogl G., Chen X.Q., Khan R.T., Michor H., Hilscher G., Royanian E., Kumagai K., Li D. Z., Li Y.Y., Podloucky R., Rogl P.,. " Unconventional superconducting phase in the weakly correlated noncentrosymmetric Mo3Al2C compound." *Phys. Rev. B*, no. 82 (2010): 064511.

Bauer E., Rogl G., Chen Xing-Qiu, Khan R. T., Michor H., Hilscher G., Royanian E., Kumagai K., Li D. Z., Li Y. Y., Podloucky R., Rogl P. "Unconventional superconducting phase in the weakly correlated noncentrosymmetric Mo3Al2C compound." *Phys. Rev. B*, no. 82 (2010): 064511 .

Bauer E., Rotter M., Podloucky R., Rogl P., Grytsiv A.V., Chen X.Q., Melnychenko Koblyuk N., Hilscher G., Kaldarar H., Michor H., Royanian E., Giester G.,. "Superconductivity in novel Ge-based skutterudites: (Sr,Ba)Pt4Ge12." *Phys. Rev. Lett.*, 2007: 21700-1.

Bazela W. "The influence of the crystal structure on the magnetic ordering in RT2X2 and RTX3 compounds." *J. Alloys and Compounds*, no. 442 (2007): 132-135.

Beaurepaire E., Krill G., Kappler J. P., Röhler J.,. " 4f ground state properties of cerium in AuCu3 intermetallic compounds studied by x-ray absorption spectroscopy." *Solid State Commun.*, no. 49 (1984): 65.

Bednorz J.G., Müller K.A.,. "Possible high Tc superconductivity in the Ba−La−Cu−O system, ." *Zeitschrift für Physik B Condensed Matter* 2, no. 64 (1986): 189-193.

Beekman M., Nolas G.S.,. "Inorganic clathrate-II materials of group 14: synthetic routes and physical properties." *J. Mater. Chem.*, no. 18 (2008): 842-851.

Berger S. "Novel thermoelectric materials: PhD Thesis." TU Vienna, Austria, 2003.

Betz A., Schäfer H., Weiss A., Wulf R.,. "Zur Kenntnis der Digermanide des Strontiums und Bariums, SrGe2 und BaGe2." *Zeitschrift für Naturforschung B*, 1968: 878.

Betz A., Schäfer H., Weiss A.,. "Die Kristallstruktur von SrGe." *Zeitschrift für Naturforschung B*, 1967: 103.

Bin L., Corbett J.D.,. " Syntheses and Structures of New Phases AeMxIn4-x (Ae = Sr, Ba; M = Mg, Zn): Size Effects and Site Preferences in BaAl4-Type Structures." *J. of Inorganic Chem.* 21, no. 46 (2007): 8812-8818.

Blatt F. J. *Physics of electronic conduction in solids.* McGraw-Hill, New York, 1968.

Bobev S., Sevov S.C.,. " Clathrates of Group 14 with Alkali Metals: An Exploration." *J. Solid State Chem.*, no. 153 (2000): 92-105.

Bock O., Müller U.,. "Symmetry in perovskite variants." *Acta Cryst.B*, no. 58 (2002): 594-606.

Brauer G., Mitius A.,. "Die Kristallstruktur des Thoriumsilicids ThSi2." *Z. Anorg. Allg. Chem.*, no. 249 (1942): 325-339.

Braun H. F., Engel N., Parthe E.,. "Polymorphism and superconductivity of LaIr2Si2." *PHYS. REV. B* 3, no. 28 (1983): 1389.

Braun H.F., Jarlborg T., Junod A.,. "Specific Heat and Bandstructure of two polymorphs of LaIr2Si2." *Physica B*, no. 397-399 (1985): 397-399.

Brazhkin V., Dubrovinskaia N., Nicol M., Novikov N., Riedel R., Solozhenko V., Zhao Y.,. "What does 'harder than diamond' mean?" *Nature Materials,*, no. 3 (2004): 576-577.

Bridges F., Downward L.,. "Possible mechanism for glass-like thermal conductivities in crystals with off-center atoms." *Phys. Rev. B*, no. 70 (2004): 140102.

Brukl C.E., Rudy E. "Ternary Phase Equilibria in the Transition-Metal-Boron-Carbon-Silicon System." *Air Force Materials Laboratory Technical Report (AFML-TR-65-2)*, 1967: 31-42.

Bruzzone G., Bonino G.B.,. "Alcuni composti intermetallici MX2 formati dal Ca, Sr e Ba." *Atti Accad. Naz. Lincei, Cl. Sci. Fis., Mat. Nat., Rend.*, 1970: 235-241.

Bruzzone G., Ferretti M., Merlo F.,. "The Ba-Ag System." *J. Less.- Comm. Met.*, no. 128 (1987): 259-264.

Buddery J.H., Welch A.J.E.,. "Borides and Silicides of the Platinum Metals." *Nature* 3, no. 167 (1951): 362.

Cahill D., Pohl R.,. "Heat flow and lattice vibrations in glasses." no. 70 (1989): 927.

Cai K.F., Zhang L.C., Lei Q.,. " Preparation and Characterization of Sr, Ba Filled Type-I Ge Clathrate Single Crystals." *Key Engineering Materials*, no. 336-338 (2007): 896-899.

Callaway J., von Baeyer HC.,. "Effect of Point Imperfections on Lattice Thermal Conductivity." *Phys. Rev.*, no. 120 (1969): 1149.

Candolfi C., Aydemir U., Baitinger M., Oeschler N., Steglich F., Grin Yu.,. "High temperature thermoelectric properties of the type-I clathrate Ba8AuxSi46−x." *Journal of Applied Physics*, 2012: 043706.

Cardoso Gil R., Carrillo-Cabrera W., Schultheiss M., Peters K.von Schnering H.G., Grin Y.,. "New Examples for the Unexpected Stability of the 10p-Electron HÜckel Arene [Si6]10-." *Z. anorg. allg. Chem.* 625 (1999): 285-293.

Carrillo Cabrera W., Curda J., von Schnering H.G., Paschen S., Grin Y.,. "Crystal structure of hexabarium pentacosagermanide, Ba6Ge25." *Zeitschrift fuer Kristallographie - New Crystal Structures*, no. 215 (2000): 207-208.

Carrillo-Cabrera W., Budnyk S., Prots Yu., Grin Y.,. "Ba8Ge43 revisited: a 2a′×2a′×2a′ Superstructure of the Clathrate-I Type with Full Vacancy Ordering." *Z. Anorg. Allg. Chem.*, no. 630 (2004): 2267-2276.

Carrillo-Cabrera W., Curda J., Peters K., Paschen S., Baenitz M., Grin Yu. , von Schnering H.G.,. "Crystal structure of the defect clathrate-I, Ba8Ge43." *Z. Kristallogr. NCS*, no. 215 (2000): 321.

Chen X.-Q., Fu C.L., Krcmar M., Painter G.S.,. " Electronic and Structural Origin of Ultraincompressibility of 5d Transition Metal Diborides MB2 (M=W,Re,Os)." *Phys. Rev. Lett.*, no. 100 (2008): 196403.

Chevalier B., Lejay P., Cole A., Vlasse M., Etourneau J.,. "Crystal Structure, Superconducting and magnetic properties of new ternary silicides LaRhSi, LaIrSi and NdIrSi." *Solid State Communications* 1, no. 41 (1982): 801-804.

Chiu J.C.H. " Deviations from linear temperature dependence of the electrical resistivity of V-Cr and Ta-W alloys." *Phys. Rev. B*, no. 13 (1976): 1507–14.

Chretien A., Helgorsky J.,. "Sur les borures de molybdene et de tungstene MoB4 et WB4 composes nouveaux." *Compt. Rend. Hebd. Seances Acad. Sci. Colon. (Paris)*, no. 252 (1961): 742-744.

Christensen M., Johnsen S., Brummerstedt-Iversen B.,. "Thermoelectric clathrates of type I." *Dalton Trans.*, no. 39 (2010): 978-992.

Chung H.Y., Yang J.M. , Weinberger M.B. , Tolbert S.H. , Levine J.B. , Kaner R.B. , A. Kavner. "Synthesis of Ultra-Incompressible Superhard Rhenium Diboride at Ambient Pressure." *Science* 316, no. 5823 (2007): 436-439.

Condron C.L., Kauzlarich S.M., Gascoin F., Snyder G.J.,. "Thermoelectric Properties and Microstructure of Ba8Al14Si31 and EuBa7Al13Si33." *Chem. Mater.*, no. 18 (2006): 4939-4945.

Condron C.L., Kauzlarich S.M., Ikeda T., Snyder G.J., Haarmann F., Jeglic P.,. "Synthesis, Structure, and High-Temperature Thermoelectric Properties of Boron-Doped Ba8Al14Si31 Clathrate-I Phases." *Inorganic Chemistry* 18, no. 47 (2008): 8204-8212.

Condron C.L., Kauzlarich S.M.,. "Structure and Thermoelectric Characterization of AxBa8-xAl14Si31 (A = Sr, Eu) Single Crystals." *Inorganic Chemistry* 7, no. 46 (2007): 2556-2562.

Condron C.L., Martin J., Nolas G.S., Piccoli P.M.B., Schultz A.J., Kauzlarich S.M.,. "Structure and Thermoelectric Characterization of Ba8Al14Si31." *Inorganic Chemistry* 23, no. 45 (2006): 9381-9386.

Cordier G., Woll P. J.,. "Neue ternäre intermetallische Verbindungen mit Clathratstruktur: Ba8(T,Si)6Si40 und Ba6(T,Ge)6Ge40 mit T ≡ Ni, Pd, Pt, Cu, Ag, Au." *J. Less-Common. Met.* 169 (1991): 291.

Crespo A.J., Tergenius L.-E.,Lundström T.,. "The solid Solution of 4d, 5d and some p-Elements in ß-rhombohedral Boron." *J. Less-Common Metals*, no. 77 (1981): 147-150.

Demchyna R., Prots Yu., Schnelle W., Burkhardt U., Schwarz U.,. "Crystal structures of (barium, europium) platinum trigermanium, Ba1-xEuxPtGe3 (x = 0, 0.27, 1)." *Z. Kristallogr. NCS*, no. 221 (2006): 109.

Dhar S. K., Gschneidner K. A., Bredl C. D., Steglich F.,. "Magnetic susceptibility and low-temperature heat capacity of CePd3B0.3." *Phys. Rev. B*, no. 39 (1989): 2439.

Dhar S. K., Malik S. K., Vijayaraghavan P. R.,. "Boron-induced valence change of cerium in CePd3." *Phys. Rev. B*, no. 10 (1981): 6182.

Doerrscheidt W., Schaefer H.,. "Die Struktur der Phase BaNi2Si2 und ihre Verwandtschaft zum ThCr2Si2 – Strukturtyp." *Zeitschrift fuer Naturforschung B*, no. 35 (1980): 297-299.

Dörrscheidt W., Niess N., Schäfer H.,. „Neue Verbindungen AB2X2 (A= Erdalkalimetall, B= Übergangselement, X= Element(IV)) im ThCr2Si2-Typ.“ *Z. Naturforsch. B*, 1976: 890-891.

Dörrscheidt W., Schäfer H.,. " Die Struktur des BaPtSn3, BaNiSn3 und SrNiSn3 und ihre Verwandtschaft zum ThCr2Si2-Strukturtyp." *J Less-Comm. Met.*, no. 58 (1978): 209-216.

Dörrscheidt W., Schäfer H.,. "Darstellung und Kristallstruktur von BaPdSn3, SrPdSn3 und La3Co2Sn7." *J. Less-Comm. Met.*, no. 70 (1980): P1 – P10.

—. „ Beiträge zu den Stabilitätskriterien der AlB2-Struktur.“ *J. Less-Common Met.*, 1981: 69-79.

Dubrovinskaia N., Dubrovinsky L., Solozhenko V.L.,. "Comment on ‘Synthesis of Ultra-Incompressible Superhard Rhenium Diboride at Ambient Pressure’." *Science*, no. 318 (2007): 1550c.

DünnerJ., Mewis A., Roepke M., Michels G.,. "Neue ternäre Kupferpnictide mit modifizierten BaAl4-Strukturen." *Zeitschrift für anorganische und allgemeine Chemie* 621, no. 9 (1995): 1523–1530.

Duschanek H., Rogl P.,. "Critical Assessment and Thermodynamic Calculation of the Binary System Boron-Tungsten." *JPE*, no. 16 (1995): 150-161.

Duschanek H., Rogl P.,. "Critical Assessment and Thermodynamic Calculation of the Binary System Boron-Tungsten." *JPE*, no. 16 (1995): 150-161.

Eisenmann B., May N., Müller W., Schäfer H., Eine neue strukturelle Variante des BaAl4-Typs: Der CaBe2Ge2-Typ. *Z. Naturforsch. B*, no. 27 (1972): 1155-1157.

Eisenmann B., May N., Müller W., Schäfer H., Weiss A., Winter J., Ziegleder G.,. „ Neue Vertreter des ThCr2Si2-Typs und dessen Verwandtschaft zum Anti-PbFCl-Gitter.“ *Z. Naturforsch. B*, 1970: 1350-1352.

Eisenmann B., Schäfer H., Turban K.,. "Neue intermetallische Verbindungen im anti-PbCl2Typ." *Zeitschrift für Naturforschung B*, 1975: 677-680.

Eisenmann B., Schäfer H., Turban K.,. "Zur Kenntnis einer neuen SrSi-Modifikation und der Phase SrGe0.76." *Z. Naturforsch. B*, no. 29 (1974): 464-468.

Eisenmann B., Schäfer H., Zagler R.,. „Die verbindungen AII8BIII16BIV30 (AII ≡ Sr, Ba; BIII≡ Al, Ga; BIV ≡ Si, Ge, Sn) und ihre Käfigstrukturen.“ *J. Less-Comm. Met.*, Nr. 118 (1986): 43-55.

Ellner M., Grin J., Fischer P., Rogl P.,. "Röntgen- und Neutronenbeugungsuntersuchungen der Struktur von Pt3B2." *Z. Metallkd.*, no. 84 (1993): 788-791.

Engquist H.L. "Solution of the linearized Boltzmann equation for electrical transport in metals." *Phys. Rev. B*, no. 21 (1980): 2067.

Evers J., Oehlinger G., Weiss A., Probst C., Superconductivity of LaPtSi and LaPtGe. *Solid State Communications* 1, no. 50 (1984): 61-62.

F. Kneidinger, Salamankha L., Bauer E., Zeiringer I., Rogl P., Blaas-Schenner C., Podloucky R., Reith D.,. "Superconductivity in noncentrosymmetric BaAl4 derived structures." *Phys. Rev. B*, 2014: 024504-1-12.

Falmbigl M., Chen M.X., Grytsiv A., Rogl P., Royanian E., Michor H., Bauer E., Podloucky R., Giester G.,. " Type-I clathrate Ba8NixSi46-x: phase relations, crystal chemistry and thermoelectric properties." *Dalton Trans.*, 2012: 8839-8849.

Falmbigl M., Grytsiv A., Rogl P., Giester G.,. " Clathrate formation in the systems Ba–Ir–Ge and Ba-{Rh, Ir}-Si: Crystal chemistry and phase relations." *Intermetallics*, 2013: 61–72.

Falmbigl M., Kneidinger F., Chen M., Grytsiv A., Michor H., Royanian E., Bauer E., Effenberger H., Podloucky R., Rogl P.,. "Cage-forming compounds in the Ba-Rh-Ge system: from thermoelectrics to superconductivity." *Inorg Chem.*, 2013: 931-943.

Falmbigl M., Rogl G., Rogl P., Kriegisch M., Müller H., Bauer E., Reinecker M., Schranz W.,. "Thermal expansion of thermoelectric type-I-clathrates." *J. Appl. Phys.* 4, no. 108 (2010): 1.

Falmbigl M., Romaka V.V., Grytsiv A., Rogl P.,. "Formation and stability of the clathrate-I structure in the systems Sr–(Ni,Cu,Zn)–Ge based on experimental and DFT studies." *Intermetallics*, 2014: 185–189.

Farrugia L. J. "WINGX suite for small-molecule single-crystal crystallography." *J. Appl. Crystallogr.*, 1999: 837-838.

FCT System GmbH. "Betriebsanleitung Heisspresse." 2006.

Feller Kniepmeier M., Heumann T.,. " Das Zustandsbild Gold-Strontium." *Z. Metallkd.*, 1960: 404-408.

Fischer H. A. *PhD Thesis: Ternäre Silicide der schweren Erdalkali-Elemente mit Palladium und Platin* . University Köln, 2000.

Fokwa B.P.T., Eck B., Dronskowski R.,. "Ti2Rh6B – a new boride with a double perovskite-like structure containing octahedral Rh6 clusters." *Z. Kristallogr.*, no. 221 (2006): 445-449.

Fornasari L. "Diploma Thesis." University of Pavia, Italy, 2006.

Fornasini M.L., Merlo F., Pani M.,. "Structures of Ca3Au, Ca5Au2, Sr3Au2, Ba3Au2 and alloying behaviour of the alkaline earths with Cu, Ag, Au." *Rev. Chim. Miner.*, 1985: 791-798.

Frigeri P.A., Agterberg D.F., Sigrist M.,. "Spin susceptibility in superconductors without inversion symmetry." *New J. Phys.*, no. 6 (2004): 115.

Frik L., Johrendt D., Mewis A.,. " Eine neue Verzerrungsvariante des CaBe2Ge2-Typs – Die Kristallstrukturen von SrPd2Bi2, BaPd2Bi2 und BaAu2Sb2." *Z. Anorg. Allg. Chem.*, no. 632 (2006): 1514.

Fritsch GmbH. "Instruction manual for Fritsch ``Pulverisette 4´´ Vario-planetary mill." 2007. www.fritsch.de.

Fujii H., Sato A.,. "BaNiSn3-type ternary germanides SrMGe3 (M = Ir; Pd and Pt)." *Journal of Alloys and Compounds*, no. 508 (2010): 338–341.

Fujii H., Sato A.,. "Superconductivity in SrPd2Ge2." *Phys. Rev. B*, no. 79 (2009): 224522-1.

Gabouskas M.F., Kasper J.S., Slack G.A.,. "The Incorporation of Vanadium in ß- rhombohedral Boron as Determined by Single-Crystal Diffractometry." *J Solid State Chemistry*, no. 63 (1986): 424-430.

Gambke T., Elschner B., Schaafhausen J., Schaeffer H.,. *Valence Fluctuations in Solids.* North Holland: Falicov L. M., Hanke W., Maple M. B., 1981.

Gelato L.M., Parthé E.,. " STRUCTURE TIDY - a Computer Program to Standardize Crystal Structure Data." *J. Appl. Cryst.*, 1987: 139-143.

Gilman J.J., Cumberland R.W., Kaner R.B. " Design of Hard Crystals." *Int. J. Refract. Metals Hard Mater.*, no. 24 (2006): 1–5.

Gou H., Li Z., Wang L.M., Lian J., Wang Y.,. "Peculiar structure and tensile strength of WB4: nonstoichiometric origin." *AIP Adv.*, no. 2 (2012): 012171.

Gout D., Barker T.J., Gourdon O., Miller G.J. " La2NiAl7, A New Superstructure for the BaAl4-Structure Type: An Experimental and Theoretical Study of La2NiAl7." *Chem. Mater*, no. 17 (2005): 3661-3667.

Grosche F.M., Julien S.R., Mathur N.D., Lonzarich G.G.,. "Magnetic and superconducting phases of CePd2Si2." *Physica B*, no. 50 (1996): 224.

Grytsiv A., Melnychenko-Koblyuk N., Nasir N., Rogl P., Saccone A., Schmid H.,. "Formation of clathrates Ba–M–Ge(M=Mn,Fe,Co)." *International Journal of Materials Research*, 2009: 189-202.

Grytsiv A.V., Rogl P., Bauer E., Michor H., Royanian E., Giester G.,. "Novel silicide BaPt5Si12: Crystal structure and physical properties." *Intermetallics*, 2010: 173-178.

Gu Q., Krauss G., Steurer W. "Transition Metal Borides: Superhard versus Ultra Incompressible." *Advanced Materials* 20 (2008): 3620-3626.

H.M. Rietveld. *J. Appl. Cryst*, no. 2 (1969): 65.

H.M. Rietveld. *Acta Cryst*, no. 22 (1967): 151.

Haines J., Leger J.M., Bocquillon G.,. "Synthesis and Design of Superhard Materials." *Annu. Rev. Mater. Res.*, no. 31 (2001): 1–23.

Hao X., Wu Z., Xu Y., Zhou D., Liu X., Meng J.,. " Trends in elasticity and electronic structure of 5d transition metal diborides: first-principles calculations; 19 () (15pp)." *J. Phys.: Condens. Matter*, 2007: 196212 .

Harris I. R., Norman M., Gardner W. E.,. "The electronic state of cerium in some CeRh3-xPdx." *J. Less-Common Met.*, no. 29 (1972): 299-309.

Haschke H. *Structural Chemical Investigations on Complex Borides and Carbides, as well as on Silicides and Germanides of Rare Earth Metals: PhD-Thesis.* University of Vienna, 1966.

Hassler E., Lundström T., Tergenius L.E.,. "The crystal chemistry of platinum metal borides." *J. Less-Common Met.*, no. 67 (1979): 567-572.

Hegger H., Petrovic C., Moshopoulou E.G., Hundley M.F., Sarrao J.L., Fisk Z., Thompson J.D.,. "Pressure-Induced Superconductivity in Quasi-2D CeRhIn5." *Phys. Rev. Lett.*, no. 84 (2000): 4986.

Hellmann A., Löhken A., Wurth A., Mewis A.,. " New Arsenides with ThCr2Si2-type or Related Structures: The Compounds ARh2As2 (A: Eu, Sr, Ba) and BaZn2As2." *Z. Naturforsch.*, no. 62b (2007): 155-161.

Hermus M., Fokwa B. P. T.,. "Zr2Ir6B with an eightfold superstructure of the cubic perovskite-like boride ZrIr3B0.5: Synthesis, crystal structure and bonding analysis." *J. Solid State Chem.*, no. 183 (2010): 784-788.

Herrmann R.F.W., Tanigaki K., Kuroshima S., Suematsu H.,. "Superconductivity in silicon based barium-inclusion clathrates." *Chemical Physical Letters*, no. 283 (1998): 29-32.

Herrmann RFW, Tanigaki K, Kawaguchi T, Kuroshima S, Zhou O.,. " Electronic structure of Si and Ge gold-doped clathrates." *Phys. Rev. B*, no. 60 (1999): 13245.

Heying B., Pöttgen R., Valldor M., Rodewald U.Ch., Mishra R., Hoffmann R.D.,. " Synthesis, Structure, and Magnetic Properties of the Silicides REIrSi (RE = Ce, Pr, Er, Tm, Lu) and SmIr0.266(8)Si1.734(8)." *Monatshefte für Chemie*, no. 135 (2004): 1335-1347.

Hidenobu K., Ryoji S., Toestu S., Akiko N., Kunio K., Shigeru O., Vijay K., Kazuo N., Yoshiyuki K.,. "Ab initio studies of structural, elastic, and electronic properties of RRh3BX (R=Sc, Y, La, and Ce)." *Applied Phys. Lett.*, no. 91 (2007): 081901.

Hlukhyy V., Senyshyn A., Trots D., Fässler T.F.,. "High temperature phase transitions and crystal structure of BaNi2Ge2." *HASYLAB Annual Report*, 2007: 1021.

Hoffmann R. D., Pöttgen R.,. "AlB2-related intermetallic compounds — a comprehensive view." *Z. Kristallogr.* 216 (2001): 127–145.

Höhne G.W.H., Hemminger, W.F., Flammersheim H.J.,. *Differential Scanning Calorimetry.* New York: Springer Verlag Heidelberg, 2003.

Holeck H. "The Effect of carbon on the occurrence of Cu3Au-type phases in actinide and lanthanide-platinum metal Systems." *Journal of Nuclear Materials*, no. 42 (1972): 278-284.

Huber. "Manual Guinier Camera G670." n.d. http://www.xhuber.de/en/product-groups/2-applications/22-x-ray-cameras/guinier-g670/.

Int. Tabl. of Crystallogr. C. Vol. 3rd Edition. Chichester: Prince E.,, 2004.

Ipser H., Rogl P.,. " Constitution Diagrams of the Binary Systems Pd-B and Ir-B." *Journal of Less-Common Metals*, 1981: 362.

Isobe M., Yoshida H., Kimoto K., Arai M.,Takayama-Muromachi E. "SrAuSi3: A Noncentrosymmetric Superconductor." *Chem. Mater.*, no. 26 (2014): 2155−2165.

Ivanovskii A.L. "The Search for Novel Superhard and Incompressible Materials on the Basis of Higher Borides of s, p, d Metals." *Journal of Superhard Materials* 33, no. 2 (2011): 73-87.

Jaccard D., Behnia K., Sierro J.,. "Pressure induced heavy fermion superconductivity of CeCu2Ge2." *Phys. Lett. A*, no. 163 (1992): 475.

Jaussaud N., Gravereau P., Pechev S., Chevalier B., Menetrier M., Dordor P., Decourt R., Goglio G., Cros C., Pouchard M.,. "n- and p-Type behaviour of the gold-substituted type-I clathrate, Ba8AuxSi46–x (x = 5.4 and 5.9)." *C. R. Chimie*, no. 8 (2005): 39-46.

Johnsen S., Thomsen B., Christensen M., Madsen G.K.H., Nygren M., Inversen B.,. *ICT*, 2007: 219-221.

Jones C. D. W., Gordon R. A., Cho B. K., Di Salvo F. J., Kim J. S.,. "Stewart G.R., Comparisons of electrical, magnetic and low temperature specific heat properties in group 13 and group 14 Ce8Pd24M compounds (M=B, Al, Ga, In and Si, Ge, Sn, Pb)." *Physica B: Condensed Matter*, no. 262 (1999): 284–295.

Joshi D. A., Kumar N., Thamizhavel A., Dhar S. K.,. "Magnetic behavior in RRh3X (R=rare earth; X=B, C)." *Phys. Rev. B: Condens. Matter*, no. 80 (2009): 224404.

Junod A. "Heat-capacity analysis of a large number of A15-type compounds." *Phys. Rev. B*, no. 27 (1983): 1568.

Junod A., Bichsel D., Mueller J.,. " Modification du spectre de phonons acoustiques en function de la densité d'états électroniques dans les supraconducteurs de type A 15." *Helv. Phys. Acta.*, no. 52 (1979): 580.

Kamakura N., Nakano T., Ikemoto Y., Usuda M., Fukuoka H., Yamanaka S., Shin S., Kobayashi K.,. "Role of Ag doping in Ba8Si46 compounds." *Phys. Rev. B*, no. 72 (2005): 014511.

Kawai H., Horie H.O., Yamanaka S., Ishikawa M.,. "Superconductivity in the silicon clathrate compound (Na,Ba)xSi46." *Phys. Rev. Lett.* 8, no. 74 (1995): 1427- 1429.

Kimura N., Ito K., Saitoh K., Umeda Y., Aoki H., Terashima T.,. "Pressure-Induced Superconductivity in Noncentrosymmetric Heavy-Fermion CeRhSi3." *Phys. Rev. Lett.*, no. 95 (2005): 247004.

Kishimoto K., Ikeda N., Akai K., Koyanagi T.,. "Synthesis and Thermoelectric Properties of Silicon Clathrates Sr8AlxGa16-xSi30 with the Type-I and Type-VIII Structures." *Applied Physics Express*, no. 1 (2008): 031201.

Kishimoto K., Koyanagi T., Akai K., Matsuura M.,. "Synthesis and Thermoelectric Properties of Type-I Clathrate Compounds Si46-xPxTe8." *Jpn. J. Appl. Phys.* 29-32, no. 46(2) (2007): L746-L748.

Klepp K., Parthe E.,. "RPtSi Phases (R = La, Ce, Pr, Nd, Sm and Gd) with an Ordered ThSi2 Derivative Structure." *Acta Cryst. B*, no. 38 (1982): 1105-1108.

Klesnar H.P., Aselage T.L., Morosin B., Kwei G.H., Lawson A.C.,. "The diboride compounds of molybdenum: MoB2-x and Mo2B5-y." *J. Alloys Compd.*, no. 241 (1996): 180-186.

Kneidinger F. "Non-centrosymmetric superconductivity of intermetallic compounds in absence of strong correlations among electrons." *PhD thesis; TU Vienna;* , 2014.

Kneidinger F., Michor H.,Sidorenko A., Bauer E., Zeiringer I., Rogl P., Blaas-Schenner C., Reith D., Podloucky R.,. "Synthesis, characterization, electronic structure, and phonon properties of the noncentrosymmetric superconductor LaPtSi." *Physical Review B* 10, no. 88 (2013): 104508.

Koblyuk-M. N., Berger St., Grytsiv A., Kaldarar H., Michor H., Röhrbacher F., Royanian E., Bauer E., Rogl P., Schmid H., Giester G.,. "Ternary clathrates Ba–Cd–Ge: phase equilibria, crystal chemistry and physical properties;." *J. Phys.: Condens. Matter*, 2007: 046203.

Koblyuk-M. N., Grytsiv A., Fornasari L., Kaldarar H., Michor H., Röhrbacher F., Koza M., Royanian E., Bauer E., Rogl P., Rotter M., Schmid H., Marabelli F., Devishvili A., Doerr M., Giester G.,. "Ternary clathrates Ba–Zn–Ge: phase equilibria, crystal chemistry and physical properties." *J. Phys.: Condens. Matter*, 2007: 216223.

Koblyuk-M. N., Grytsiv A., Rogl P., Bauer E., Lackner R., Royanian E., Rotter M., Giester G.,. "Structure and Physical Properties of Clathrate I Systems Ba8PdxSi46-x and Ba8PtxSi46-x." *J. Phys. Soc. Jpn.*, 2008: 54-60.

Koblyuk-M. N., Grytsiv A., Rogl P., Rotter M., Bauer E., Durand G., Kaldarar H., Lackner R., Michor H., Royanian E., Koza M., Giester G.,. "Clathrate formation in the Ba-Pd-Ge system: Phase equilibria, crystal structure, and physical properties." *Phys. Rev. B*, 2007: 144118.

Koblyuk-M. N., Grytsiv A., Rogl P., Schmid H., Giester G.,. "The clathrate Ba8CuxGe46-x-y□y: Phase equilibria and crystal structure." *Journal of Solid State Chemistry*, 2009: 1754-1760.

Koblyuk-M. N., Rotter M., Grytsiv A., Rogl P., Lackner R., Bauer E., Fornasari L., Marabelli F., Giester G.,. "Structure and physical properties of type-I clathrate solid-solution Ba8PtxGe46−x−y□y (□=vacancy)." *Phys. Rev. B*, 2007: 195124.

Kosenko, V. A., and T. G., Zhidkova. ""“Synthesis and Some Chemical Properties of Iridium Boride IrB1.1." *Ukr. Khim. Zh.* 1, no. 40 (1974): 18-20.

Köster W., Meixner J.,. "Der Aufbau der Systeme des Europiums mit Silber, Kadmium und Indium sowie das System Kadmium-Strontium." *Z. Metallkd.,*, 1965: 695-703.

Kovnir K.A., Sobolev A.V., Presniakov I.A., Lebedev O.I., Van Tendeloo G., Schnelle W., Grin Y., Shevelkov A.V.,. "Sn19.3Cu4.7As22I8: a New Clathrate-I Compound with Transition-Metal Atoms in the Cationic Framework." *Inorg. Chem.*, no. 44 (2005): 8786-8793.

Kranenberg C., Mewis A.,. "ACu9X4 - Neue Verbindungen mit der CeNi8.5Si4.5-Struktur (A: Sr, Ba; X: Si, Ge)." *Z. Anorg. Allg. Chem.*, no. 629 (2003): 1023-1026.

Krupka M.C., Giorgi A. I., Krikorian N.H., Sklarz E.G.,. "High pressure synthesis and Superconducting properties of yttrium sesquicarbide." *J. Less-Common Metals*, no. 17 (1969): 91-98.

Krypyakevich P.I., Markiv V.Y., Melnyk Y.V.,. "Crystal Structures of the Compounds ZrNiAl, ZrCuGa and their Analogues." *Dopov. Akad. Nauk Ukr. RSR, Ser. A*, 1967: 750-753.

Kuentzler R., Dhar S. K., Malik S. K., Vijayaraghavan P. R., Boqlin R.,. "Valence change and nonmagnetic-magnetic transition in CePd3Bx alloys." *Solid State Communications* 2, no. 50 (1984): 145-150.

Kume T., Fukushima T., Sasaki S., Shimizu H., Fukuoka H., Yamanaka S.,. "Raman study of semiconductor clathrates under high pressure." *Phys. Stat. Sol. B* 1, no. 244 (2007): 352-356.

Kußmann D., Pöttgen R., Künnen B., Kotzyba G., Müllmann R., Mosel B. D.,. "Dimorphic YbPdSn with ZrNiAl and TiNiSi type structure." *Z. Kristallogr.*, no. 213 (1998): 356-363.

Kußmann D., Pöttgen R., Rodewald U. Ch., Rosenhahn C. , Mosel B. D., Kotzyba G., Künnen B.,. "Structure and Properties of the Stannide Eu2Au2Sn5, and its Relationship with the Family of BaAl4-Related Structures." *Z. Naturforsch.*, no. 54b (1999): 1155-1164.

Kuznetsov V.L., Kuznetsova L.A., Kaliazin A.E., Rowe D.M.,. "Preparation and thermoelectric properties of AII8BIII16BIV30 clathrate compounds." *J. Appl. Phys.*, no. 87 (2000): 7871.

Lackner R., Bauer E., Rogl P.,. "Study of the thermoelectric properties of CePd3Bx." *Physica B*, no. 378–380 (2006): 835-836.

Latini A., Rau J.V., Teghil R., Generosi A. , Albertini V.R. "Superhard properties of Rhodium and Iridium boride films." *Journal of Applied Materials and Interfaces* 2, no. 2 (2010): 581-587.

Lee W.H., Shelton R.N.,. "CePtSi: A new heavy-fermion compound." *Phys. Rev. B* 10, no. 35 (1987): 5369-5371.

Lejay P., Higashi I., Chevalier B., Etourneau J., Hagenmuller P.,. " Crystal structure of new superconducting materials LaIrSi3 and LaRhSi3. Structural relation between LaRh2Si2, La2Rh3Si5 and LaRhSi3." *Mat. Res. Bull.*, no. 19 (1984): 115-123.

Lenz J., Schubert K.,. " Über einige Leerstellen- und Stapelvarianten der Beta-Messing Strukturfamilie." *Z. Metallkunde*, no. 62 (1971): 810.

Levine J.B., Nguyen S.L., Brown S.E., Rasool H.I., Kaner R.B., Wright J.A.,. " Preparation and Properties of Metallic, Superhard Rhenium Diboride Crystals." *J. Am. Chem. Soc.*, no. 130 (2008): 16953–16958.

Levine J.B., Tolbert S.H., Kaner R.B.,. "Advances in the Search for Superhard Ultra-Incompressible Metal Borides." *Adv. Funct. Mater*, no. 19 (2009): 3519-3533.

Li D.C., Fang L., Deng S.K., Kang K.Y., Wie W.H., Ruan H.B.,. "Synthesis and first-principles calculations of the structural and electronic properties of type-I clathrates Sr8Ga16SnxGe30 − x." *Physica Status Solidi B* 7, no. 249 (2012): 1423–1430.

Li Q., Zhou D., Zheng W. , Ma Y.,. "Global structural optimization of tungsten borides." *PRL*, no. 110 (2013): 136403.

Li Y., Chi J., Gou W., Khandekar S., Ross J.H.,. " Structure and stability of Ba–Cu–Ge type-I clathrates." *J. Phys. Condens. Matter*, no. 15 (2003): 5535–5542.

Liang Y., Fu Z., Yuan X., Wang S., Zhong Z., Zhang W.,. "An unexpected softening from WB3 to WB4." *EPL*, no. 98 (2012): 66004.

Liang Y., Yuan X., Fu Z., Li Y., Zhong Z.,. " An unusual variation of stability and hardness in molybdenum borides." *Appl. Phys. Lett.*, no. 101 (2012): 181908.

Liang Y., Yuan X., Zhang W.,. "Thermodynamic identification of tungsten borides." *Phys. Rev. B*, no. 83 (2001): 220102.

Lin Q., Corbett J.D.,. " Formation of Nets of Corner-Shared Bicapped Gold Squares in SrAu3Ge: How a BaAl4-Type Derivative Reconciles Fewer Valence Electrons and the Origin of Its Uniaxial Negative Thermal Expansion." *J. Am. Chem. Soc.*, 2012: 4877−4884.

Lugscheider E., Knotek O., Reimann H.,. "Das Dreistoffsystem Nickel-Chrom-Bor." *Monatsh. Chem.*, no. 105 (1974): 80-90.

Lundström T. " The structure of Ru2B3 andWB2.0 as determined by single crystal diffractometry, and some notes on the W-B system." *Arkiv. Kemi.*, no. 30 (1969): 115-127.

Lundström T., Rosenberg I.,. " The Crystal Structure of the Molybdenum Boride Mo1-xB3." *J. Solid State Chem.*, no. 6 (1973): 299-305.

Lundström T., Tergenius L.E.,. "Refinement of the crystal structure of the Non-stoichiometric Moride IrB1.35 (approximate composition)." *Acta Chem. Scand.* 27 (1973): 3705-3711.

M. Falmbigl, P.F. Rogl,. *CRC Handbook of Thermoelectrics: Thermoelectrics and its Energy Harvesting.* RC Boca Raton, FL, USA,: D. M. Rowe, 2012.

M., Christensen, Johnson S., and Iversen B.B. "Thermoelectric clathrates of type I." *Dalton Trans.*, no. 39 (2010): 978-992.

Malik S. K., Dhar S. K., Vijayaraghavan P. R.,. "Studies on the valence state of Ce and Eu in some new boron and silicon containing rare earth intermetallic compounds." *Pramana*, no. 22 (1984): 329.

Martin J., Nolas G.S., Wang H., Yang J.,. "Thermoelectric properties of silicon-germanium type I clathrates." *J. Appl. Phys.*, no. 102 (2007): 103719.

Massa W. *Kristallstrukturbestimmung.* Edited by Vieweg und Teubler Verlag. Elschenbroich C., Hensel F., Hopf H., 2011.

Massalski T.B., Okamoto H., Subramanian P.R., Kacprzak L.,. *Binary alloy phase diagrams* . 2. Vol. 3. Ohio: ASM Internationa, 1990.

Materials Research Laboratory,. "X-ray basics." *Santa Barbara, UC.* 2014. http://www.mrl.ucsb.edu/centralfacilities/x-ray/basics.

May N., Schäfer H.,. „Neue Verbindungen im ThCr2Si2-Typ.“ *Z. Naturforsch. B*, 1972: 864-865.

Mayer I., Yetor P.D.,. "MPt2Si2 compounds of the ThCr2Si2 type." *J. Less-Comm. Met.*, no. 55 (1977): 171-176.

McArdle P., Gilligan K., Cunningham D., Dark R., Mahon M.,. "Oscail-X." *Cryst. Eng. Community*, no. 6 (2004): 303 – 309.

McCullough J.D., Brewer L., Bromley L.A.,. "The Crystal Structure of Zirconium Oxysulfide, ZrOS, ." *Acta Crystallogr.*, no. 1 (1948): 287-289.

Meissner W., Ochsenfeld R.,. "Ein neuer Effekt bei Eintritt der Supraleitfähigkeit." *Die Naturwissenschaften* 21, no. 44 (1933): 787-788.

Menke H., von Schnering H.G.,. "New clathrates of the type Ge38A8X8 with A= P, As, Sb and X= Cl, Br, I." *Naturwiss.* 9, no. 59 (1972): 420.

Merlo F., Fornasini M.L.,. "The Structures of α-CaCu, β-CaCu, SrAg and BaAg: Four Different Stacking Variants Based on Noble-Metal-Centred Trigonal Prisms." *Acta Crystallogr. B*, 1981: 500-503.

Merlo F., Fornasini M.L.,. "CrB-type equiatomic compounds of europium, ytterbium and alkaline-earth metals with Si, Ge, Sn, Pb,." *J. Less-Comm. Met.*, no. 13 (1967): 603-610.

—. "Crystal structure of the phases Sr3Ag2, Ca5Au3, Sr7Au3 and Sr7Ag3." *Rev. Chim. Miner.*, 1984: 273-281.

Merlo F., Pani M., Fornasini M.L.,. "RMX compounds formed by alkaline earths, europium and ytterbium. IV: Ternary phases with M= Ag and X= Si, Ge, Sn, Pb." *J. Alloys Compd.*, 1996: 289-295.

Meschel S.V., Kleppa O.J.,. " Enthalpies of formation of refractory borides of 5d elements by high temperature direct synthesis calorimetry: IrB1.35 and OsB2.5." *Journal of Alloys and Compounds*, 1991: 159-166.

Microscopy, Scanning Electron. "Cobham Technical Sevices." 2014. http://www.cobham.com/media/160745/rfa21_semedx_imaging_modes_4pg_041209.pdf.

Mihalisin P., Scoboria P., Ward J. A.,. *Valence Fluctuations in Solids.* Edited by North-Holand Pub. Co. Falicov L. M., Hanke W., Maple M.B. , 1981.

Miliyanchuk K., Kneidinger F., Blaas-Schenner C., Reith D., Podloucky R., Rogl P., Khan T., Salamakha L., Hilscher G., Michor H., Bauer E., Hillier A.D.,. "Platinum metal silicides and germanides: superconductivity in non-centrosymmetric intermetallics." *J. Phys.: Conf. Ser.*, no. 273 (2011): 012078.

Mohammadi R., Lech A.T., Xie M., Weaver B.E., Yeung M.T., Tolbert S.H., Kaner R.B.,. "Tungsten tetraboride, an inexpensive superhard material." *PNAS*, no. 108 (2011): 10958-10962.

Moore J.C., Grovenor C.R.M.,. *Handbook of Superconducting Materials, Volume 2.* Edited by IOP Publishing Ltd. Cardwell D. A., Ginley D. S.,, 2003.

Movshovich R., Graf T., Mandrus D., Thompson J.D., Smith J.L., Fisk Z.,. "Superconductivity in heavy-fermion CeRh2Si2." *Phys. Rev. B*, no. 53 (1996): 8241.

Mudryk Y., Rogl P., Paul C., Berger S., Bauer E., Hilscher G., Godart C., Noël H.,. "Thermoelectricity of clathrate I Si and Ge phases." *J. Phys. Condens. Matter*, no. 14 (2002): 7991–8004.

Mühlschlegel B. "Die thermodynamischen Funktionen des Supraleiters." *Z. f. Physik*, no. 155 (1959): 313 -327.

Nakano T., Ohashi M., Oomi G., Matsubayashi K., Uwatoko Y.,. "Pressure-induced superconductivity in the orthorhombic Kondo compound CePtSi2." *Phys. Rev. B*, no. 79 (2009): 172507.

Nasir N., Grytsiv A., Melnychenko-Koblyuk N, Rogl P., Bauer E., Lackner R., Royanian E., Giester G., Saccone A.,. "Clathrates Ba8{Zn,Cd}xSi46−x, x~7: synthesis, crystal structure and thermoelectric properties." *J. Phys.: Condens. Matter*, 2009: 385404.

Nasir N., Melnychenko-Koblyuk N., Grytsiv A., Rogl P., Giester G., Wosik J., Nauer G. E.,. "Ternary systems Sr–{Ni,Cu}–Si: Phase equilibria and crystal structure of ternary phases." *Journal of Solid State Chemistry*, 2010: 565-574.

Nesper R., Curda J., von Schnering H.G.,. "Ge4.06I, ein unerwartetes Germaniumsubiodid – ein Tetragermanioiodonium(III)-iodid mit Clathratstruktur [Ge46-xIx]I8, X=8/3." *Angew. Chemie* 4, no. 98 (1986): 369-370.

Nesper R., Zürcher F.,. " Redetermination of the crystal structure of pentastrontium trisilicide, Sr5Si3." *Z. Kristallogr., New Cryst. Struct.*, 1999: 19.

Nielsen J.A., McMorrow D.,. *Elements of Modern X-ray Physics.* Edited by Ltd. John Wiley & Sons. West Sussex, United Kingdom, 2001.

Nieva G.L. *PhD Thesis.* Instituto Balseiro, Universidad Nacional de Cuyo, 1988.

Norton J.T., Blumenthal H., Sindeband S.J.,. "Structure of Diborides of Titanium, Zirconium, Columbium, Tantalum and Vanadium." *Trans. Am. Inst. Min. Metall. Pet. Eng.*, no. 185 (1949): 749-751.

Nowotny H., Haschke H., Benesovsky F.,. "Bor-reiche Wolframboride, Boron rich tungsten borides." *Monatsh. Chem.*, no. 98 (1967): 547-554.

Okamoto H. "Ba-Ge Phase diagram." *Journal of Phase Equilibria and Diffusion* 1, no. 30 (2009): 114.

Okamoto N.L., Oh M.W., Nishii T., Tanaka K., Inui H.,. "Crystal structure and thermoelectric properties of the type-I clathrate compound Ba8Ge43 with an ordered arrangement of Ge vacancies." *J. Appl. Phys.*, no. 99 (2006): 033513.

P. Rogl.,. *Phase Diagrams of Ternary Metal-Boron-Carbon Systems.* ASM International, Materials Park, Ohio 44043: Günter Effenberg, 1988.

Palenzona A., Bonino G.B.,. "Su alcune nuove fasi di formula MX5 dell'Eu e dell'Yb aventi struttura tipo CaCu5." *Atti Accad. Naz. Lincei, Cl. Sci. Fis., Mat. Nat., Rend.,*, 1967: 504-509.

Palenzona A., Pani M.,. "The phase diagram of the Sr–Ge system." *Journal of Alloys and Compounds*, 2005: 136–140.

Palenzona A., Pani M.,. "The phase diagram of the Sr–Si system." *Journal of Alloys and Compounds*, 2004: 214–219.

Palenzona, A., Cirafici, S., Canepa, F.,. "High temperature behaviour of unstable EuPd2Si2 and reference MPd2Si2 compounds (M ≡ All rare earths and alkaline earths)." *J. Less-Comm. Met.*, no. 135 (1987): 185-194.

Pani M., Fornasari M.L., Manfrinetti P., Merlo F., Intermetallic compounds in the M–Cu–Sn systems with M = Eu, Sr, Ba,). *Intermetallics*, no. 19 (2011): 957.

Pani M., Merlo F., Fornasari M.L.,. "Intermetallic Phases in the Ca-Cu-Sn System." *Z. Anorg. Allg. Chem.*, no. 633 (2007): 1581-1586.

Pani M., Palenzona A.,. "The Phase Diagram of the Ba-Ge System." *J. Alloy. Compds*, no. 462 (2008): 9-11.

Parthe E., Klepp K.,. "LaIrSi with an Ordered SrSi2 Derivative Structure." *Acta Cryst. B*, no. 38 (1982): 1541-1544.

Parthé E., Rieger W.,. "Ternäre Erdalkali- und Seltene Erdmetall-Silicide und -Germanide mit ThCr2Si2-Struktur." *Monatsh. Chem.*, no. 100 (1969): 444-454.

Paschen S., Budnyk S., Köhler U., Prots Yu., Hiebl K., Steglich F., Grin Yu.,. "New type-I clathrates with ordered Eu distribution." *Physica B: Condens. Matter*, no. 383 (2006): 89-92.

Paschen S., Carrillo-Cabrera W., Bentien A., Tran V.H., Baenitz M., Grin Yu., Steglich F.,. "Structural, transport, magnetic, and thermal properties of Eu8Ga16Ge30." *Phys. Rev. B*, no. 64 (2001): 214404.

Percharskij V.K., Pankevich Ju.V., Bodak O.I.,. " The crystal structure of new antimonides 't-CeNi2Sb2' and 'p-CeNi2+Sb2-." *Dopov. Akad. Nauk. Ukr. RSR, Seriya B,*, no. 4 (1982): 44-48.

Perez I., Croft M., Liang G., Zhou J. B., Shaheen S. A., Jhans H.,. " Resistivity effects in the Ce(Pd,Rh)3B1 and Ce(Rh,Ru)3B2 system." *J. Appl. Phys.* 8, no. 61 (1987): 3180.

Petrovic C., Movshovich R., Jaime M., Pagliuso P.G., Hundley M.F., Sarrao J. L., Fisk Z., Thompson J.D.,. "A new heavy-fermion superconductor CeIrIn5: A relative of the cuprates? ." *Europhys. Lett.*, no. 53 (2001): 354.

Petrovic C., Pagliuso P.G., Hundley M.F., Movshovich R., Sarrao J.L., Thompson J.D., Fisk Z., Monthoux P.,. "Heavy-fermion superconductivity in CeCoIn5 at 2.3K." *J. Phys.: Cond. Mat.*, no. 13 (2001): L337.

Philipp F., Schmidt P.,. "The cationic clathrate Si46−2xP2xTex crystal growth by chemical vapour transport." *J. Crystal Growth*, no. 310 (2008): 5402-5408.

Pountney J. M., Winterbottom J. M., Harris I. R.,. " A comparison of the electronic and crystal structure of some CeRh3-xPdx and ZrRh3Pdx alloys and the catalytic behavior of some CeRh3-xPdx alloys." *Inst. Phys. Conf. Ser.*, no. 37 (1978): 85-91.

Pringle G.E. "The Structure of SrSi2: a Crystal of Class O." *Acta Crystallogr. B*, no. 28 (1972): 2326-2328.

Qiu L., Swainson I.P., Nolas G.S., White M.A.,. "Structure, thermal, and transport properties of the clathrates Sr8Zn8Ge38, Sr8Ga16Ge30, and Ba8Ga16Si30." *Phys. Rev. B*, no. 70 (2004): 035208.

Ramakrishnan S., Ghos K., Chinchure A.D., Marathe V.R., Chandra G.,. "Magnetism and superconductivity in RPtSi (R=La, Ce, Nd, and Sm)." *Phys. Rev. B* 9, no. 52 (1995): 6784-6795.

Rau J.V., Latini A. “New Hard and Superhard Materials: RhB1.1 and IrB1.35.” *Chemistry of Materials* 21, no. 8 (2009): 1407-1409.

Reinacher G. "Hot-stage Microscope Determination of the Solidus Temperatures of Iridium Alloys with about 1 wt.% Boron, Phosphorus or Silicon." *Metall*, 1965: 707-711.

Riedel R. "Novel Ultrahard Materials." *Adv. Mater.*, no. 6 (1994): 549–560.

Rieger W., Parthé E.,. "Ternäre Erdalkali- und Seltene Erd-Silicide und -Germanide mit AlB2-Struktur." *Monatsh. Chem.*, no. 100 (1969): 439-443.

Rocktäschel G., Weiss A.,. "Zur Kenntnis der Strontiumsilicide." *Z. Anorg. Allg. Chem.*, 1962: 231-236.

Rodriguez-Carajalv J.,. "Recent Developments of the Program FULLPROF." *Physica B*, 1993: 192.

Rodriguez-Carvajal J.,. "FULLPROF Manual." 2006. http://www.ill.eu/sites/fullprof/php/tutorials.html.

Rogl P.,. *Existence and Crystal Chemistry of Borides, in Inorganic Reactions and Methods: Formation of Bonds to Group-I, -II, and -IIIB Elements.* Edited by Inc. John Wiley & Sons. Vol. 13. Hoboken, NJ,: John Wiley & Sons, Inc., 1991.

Rogl P.,. *Phase Diagrams of Ternary Metal-Boron-Carbon Systems.* Edited by Günter Effenberg. Materials Park, Ohio 44043: ASM International, 1988.

Rogl P., Benesovsky F., Nowotny H.,. „Komplexboride mit ReB2 Struktur.“ *Monatsh. Chem.*, Nr. 101 (1970): 27-31.

Rogl P., Nowotny H., Benesovsky F.,. "Complex Borides with Platinum Metals." *Monatsh. Chem.*, no. 103 (1972): 965-989.

Rogl P., Nowotny H., Benesovsky F.,. "Ein Beitrag zur Strukturchemie der Iridiumboride." *Monatsh. Chem.*, 1971: 678-686.

Rogl P., Nowotny H., Benesovsky F.,. „Ternary Complex Borides in the Systems: {Mo, W}-{Ru, Os}-B and W-Ir-B.“ *Monatsh. Chem.*, Nr. 101 (1970): 850-854.

Rogl P., Rudy E.,. "New complex borides with ReB2- and Mo2IrB2-type structure." *J. Solid State Chem.* 2, no. 24 (1978): 175-181.

Romaka V.V., Falmbigl M., Grytsiv A., Rogl P.,. "The systems Sr-Zn-{Si,Ge}: phase equilibria and crystal structure of ternary phases." *J. Solid State Chem.*, 2012: 87-93.

Romaka V.V., Falmbigl M., Grytsiv A., Rogl P.,. "The Sr-poor part of the Sr–{Pd,Pt}–{Si,Ge} systems: Phase equilibria and crystal structure of ternary phases." *Journal of Alloys and Compounds*, 2015: 656–665.

Romans P. A., Krug M. P.,. "Composition and crystallographic data for the highest boride of tungsten." *Acta Crystallogr.*, no. 20 (1966): 313-315.

Roof R.B. Jr., Kempter C.P.,. "New Orthorhombic Phase in the Ru-B and Os-B Systems." *J. Chem. Phys.*, no. 37 (1962): 1473-1476.

Roudebush J.H., Toberer E.S., Hope H., Snyder G.F., Kauzlarich S.M.,. "Crystal structure, characterization and thermoelectric properties of the type-I clathrate Ba8−ySryAl14Si32 (0.6≤y≤1.3) prepared by aluminum flux." *J. Solid State Chem.*, no. 184 (2011): 1176-1185.

Rudy E., Benesovsky F., Toth L.,. "The Investigation of the ternary systems of the group V and VI Metals with Boron and Carbon." *Z. Metallkd.*, no. 54 (1963): 345-353,.

Rudy E., Windisch W. *The Systems Mo-B and W-B,*. Vols. AFML-TR-2, Part I, Vol. III. Wright Patterson Air Force Base, OH, USA,, 1965.

Sales B.C., Chakoumakos B.C., Jin R., Thompson J.R., Mandrus D.,. "Structural, magnetic, thermal, and transport properties of X8Ga16Ge30 (X=Eu, Sr,Ba) single crystals." *Phys. Rev. B*, no. 63 (2001): 245113.

Samsonov G.V., Kosenko V.A., Rud' B.M., Sidorova V.G. "Preperation and Properties of the Compound IrB1.1." *Inorg. Mater. (Transl. of Neorg. Mater.)* 8 (1972): 671-672.

Saparov B., Sefat A.S.,. "Metallic properties of Ba2Cu3P4 and BaCu2Pn2 (Pn=As, Sb)." *Journal of Solid State Chemistry*, no. 191 (2012): 213–219.

Schäfer M.C., Yamasaki Y., Fritsch V., Bobev S.,. "Synthesis and Structural Characterization of ACu9Tt4 (A = Ca, Sr, Ba, Eu; Tt= Si, Ge, Sn) – Tetragonally Distorted Ternary Variants of the Cubic NaZn13 Structure Type. Improved Structure Refinement of SrCu2Ge2." *Zeitschrift für anorganische und allgemeine Chemie* 7-8, no. 638 (2012): 1204–1211.

Schäfer M.C., Yamasaki Y., Fritsch V., Bobev S.,. "Ternary Compounds in the Sn-Rich Section of the Ba–Ga–Sn System: Ba8Ga16–xSn30+x (1.1 ≤ x ≤ 2.8) Clathrates of Type-I and Type-VIII, and BaGa2–xSn4+x (x ≈ 0.2) with a Clathrate-like Structure." *Crystals* 3, no. 1 (2011): 145-162.

Schubert K., Brandauer G.,. "Zum Aufbau des Systems Kupfer-Germanium." *Z. Metallkunde*, no. 43 (1952): 262.

Schubert K., Breimer H., Burkhardt W., Günzel E., Haufler R., Lukas H.L., Vetter H., Wegst J., Wilkens M.,. " Einige strukturelle Ergebnisse an metallischen Phasen II." *Naturwiss.*, no. 44 (1957): 229-230.

Sereni J. G. *Proc. Valence Instabilities.* North Holland: Wachter E., Boppart T.,, 1982 .

Sereni J. G., Schmerber G., Kappler J. P.,. "Thermodynamic Behavior of Ce Compounds Close to a T-> 0 Critical Point." *IEEE Transaction on Magnetics*, no. 49 (2013): 4647.

Sereni J., Nieva G., Kappler J. P., Besnus M. J., Meyer A.,. " Low-temperature thermal properties in the CePd3Bx system." *J. Phys. F: Met. Phys.*, no. 16 (1986): 435.

Sheldon E.A., King A.J.,. "Structure of the allotropic forms of strontium." *Acta Crystallographica*, 1953: 100.

Sheldrick G. M. "Program SHELX-97 for Crystal Structure Determination." University of Goettingen, 1997.

Sheldrick, G.M. "SHELXS-97." *Acta Cryst*, no. A46 (1990): 467-473.

Shevelkov A.V., Kovnir K.,. *Structure Bonding.* Vol. 990. Berlin: Springer, 2011.

Shiotsuki M., Motoyama G., Oda Y., Yamaguchi A., Sumiyama A., Takeuchi T., Settai R., Ōnuki Y.,. "Specific Heat on the Non-centrosymmetric Superconductor LaPt3Si." *J. Phys. Soc. Jpn.*, no. 80 (2011): SA070.

Shishido T., Sugawara T., Obara K., Sahara R., Yubuta K., Kojima H., Kumar V., Tanaka M., Shimamura K., Oishi S., Kohiki S., Oku M., Kawazoe Y., Nakajima K., Ye J., Okada S., Kudou K., Iizumi K., Sawada Y., Ishizawa Y., Nomura A.,. "Boron nonstoichiometry, hardness and oxidation resistance of perovskite-type CeRh3Bx (x = 0–1)." *Journal of Alloys and Compounds*, no. 426 (2006): 304-307.

Sigrist M. *Lectures on the physics of strongly correlated systems.* Edited by American Institute of Physics AIP Conference Proceedings 789. A. Avella, F. Mancini, 2005.

Sigrist M., Agterberg D.F., Frigeri P.A., Hayashi N., Kaur R.P., Koga A.,. "Superconductivity in non-centrosymmetric materials." *Journal of Magnetism and Magnetic Materials*, no. 310 (2007): 536-540.

Sigrist M., Ueda K.,. "Phenomenological theory of unconventional superconductivity." *Rev. Mod. Phys.*, no. 63 (1991): 239.

Simonson J.W., Wu D., Poon S.J., Wolf S.A.,. " Superconductivity in Transition Metal Doped MoB4." *J. Supercond. Nov. Magn.*, no. 23 (2010): 417–422.

Slack G.A. *CRC Handbook of Thermoelectrics.* Edited by CRC Press. Boca Raton, FL: Rowe D.M., 1995.

Smid I., Rogl P.,. "Phase Equilibria and Structural Chemistry in Ternary Systems: Transition Metal-Boron-Nitrogen." Edited by Adam Hilger Ltd. *Science of Hard Materials, Inst. Phys. Conf. Ser.*, no. 75 (1986): 249-257.

Sologub O., Rogl P., Salamakha L. P., Bauer E., Hilscher G., Michor H., Giester G.,. " On phase equilibria and crystal structures in the systems Ce-Pd-B and Yb-Pd-B. Physical properties of R2Pd13.6B5 (R=Yb, Lu)." *J. Solid State Chem.*, no. 183 (2010): 1013-1037.

Spear K.E. "Correlations and Predictions of Metal-Boron Phase Equilibria." Edited by Natl. Bur. Stand. *Proc. of a Workshop held in Gaithersburg.* Gaithersburg: Spec. Publ. SP-496, 1977.

Steglich F., Aarts J., Bredl C. D., Lieke W., Meschede D., Franz W., Schäfer H.,. "CeCu2Si2, Superconductivity in the Presence of Strong Pauli Paramagnetism." *Phys. Rev. Lett.*, no. 43 (1979): 1892.

Sugitani I., Okuda Y., Shishido H., Yamada T., Thamizhavel A., Yamamoto E., Matsuda, Y. Haga T.D., Takeuchi T., Settai R., Onuki Y.,. "Pressure-Induced Heavy-Fermion Superconductivity in Antiferromagnet CeIrSi3 without Inversion Symmetry." *J. Phys. Soc. Japan*, no. 75 (2006): 043703.

Swaminathan P. "Course on Materials Characterization." 2013. http://mme.iitm.ac.in/swamnthn/.

Taetum E., Gschneidner K., Waber J.,. *The Crystal Chemistry and Physics of Metals and Alloys,*. Edited by Wiley-Interscience. New York, USA: Pearson W.B., 1972.

Takahashi S., Fukuoka H., Yamanaka S., Chen X.,. "High pressure sythesis of BaAu2Si2." *Nippon Kagakkai Koen Yokoshu*, no. 79 (2001): 268.

Takei H., Shishido T.,. "Rare earth rhodium borides with the perovskite structure." *Less-Common Met.*, no. 97 (1984): 223-229.

Takimoto T., Thalmeier P.,. "Triplet Cooper Pair Formation by Anomalous Spin Fluctuations in Non-centrosymmetric Superconductors." *J. Phys. Soc. Japan*, no. 78 (2009): 103703.

Takimoto T., Thalmeier P.,. "Triplet Cooper pairing by spin fluctuations peculiar to non-centrosymmetric System." *Physica C*, no. 470 (2010): 566.

Tay C. Y., Harris I. R.,. "The effects of different sample preparations and hydrogenation on the properties of some CeRh3−xPdx." *J. Less-Common Met.*, no. 53 (1977): 177-192.

Tkachuk A.V., Mar A.,. "Electron-poor SrAuxIn4−x (0.5⩽x⩽1.2) and SrAuxSn4−x (1.3⩽x⩽2.2) phases with the BaAl4-type structure." *J. Solid State Chem.*, no. 180 (2007): 2298–2304.

Toberer E.S., May A.F., Snyder G.J.,. "Zintl Chemistry for Designing High Efficiency Thermoelectric Materials." *Chem. Mater.*, no. 22 (2010): 624-634.

Togano K., Badica P., Nakamori Y., Orimo S., Takeya H., Hirata K.,. "Superconductivity in the Metal Rich Li-Pd-B Ternary Boride." *Phys. Rev. Lett.*, no. 93 (2004): 247004.

Tse J. S., Itaka T., Kume T., Shimizu H., Parlinski K., Fukuoka H.,Yamanaka S.,. "Electronic structure and vibrational properties of Ba8Si46, Ba8AgnSi46−n, and Ba8AunSi46−n." *Phys. Rev. B*, no. 72 (2005): 155441.

Tsujii N., Roudebush J.H., Zevalkink A., Cox-Uvarov C.A., Snyder G.J., Kauzlarich S.M.,. "Phase stability and chemical composition dependence of the thermoelectric properties of the type-I clathrate Ba8AlxSi46−x (8≤x≤15)." *J. Solid State Chem.*, no. 184 (2011): 1293-1303.

Turban K., Schaefer H.,. "Preparation and Crystal Structure of Ba2Ge." *Zeitschrift fuer Naturforschung B*, no. 28 (1973): 220-222.

V.V. Brazhkin, A.G. Lyapin, and R.J. Hemley,. "Harder than diamond: Dreams and reality." *Phil. Mag.*, no. 82 (2002): 231-253.

Van der Auwera-Mahieu A., Peeters R., McIntyre N.S., Drowart J.,. "Mass spectrometric determination of dissociation energies of the borides and silicides of some transition metals." *Transactions of the Faraday Society* 4, no. 66 (1970): 809-816.

Vandenberg J. H., Matthias B. T., Corenzwit E., Barz H.,. "Superconductivity of some Binary and Ternary Transition Metal Borides." *Mat. Res. Bull.*, 1975: 889-894.

Vaughey J.T., Miller G.J., Gravelle S., Leon Escamilla E.A., Corbett J.D.,. "Synthesis, Structure, and Properties of BaGe2: A Study of Tetrahedral Cluster Packing and Other Three-Connected Nets in Zintl Phases." *J. Solid State Chem.*, no. 133 (1997): 501-507.

Veprek S. "The Search for Novel Ultrahard Materials." *J. Vac. Sci. Technol. A*, no. 17 (1999): 2401–2420.

Villars P., Cenzual K.,. *Pearson's Crystal Data CD-ROK,.* ASM International, Ohio, USA, 2013/14.

Von Schnering H.G., Bolle U.M., Curda J., Carrillo Cabrera W., Peters K., Somer M., Schultheiss M., Wedig U., Von Schnering H.G.,. "Hückel Arenes with Ten π Electrons: Cyclic Zintl Anions Si610-, Isosteric to P6(4-) and As6(4-)." *Angew. Chem.* 108 (1996): 1062-1064.

W. Carrillo-Cabrera, H. Borrmann, S. Paschen, M. Baenitz, F. Steglich, Y. Grin,. "Ba6Ge25: low-temperature Ge–Ge bond breaking during temperature-induced structure transformation." *J. Solid State Chem.* 3, no. 178 (2005): 715-728.

Wacha W. "Program STRUKTURE, Diploma Thesis." TU Wien, 1989.

Wang D.Y., Wang B. , Wang X.Y. "New Crystal Structures of IrB and IrB2: First-Principles Calculations." *Journal of physical chemistry C*, 2012: 21961-21966.

Wang Y., Chen W., Chen X., Liu H.Y., Ding Z.H., Ma Y.M., Wang X.D., Cao Q.P., Jiang J.Z. "Crystal structures, stability, electronic and elastic properties of 4d and 5d transition metal monoborides: First-principles calculations." *Journal of Alloys and Compounds*, 2012: 115-124.

Weibke F. "The Ba-Ag System." *Z. Anorg. Chem.*, no. 193 (1930): 296.

Widera A., Eisenmann B., Schäfer H.,. „Darstellung und Kristallstruktur des Sr2Si." *Z. Naturforsch. B*, 1976: 520-521.

Wilson A. H. *Proc. R. Soc. Lond. A*, no. 167 (1938): 580.

Wuilloudt E., Schneidert W. D., Delley B., Baer Y., Hulliger F.,. "Boron induced changes in the electronic structure of CePd3." *J. Phys. C: Solid State Phys.*, no. 17 (1984): 4799-4806.

Yamanaka S., Enishi E., Fukuoka H., Yasukawa M.,. "High-Pressure Synthesis of a New Silicon Clathrate Superconductor Ba8Si46." *Inorg. Chem.*, no. 39 (2000): 56.

Yan X., Giester G., Rogl P.F., Paschen S.,. " Ba-Cu-Si clathrates: Phase equilibria and crystal chemistry." *Journal of Electronic Materials*, 2010: 1634 - 1639.

Yuan H. Q., Agterberg D. F., Hayashi N., Badica P., Vandervelde D., Togano K., Sigrist M., Salamon M. B.,. "S-Wave Spin-Triplet Order in Superconductors without Inversion Symmetry: Li2Pd3B and Li2Pt3B." *Phys. Rev. Lett.*, no. 97 (2006): 017006.

Yubuta K., Nomura A., Nakaijma K., Shishido T.,. "Crystal structure of a Cu3Au-type compound CeRh3B0.5 studied by high-resolution electron microscopy." *Journal of Alloys and Compounds*, no. 426 (2006): 308–311.

Yubuta K., Nomura A., Yamamura T., Shishido T.,. "Anomalous behavior of hardness and crystal structure in CeRh3Bx (x = 0–1) phase." *Journal of Alloys and Compounds*, no. 451 (2008): 301-304.

Zaikina J. V., Kovnir K.A., Haarmann F., Schnelle W., Burkhardt U., Borrmann H., Schwarz U., Grin Y., Shevelkov A.V.,. "The First Silicon-Based Cationic Clathrate III with High Thermal Stability: Si172−xPxTey (x=2y, y>20)." *Chem. Eur. J.* 18, no. 14 (2008): 5414.

Zaikina J.V., Kovnir K.A., Burkhardt U., Schnelle W., Haarmann F., Schwarz U., Grin Yu., Shevelkov A.V.,. "Cationic Clathrate I Si46-xPxTey (6.6(1) ≤ y ≤ 7.5(1), x ≤ 2y): Crystal Structure, Homogeneity Range, and Physical Properties." *Inorg. Chem.*, no. 48 (2009): 3720-3730.

Zang C., Sun H., Chen C.,. "Unexpectedly low indentation strength of WB3 and MoB3 from first principles." *Phys. Rev. B*, no. 86 (2012): 180101.

Zeiringer I., Bauer E., Grytsiv A., Rogl P., Effenberger H.,. "Phase Equilibria, Crystal Chemistry, and Physical Properties of Ag-Ba-Si Clathrates ." *Japanese Journal of Applied Physics*, 2011: 05FA01.

Zeiringer I., Chen M.X., Bauer E., Podloucky R., Grytsiv A., Rogl P., Effenberger H.,. "The Ternary System Au-Ba-Si: Clathrate Compound, Electronic Structure, Physical Properties, Phase Equilibria and Crystal Structures." *Acta Materialia*, 2012: 2324-2336.

Zeiringer I., Chen M.X., Bednar I., Royanian E., Bauer E., Podloucky R., Grytsiv A., Rogl P., Effenberger H.,. "Phase Equilibria, Crystal Chemistry, Electronic Structure and Physical Properties of Ag – Ba – Ge Clathrates." *Acta. Mater.*, 2011: 2368-2384.

Zeiringer I., Grytsiv A., Brož P., Rogl P.,. " Liquidus projection of the Ag–Ba–Ge system and melting points of clathrate type-I compounds." *Journal of Solid State Chemistry*, no. 196 (2012): 125–131.

Zeiringer I., Grytsiv A., Kneidinger F., Royanian E., Bauer E., Giester G., Falmbigl M., Rogl P.,. "Clathrate formation in the systems Sr-Cu-Ge and {Ba,Sr}-Cu-Ge;." *Journal of Solid State Chemistry*, 2014: 169-179.

Zeiringer I., Melnychenko-Koblyuk N., Grytsiv A., Bauer E., Giester G., Rogl P.,. "Phase Equilibria, Crystal Chemistry and Physical Properties of Au – Ba – Ge Clathrates." *Journal of Phase Equilibria and Diffusion*, 2011: 115-122.

Zeiringer I., Rogl P., Polt J., Grytsiv A., Giester G., Bauer E.,. "Crystal Structure of W1-xB3 and Phase Equilibria in the Boron-rich Part of the Systems Mo-Rh-B and W-{Ru,Os,Rh,Ir,Ni,Pd,Pt}-B." *Journal of Phase equilibria and Diffusion* 4, no. 35 (2014): 384-395.

Zeiringer I., Sereni J. G., Berisso M. G., Yubuta K., Rogl P., Grytsiv A., Bauer E.,. "Crystal structure and Ce valence variation in the solid solution CeRh3-xPdxB0.5." *Materials Research Express*, no. 1 (2014): 016101.

Zhang H., Borrmann H., Oeschler N., Candolfi C., Schnelle W., Schmidt M., Burkhardt U., Baitinger M., Zhao J.T., Grin Y.,. "Atomic Interactions in the p-Type Clathrate I Ba8Au5.3Ge40.7." *Inorg. Chem.* 4, no. 50 (2011): 1250–1257.

Zhang R.F., Legut D., Lin Z.J., Zhao Y.S., Mao H.K., Veprek S.,. "Stability and Strength of Transition-Metal Tetraborides and Triborides." *PRL*, no. 108 (2012): 255502.

Zhang Y., Lee P.L., Nolas G.S., Wilkinson A.P.,. " Gallium distribution in the clathrates Sr8Ga16Ge30 and Sr4Eu4Ga16Ge30 by resonant diffraction." *Appl. Phys. Letters* 16, no. 80 (2002): 2931-2933.

Zhao W.J., Wang J.X. "Structural, mechanical, and electronic properties of TaB2, TaB, IrB2, and IrB: First-principle calculations; Journal of Solid State Chemistry." 2009: 1280-1286.

Zhong W.X., Chevalier B., Etourneau J.R., Hagenmuller P.,. "Crystal structure and superconductivity of new ternary MTGe germanides (M= Ti, Zr, Hf and T= Ru, Os, Rh, Ir)." *Mater. Res. Bull.* 22 (1987): 331-336.

Zivkovic D., Stuparevic L.,. "Calculations of the thermodynamic properties in the Ir-B system based on the known phase diagram." *RMZ- Materials and Geoenvironmen*, 2005: 463-468.

Zmii O.F., Gladyshevskii E.I.,. "Crystal structure of CeMg2Si2." *Sov. Phys. Crystallogr.*, no. 15 (1971): 817-819.

Zuercher F., Nesper R.,. "Ba3Ge4: Polymerization of Zintl Anions in the Solid and Bond Stretching Isomerism." *Angew. Chem. Int. ed.*, no. 37 (1998): 3314-3318.

Zumdick M. F., Pottgen R.,. "Determination of the superstructures for the stannides ZrlrSn, HfCoSn, and HfRhSn." *Z. Kristallogr.*, no. 214 (1999): 90-97.

Curriculum Vitae

First name:	Isolde
Surname:	Zeiringer
Title:	Mag.rer.nat.
Date of birth:	21.2.1983
Personal Status:	Married, 1 Daughter
Address:	Alszeile 117/32; 1170 Wien

Education

April 2010 – actual	PhD Thesis on "Non-centrosymmetric superconductors" in the working group of Prof. Peter Franz Rogl at the Institute of Physical Chemistry (University of Vienna, supported by the Austrian Science Fund (FWF))
2001 – 2010	Chemistry studies at the University of Vienna, focusing on material science Diploma Thesis: „The clathrates $Ba_8TM_xGe_{46-x-y}\square_y$ and $Ba_8TM_xSi_{46-x}$ (TM=Ag, Au): phase equilibria and physical properties" at the Institute of Physical Chemistry, University of Vienna Master degree: 27.03.2010
2000 – 2008	Student trainee/worker at Treibacher Industrie AG (each year in July/August)
1993 – 2001	Grammar school (Bundesreal Gymnasium St. Veit/Glan)
1989 – 1993	Primary school (Volksschule Kappel/Krappfeld)

List of publications

1) I. Zeiringer, A. Grytsiv, E. Bauer, G. Giester, P. Rogl; *Phase relations and crystal structures in the ternary systems Sr-{Ag,Au}-{Si,Ge}*; to be submitted
2) I. Zeiringer , P. Rogl, E. Bauer, G. Giester; *Crystal Structures and Constitution of the Binary System Ir-B*; to be submitted
3) F. Kneidinger, L. Salamankha, I. Zeiringer, E. Bauer, P. Rogl, C. Blaas-Schenner, D. Reith, R. Podloucky: *Superconductivity in non-centrosymmtric $BaAl_4$ derived structures*. Physical Review B 07/2014; 90(024504).
4) I. Zeiringer, P. Rogl, J. Polt, A. Grytsiv, G. Giester, E. Bauer: *Crystal Structure of $W_{1-x}B_3$ and Phase Equilibria in the Boron-rich Part of the Systems Mo-Rh-B and W-{Ru,Os,Rh,Ir,Ni,Pd,Pt}-B*. Journal of Phase Equilibria and Diffusion 03/2014; 35(4):384-395.
5) I. Zeiringer, J. G. Sereni, M. G. Berisso, K. Yubuta, P. Rogl, A. Grytsiv, E. Bauer: *Crystal structure and Ce valence variation in the solid solution $CeRh_{3-x}Pd_xB_{0.5}$*. Materials Research Express. 01/2014; 1(016101).

6) I. Zeiringer, R. Moser, F. Kneidinger, R. Podloucky, E. Royanian, A. Grytsiv, E. Bauer, G. Giester, M. Falmbigl, P. Rogl: *Clathrate formation in the systems Sr–Cu–Ge and {Ba,Sr}–Cu–Ge*. Journal of Solid State Chemistry 01/2014; 217:169–179.
7) F. Kneidinger, H. Michor, A. Sidorenko, E. Bauer, I. Zeiringer, P. Rogl, C. Blaas-Schenner, D. Reith, R. Podloucky: *Synthesis, characterization, electronic structure, and phonon properties of the noncentrosymmetric superconductor LaPtSi*. Physical Review B 09/2013; 88(10):104508.
8) I. Zeiringer, A. Grytsiv, P. Brož, P. Rogl: *Liquidus projection of the Ag–Ba–Ge system and melting points of clathrate type-I compounds*. Journal of Solid State Chemistry 12/2012; 196:125–131.
9) I. Zeiringer, MingXing Chen, A. Grytsiv, E. Bauer, R. Podloucky, H. Effenberger, P. Rogl: *The ternary system Au–Ba–Si: Clathrate solution, electronic structure, physical properties, phase equilibria and crystal structures*. Acta Materialia 03/2012; 60(5):2324–2336.
10) I. Zeiringer, N. Melnychenko-Koblyuk, A. Grytsiv, E. Bauer, G. Giester, P. Rogl: *Phase Equilibria, Crystal Chemistry and Physical Properties of Au-Ba-Ge Clathrates*. Journal of Phase Equilibria and Diffusion 01/2011; 32(2):115-127.
11) I. Zeiringer, E. Bauer, A. Grytsiv, P. Rogl, H. Effenberger: *Phase Equilibria, Crystal Chemistry, and Physical Properties of Ag-Ba-Si Clathrates*. Japanese Journal of Applied Physics 01/2011; 50:5.
12) I. Zeiringer, MingXing Chen, I. Bednar, E. Royanian, E. Bauer, R. Podloucky, A. Grytsiv, P. Rogl, H. Effenberger: *Phase equilibria, crystal chemistry, electronic structure and physical properties of Ag–Ba–Ge clathrates*. Acta Materialia 01/2011; 59(6):2368-2384.

Conference contributions

1) *The clathrates $Ba_8T_xGe_{46-x-y}\square_y$ and $Ba_8T_xSi_{46-x}$ (T = Ag, Au; □ = vacancy): phase equilibria and physical properties*; International Conference on Solid Compounds of Transition Elements (SCTE 2010); Annecy, France; 5.-10.9.2010
2) *Thermoelectric Clathrates: $Ba_8(Ag,Au)_x(Si,Ge)_{46-x-y}\square_y$*; Advanced Research Workshop: New materials for thermoelectric applications: theory and experiment; Hvar, Croatia, 2. – 7.10.2010
3) *The Ternary Systems Ba-Au-Ge and Ba-Au-Si: Clathrate Compounds and Physical Properties, Phase Equilibria and Crystal Structures*; XIII Scientific Conference "Lviv Chemical Readings-2011", Ukraine, 28.5-2.6.2011
4) *Formation and homogeneity range of the clathrates type-I in the ternary systems (Sr, Ba)-(Ag, Au)-(Si, Ge)*; European Conference on Thermoelectrics (ECT 2011); Thessaloniki, Greece; 28.-30.9.2011
5) *Thermoelectric Clathrates: $Ba_8(Ag,Au)_x(Si,Ge)_{46-x-y}\square_y$* ; Workshop on Correlated Thermoelectrics: New materials for thermoelectric applications: theory and experiment; Hvar, Croatia; 19.-25.9.2011
6) *Non-centrosymmetric $EpTMX_3$ Superconductors: Crystal Structure and Physical Properties*; International Conference on Solid Compounds of Transition Elements (SCTE 2012); Lisbon, Portugal; 31.3.-5.4.2012
7) *Phase relations and melting behavior in clathrate systems $Ba_8\{Cu,Ag,Au\}_x\{Si,Ge\}_{46-x}$* ; Discussion Meeting on Thermodynamics of Alloys (TOFA 2012); Pula, Croatia; 23.9.-28.9.2012